## Physics-Based Compact Modeling of Valence-Change-Based Resistive Switching Devices

Von der Fakultät für Elektrotechnik und Informationstechnik der Rheinisch-Westfälischen Technischen Hochschule Aachen zur Erlangung des akademischen Grades einer Doktorin der Ingenieurwissenschaften genehmigte Dissertation

vorgelegt von

Camilla La Torre

M.Sc.

aus Duisburg

Berichter: Univ.-Prof. Dr.-Ing. Rainer Waser

Univ.-Prof. Dr.-Ing. Christoph Jungemann

Tag der mündlichen Prüfung: 25.07.2019

Diese Dissertation ist auf den Internetseiten der Universitätsbibliothek online verfügbar.

### **Abstract**

The demand for energy-efficient, fast, and small electronic memories is steadily rising in today's information technology. Redox-based resistive switching memories (ReRAM) based on the valence change mechanism (VCM) are a promising candidate for high-density data storage, neuromorphic computing, and logic-in-memory computing applications. Resistive switching memories are two-terminal devices whose physical storage principle relies on the change of the electrical resistance. The nonvolatile resistance state can be switched reversibly between at least two different levels by applying appropriate voltage signals. VCM-type memory cells are composed of a mixed ionic-electronic conducting oxide that is sandwiched between two electrodes. Typically, the two electrodes consist of metals with different work functions and oxygen affinities. Bipolar resistive switching is induced by the migration of ionic defects (oxygen vacancies) and a concurrent valence change of the cation sublattice.

To enable future design of memory, logic, and neuromorphic computing applications, circuit simulations based on precise and predictive compact models are crucial. Physics-based compact models do not use fitting parameters, but stick to material and geometrical parameters. Their great advantage lies in the power to predict the switching behavior upon changes in the input voltage amplitude and initial values. Compact models are developed based on the knowledge gained from more detailed, space-resolved models. Despite intensive research, open questions still remain, in particular, regarding the limiting physical mechanisms that are involved in resistive switching.

In this thesis, three physics-based compact models with different levels of detail are developed to study various switching effects in filamentary VCM-type ReRAM devices. All simulations are performed using MATLAB. Compact model 1.0 describes bipolar switching based on the drift of oxygen vacancies along a filament. The vacancies act as donors causing a change in conductivity, and thereby resistance, by modulating the Schottky barrier at the metal/oxide interface and the donor concentration in the adjacent oxide region. In compact model 1.5, the ion migration process is extended to include diffusion. Moreover, the modulation of both metal/oxide junctions is considered, allowing the model to cover complementary switching. In compact model 2.0, oxygen exchange at the metal/oxide interfaces is added enabling the simulation of the initial forming step as well as different endurance and retention behaviors. In addition to standard bipolar and complementary switching, a second bipolar switching mode is also covered. For the three models, the used assumptions and the model limits are emphasized to allow a correct interpretation of the simulation results. Various parameter studies are performed to identify the influence of material parameters, voltage excitation, and current compliance on the switching. This understanding will help to control the occurrence/suppression of intended/unintended effects by material choice or external excitation design.

## Kurzfassung

Der Bedarf an energieeffizienten, schnellen und kleinen Datenspeichern steigt im heutigen Informationszeitalter stetig an. Auf Redoxreaktionen basierende, resistiv schaltende Speicherzellen (ReRAM), die auf dem Valenzwechselmechanismus (VCM) beruhen, sind eine vielversprechende Technologie und werden als Kandidaten für zukünftige hochintegrierte Speicher- und Logikanwendungen gehandelt. Ebenso wird ihr Einsatz in neuronalen Netzen und neuromorphen Systemen diskutiert. Resistive Speicherzellen sind zweipolige, nichtflüchtige Bauelemente, deren physikalisches Speicherprinzip auf einer Anderung des elektrischen Widerstands basiert. Dabei wird der Widerstand der Speicherzelle durch Anlegen von geeigneten Spannungen reversibel zwischen mindestens zwei Zuständen geschaltet. VCM-Speicherzellen bestehen aus einer Oxidschicht, in der sowohl Elektronen als auch Ionen beweglich sind und zur Leitfähigkeit beitragen. Das Oxid wird durch zwei Elektroden kontaktiert, die typischerweise metallisch sind und unterschiedliche Austrittsarbeiten und Sauerstoffaffinitäten aufweisen. Bipolares Schalten wird durch die Bewegung von ionischen Defekten ausgelöst, die als Donatoren wirken. In der Regel handelt es sich dabei um Sauerstoffleerstellen. Die Bewegung führt – namensgebend für den VCM-Mechanismus – zu einem Valenzwechsel der Metallkationen.

Damit das Design von Schaltungen für Speicher-, Logik- und neuromorphe Anwendungen gelingt, werden Schaltungssimulationen benötigt, die akkurate Kompaktmodelle mit Prognosefähigkeit verwenden. Der große Vorteil von physikalisch-basierten Kompaktmodellen liegt in ihrer Fähigkeit, Änderungen des Schaltverhaltens bei Modifikation der Ansteuerung oder der Initialbedingungen richtig vorherzusagen. In diesen Modellen werden die Gleichungen und Parameter nicht frei gewählt, sondern nur physikalisch begründete Parameter und Funktionen verwendet. Die Entwicklung von Kompaktmodellen erfolgt mithilfe von Erkenntnissen, die aus detaillierteren und ortsaufgelösten Modellen gewonnen werden. Trotz intensiver Forschung konnten noch nicht alle limitierenden physikalischen Prozesse, die beim resistiven Schalten eine Rolle spielen, hinreichend geklärt werden.

In dieser Arbeit wird die Entwicklung von drei physikalisch-basierten Kompaktmodellen beschrieben, die sich in der Anzahl der berücksichtigten physikalischen Prozesse und damit in ihrem Detailgrad unterscheiden. Ziel dabei ist die Untersuchung von verschiedenen Schalteffekten, die in filamentär schaltenden VCM-Speicherzellen auftreten. Alle Simulationen wurden mit MATLAB durchgeführt. Kompaktmodell 1.0 beschreibt die durch das angelegte elektrische Feld gesteuerte Bewegung von Sauerstoffleerstellen in einem Filament. Dies führt zu einer Änderung der Leitfähigkeit und damit des Widerstands, da die Schottky-Barriere am Metall/Oxid-Übergang und die Donatordichte im Oxid moduliert werden. Im nächsten Schritt werden in Kompaktmodell 1.5 die Diffusion von Sauerstoffleerstellen sowie die Modulation des zweiten Metall/Oxid-Übergangs

ergänzt. Letzteres ermöglicht die Beschreibung von komplementärem Schalten zusätzlich zum standardmäßigen bipolaren Schalten. In Kompaktmodell 2.0 wird der Austausch von Sauerstoff an den Metall/Oxid-Übergängen hinzugefügt. Durch diese beträchtliche Erweiterung können sowohl der Initialisierungsprozess als auch verschiedene Lebensdaueranalysen sowie eine zweite bipolare Schaltart beschrieben werden. Um eine korrekte Interpretation der Ergebnisse zu ermöglichen, werden jeweils die Modellannahmen und die Grenzen der Modelle hervorgehoben. Parameterstudien helfen dabei, den Einfluss von Materialparametern, Spannungsansteuerung und Strombegrenzung auf das Schaltverhalten aufzuzeigen. Das so gewonnene Verständnis kann bei der Wahl der Materialien und dem Design der Ansteuerschaltung eingesetzt werden, um gewünschte Schalteffekte zu erzeugen bzw. unerwünschte zu vermeiden.

## **Acknowledgements**

This thesis was written during my time as a doctoral researcher at the IWE2 (Institut für Werkstoffe der Elektrotechnik 2) of RWTH Aachen University. This thesis would not have been possible without the support of many people and I would like to thank all contributors, colleagues, and friends for their assistance.

First, I would like to express my gratitude to Prof. Rainer Waser for giving me the opportunity to do research in his group. Further, I would like to thank Prof. Christoph Jungemann for kindly agreeing to be the co-examiner of my thesis.

I am truly thankful to Dr. Stephan Menzel for the excellent supervision of my work and great overall support. I deeply appreciate his continuous advice and encouragement which helped me to develop and pursue my own ideas. His valuable feedback had a great impact on the successful completion of my research.

I am deeply grateful to Andreas Kindsmüller for always sharing his insights on recent experimental findings. He ensured that I never lost the connection to the 'reality' of resistive switching devices. Special thanks also go to Alexander Zurhelle who worked with me on the modeling of the oxygen exchange. Without him, (electro-)chemistry would still be my nightmare.

This work has benefited greatly from experimental results, and I owe my thanks to Karsten Fleck, Alexander Hardtdegen, Thomas Breuer, and Andreas Kindsmüller for sharing their data and for many fruitful collaborations.

For providing an excellent working atmosphere, I would like to thank the whole research group at the IWE2 in Aachen and the PGI-7/10 in Jülich and especially my great office mates Sergej Starschich, Inka Nielen, Carlos Rosário, Anne Siemon, and Alexander Zurhelle.

Furthermore, I would like to thank Ulrich Böttger and Martina Heins for the great administrative help and support, Thomas Pössinger for the excellent graphical assistance, and Udo Evertz for the outstanding technical support.

Special thanks go to Eike Linn for all his support and guidance during my time as bachelor and master student. I learned a lot from him.

I further acknowledge the helpful support of my student research assistants Maximilian Kühn, Florian Renneke, Sebastian Siegel, Michael Schulten, Veit Langrock, Michael Frentzen, Jonas Meyer, Fenja Berg, Michael Burgardt, Qian Ding, and Kaihua Zhang.

Finally, special thanks go to Matthias for simply being there whenever it was needed.

## **Contents**

1	Intr	troduction					
2	Fun 2.1 2.2 2.3 2.4 2.5 2.6	2.2 Valence Change Memory					
3	Con	npact Model 1.0	35				
	3.1	Model Description and Equations	36				
	3.2	Simulation Results	39				
		3.2.1 General Model Characteristics	39				
		3.2.2 Gradual and Abrupt RESET	44				
		3.2.3 Gradual and Abrupt SET	48				
	3.3	Conclusion	57				
4	Con	pact Model 1.5	59				
	4.1	Model Description and Equations	60				
	4.2	Simulation Results	65				
		4.2.1 General Model Characteristics	65				
		4.2.2 Complementary Switching (CS)	72				
		4.2.3 CS Influence on Bipolar Switching	83				
	4.3	Conclusion	87				
5	Con	pact Model 2.0	89				
	5.1	Oxygen Exchange at the Electrode	90				
	5.2	Model Description and Equations	93				
	5.3	Simulation Results	100				
		5.3.1 Forming	100				
		5.3.2 Forming and Subsequent Sweeps					
		5.3.3 Endurance and Retention					
		5.3.4 Eightwise Switching					
	5 4	Conclusion	133				

6	Con	clusions	137
	6.1	Summary	. 137
		Outlook	
Α	Арр	pendices	143
	A.1	Derivation of the Ionic Current Density	. 143
	A.2	Additional Parameters	. 145
	A.3	Volatile HRS Asymmetry and Subloops	. 146
Bi	bliog	raphy	147
Lis	t of	Publications	163

## **Abbreviations**

 $8w\ \dots \dots \ eightwise$ 

AE ...... active electrode
BS ..... bipolar switching
c8w ..... counter-eightwise

CS ..... complementary switching

HRS ...... high resistive state
LRS ..... low resistive state
OE ..... ohmic electrode

ReRAM ..... redox-based resistive switching random access memory

VCM ..... valence change memory

CBRAM ...... conductive bridging random access memory

CC ..... current compliance

CRS ...... complementary resistive switches
DRAM ...... dynamic random access memory
ECM ...... electrochemical metallization memory

FE ..... field emission

MIEC ..... mixed ionic electronic conducting layer MRAM ..... magnetoresistive random access memory

ODE ..... ordinary differential equation

OEL ..... oxygen exchange layer

OxRAM ..... oxide-based random access memory

PCM ..... phase change memory

PMC ..... programmable metallization cells

RESET ..... transition from LRS to HRS (no abbreviation)

RRAM ..... resistive random access memory

SET ..... transition from HRS to LRS (no abbreviation)

SRAM ...... static random access memory
TCM ..... thermochemical memory
TE ..... thermionic emission
TFE ..... thermionic field emission

## 1 Introduction

The demand for energy-efficient, fast and ultimately small electronic memories is steadily rising in today's information technology. The exponentially growing need of integrated circuits consisting of more and more components was already foreseen by Gordon Moore more than 50 year ago [1]. His prediction is well known as Moore's law and it served the semiconductor industry over decades as roadmap for fast progress in computing technology [2]. As the transistor size approaches its physical limit, (geometrical) scaling is not a feasible route anymore. Common memory technologies like DRAM (dynamic random access memory), SRAM (static random access memory) or flash memory require the use of transistors. Therefore, they are affected by the transistor scaling capability. Future progress in these conventional memory technologies can only be achieved by material improvement ('equivalent scaling') or stacking in vertical direction ('3D power scaling') [2]. Another approach to overcome the scaling limit is the development of new memory architectures that are not based on transistors and thus can be scaled even further. New memory devices, however, can only be integrated successfully in the market if they clearly outperform a conventional technology or bridge a gap in the market. Besides the feature size, the performance of memory technologies is measured for example in terms of volatility/data retention, endurance, power consumption, read and write times (access time), or multilevel capability (number of bits per cell). The ideal memory would comprise an ultra-high retention and endurance while using nearly no power and allowing ultra-short access times. In the real world, however, trade-offs are unavoidable. For example, the trade-off between a high retention and a short write time is known as voltage—time dilemma [3]. For two-terminal devices, an ultrahigh nonlinearity of the switching kinetics is needed if, on one hand, a state has to be stable at a low read voltage for a constant read-out and, on the other hand, very fast switching at a write voltage is required that is only slightly higher to keep the power consumption low.

DRAM and SRAM are volatile memories, i.e. power is required to maintain the stored information. DRAM is used as main memory because the write time is low and it can sustain many write cycles, i.e. it has a high endurance. The information is stored as

electric charge on a capacitor. The main drawback lies in the necessary refresh cycles, which lead to a comparatively high power consumption. SRAM, which uses a storage principle based on flip-flops, is faster than DRAM and has a lower power consumption. It is less dense than DRAM though and consequently more expensive because it requires six transistors instead of one as DRAM does. It is typically used in processor cache memories where speed is most important. Nonvolatile flash memories are used for data storage in, for example, solid state drives, USB flash drives, or memory cards. The information is stored by charging the floating gate of a transistor. As only one transistor is required, the device area is small. Flash memories suffer from high write and read voltages and a slow access time. A performance comparison of SRAM, DRAM, and flash memories can be found in [4]; a detailed description of the physical mechanisms of DRAM and flash memories is given in [5, 6].

Redox-based resistive switching random access memories (ReRAM) are a promising candidate for the so-called storage class memory that bridges the gap between the fast volatile memories (SRAM, DRAM) and slower but nonvolatile memories for data mass storage (flash memory) [7–12]. Moreover, they are studied intensely due to their beyondmemory functionality in neuromorphic computing and logic-in-memory computing applications [4, 12–16]. A ReRAM cell is a two-terminal device, which consists of a thin functional (oxide) layer sandwiched between two electrodes. The information is stored in the resistance level, which can be switched between at least two different states by applying appropriate voltage signals. Due to its simple structure, it offers an excellent scaling capability. ReRAMs based on the valence change mechanism are, at least for non-exotic material stacks, fully CMOS-compatible and show multilevel capability [17– 19] and 3D-scaling capability [20, 21]. The write voltage, being in the range of 1–2 V, is far smaller than for flash memories. With write times in sub-nanosecond range [22–24], it is potentially as fast as DRAM. The energy consumption is low; it was shown to be  $< 1\,\mathrm{pJ/bit}$  for fast switching [25, 26]. The endurance can exceed  $10^{12}$  cycles [27] and an extrapolated retention over 10 years at 150 °C was shown [28].

Resistive switching phenomena were already reported in the 1960s, but the research activities faded in the 1980s until a new era of intensive research started in the late 1990s. Reviews of the early research can be found in [29–31]. In 2008, ReRAM devices were linked to the theoretical concept of a memristor [32], which was introduced by Leon Chua in the 1970s [33, 34], because their current–voltage characteristics bear a certain resemblance. The link to the memristor concept, 'memristor' being a combination of 'memory' and 'resistor', attracted a lot of attention amongst circuit designers. Although ReRAM

devices are no true memristors according to theoretical reasoning [35], 'ReRAM', 'memristor', and 'memristive device' are often used interchangeably in literature. At the beginning of the 2010s, the idea of using ReRAM in bio-inspired/neuromorphic computing further increased the research activity [12, 36, 37].

To reveal the underlying physical processes, numerous simulation studies were presented in literature, besides various experimental studies. Thereby, the simulations range from atomistic calculations [38–41] over space-resolved continuum models [42–44] and kinetic Monte Carlo models [45–47] to compact models [48–56]. In general, the simulation time increases with the level of detail and this limits the typical application. For example, specific questions regarding material parameters or electronic/ionic conduction can be addressed successfully on an atomistic level. The simulation of a whole switching transition, however, is not feasible. The findings of an atomistic study can be employed in less detailed, but potentially also highly accurate, space-resolved models that can simulate the whole switching process of ReRAM devices. In turn, compact models rely on the knowledge gained from these continuum models. Despite the intensive research, open questions still remain, in particular, regarding the limiting physical mechanisms that are involved in resistive switching.

To enable future design of memory, logic, and neuromorphic computing applications, circuit simulations based on precise and predictive compact models are crucial. The complexity of compact models is reduced to allow for circuit simulations of crossbar arrays with numerous devices. Therefore, a loss of accuracy has to be accepted. Basically, three types of compact models can be distinguished: models based on generalized equations fitted to match the current-voltage characteristic of one specific device, physics-related models, and physics-based models. In contrast to the other, physics-based compact models do not use fitting parameters, but stick to material and geometrical parameters. Many compact models in the literature can be classified as physics-related models: physicsbased equations combined with a mixture of material and fitting parameters. Physicsbased models may be less appropriate if precise conformity of a simulated and one experimental I-V curve is the only requirement. Their advantage, however, lies in the power to predict the switching behavior upon changes in the input voltage amplitude and initial values. Thereby, the switching dynamics play a key role as, for example, unavoidable voltage drops across non-selected devices in crossbar arrays can present a severe reliability issue, if they are disregarded. Circuit simulations based on predictive compact models can reveal and help to solve such problems. Several criteria have been formulated, which should be met by compact models in order to qualify for the application in predictive circuit simulation analyses [57, 58]. Besides providing nonlinear switching kinetics and an appropriate response to changes in the voltage signal, these include multilevel capability and state-dependent switching times. Moreover, the models needs to be applicable to describe complimentary resistive switches (CRS) consisting of an anti-serial connection of two single devices, which results in a switching between two high resistive states. Due to the fast simulation time, physics-based compact models are particularly well suited to study retention and endurance of ReRAM devices and to address the impact of different materials on the switching.

Besides being physics-based or physics-related, compact models for filamentary switching ReRAM devices differ in the state variable(s) and the kind of physical processes that are implemented. For the state variable, various parameters have been used, e.g. the gap between the conductive filament and the electrode (sometimes referred to as tunneling gap) [48, 49, 59, 60], the diameter of the conductive filament [61, 62], the cross-sectional area of a quantum-point-contact constriction [50, 63], or the dopant concentration near a Schottky barrier [52]. Models with two state variables often combine approaches that use the gap, the filament diameter (cross-sectional area), and/or the temperature [53, 54, 56, 64, 65]. The dynamic equations that describe the filament change are based on, or often just motivated with, different physical processes. Some are speculative in nature. Examples for the considered processes are recombination/generation of oxygen vacancies and oxygen interstitials [66], field- and temperature-driven migration of dopants [61], diffusion and thermodiffusion of dopants [56], or generalized oxidation and reduction reactions [64]. Often, one temperature is considered for the whole filament, but some models apply different temperatures for critical parts of the filament or describe an additional temperature for the surrounding oxide, which differs from the ambient temperature [56, 64, 67]. The electrical model usually comprises generalized equations with fitting parameters [51, 53, 55, 56]. Switching variability can be addressed in compact models by applying distribution functions to specific parameters [65, 68, 69]. So far, retention failures and state instabilities were only studied based on analytical models, e.g. in [70, 71], which do not describe the whole switching process. Except for the models considering contact potentials (Schottky barriers) [48, 52], the vast majority of the models is independent of the electrodes and their work functions, neglecting the important polarity dependence of ReRAM devices. If the change of the filament diameter is modeled based on the drift of dopants [61, 62], the polarity of the applied voltage and the direction of the electric field are completely ignored because the applied electric field is perpendicular to the assumed migration direction of the ions.

This thesis focuses on the development of predictive physics-based compact models for filamentary switching ReRAM devices based on the valence change mechanism (VCM). The simulations are performed using MATLAB. Chapter 2 gives a brief description of the classification of ReRAMs, the physics of the valence change mechanism, the involved processes, and the simulation methods required for compact modeling. In total, three compact models with different levels of detail are presented in chapters 3-5. In each chapter, the general model characteristics are demonstrated after a complete model description. Subsequently, the simulation results are compared to experimental data. Chapter 3 presents a physics-based compact model for filamentary, counter-eightwise switching VCM devices that meets all the standard criteria for predictive models described above. It is based on the previous work by Siemon et al. [52] and describes the switching using field- and temperature-driven migration of dopants that leads to a concentration change near a Schottky barrier. A detailed and comprehensive analysis of both switching transitions (SET and RESET) reveals the critical factors for gradual and abrupt switching. This model is improved further in chapter 4 as both filament regions are made variable exchanging ions by drift and diffusion. The extension enables the model to capture bipolar and complementary switching consistently, which has not been shown before with a compact model. Moreover, including complementary switching allows to explain anomalies and failures of bipolar switching. In chapter 5, the compact model is taken to the next level by incorporating electrode reactions that play a crucial role in filamentary VCM devices during forming and switching. For the first time, the forming step can be described consistently with subsequent switching sweeps. Moreover, the extended compact model allows the simulation of various endurance and retention studies. Besides the more common counter-eightwise switching mode, the eightwise switching direction can occur depending on different parameters concerning the electronic and ionic conduction and the electrode interfaces. So far, no other compact model combines the possibilities to perform forming, switching, endurance, and retention studies. Finally, the results of this thesis are summarized in chapter 6 and an outlook on further model improvements and simulations is presented.

## 2 Fundamentals

#### 2.1 General Characteristics and Classification of ReRAM

Redox-based resistive switching random access memory (ReRAM) belongs to the class of nonvolatile resistive RAM (RRAM) [72]. RRAM comprises various memories whose physical storage principle relies on the change of the electrical resistance. Besides ReRAM, other prominent examples for RRAM are phase change memory (PCM) and magnetoresistive random access memory (MRAM). In contrast to PCM and MRAM, the resistance variation in ReRAM devices is induced by local redox reactions. The terms ReRAM and RRAM are sometimes used synonymously in literature; this thesis follows the definition in [72]. In general, a ReRAM device consists of a MIM structure, i.e. two (metal) electrodes (M) and an I-layer that is either an insulating ion conductor or a mixed ionic electronic conductor [8].

The resistance state in ReRAM cells can be switched reversibly between at least two different levels by applying appropriate voltage pulses or sweeps. The transition from the low resistive state (LRS/ON) to the high resistive state (HRS/OFF) is called RESET, the reverse process is the SET process. If more than two resistance levels are stable and can be programmed reversibly, the cell shows multilevel capability. Based on the polarity of the write voltage, ReRAM devices are divided into unipolar and bipolar switching cells. In bipolar switching (BS) devices, the polarity of the voltage required to trigger SET and RESET transition differs.

Based on the microscopic switching mechanism, three different types of ReRAM are distinguished [8]: electrochemical metallization memory (ECM), also called conductive bridging random access memory (CBRAM) or programmable metallization cells (PMC), valence change memory (VCM), also called oxide-based random access memory (Ox-RAM), and thermochemical memory (TCM). ECM cells consist of an ion-conducting insulating layer sandwiched between a chemically active electrode (Ag or Cu) and a chemically inert electrode. The bipolar switching relies on the electrochemical growth and dissolution of a Ag or Cu conductive filament. In TCM cells, thermochemical pro-

cesses dominate over electrochemical processes. The switching in the metal oxides only depends on the current amplitude and not on the voltage polarity as local temperature gradients lead to stoichiometric variations. Thus, the switching is unipolar. Detailed descriptions of ECM and TCM are given in [72–76] and [72, 77, 78], respectively. VCM cells consist of a mixed ionic electronic conducting layer (MIEC) and two typically different electrodes. Bipolar resistive switching is induced by the migration of ionic defects and a concurrent valence change of the cation sublattice [75]. This thesis solely addresses VCM devices and their switching mechanism is discussed in detail in the next section.

#### 2.2 Valence Change Memory

VCM switching is found in ReRAM devices based on binary oxides like  $HfO_x$ ,  $ZrO_x$ ,  $TaO_x$ ,  $TiO_x$  and ternary oxides like  $SrTiO_x$  [8, 9, 72]. Typically, the two electrodes consist of metals with different work functions and oxygen affinities. The electrode with a high work function and a low oxygen affinity forms a Schottky-type contact with the oxide. This electrode is called (electronically) active electrode (**AE**) as the switching is assumed to take place at or near this interface. Pt and TiN are often used as active electrode. The opposite electrode with a low work function forms, in the ideal case, an ohmic contact with the oxide. Thus, it is called ohmic electrode (**OE**). The ohmic electrode usually consists of easily oxidizable metals like Hf, Zr, Ta, Ti, so that an oxygen exchange between the deposited oxide and the electrode is likely [79]. If the electrode is oxidized near the interface, the term oxygen exchange layer (**OEL**) is also used. To improve the switching characteristics, the formation of an OEL can be facilitated by defect engineering of the oxide [27] or by bilayer approaches with two stacked oxides [80, 81].

#### **Forming**

If the oxide is stoichiometric or nearly stoichiometric and thus highly insulating in the pristine state, an electroforming step — in short called *forming* — is required to enable stable switching. By applying a comparatively high voltage, the oxide is locally reduced during forming, i.e. oxygen vacancies are generated in the oxide, and the device resistance decreases considerably [8, 82]. If a conductive filament, i.e. a confined region which is well conducting, is generated during the forming process, the switching is called filamentary. The opposite is known as homogenous or interface-type switching. In that case, the device resistance scales with the device area as the whole electrode area is

involved in the switching process [72]. Both switching modes can occur in the same device [83]. This thesis only deals with n-conducting filamentary VCM devices.

Depending on the material stack, the device after forming is in a state that resembles the LRS or HRS [84]. Also the required polarity of the forming voltage varies for different material systems [84]. If the forming is done with the same polarity as the SET, the device is usually in the LRS afterwards. In that case, a current compliance is often applied to prevent a destruction of the device. In general, an efficient current control is necessary if the forming proceeds abruptly (hard breakdown) as this involves an abrupt current increase. If the voltage required to trigger the forming process is close to the subsequent SET switching voltage, the device is called forming-free.

The most plausible mechanism for oxygen vacancy generation is the extraction of oxygen at the interface [85–87]. The generation of anti-Frenkel pairs in the bulk, i.e. oxygen vacancies and oxygen interstitials, is highly unlikely under the present electric fields during forming [85]. In addition, generated anti-Frenkel pairs would recombine on a time scale < 1 ps [85, 87]. The oxygen is then either stored in the anode, e.g. by oxidizing the anode [88], or released as gaseous oxygen [82, 89]. The oxygen vacancies that remain in the oxide are positively charged relative to the perfect crystal<sup>1</sup> and migrate through the MIEC in the direction of the electric field.

One experimental study [91] and several simulation studies [47, 92, 93] have shown that the filament can grow either from the cathode to the anode or the other way round. The growth direction depends on the used material stack, as the relation between oxygen exchange rate and ion migration barrier is crucial [92]. In devices with OEL, the filament grows most likely from the OEL to the other electrode regardless of the polarity of the forming voltage [91]. For a Hf/HfO<sub>x</sub>/TiN device, a 3D conductivity tomography experiment revealed that the conductive filament is of conical shape and exhibits a constriction near the oxygen-inert electrode [94]. If the filament grows from the cathode to the anode, the generated vacancies migrate to the cathode and pile up there. This creates a conducting region at the cathode, often called 'virtual cathode', which propagates to the anode [8].

Experimental evidence for the presence of oxygen vacancies in the conductive filament was presented for a Fe-doped SrTiO<sub>3</sub> device using scanning transmission electron microscopy and core-less spectroscopy [95]. The conical filaments exhibit a high local

They are denoted by  $V_O^{\bullet \bullet}$  in the common Kröger–Vink notation, which describes the electric charge and lattice position of point defects in crystals [90]. The V indicates the species, here V stands for vacancy. The subscript corresponds to the lattice site, here an oxygen site (O). The superscript specifies the electric charge of the species relative to the lattice site. Thereby,  $^{\bullet}$ , ', and  $^{\times}$  indicate a net positive, negative, and zero charge, respectively.

concentration of Ti<sup>3+</sup>, which correlates to the presence of oxygen vacancies. Strontium vacancies also exist in the filaments. Despite the high defect concentration, the perovskite lattice structure is essentially preserved. The experiment showed that not one
but several defect areas developed during forming. They were advanced to different
stages of completion, but only one was grown completely.

Prior to the formation of a stable filament due to atomic migration, initial electronic processes play an important role [96]: Pulse measurements revealed that the initial part of the sharp resistance decrease in Pt/Ta<sub>2</sub>O<sub>5-x</sub>/Pt and Pt/TiO<sub>2-x</sub>/Pt crossbar devices is volatile and therefore has to be electronic in nature rather than involving atomic motion. Electronic instabilities lead to a reversible constriction of the current flow. Eventually, the high localized current causes a sufficiently high local temperature due to Joule heating that triggers the atomic processes leading to a formation of a permanent filament: The high temperature increases the oxygen mobility and exchange rate. Continuously, the rising oxygen vacancy concentration leads to an increase in current, which in turn increases the temperature. If Joule heating plays a crucial role, this process becomes self-accelerating and results in an abrupt current jump that is characteristic for the forming process [72, 75]. Consequently, the forming process can be structured into four stages: initial electronic processes, creation of oxygen vacancies, filament growth, and completion.

The filament formation may be favored at spots where initial defects exist that favor the oxygen release [95], assisted by initial electronic processes [96]. These may initiate the formation in cases where local defects do not exist. It is unlikely that the filament growth proceeds along dislocations or grain boundaries as the oxygen diffusion is slower there than in the bulk [97, 98]. The presence of moisture/hydrogen is discussed to be necessary for the interface reaction to take place during forming [99]. Experiments and simulations revealed that a treatment with hydrogen leads to improved switching characteristics and device yields [41, 100–102].

#### Bipolar switching modes

Two fundamental switching modes can be distinguished in VCM cells by considering the voltage polarity that is necessary to trigger SET and RESET: eightwise (8w) switching and counter-eightwise (c8w) switching. The name refers to the drawing direction of a handwritten, tilted "8" [72]. If the voltage is applied to the active electrode and the ohmic electrode is grounded, the SET occurs with a negative polarity in c8w switching systems and with a positive polarity in 8w switching systems. Standard I-V characteristics of

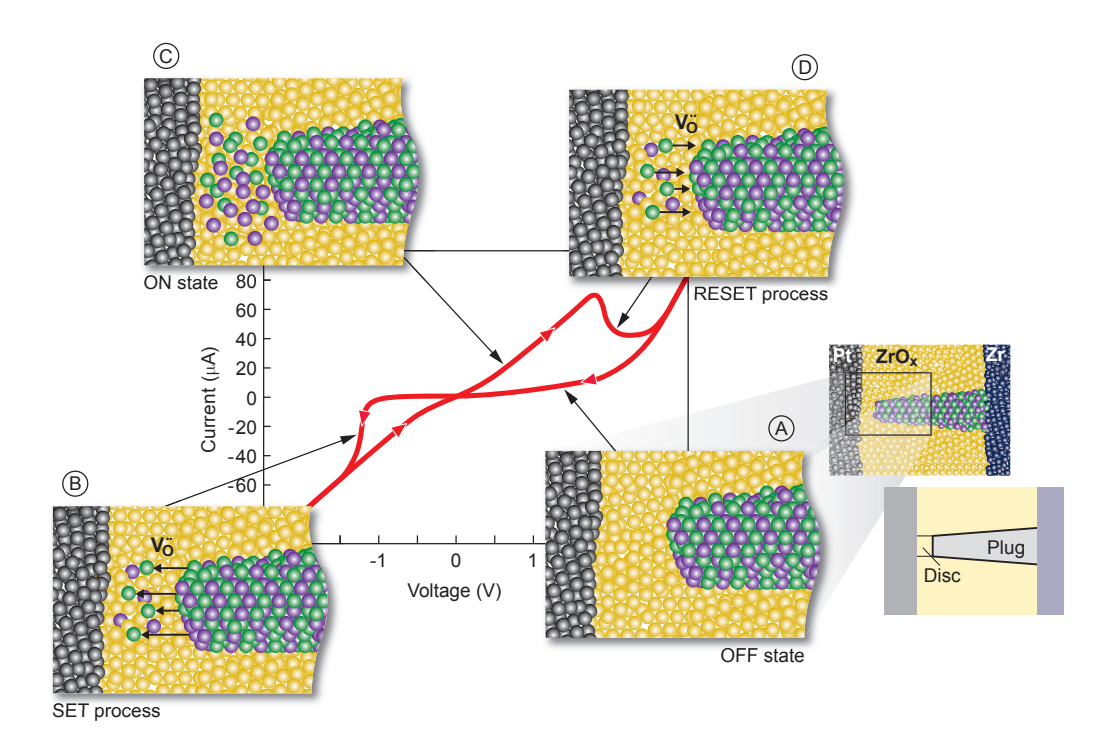


Figure 2.1: VCM counter-eightwise (c8w) switching mechanism. Schematic I-V characteristic of the c8w switching mode in combination with sketches of the internal states and processes during switching. The bipolar switching is based on the redistribution of oxygen vacancies in the filament near the active electrode. The SET occurs for a negative potential applied to the active electrode. Oxygen vacancies and immobile metal cations in a lower valence state, here Zr ions, are indicated by green and violet spheres, respectively. Yellow spheres represent the stoichiometric oxide. The active electrode, here Pt, is shown in gray on the left side. Reproduced with permission from [72], ©2012 Wiley-VCH Verlag GmbH & Co. KGaA, Weinheim.

c8w and 8w switching modes are depicted in Figs. 2.1 and 2.2, respectively. The c8w mode is the more common switching mode, accordingly, 8w switching is also named anomalous switching [103]. They are not mutually exclusive but there are several reports on devices that show both switching polarities [104–107]. Thus, the following model descriptions for c8w and 8w switching refer to ideal cases.

The c8w switching mechanism is based on the redistribution of oxygen vacancies (or other mobile donors) in the filament near the active electrode [72, 75]. The electrodes are regarded as oxygen-inert during switching. Thus, the total amount of vacancies in the filament stays constant during switching and is determined by the forming step. The filament consists roughly of two parts, *plug* and *disc*, see Fig. 2.1. The disc is the region near the active electrode in which the concentration of oxygen vacancies changes during switching. Because oxygen vacancies act as mobile donors, the interface conduction and

the local oxide conductivity are modified. Thus, the disc is the part of the filament where the actual switching takes place. The influence of donors on the conduction across the AE/oxide interface is described in detail in section 2.3. The plug is composed of a reduced oxide and stays well conducting throughout the whole switching process. In the HRS, the disc is oxidized and consequently, the current is low. This state with (nearly) no oxygen vacancies in the disc is depicted in Fig. 2.1(A). The oxygen vacancies are symbolized as green spheres, whereas the violet spheres indicate metal ions in a lower valence state. Applying a negative voltage to the active electrode attracts the positively charged vacancies into the disc, which results in a valence change in the cation sublattice (Fig. 2.1(B)). Through the reduction of the oxide at the interface, the conductivity is increased as the barrier width and height are decreased. Similar to the forming, the rising current increases the temperature by Joule heating and enhances the vacancy mobility resulting in a positive feedback. After the SET, the device is in the LRS (Fig. 2.1(C)). The RESET is started by applying a positive potential to the AE, which repels the vacancies from the AE. The ions migrate from the disc into the plug oxidizing the cation sublattice in the disc (Fig. 2.1(D)).

The c8w switching mechanism is commonly acknowledged to rely on the redistribution of mobile donors and several numerical simulations have been published reproducing this switching mode [42, 43, 108, 109]. In [42, 43], however, solely bulk conduction is assumed making it impossible to define a switching mode in terms of c8w or 8w switching. In the simulations by Marchewka et al. [108, 109], the contact potential of both electrodes is considered in addition, correctly reproducing the c8w switching mechanism as described above. Besides oxygen vacancies, the migration of cation interstitials could also explain the switching direction, as they could act as donors and they have been shown to be mobile in oxides [110]. In the simplified picture described above, the ohmic electrode does not play a role during switching as long as the contact resistance is small enough. On the other hand, several reports have shown that devices with different ohmic electrodes exhibit different switching characteristics [111–113]. This can result from the changed starting conditions obtained by the forming step. It was also shown though that the SET and RESET kinetics of TaO<sub>x</sub>-based devices were influenced by the ohmic electrode material in opposite ways [114]. Therefore, a more accurate model of c8w switching has to consider oxygen exchange at the electrodes during switching and, possibly, the influence of hydrogen [41, 100–102].

The 8w switching mode can be explained by considering an oxygen evolution and reincorporation at the active electrode during SET and RESET [103]. In that case, the

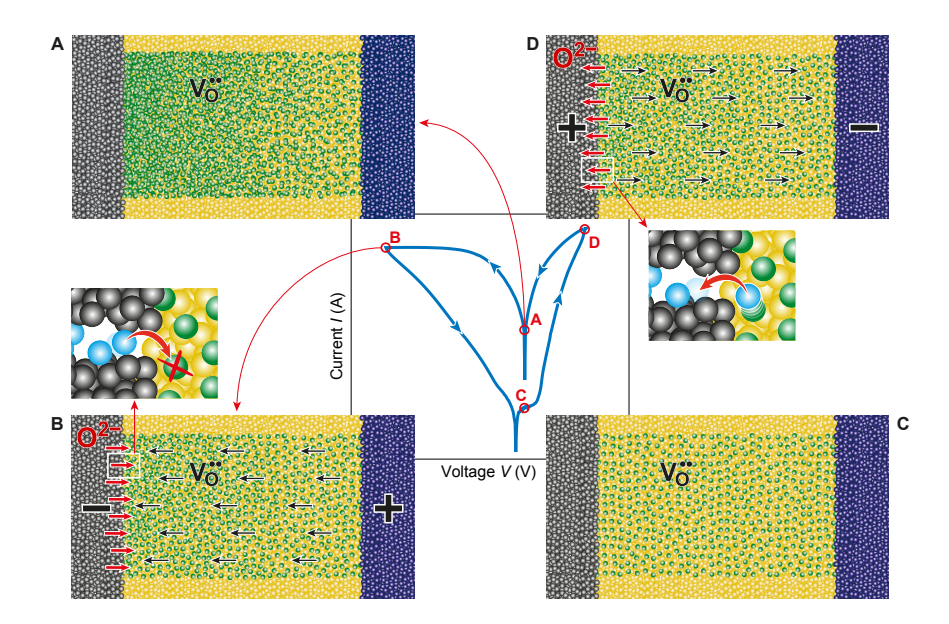


Figure 2.2: VCM eightwise (8w) switching mechanism. Schematic  $\log(I)$ –V characteristic of the 8w switching mode in combination with sketches of the internal states and processes during switching. The bipolar switching relies on oxygen evolution and reincorporation at the active electrode. The SET occurs for a positive potential applied to the active electrode. Oxygen and oxygen vacancies are indicated by blue and green spheres, respectively. Yellow spheres represent the stoichiometric oxide. The active electrode is shown in gray on the left side. Reproduced with permission from [103], © 2017 Wiley-VCH Verlag GmbH & Co. KGaA, Weinheim.

total amount of oxygen vacancies in the filament varies during switching. The LRS is characterized by a high concentration of oxygen vacancies near the active electrode, see Fig. 2.2A. If the active electrode forms a much higher Schottky barrier with the oxide than the counter electrode, the vacancy concentration should be higher at the active electrode due to internal electric fields, as depicted in the inset. Applying a negative voltage at this electrode leads to a reincorporation of oxygen into the reduced oxide, thereby annihilating oxygen vacancies (Fig. 2.2B). This implies that oxygen exists as adsorbed species in the electrode in the LRS. How exactly the oxygen is adsorbed in the electrode, i.e. whether this is an effect of physisorption or chemisorption within grain boundaries, is subject to current research. Due to the electric field in the oxide, the vacancies migrate to the AE providing a constant supply of reactants for the exchange process during the RESET. As the oxygen vacancy concentration is reduced by the exchange reaction, the conductivity is lowered and the device is in the HRS (Fig. 2.2C). The SET takes place at a positive applied voltage to the AE when oxygen ions are removed from the oxide, thereby increasing the concentration of oxygen vacancies in

the filament again (Fig. 2.2D). As shown in the exemplary  $\log(I)-V$  curve, SET and RESET proceed rather gradual.

The proposed 8w switching mechanism was experimentally validated. In operando spectromicroscopy revealed that redox reactions drive the resistance change and the modification of the charge carrier concentrations could be quantified, at least in the studied 8w switching  $SrTiO_3$ -based device [115]: The charge carrier concentrations near the active electrode were determined to  $1.5 \cdot 10^{21}$  cm<sup>-3</sup> (LRS) and  $6.7 \cdot 10^{20}$  cm<sup>-3</sup> (HRS) by XPEEM (photoemission electron microscopy (PEEM) operated in absorption mode with X-ray excitation). Based on these values, a simulation showed that a change in device resistance of more than two orders of magnitude by modulating the effective Schottky barrier [115].

The main focus of this thesis lies on the modeling of c8w switching devices.

#### **Complementary Switching**

Complementary switching (CS) is an additional switching mode that is found in VCM devices [116–118]. A schematic I-V characteristic is shown in Fig. 2.3. By applying bipolar voltage signals, CS devices can be switched between two high resistive states that may have the same resistance but differ internally, see Fig. 2.3 (A) and (B). Only during switching, a transition state occurs in which the CS device is shortly in a low resistive state. Like c8w switching, CS is based on the redistribution of oxygen vacancies (or other mobile donors) in the filament. In contrast to the c8w mode, switching takes place at both interfaces [119, 120]. The oxygen vacancies are shifted between the two interfaces modifying the conductivity of the metal/oxide contacts. This shifting was shown by space-resolved numerical models [43, 108, 121, 122] and by measurements exploiting the multilevel capability of the bipolar switching at both interfaces [123]. Experiments have also shown that both rectifying interfaces in a symmetric device can dominate the electrical conductivity alternately [124]. Due to their related physical switching mechanism, CS and BS can coexist in one device [119, 120, 125–128]. The switching of CS devices is covered in detail in chapter 4.

CS devices show the same characteristics as complementary resistive switches (CRS), which consist of two anti-serially connected bipolar switching cells [129]. In 2010, CRS cells were introduced as a concept to reduce the amount of sneak currents through non-selected elements in passive crossbar arrays during read operation. Due to the anti-serial connection, one of the two bipolar cells is always in the HRS. Thus, in CRS devices the

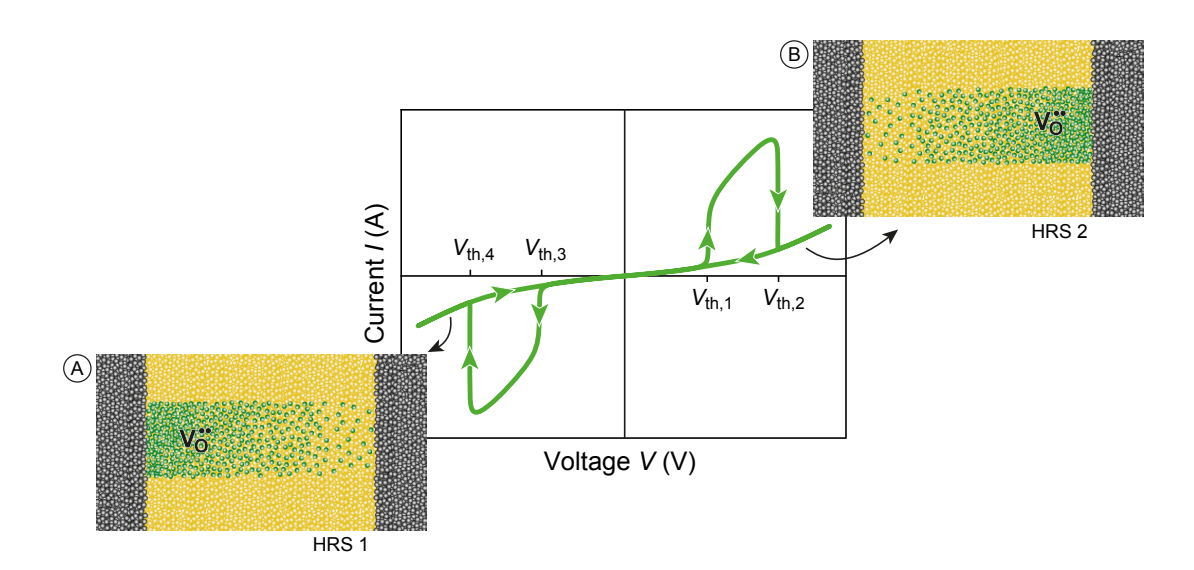


**Figure 2.3:** Schematic *I–V* characteristic of a complementary switching device in combination with sketches of the two stable internal states. CS devices switch between two high resistive states by applying bipolar voltages. During the transition, the overall resistance is low. Oxygen vacancies and the stoichiometric oxide are indicated by green and yellow spheres, respectively.

information is also stored in two overall high resistive states. Consequently, all non-selected elements have a high resistance during read operation, thereby reducing the amount of sneak current that adds to the read signal. Regarding the fabrication costs, CS cells are beneficial compared to CRS cells as they have a simpler layer structure. Besides the application of CS/CRS cells as memory, logic-in-memory approaches based on CRS or CS devices have been proposed (CRS) [130–132], simulated (CRS) [133] and experimentally confirmed (CRS and CS) [15, 134, 135].

If the two high resistive states HRS 1 and HRS 2 are not distinguishable by a (non-destructive) read-out at a low voltage, a destructive 'spike-read' scheme has to be applied [134]: Switching from HRS 1 (state A) to HRS 2 (state B) requires a transition through a low resistive state. Thus, applying a voltage  $V > V_{\text{th},2}$  leads to a current spike if the cell is in HRS 1. If the cell is in HRS 2, the internal state is not changed upon application of a voltage  $V > V_{\text{th},2}$  and consequently, no current spike occurs. Analogously, the scheme works with a voltage  $V < V_{\text{th},4}$ .

# 2.3 Electrical Conduction across Metal/Semiconductor Contacts

The resistance change in metal/oxide/metal systems is attributed to a modulation of the Schottky barriers. Due to the difference between the work function of the metal and the electron affinity of the semiconductor, a potential barrier forms at a metal/semiconductor (or metal/insulator) interface. An accurate description of the current conductance across a Schottky junction, also called Schottky diode or contact, is therefore crucial for the simulation of VCM-type ReRAM devices. In contrast to a Schottky contact, an ohmic contact is non-rectifying and provides a low ohmic connection between semiconductor and metal for all voltages and both voltage polarities. The current transport through a Schottky junction can be calculated accurately by applying the Tsu–Esaki formalism and solving it numerically [136, 137]:

$$J = \frac{4\pi m_{\text{eff}}e}{h^3} \int_{W_{\text{min}}}^{W_{\text{max}}} TC(W) \cdot N_{\text{supply}}(W) \, dW.$$
 (2.1)

Here, TC and  $N_{\text{supply}}$  are the transmission coefficient and the supply function, respectively. The effective mass is denoted by  $m_{\text{eff}}$ . Furthermore, e is the elementary charge and h is the Planck constant. The supply function incorporates the information of the distribution function of the electrons at both sides of the barrier, whereas the transmission coefficient includes the barrier shape that is tunneled through. Both depend on the energy W of the electron and an integration over an energy interval from  $W_{\min}$ to  $W_{\text{max}}$  yields the whole current density. The choice of  $W_{\text{min}}$  and  $W_{\text{max}}$  depends on the conduction process that is studied. In [44], this formalism is applied to model the Schottky junctions in a ReRAM device using appropriate approximations. Solving an integral over energy numerically in every step, however, is not only computationally intensive but it is also difficult to implement in a circuit simulator. Thus, compact models have to use simplified analytic expressions for the current to be applicable for circuit simulations. In general, the current through a Schottky junction can be classified into three regimes [138]: thermionic emission (TE), thermionic field emission (TFE) and field emission (FE). Thermionic emission describes the conduction of electrons with an energy higher than the barrier. Field emission means tunneling of electrons near the Fermi level, and thermionic field emission is characterized by tunneling of thermally excited electrons. Analytic expressions for the current were derived by Bethe for the thermionic emission [139] and by Padovani and Stratton for thermionic-field emission

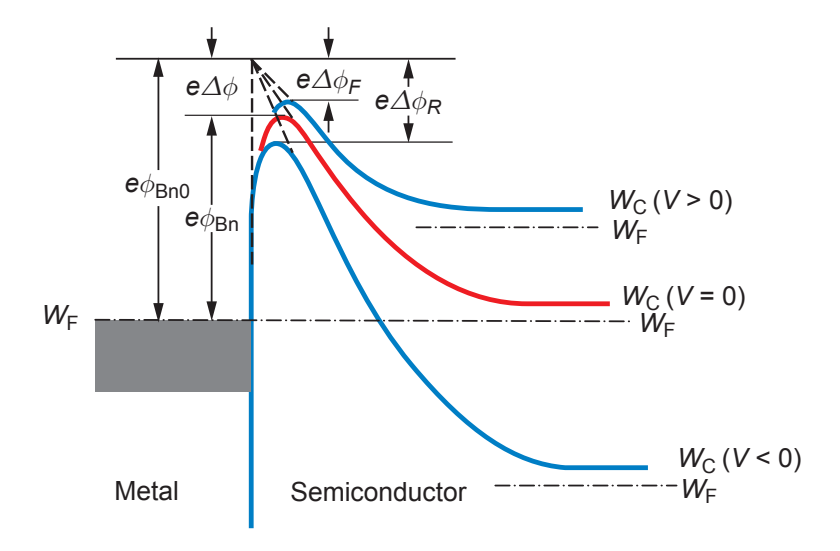


Figure 2.4: Band diagram of a Schottky barrier at a metal/semiconductor interface including the Schottky effect for foward (F, V > 0), zero and reverse (R, V < 0) bias. The semiconductor is n-type doped and the metal work function is higher than the semiconductor electron affinity. The barrier height at thermal equilibrium is  $e\phi_{\rm Bn}$  and differs from the intrinsic barrier  $e\phi_{\rm Bn0}$  by a barrier lowering  $e\Delta\phi$ . [138]. Figure reprinted with permission from [141].

and field emission [140]. The theories are summarized in the textbook of Sze and Ng [138] and the equations below are given according to [138].

Due to the electric field in the space charge region, the intrinsic Schottky barrier  $e\phi_{\rm Bn0}$  is reduced by  $e\Delta\phi$ . This image-force barrier lowering is also called Schottky effect. By applying a voltage in forward direction, the barrier lowering is reduced  $(e\Delta\phi_{\rm F} < e\Delta\phi_{V=0\,\rm V})$  and the barrier  $e\phi_{\rm Bn}$  is slightly higher than in the zero bias case, see Fig. 2.4. The opposite is true for a voltage in reverse direction  $(e\Delta\phi_{\rm R} > e\Delta\phi_{V=0\,\rm V})$ . The voltage V across the junction is defined as positive if a positive potential is applied to the metal with respect to the semiconductor. The junction is biased in forward direction for  $V > 0\,\rm V$  ( $V_{\rm F} = V$ ). For a voltage in reverse direction ( $V < 0\,\rm V$ ),  $V_{\rm R} = -V$  holds. The effective barrier height  $e\phi_{\rm Bn}$  is calculated via

$$\phi_{\rm Bn} = \phi_{\rm Bn0} - \Delta\phi = \phi_{\rm Bn0} - \sqrt{\frac{eE_{\rm max}}{4\pi\epsilon_{\phi_{\rm B}}}} = \phi_{\rm Bn0} - \sqrt{\frac{e^3N_{\rm D}(\phi_{\rm Bn0} - \phi_{\rm n} - V)}{8\pi^2\epsilon_{\phi_{\rm B}}^3}} [138]. \quad (2.2)$$

The donor concentration is denoted by  $N_{\rm D}$ . In case of oxygen vacancies acting as doubly-charged donors,  $N_{\rm D}=2N_{\rm Vo}$  applies. The maximum electric field is  $E_{\rm max}$  and  $e\phi_{\rm n}$  is the energy difference between the Fermi level and the conduction band in the undisturbed semiconductor. Here,  $\epsilon_{\phi_{\rm B}}$  is the permittivity related to the process of image-force barrier

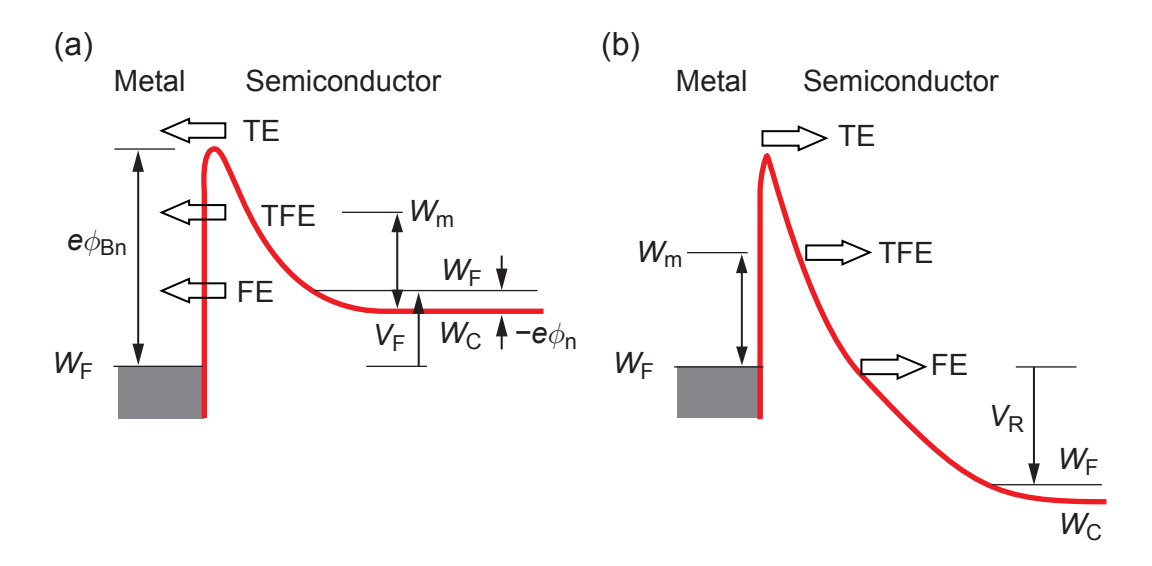


Figure 2.5: Band diagram of a Schottky barrier illustrating the three components of the current across the junction under forward (a) and reverse (b) bias: TE = thermionic emission, TFE = thermionic field emission, FE = field emission. The shown n-type semiconductor is degenerated and the energy difference between Fermi level and conduction band  $e\phi_n$  is therefore negative. Under forward bias  $V_F$ , the barrier for the electrons traversing from the semiconductor to the metal is reduced. In contrast, the barrier for the electrons traversing from the metal to the semiconductor is increased under reverse bias  $V_R$ . However, the barrier is thinner. [138]. Figure reprinted with permission from [141].

lowering, which can differ from the static permittivity. Only at ideal metal/semiconductor contacts, the intrinsic barrier height  $e\phi_{\rm Bn0}$  is the difference between metal work function and semiconductor electron affinity. In practice, interface layers and interface states play an important role [138], but the exact effect in ReRAM devices is largely unknown.

The current through a Schottky junction can be categorized into the three components TE, TFE and FE as illustrated in Fig. 2.5. Depending on the temperature, the donor concentration and the bias polarity, one process dominates and the other two can be neglected in a good approximation. In general, the thermionic emission of electrons over the potential barrier is high if the barrier is low but thick or the energy of the electrons is high. The former can be achieved by applying a high voltage in forward direction, whereas the latter holds for high temperatures. Thus, for low to moderate doping concentrations, the current through the Schottky diode in forward direction can be approximated using the thermionic emission equation, which reads in forward and reverse direction:

$$I_{\rm TE} = AA^*T^2 \exp\left(-\frac{e\phi_{\rm Bn}}{k_{\rm B}T}\right) \left(\exp\left(\frac{eV}{k_{\rm B}T}\right) - 1\right) [138], \tag{2.3}$$

where

$$A^* = \frac{4\pi e m_{\text{eff}} k_{\text{B}}^2}{h^3} \quad [138]$$

is the effective Richardson constant. A denotes the cross-sectional area of the junction, T is the temperature and  $k_{\rm B}$  is the Boltzmann constant. For a higher donor concentration, the potential barrier becomes thinner and the tunneling probability increases. At low temperatures, the electrons tunnel near the Fermi level through the barrier (field emission). At moderate to high temperatures, more electrons are thermally excited and tunnel at an energy higher than the Fermi level, as the barrier is thinner at higher energies. In addition to a high doping concentration, the application of a voltage in reverse direction further thins the barrier. Thus, thermionic field emission is particularly important for the conduction in reverse direction. The corresponding current equation reads:

$$I_{\text{TFE},V<0} = A \frac{A^*T}{k_{\text{B}}} \sqrt{\pi W_{00} e \left(-V + \frac{\phi_{\text{Bn}}}{\cosh^2(W_{00}/k_{\text{B}}T)}\right)} \exp\left(\frac{-e\phi_{\text{Bn}}}{W_0}\right) \left(\exp\left(\frac{-eV}{\zeta}\right) - 1\right)$$
[138], (2.5)

where the parameters  $W_{00}$ ,  $W_0$ , and  $\zeta$  are defined as

$$W_{00} = \frac{eh}{4\pi} \sqrt{\frac{N_{\rm D}}{m_{\rm eff}\epsilon_{\rm s}}} [138], \qquad (2.6)$$

$$W_0 = W_{00} \coth\left(\frac{W_{00}}{k_{\rm B}T}\right)$$
 [138], and (2.7)

$$\zeta = \frac{W_{00}}{(W_{00}/k_{\rm B}T) - \tanh(W_{00}/k_{\rm B}T)} [138]. \tag{2.8}$$

For a low doping concentration (and a high barrier), the current in reverse direction is much lower than in forward direction, which is the characteristic of a rectifying junction. Only for high doping concentrations, a substantial current flows for a bias in reverse direction. For a high barrier and a high doping concentration, the thermionic field emission also contributes considerably under forward bias. In forward direction,

$$I_{\text{TFE},V>0} = A \frac{A^*T\sqrt{\pi W_{00}e(\phi_{\text{Bn}} - \phi_{\text{n}} - V)}}{k_{\text{B}}\cosh(W_{00}/k_{\text{B}}T)} \exp\left(\frac{-e\phi_{\text{n}}}{k_{\text{B}}T} - \frac{e(\phi_{\text{Bn}} - \phi_{\text{n}})}{W_0}\right) \left(\exp\left(\frac{eV}{W_0}\right) - 1\right)$$
[138] (2.9)

holds for the TFE current.

For use in a circuit simulator and differing from the original equations in [138], the terms  $\exp\left(\frac{-eV}{\zeta}\right)$  and  $\exp\left(\frac{eV}{W_0}\right)$  were expanded to  $\left(\exp\left(\frac{-eV}{\zeta}\right) - 1\right)$  and  $\left(\exp\left(\frac{eV}{W_0}\right) - 1\right)$  in Eqs. (2.5) and (2.9), respectively, to enforce the current being zero for zero applied voltage. At very high doping concentrations leading to a degenerate semiconductor, a non-rectifying ohmic contact is formed. The tunneling current due to pure field emission, which is significant at low temperatures, can be calculated as

$$I_{\text{FE},V>0} = A \frac{A^* T \pi \exp(-e(\phi_{\text{Bn}} - V)/W_{00})}{c_1 k_{\text{B}} \sin(\pi c_1 k_{\text{B}} T)} (1 - \exp(-c_1 eV))$$
[138] (2.10)

with

$$c_1 = \frac{1}{2W_{00}} \log \left( \frac{4(\phi_{\text{Bn}} - V)}{-\phi_{\text{n}}} \right) [138]$$
 (2.11)

in forward direction and as

$$I_{\text{FE},V<0} = AA^* \left(\frac{W_{00}}{k_{\text{B}}}\right)^2 \left(\frac{\phi_{\text{Bn}} - V}{\phi_{\text{Bn}}}\right) \left(\exp\left(-\frac{2e\phi_{\text{Bn}}^{3/2}}{3W_{00}\sqrt{\phi_{\text{Bn}} - V}}\right) - 1\right) [138] \quad (2.12)$$

in reverse direction. Similar to the approach for TFE, the exponential terms in Eqs. (2.10) and (2.12) were expanded to enforce the current being zero for zero applied voltage.

Comparing the thermal energy  $k_{\rm B}T$  to  $W_{00}$  (Eq. (2.6)) gives a rough criterion to determine which current component dominates [138]: If  $k_BT \approx W_{00}$ , TFE is the main mechanism. TE determines the current for  $k_{\rm B}T\gg W_{00}$ , and FE is decisive for  $k_{\rm B}T\ll$  $W_{00}$ . A detailed comparison at room temperature between the analytic equations and a simulation with a numerical model of a metal/semiconductor junction in series with a resistor was performed in [122]. The calculations revealed that the current can only roughly be described by the three equations. For a high nominal barrier ( $\phi_{Bn0} = 0.9 \,\mathrm{V}$ ) and a donor concentration of  $N_D = 2 \cdot 10^{26} \,\mathrm{m}^{-3}$ , the numerically calculated current under reverse bias is dominated by the tunneling current. Under forward bias, the numerical model shows that the tunneling current determines the total current up to roughly 0.9 V. For a higher forward bias, the current is driven by thermionic emission. For this parameter set, the  $W_{00}$  criterion predicts that the current should be best described by the analytical equations for TE or TFE. For the reverse direction, however, the FE equation fits best to the result. It overestimates the current though; the deviation is especially high in the low-voltage regime. In contrast, the TFE equation strongly underestimates the current for low voltages under reverse bias. Under forward bias, the FE description is suitable in the low-voltage regime but cannot be used for higher voltages, for which TE offers the best description. The TFE equation overestimates the current under forward

bias, particularly in the low-voltage regime. A combination of FE and TE, however, is not always the best choice. For a donor concentration of  $N_{\rm D}=2\cdot 10^{25}\,{\rm m}^{-3}$ , TFE presents the best description under both forward and reverse bias. The FE component highly underestimates the current. In the second case, the  $W_{00}$  criterion predicts TFE or FE to be the main contributor. As  $W_{00}$  only contains the doping concentration but not the barrier height, it is hardly surprising that the described criterion is often unreliable. For a low barrier ( $\phi_{\rm Bn0}=0.4\,{\rm V}$ ) and a high donor concentration ( $N_{\rm D}=2\cdot 10^{26}\,{\rm m}^{-3}$ ), the series resistance due to the bulk dominates because barrier lowering nearly eliminates the barrier. If the conduction is limited by the bulk, using TE or TFE formulation hardly makes a difference.

When deciding which current component should be used in a compact model, the limited voltage range of the TFE and FE equations must be taken into account as well: Under forward bias, the TFE and FE equations contain a square root or logarithm of a sum that can become negative depending on the applied voltage. The FE current component can only be calculated when  $V < \phi_{\rm Bn}$ , see Eq. (2.11). The contrary condition  $(V > \phi_{\rm Bn})$  corresponds to the situation that the tunnel barrier has vanished. A similar criterion holds for the TFE component, which can be evaluated for  $V < (\phi_{\rm Bn} - \phi_{\rm n})$ , see Eq. (2.9). Here, it becomes apparent that the choice/calculation of  $\phi_{\rm n}$  is significant as well. The FE current under reverse bias can be determined as long as  $\phi_{\rm Bn}$  is non-zero because  $\phi_{\rm Bn}$  appears in the denominator in Eq. (2.12). If the intrinsic barrier height  $\phi_{\rm Bn0}$  is small and the donor concentration is high, a voltage in reverse direction easily results in a vanishing barrier, see Eq. (2.2). In that case,  $\phi_{\rm Bn}$  is set to 0 V. In contrast to FE, the TFE equation provides a result for  $\phi_{\rm Bn} = 0$  V, see Eq. (2.5).

In summary, the compact analytic equations can be used as rough estimates of the current across Schottky junctions; precise results cannot be obtained though. Thus, in the absence of a better alternative, they are used for compact modeling of VCM ReRAM devices but deviations between model and measured I-V characteristic should be expected.

#### 2.4 Ion Migration in Solids

Ions in solids can migrate to neighboring, unoccupied lattice sites if they have enough energy to overcome an activation barrier  $\Delta W_{\rm A}$ . This process is called ionic hopping conduction. Accordingly, the space between the lattice sites is the hopping distance and it is denoted by a. The jumps are attempted with the frequency  $\nu_0$ . If an electric field E is present, the potential barrier is modified establishing a preferred migration direction:

the barrier is lowered for forward jumps ( $\Delta W_{\rm A}^{\rm f}$ ) and raised for reverse jumps ( $\Delta W_{\rm A}^{\rm r}$ ) according to [142]

$$\Delta W_{\text{A, Mott and Gurney}}^{\text{f/r}} = \Delta W_{\text{A}} \mp |z| e E \frac{a}{2}.$$
 (2.13)

The ion charge is denoted by ze. The mean drift velocity  $v_D$  is proportional to the difference between forward and reverse rates. Based on  $v_D$ , the current density takes it well-known form derived by Mott and Gurney [142]:

$$J_{\text{ion, Mott and Gurney}} = zeN v_{\text{D}}$$

$$= zeN a\nu_{0} \left[ \exp\left(-\frac{\Delta W_{\text{A}}^{\text{f}}}{k_{\text{B}}T}\right) - \exp\left(-\frac{\Delta W_{\text{A}}^{\text{r}}}{k_{\text{B}}T}\right) \right]$$

$$= zeN a\nu_{0} \exp\left(-\frac{\Delta W_{\text{A}}}{k_{\text{B}}T}\right) \left[ \exp\left(\frac{|z|eEa}{2k_{\text{B}}T}\right) - \exp\left(-\frac{|z|eEa}{2k_{\text{B}}T}\right) \right]$$

$$= zeN a\nu_{0} \exp\left(-\frac{\Delta W_{\text{A}}}{k_{\text{B}}T}\right) 2 \sinh\left(\frac{|z|eEa}{2k_{\text{B}}T}\right). \tag{2.14}$$

Here, N is the ion concentration. Equivalent to ions, the hopping of ionic defects like vacancies can be described as well with Eq. (2.14).

Genreith-Schriever et al. compared the results from a molecular dynamics simulation with the prediction based on the standard Mott–Gurney approach [143]. They showed that the Mott–Gurney approach overestimates the ion mobility by two orders of magnitude at high electric fields. To derive the migration barriers mathematically exact, they superimposed a linear field on a cosinusoidal energy landscape and obtained

$$\Delta W_{\text{A, Genreith-Schriever }et \, al.}^{\text{f/r}} = \Delta W_{\text{A}} \left[ \sqrt{1 - \gamma^2} \mp \gamma \left( \frac{\pi}{2} \right) + \gamma \arcsin \gamma \right]$$
 (2.15)

with  $\gamma$  as

$$\gamma = \frac{|z|eEa}{\pi\Delta W_{\rm A}}.\tag{2.16}$$

In accordance with density functional theory calculations, the approach by Genreith-Schriever et~al. shows that a/2, which is the distance between potential minimum and maximum, is shortened for forward jumps to  $a^{\rm f}/2$  and lengthened for reverse jumps to  $a^{\rm r}/2$ . The different approaches for the potential barriers in an ion hopping process are depicted in Fig. 2.6. A detailed comparison between the approaches by Mott and Gurney and by Genreith-Schriever et~al. can be found in [144]. Note that the definition of the hopping distance a deviates from the definition of  $a_i$  used in [143], where  $a_i$  is the

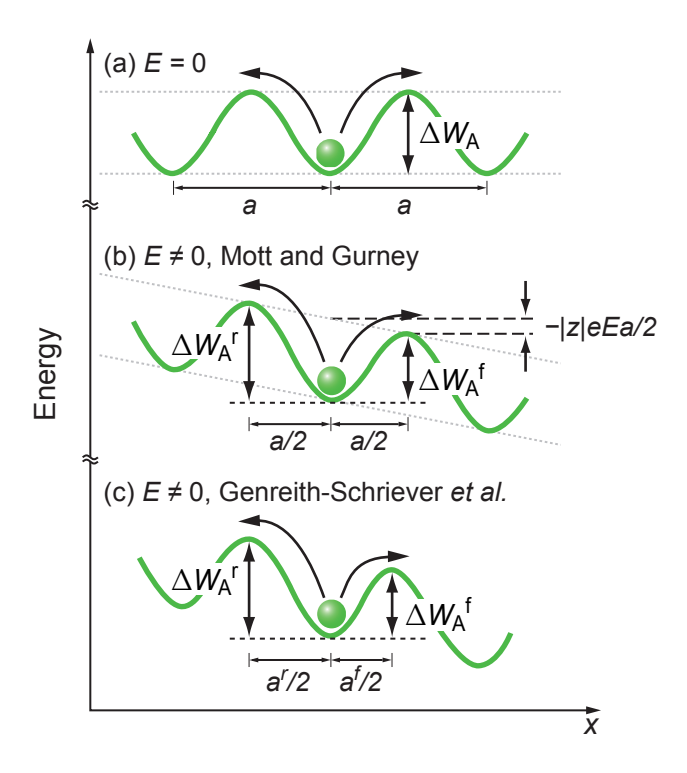


Figure 2.6: Activation barrier for ion hopping. (a) Without applied electric field the activation barrier for a jump is similar in every direction. (b) The barriers for forward and reverse jumps are lowered and increased by |z|eEa/2, respectively. This is the standard approach by Mott and Gurney [142]. (c) Genreith-Schriever *et al.* present a mathematically exact derivation for the potential barriers in forward and reverse direction, see Eq. (2.15) [143].

distance between the initial and the saddle-point configuration. For consistency,  $a=2a_{\rm i}$  was applied.

Analogous to the Mott–Gurney approach and based on Eq. (2.13), Noman *et al.* derived an equation for the ionic current density considering forward and backward hopping rates [145]:

$$J_{\text{ion, Noman }et \, al.} = zeN_{\text{L}}a\nu_0 \exp\left(-\frac{\Delta W_{\text{A}}}{k_{\text{B}}T} + \frac{|z|eEa}{2k_{\text{B}}T}\right) \left(1 - \frac{N_{\text{R}}}{N_{\text{max}}}\right)$$
$$- zeN_{\text{R}}a\nu_0 \exp\left(-\frac{\Delta W_{\text{A}}}{k_{\text{B}}T} - \frac{|z|eEa}{2k_{\text{B}}T}\right) \left(1 - \frac{N_{\text{L}}}{N_{\text{max}}}\right)$$
(2.17)

In contrast to Eq. (2.14), the concentrations on the left and on the right side of the energy barrier,  $N_{\rm L}$  and  $N_{\rm R}$ , are distinguished. The electric field is defined from left to

right. Based on a possible concentration gradient dN/dx,  $N_{\rm L}$  and  $N_{\rm R}$  are calculated according to

$$N_{\rm L} = N - \frac{a}{2} \frac{\mathrm{d}N}{\mathrm{d}x} \text{ and} \tag{2.18}$$

$$N_{\rm R} = N + \frac{a}{2} \frac{\mathrm{d}N}{\mathrm{d}x}.\tag{2.19}$$

This modification generates a diffusion component in the ionic current. In addition, a limiting term is added to ensure that the concentrations always stay below a defined maximum concentration  $N_{\text{max}}$ . Neglecting second-order derivatives and substituting Eqs. (2.18) and (2.19) in Eq. (2.17) results in

$$J_{\text{ion, Noman }et \, al.} = zeNa\nu_0 \exp\left(-\frac{\Delta W_{\text{A}}}{k_{\text{B}}T}\right) 2 \sinh\left(\frac{|z|eEa}{2k_{\text{B}}T}\right) \left(1 - \frac{N}{N_{\text{max}}}\right)$$

$$- ze\frac{1}{2}a^2\nu_0 \frac{dN}{dx} \exp\left(-\frac{\Delta W_{\text{A}}}{k_{\text{B}}T}\right) 2 \cosh\left(\frac{|z|eEa}{2k_{\text{B}}T}\right)$$

$$= J_{\text{ion,drift}} + J_{\text{ion,diffusion}}$$

$$= ze\frac{4}{a}D_{\text{ion}}N \sinh\left(\frac{|z|eEa}{2k_{\text{B}}T}\right) \left(1 - \frac{N}{N_{\text{max}}}\right)$$

$$- ze2D_{\text{ion}} \frac{dN}{dx} \cosh\left(\frac{|z|eEa}{2k_{\text{B}}T}\right). \tag{2.21}$$

Equation (2.20) can be rewritten in (2.21) by defining the diffusion coefficient

$$D_{\rm ion} = \frac{1}{2}a^2\nu_0 \, \exp\left(-\frac{\Delta W_{\rm A}}{k_{\rm B}T}\right). \tag{2.22}$$

In contrast to the original derivation by Noman  $et\ al.$  in [145], a factor of 2 was added in Eq. (2.17) in order to ensure that the drift component of Eq. (2.20) equals the standard Mott–Gurney derivation in Eq. (2.14), except for the limiting factor  $(1-(N/N_{\rm max}))$ . Moreover, the ionic charge number z was added in the term that lowers/raises the energy barrier under an applied electric field. In addition, the particle current was converted to an ionic charge current by adding ze in the prefactor.

Combining the derivation for the energy barrier in forward and backward direction by Genreith-Schriever *et al.*, Eqs. (2.15) and (2.16), and the derivation for the ionic current comprising a drift and diffusion component by Noman *et al.*, Eqs. (2.17) to (2.19), yields

 $J_{\text{ion, Noman } et \ al.}$  + Genreith-Schriever  $et \ al.$ 

$$= zeN_{L}a\nu_{0} \exp\left(-\frac{\Delta W_{A}^{f}}{k_{B}T}\right) \left(1 - \frac{N_{R}}{N_{\max}}\right) - zeN_{R}a\nu_{0} \exp\left(-\frac{\Delta W_{A}^{r}}{k_{B}T}\right) \left(1 - \frac{N_{L}}{N_{\max}}\right)$$

$$= CN \sinh\left(\frac{|z|eEa}{2k_{B}T}\right) \left(1 - \frac{N}{N_{\max}}\right) - C\frac{a}{2}\frac{dN}{dx} \cosh\left(\frac{|z|eEa}{2k_{B}T}\right)$$

$$= J_{\text{ion,drift}} + J_{\text{ion,diffusion}}$$

$$(2.23)$$

with C as

$$C = 2zea\nu_0 \exp\left(-\frac{\Delta W_{\rm A} \left[\sqrt{1-\gamma^2} + \gamma \arcsin \gamma\right]}{k_{\rm B}T}\right). \tag{2.24}$$

The detailed derivation is given in Appendix A.1.

### 2.5 Kinetics of Electrode Reactions

Electrode reactions play a crucial role in (filamentary) VCM ReRAM devices during electroforming and switching, see section 2.2. In general, many steps of the charge transfer reaction may be the rate-limiting step and have to be considered therefore [146]. In this section, the kinetics of an electrode reaction are described for an ion transfer process. The equations below are given according to the description in the standard textbook by Wedler and Freund [147]. In contrast to the defintions in [147], which are based on the amount of substance in mol as reference quantity, the equations are rewritten to refer to the number of particles. For example, the enthalpy is given in eV and not in J/mol. The ion transfer reaction at a solid/aqueous interface

$$Me \frac{k_a}{k_k} Me^{z+} + ze^-$$
 (2.25)

describes the transfer of a metal ion in an electrochemical half cell. The anodic process, i.e. the oxidation of the metal atom, and the cathodic process, i.e. the reduction of the metal ion, take place with the rate constants  $k_a$  and  $k_k$ , respectively. The electrons remain in the metal if the ion is located in the aqueous solution. For the anodic (cathodic) process, the activation enthalpy  $\Delta G_a$  ( $\Delta G_k$ ) has to be overcome. In general, the kinetic barriers differ from the thermodynamical difference between the two states. This is shown exemplarily in Fig. 2.7: Curve 1 shows the free standard enthalpy profile in absence of an electrical double layer. The kinetic activation barriers for this theoretical case are denoted by  $\Delta G_a^0$  and  $\Delta G_k^0$ . An electrical double layer is formed at the interface between the two phases (aqueous solution and solid). Its potential profile  $ze\varphi$  is given by curve 2.

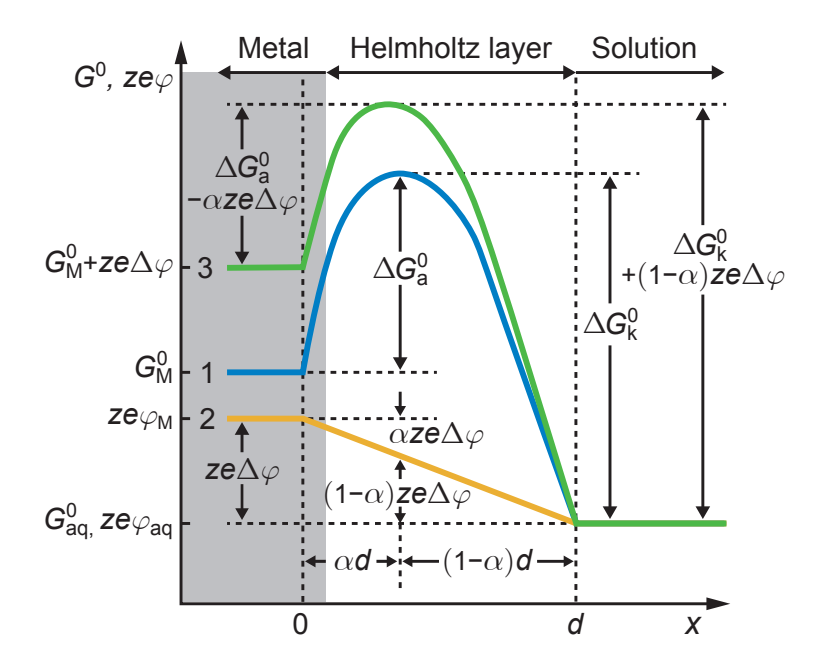


Figure 2.7: Ion transfer process as described by Eq. (2.25). The free standard enthalpy profile of the system in absence of an electric potential is given by curve 1. Curve 2 illustrates the electric potential energy profile. The superposition of both gives the effective enthalpy profile (curve 3). In the shown example with  $\Delta \varphi > 0$ , the anodic process is favored over the cathodic one. Adapted from [147].

The effective enthalpy profile (curve 3) develops by the superposition of curve 1 and 2. Depending on the sign of the potential, one effective kinetic barrier is reduced and one is increased according to

$$\Delta G_{\rm a} = \Delta G_{\rm a}^0 - \alpha z e \Delta \varphi, \tag{2.26}$$

$$\Delta G_{\mathbf{k}} = \Delta G_{\mathbf{k}}^{0} + (1 - \alpha)ze\Delta\varphi. \tag{2.27}$$

Here,  $\alpha$  is the dimensionless charge transfer coefficient and defines which ratio of the potential difference  $\Delta \varphi$  affects the anodic process. Other definitions of  $\alpha$  are possible and also common. Here, the definition from [147] is used. The rate constants for the anodic and cathodic process follow an Arrhenius equation with  $k^{00}$  as pre-exponential factor:

$$k_{\rm a} = k_{\rm a}^{00} \exp\left(-\frac{\Delta G_{\rm a}}{k_{\rm B}T}\right) = k_{\rm a}^{00} \exp\left(-\frac{\Delta G_{\rm a}^0}{k_{\rm B}T}\right) \exp\left(\frac{\alpha z e \Delta \varphi}{k_{\rm B}T}\right),\tag{2.28}$$

$$k_{\rm k} = k_{\rm k}^{00} \exp\left(-\frac{\Delta G_{\rm k}}{k_{\rm B}T}\right) = k_{\rm k}^{00} \exp\left(-\frac{\Delta G_{\rm k}^0}{k_{\rm B}T}\right) \exp\left(-\frac{(1-\alpha)ze\Delta\varphi}{k_{\rm B}T}\right). \tag{2.29}$$

The potential difference  $\Delta \varphi$  in the Helmholtz layer consists of two components, the Galvani potential  $\Delta \varphi_{\text{ref}}$ , which is in fact a potential difference, and the overpotential  $\eta$ :

$$\Delta \varphi = \Delta \varphi_{\text{ref}} + \eta. \tag{2.30}$$

If the system is in its electrochemical equilibrium state, the overpotential is zero and  $\Delta \varphi = \Delta \varphi_{\rm ref}$  holds. Substituting  $\Delta \varphi$  in Eqs. (2.28) and (2.29) by Eq. (2.30) results in

$$k_{\rm a} = k_{\rm a}^{00} \exp\left(-\frac{\Delta G_{\rm a}^{0}}{k_{\rm B}T}\right) \exp\left(\frac{\alpha z e \Delta \varphi_{\rm ref}}{k_{\rm B}T}\right) \exp\left(\frac{\alpha z e}{k_{\rm B}T}\eta\right)$$

$$= k_{\rm a}^{0} \exp\left(-\frac{\Delta G_{\rm a}^{0}}{k_{\rm B}T}\right) \exp\left(\frac{\alpha z e}{k_{\rm B}T}\eta\right), \qquad (2.31)$$

$$k_{\rm k} = k_{\rm k}^{00} \exp\left(-\frac{\Delta G_{\rm k}^{0}}{k_{\rm B}T}\right) \exp\left(-\frac{(1-\alpha)ze\Delta\varphi_{\rm ref}}{k_{\rm B}T}\right) \exp\left(-\frac{(1-\alpha)ze}{k_{\rm B}T}\eta\right)$$

$$= k_{\rm k}^{0} \exp\left(-\frac{\Delta G_{\rm k}^{0}}{k_{\rm B}T}\right) \exp\left(-\frac{(1-\alpha)ze}{k_{\rm B}T}\eta\right). \qquad (2.32)$$

Based on the rate constants, the partial ionic current densities can be expressed as

$$J_{\text{ion,i}} = ze c k_{i}, \qquad (2.33)$$

where c is an area concentration (particles per m<sup>2</sup>). Accordingly, the rate constant  $k_i$  (and the pre-exponential factor  $k_i^0$ ) are given in units of 1/s. Combining Eq. (2.33) with Eqs. (2.31) and Eqs. (2.32) gives the anodic and cathodic current density:

$$J_{\text{ion,a}} = zec_{\text{red}}k_{\text{a}}^{0} \exp\left(-\frac{\Delta G_{\text{a}}^{0}}{k_{\text{B}}T}\right) \exp\left(\frac{\alpha ze}{k_{\text{B}}T}\eta\right), \tag{2.34}$$

$$J_{\text{ion,k}} = -zec_{\text{ox}}k_{\text{k}}^{0} \exp\left(-\frac{\Delta G_{\text{k}}^{0}}{k_{\text{B}}T}\right) \exp\left(-\frac{(1-\alpha)ze}{k_{\text{B}}T}\eta\right). \tag{2.35}$$

Here,  $c_{\rm red}$  and  $c_{\rm ox}$  are the concentration of reduced and oxidized particles, respectively. By definition, the cathodic current density is given a negative sign, whereas the anodic current density is positive. The net current density is given by

$$J_{\text{ion}} = J_{\text{ion,a}} - |J_{\text{ion,k}}|. \tag{2.36}$$

In the electrochemical equilibrium, the absolute values of the anodic and cathodic current density are equal. Thus, the net current density is zero.

The exchange current density  $J_0$  is defined to be

$$J_{0} = J_{\text{ion,a}}(\eta = 0) = |J_{\text{ion,k}}(\eta = 0)|$$

$$= zec_{\text{red}}k_{\text{a}}^{0} \exp\left(-\frac{\Delta G_{\text{a}}^{0}}{k_{\text{B}}T}\right) = zec_{\text{ox}}k_{\text{k}}^{0} \exp\left(-\frac{\Delta G_{\text{k}}^{0}}{k_{\text{B}}T}\right). \tag{2.37}$$

With  $J_0$ , Eq. (2.36) can be rewritten in a shorter form as

$$J_{\text{ion}} = J_0 \left[ \exp\left(\frac{\alpha z e}{k_{\text{B}} T} \eta\right) - \exp\left(-\frac{(1-\alpha)z e}{k_{\text{B}} T} \eta\right) \right], \tag{2.38}$$

which is the well-known Butler–Volmer equation relating current density and overpotential. If a positive voltage is applied to the metal electrode  $(\eta > 0)$ , the oxidation rate increases and the reduction rate reduces resulting in an anodic net current. Although the physical mechanism is different, the J(V) characteristic of the transfer of both an ion and an electron can be described based on the Butler–Volmer equation [146].

#### 2.6 Simulation Methods

#### **Solving Ordinary Differential Equations**

Modeling the dynamics of ReRAM devices requires the solution of at least one initial value problem, i.e. an ordinary differential equation (ODE) with a given initial condition, of the form

$$\frac{\mathrm{d}y(t)}{\mathrm{d}t} = f(t, y(t)) \tag{2.39}$$

with the initial condition  $y(t_0) = y_0$ . Equation (2.39) needs to be solved for y at every time t. The trapezoidal rule is applied to obtain the value for  $y(t+\Delta t)$  using the following procedure [148]:

$$t_{j+1} = t_j + \Delta t$$
  

$$y_{j+1} = y_j + \frac{\Delta t}{2} (f(t_j, y_j) + f(t_{j+1}, y_{j+1})).$$
(2.40)

As  $y_{j+1}$  appears on both sides, Eq. (2.40) has to be solved as part of a system of nonlinear equations. If several ODEs need to be solved simultaneously, as in the case of more than one state variable, Eq. (2.40) is set up for each ODE separately. To allow for a better convergence, the time step  $\Delta t$  is not fixed but adapted by a time-stepping algorithm, see below.

#### Solving a Set of Nonlinear Equations

All equations in a compact model describing the electrical, thermal and ionic processes are part of a system of nonlinear equations that has to be solved in every time step. Mathematically, this can be expressed as

$$\hat{A}(\vec{x})\,\vec{x} = \vec{b},\tag{2.41}$$

which is solved for the vector  $\vec{x}$ , where  $\hat{A}$  is the coefficient matrix and  $\vec{b}$  is the right-handside vector.  $\vec{x}$  contains all voltages, current, temperature, ion concentrations and other variables that are needed to calculate these quantities or depend on them. Equation (2.41) can be rewritten to

$$\vec{f}(\vec{x}) = \hat{A}(\vec{x})\,\vec{x} - \vec{b} = 0. \tag{2.42}$$

A damped form of Newton's method, which is an iterative standard procedure to find an approximate root of the function  $\vec{f}(\vec{x})$ , is applied in this work [148]. First, using a first-order Taylor series expansion, Eq. (2.42) is linearized to

$$\vec{f}(\vec{x}_{k+1}) = \vec{f}(\vec{x}_k) + \hat{\mathcal{J}}_f(\vec{x}_k)(\vec{x}_{k+1} - \vec{x}_k) = 0.$$
(2.43)

Instead of a root to Eq. (2.42), the approximate root  $\vec{x}_{k+1}$  to Eq. (2.43) is now searched for. The iteration step is indicated by k in the subscript. The Jacobian matrix  $\hat{\mathcal{J}}_f(\vec{x}_k)$  is the matrix of all first-order partial derivatives and reads

$$\hat{\mathcal{J}}_f(\vec{x}_k) = \begin{pmatrix} \frac{\partial f^1(\vec{x}_k)}{\partial x^1} & \cdots & \frac{\partial f^1(\vec{x}_k)}{\partial x^n} \\ \vdots & \ddots & \vdots \\ \frac{\partial f^n(\vec{x}_k)}{\partial x^1} & \cdots & \frac{\partial f^n(\vec{x}_k)}{\partial x^n} \end{pmatrix}, \tag{2.44}$$

where the central difference quotient is used to approximate the partial derivatives with

$$\frac{\partial f^i(\vec{x}_k)}{\partial x^j} = \frac{f^i(\vec{x}_k + \vec{\delta^j}) - f^i(\vec{x}_k - \vec{\delta^j})}{2\delta}.$$
 (2.45)

Here,  $\vec{\delta}^j$  denotes a vector, whose vector components are zero except for the jth component that has the value  $\delta$ . The solution vector  $\vec{x}_{k+1}$  can be found by solving

$$\vec{x}_{k+1} = \vec{x}_k - \lambda (\hat{\mathcal{J}}_f(\vec{x}_k))^{-1} \vec{f}(\vec{x}_k)$$
(2.46)

with a damping factor  $\lambda \in (0,1]$ . As the calculation of the inverse Jacobian matrix  $(\hat{\mathcal{J}}_f(\vec{x}_k))^{-1}$  is computationally intensive, the following equivalent procedure is applied. The equation

$$\hat{\mathcal{J}}(\vec{x}_k)\Delta \vec{x}_k = -\vec{f}(\vec{x}_k) \tag{2.47}$$

is solved for  $\Delta \vec{x}_k$  and the solution vector is updated using

$$\vec{x}_{k+1} = \vec{x}_k + \lambda \Delta \vec{x}_k, \tag{2.48}$$

as  $\Delta \vec{x}_k = (\hat{\mathcal{J}}_f(\vec{x}_k))^{-1} \vec{f}(\vec{x}_k)$  holds. In the damped Newton's method, two loops — one for the damping factor and one for the solution accuracy — are executed. In the inner loop, the damping factor is reduced by a factor of 1/2 until the simple criterion<sup>2</sup>

$$\|\vec{f}(\vec{x}_k + \lambda \Delta \vec{x}_k)\| < \|\vec{f}(\vec{x}_k)\|$$
 (2.49)

is met or  $\lambda = \lambda_{\min}$  is reached. The procedure to calculate  $\vec{x}_{k+1}$  is iterated until a predefined tolerance criterion for the solution accuracy is fulfilled. Standard stop criteria for Newton's method are to check whether the Euclidean norm of the function is sufficiently close to zero, i.e. smaller than a specified tolerance  $\varepsilon$ , or whether the change in  $\vec{x}$  between two iterations is sufficiently small:

$$\|\vec{f}(\vec{x}_{k+1})\| < \varepsilon_1 \quad \text{or} \quad \|\vec{x}_{k+1} - \vec{x}_k\| < \varepsilon_2.$$
 (2.50)

In this work, a combination of both criteria was chosen. As the components of  $\vec{x}$  differ greatly in their magnitude, the criterion based on the change in  $\vec{x}$  between two iterations was modified. The iteration stops when either

$$\|\vec{f}(\vec{x}_{k+1})\| < \varepsilon_1 \quad \text{and} \quad \frac{\|\vec{x}_{k+1} - \vec{x}_k\|}{\|\vec{x}_{k+1}\|} < \varepsilon_2$$
 (2.51)

holds<sup>3</sup> or the maximum number of iteration steps is reached. The whole method is crucially dependent on a good guess for the initial vector  $\vec{x}_0$ .

$$\|\vec{f}(\vec{x}_{k+1})\| < \varepsilon_1 \quad \text{ and } \quad \left(\frac{\|\vec{x}_{k+1} - \vec{x}_k\|}{\|\vec{x}_{k+1}\|} < \varepsilon_2 \text{ or } \|\vec{x}_{k+1} - \vec{x}_k\| < \varepsilon_2\right)$$

is used instead.

For the compact model in chapter 5,  $\|\vec{f}(\vec{x}_k + (1 - 0.01\lambda)\Delta\vec{x}_k)\| < \|\vec{f}(\vec{x}_k)\|$  is used instead.

For the compact model in chapter 5, the scaling of  $\vec{x}$  is improved and the criterion

#### **Simulation Workflow**

The simulation workflow of the compact models that are described in chapters 3-5 is illustrated in Fig. 2.8. The models were implemented in MATLAB. All model equations, i.e. all equations that are given in sections 3.1, 4.1, or 5.2 for the compact models 1.0, 1.5, or 2.0, respectively, form a set of nonlinear equations, which is solved using the damped form of the Newton's method described above. In fact, all equations except the one(s) for  $\phi_{\rm bn}$  are solved together. The implementation of Eq. (2.2) contains a fixed condition that sets  $\phi_{\rm bn}$  to 0 V if a reverse bias causes the barrier to vanish. On the one hand, this prevents a negative barrier and therefore enables a real-valued evaluation of the current. On the other hand, this results in a non-continuous function that causes convergence problems in the Newton solver. Consequently,  $\phi_{\rm bn}$  is evaluated after solving the remaining set of model equations.

In the first step, the criteria for the activation of the current compliance are checked, see Fig. 2.8. In general, a current compliance is only implemented for voltage sweep simulations and not for voltage pulse simulations. In a sweep simulation, it has to be checked whether the current that was calculated in the last time step  $|I(t_{j-1})|$  is smaller than a predefined current compliance  $|I_{cc}|$ . (To avoid oscillations, the current is checked in fact against  $I_{cc}$  plus a small tolerance value.) In addition,  $I_{cc}$  differs depending on the current polarity and the kind of sweep, i.e. forming or switching sweep. In case of the simulation start (t = 0 s),  $I(t_{i-1})$  equals an initial value that has to be defined. If the current exceeds or is equal to  $I_{cc}$ , the current control becomes active: the current  $I(t_{\rm j})$  is set to  $I_{\rm cc}$  and the model is solved for the applied voltage  $V_{\rm applied}(t_{\rm j})$ . If the current compliance is not activated, the simulation is voltage controlled and the model is solved for the current. In this case,  $V_{\text{applied}}(t_{j})$  is set to the predefined voltage sequence  $V_{\text{defined}}(t_i)$ , which can be a triangular voltage sweep or a voltage pulse. Once in the current compliance, a voltage criterion has to be fulfilled so that the simulation leaves the current compliance: if the applied voltage that was calculated in the last time step  $|V_{\text{applied}}(t_{\text{j-1}})|$  is higher than the predefined voltage sweep  $|V_{\text{defined}}(t_{\text{j}})|$ , the simulation is switched back to voltage controlled.

After solving the model equations, a time-stepping algorithm is applied. As the model contains highly nonlinear equations, the state variable(s) can change strongly during one time step. If the change is too large, convergence problems might arise in the next time step. Thus, the relative change is checked. Only if the relative change in the state variable(s) is smaller than a predefined tolerance, the solution is accepted. Otherwise, the result is discarded and the step is repeated with a smaller time step, which is half

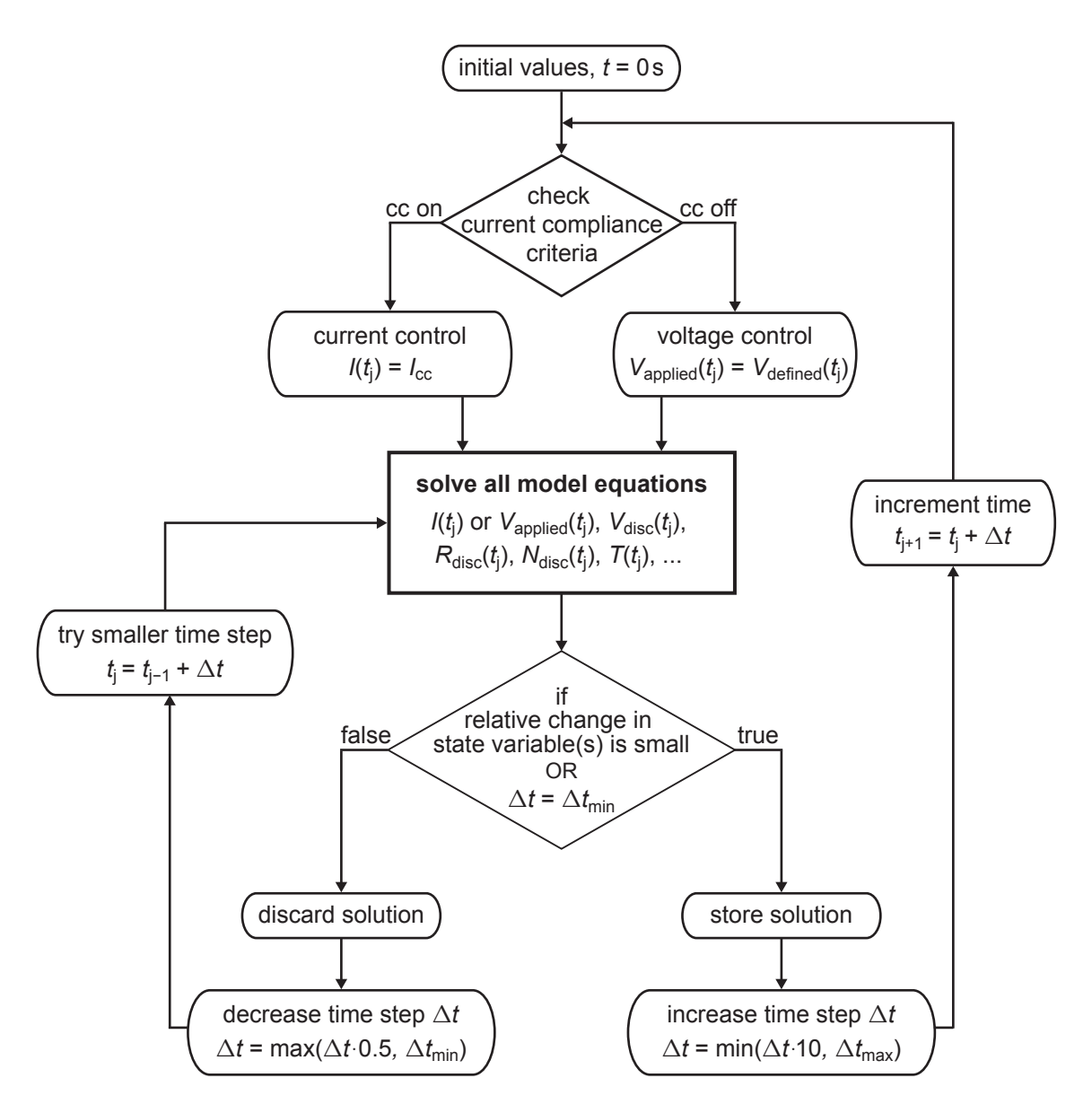


**Figure 2.8:** Flowchart of the compact model implementation in MATLAB using a time-stepping algorithm. If the current compliance is active, the model is solved current controlled instead of voltage controlled. Only for voltage sweep simulations, a current compliance is implemented.

the previous time step. The new time step, however, cannot be smaller than a predefined minimum time step  $\Delta t_{\rm min}$ . The solution is also discarded if the Newton solver did not find an accurate solution but stopped because the maximum number of iterations was reached or any other kind of error occurred. The solving is repeated until the criterion for the relative change is met or the minimum time step is reached. If the solution is accepted, the result is stored and the time step is increased. In case of an increasing time step, the previous time step is multiplied by ten, but, in turn, the new time step cannot exceed a predefined maximum time step  $\Delta t_{\rm max}$ . The time is incremented and the simulation workflow starts once again, unless the predefined final time is reached.

# 3 Compact Model 1.0

In 2014, Anne Siemon  $et\ al.$  presented a physics-based compact model that was able to reproduce the current–voltage behavior and the nonlinear SET kinetics of a TaO<sub>x</sub>-based cell switching in counter-eightwise direction [52]. Her model was adapted and extended and the resulting model is presented in this chapter. The influence of various parameters on the I-V characteristic is discussed and the ability of the model to capture abrupt and gradual behavior for both SET and RESET transitions is studied in detail. To this end, the interdependencies of resistance change, temperature and electric field are analyzed in terms of positive and negative feedback. The simulation results are also discussed with respect to experimental data. Some results of this chapter have been published before in [81, 149, 150], but based on other parameter sets and slightly different models. The experimental data shown in this chapter were provided by Alexander Hardtdegen and Karsten Fleck.

Compact model 1.0 is based on the following general assumptions:

- To enable switching, a sufficiently large number of oxygen vacancies is present in a filament. This is ensured by choosing the initial values appropriately. Forming is not covered by the model.
- The filament is cylindrical with a time-invariant, constant cross-sectional area. It is split into two regions of uniform oxygen vacancy concentration called plug and disc. The oxygen vacancy concentration in the disc is variable and represents the only state variable of the model. The concentration in the plug is assumed to be constant.
- The metal/oxide interface of the electrode with the higher work function is modeled as Schottky contact. The conduction through the other interface is assumed to be ohmic.
- Oxygen vacancies are treated as mobile, doubly-charged donors. Their movement
  along the filament is described as an electric-field-driven process that is enhanced
  by temperature. Internal electric fields under zero bias, diffusion, and thermodiffusion are neglected.

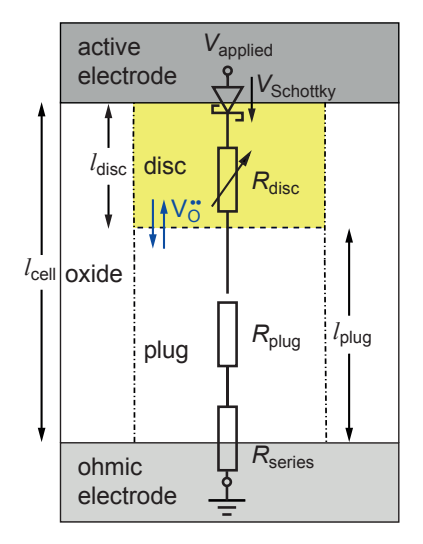


Figure 3.1: Equivalent circuit diagram for the electrical model of compact model 1.0.

- The concentration of electrons is solely determined by the donor concentration.
- No electrode reactions, like an oxygen exchange, are considered.
- The temperature is approximated to be uniform in the filament.
- No stochastic processes are considered, the simulation results are deterministic.

## 3.1 Model Description and Equations

The whole ReRAM device is modeled using four elements, see Fig. 3.1: a Schottky diode for the AE/oxide interface, a disc resistance  $R_{\rm disc}$ , a plug resistance  $R_{\rm plug}$  and a series resistance  $R_{\rm series}$ . The length of the filament  $l_{\rm cell}$  is equivalent to the oxide thickness. Disc and plug have a length of  $l_{\rm disc}$  and  $l_{\rm plug}$ , respectively. The cross-sectional area A is calculated based on the filament radius  $r_{\rm fil}$  using  $A = \pi r_{\rm fil}^2$ . The oxygen vacancy concentration in the disc and the plug is denoted by  $N_{\rm disc}$  and  $N_{\rm plug}$ , respectively. The series resistance is constant and comprises electrode and line resistances and the ohmic OE/oxide interface.

The voltage  $V_{\text{applied}}$  is applied to the active electrode while the ohmic electrode is grounded. The current is denoted by I. Using Kirchhoff's law,

$$V_{\text{applied}} - [V_{\text{Schottky}} + I \cdot (R_{\text{disc}} + R_{\text{plug}} + R_{\text{series}})] = 0$$
 (3.1)

is solved. Band conduction with temperature-dependent mobility  $\mu_n$  is assumed as electrical conduction mechanism in the filament. Thus, the disc and plug resistances are calculated using

$$R_{\rm disc} = \frac{l_{\rm disc}}{A \cdot z_{\rm Vo} e N_{\rm disc} \mu_{\rm n}(T)} = \frac{l_{\rm disc}}{A \cdot z_{\rm Vo} e N_{\rm disc} \mu_{\rm n0}} \exp\left(\frac{\Delta E_{\rm ac}}{k_{\rm B} T}\right)$$
(3.2)

and

$$R_{\text{plug}} = \frac{l_{\text{plug}}}{A \cdot z_{\text{Vo}} e N_{\text{plug}} \mu_{\text{n}}(T)} = \frac{l_{\text{plug}}}{A \cdot z_{\text{Vo}} e N_{\text{plug}} \mu_{\text{n0}}} \exp\left(\frac{\Delta E_{\text{ac}}}{k_{\text{B}} T}\right), \tag{3.3}$$

where e is the elementary charge,  $z_{\text{Vo}}$  is the charge number of the oxygen vacancies relative to the perfect crystal lattice,  $k_{\text{B}}$  is the Boltzmann constant, T is the temperature, and  $\mu_{\text{n0}}$  is the temperature-independent prefactor of the mobility. The temperature dependence of the mobility is modeled using a (small) activation energy  $\Delta E_{\text{ac}}$ .

The current through the Schottky diode is calculated based on the thermionic and thermionic field emission theory, see section 2.3:

$$I = \begin{cases} I_{\text{TE}} & V_{\text{applied}} > 0 \text{ (forward)} \\ -I_{\text{TFE,reverse}} & V_{\text{applied}} \leq 0 \text{ (reverse)}. \end{cases}$$
(3.4)

As the voltage is applied to the active electrode, a positive voltage  $V_{\rm Schottky}$  across the diode corresponds to a forward bias ( $V_{\rm forward} = V_{\rm Schottky}$ ,  $V_{\rm reverse} = -V_{\rm Schottky}$ ). Thermionic emission is chosen for the forward direction as this ensures the current to be computable for all applied voltages, especially in the LRS with a high donor concentration, see the discussion in section 2.3. Under reverse bias, tunneling cannot be neglected given the moderate to high donor concentrations. The thermionic field emission equation also provides a real-valued result for a vanishing Schottky barrier ( $\phi_{\rm Bn} = 0 \, {\rm V}$ ) and is therefore appropriate for the current description under reverse bias. For the donor concentration in Eqs. (2.2) and (2.6),  $N_{\rm D} = z_{\rm Vo} N_{\rm disc}$  holds. The energy difference between the Fermi level and the conduction band edge  $e\phi_{\rm n}$  depends on the donor concentration. Its value is approximated based on the Boltzmann statistics according to

$$\phi_{\rm n} = \frac{k_{\rm B}T}{e} \log \left( \frac{2(2\pi m_{\rm eff}k_{\rm B}T/h^2)^{3/2}}{z_{\rm Vo}N_{\rm disc}} \right).$$
 (3.5)

Although the Boltzmann approximation does not hold for degenerate semiconductors, Eq. (3.5) still provides an approximation dependent on the concentration  $N_{\rm disc}$ , which is better than using a constant value for  $\phi_{\rm n}$ .

The change of the oxygen vacancy concentration in the disc can be modeled in terms of an ionic current  $I_{\text{ion}}$  between the plug and the disc according to

$$\frac{\mathrm{d}N_{\mathrm{disc}}}{\mathrm{d}t} = -\frac{1}{z_{\mathrm{Vo}}e\,A\,l_{\mathrm{disc}}} \cdot I_{\mathrm{ion}}.\tag{3.6}$$

The plug acts as infinite reservoir with a constant and high oxygen vacancy concentration. The ionic current, which depends on the local temperature and the electric field, describes an ion hopping conduction over a potential barrier, see section 2.4. The barrier  $\Delta W_{\rm A}$  is lowered by the applied electric field E for forward jumps and raised for reverse jumps:

$$I_{\text{ion}} = AJ_{\text{ion,drift}}$$

$$= A\left(2z_{\text{Vo}}ea\nu_{0}N\exp\left(-\frac{\Delta W_{\text{A}}\left[\sqrt{1-\gamma^{2}}+\gamma\arcsin\gamma\right]}{k_{\text{B}}T}\right)\sinh\left(\frac{az_{\text{Vo}}eE}{2k_{\text{B}}T}\right)\cdot F_{\text{limit}}\right),$$
(3.7)

where a is the hopping distance,  $\nu_0$  is the attempt frequency and N is the ion concentration. The factor  $\gamma$  modifies the hopping barrier for forward and reverse jumps according to

$$\gamma = \frac{az_{\text{Vo}}eE}{\pi\Delta W_{\text{A}}}.$$
(3.8)

To account for the non-uniform distribution of the ions in the filament, the driving concentration N for the drift current is chosen as the mean of both concentrations  $N_{\rm disc}$  and  $N_{\rm plug}$ . As the concentrations vary over several orders of magnitude and the concentration profiles are assumed to resemble a sigmoid on a logarithmic scale, the geometrical mean is used instead of the arithmetic mean:

$$N = \sqrt{N_{\rm disc} \cdot N_{\rm plug}}.$$
 (3.9)

Like the choice of the driving concentration for the ionic current, the selection of the driving electric field is nontrivial. Considering the different electrical situation for SET and RESET, best results are obtained with

$$E = \begin{cases} \frac{V_{\text{disc}} + V_{\text{plug}}}{l_{\text{cell}}} & V_{\text{applied}} > 0 \text{ (RESET)} \\ \frac{V_{\text{disc}}}{l_{\text{disc}}} & V_{\text{applied}} < 0 \text{ (SET)}. \end{cases}$$
(3.10)

The ionic current is limited by the factor  $F_{\text{limit}}$  to ensure that the vacancy concentration neither exceeds a maximum nor falls below a minimum concentration,  $N_{\text{disc,max}}$  and  $N_{\text{disc,min}}$ , respectively:

$$F_{\text{limit}} = \begin{cases} \left[ 1 - \left( \frac{N_{\text{disc,min}}}{N_{\text{disc}}} \right)^{10} \right] & V_{\text{applied}} > 0 \\ \left[ 1 - \left( \frac{N_{\text{disc}}}{N_{\text{disc,max}}} \right)^{10} \right] & V_{\text{applied}} < 0. \end{cases}$$
(3.11)

The exponent of 10 is arbitrary but was chosen such that the ionic current is only influenced when  $N_{\rm disc}$  is close to the limits. An exponent of 10 ensures this much better than an exponent of 1.

Because 2D simulations have shown that the temperature along the filament is rather homogeneous [44], one single temperature for the whole filament is used. The local temperature is calculated based on the power dissipation in the filament due to the voltage drops across the disc and the plug:

$$T = (V_{\text{disc}} + V_{\text{plug}}) \cdot I \cdot R_{\text{th,eff}} + T_0, \tag{3.12}$$

where  $T_0$  is the ambient temperature. The Joule heating is described using one effective thermal resistance  $R_{\text{th,eff}}$ , which comprises the heat loss to the surrounding oxide and to the metal electrodes.

Details on the solver and on the simulation workflow can be found in section 2.6.

## 3.2 Simulation Results

The simulation results are divided in three parts. First, the switching characteristics and the general model behavior are explained in section 3.2.1. In connection to experimental data of a  $\rm Ti/TiO_x/HfO_x/Pt$  nanocrossbar device, the RESET process is analyzed in detail in section 3.2.2. Section 3.2.3 deals with the SET process by comparing simulation results to experimental data of  $\rm TiN/SrTiO_x/Pt$  nanocrossbars.

#### 3.2.1 General Model Characteristics

The model parameters used in this section are identical to those in section 3.2.2 and are listed in Table 3.1. The general behavior of compact model 1.0 is depicted in Fig. 3.2. The I-V characteristic on logarithmic scale, linear scale, and the R-V characteristic

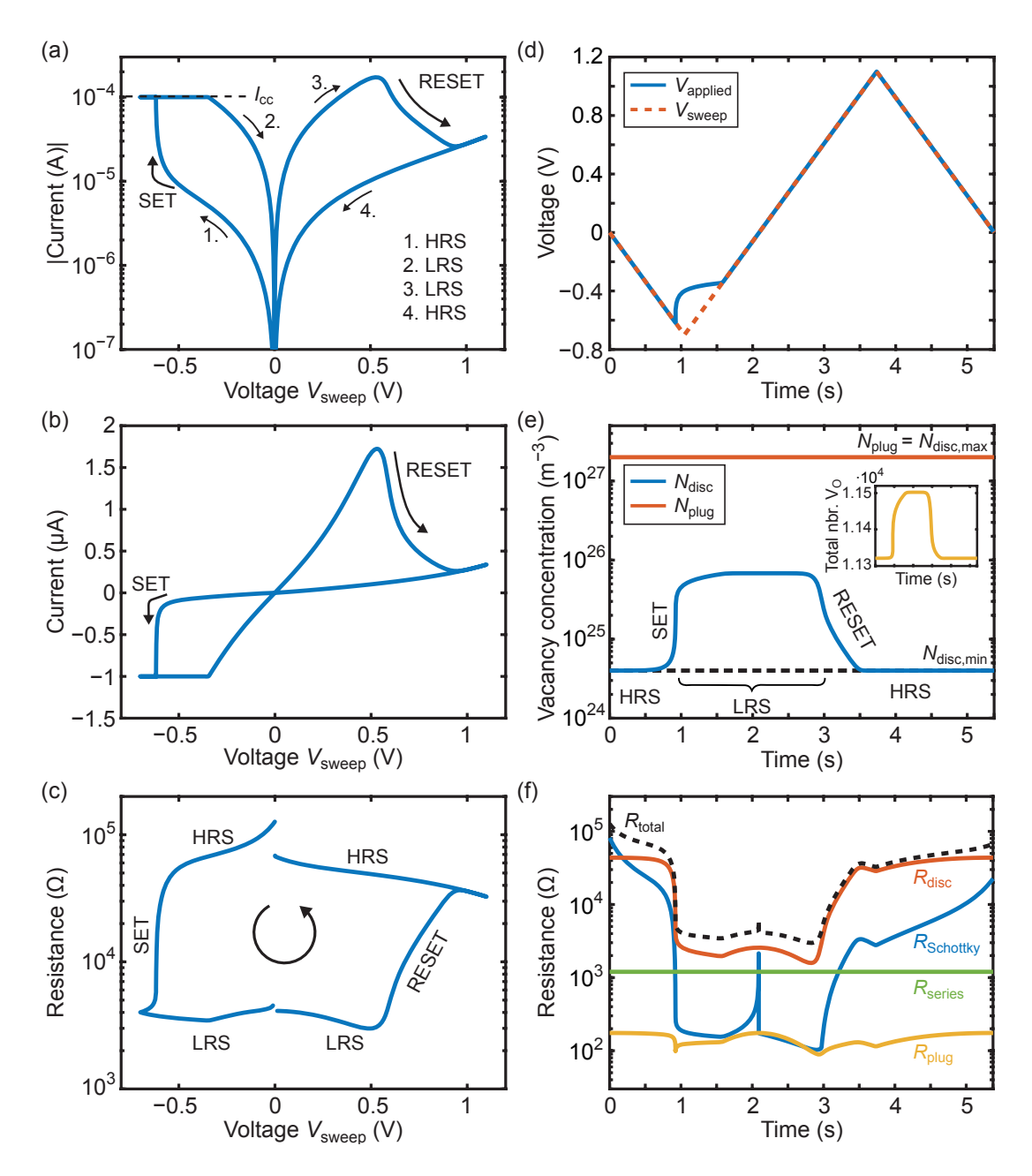


Figure 3.2: General model characteristics of compact model 1.0, simulated with the parameters in Table 3.1. (a) I-V curve on a logarithmic scale. (b) I-V curve on a linear scale. (c) Corresponding R-V curve of the total resistance. (d) Comparison of the predefined sweep voltage  $V_{\rm sweep}$  and the actually applied voltage  $V_{\rm applied}$ . Only if the current compliance is active, these voltages differ. (e) Oxygen vacancy concentration of the plug and the disc. The inset shows the total number of vacancies in the filament calculated based on the concentrations. (f) Resistances of the four lumped circuit elements and the sum of the four as total resistance.

Symbol	Value	Symbol	Value
$l_{ m cell}$	$3\mathrm{nm}$	$A^*$	$6.01 \cdot 10^5 \mathrm{A/(m^2 K^2)}$
$l_{ m disc}$	$1\mathrm{nm}$	$e\phi_{ m Bn0}$	$0.3\mathrm{eV}$
$l_{ m plug}$	$l_{ m cell} - l_{ m disc}$	$\mu_{ m n0}$	$1.5 \cdot 10^{-4}  \mathrm{m}^2 / (\mathrm{Vs})$
$r_{ m fil}$	$30\mathrm{nm}$	$\Delta E_{ m ac}$	$0.08\mathrm{eV}$
$z_{ m Vo}$	2	$N_{ m plug}$	$2 \cdot 10^{27}  \mathrm{m}^{-3}$
a	$0.4\mathrm{nm}$	$N_{ m disc,max}$	$2 \cdot 10^{27}  \mathrm{m}^{-3}$
$ u_0$	$1\cdot 10^{12}\mathrm{Hz}$	$N_{ m disc,min}$	$4 \cdot 10^{24}  \mathrm{m}^{-3}$
$\Delta W_{ m A}$	$0.9\mathrm{eV}$	$R_{ m series}$	$1200\Omega$
$\varepsilon$	$17  \varepsilon_0$	$R_{ m th,eff}$	$1.4 \cdot 10^6  { m K/W}$
$arepsilon_{\phi_{ m B}}$	$5.5\varepsilon_0$	sweep rate	$0.67\mathrm{V/s}$
$m_{ m eff}$	$m_{ m e}$	$T_0$	293 K

**Table 3.1:** Parameters for the simulations in sections 3.2.1 and 3.2.2.

are displayed in Fig. 3.2a, b, and c, respectively. The predefined sweep voltage and the applied voltage, the oxygen vacancy concentration of the plug and the disc, and all resistances are shown over time in Fig. 3.2d, e, and f, respectively. At the beginning, the cell is in the HRS as the initial concentration of oxygen vacancies in the disc is low. The overall resistance in the HRS is dominated by the resistance of the disc and the converted resistance of the Schottky diode  $(R_{\text{Schottky}} = V_{\text{Schottky}}/I)$ . Due to the voltage dependence of the conduction through the Schottky barrier,  $R_{\text{Schottky}}$  decreases considerably from the start, although the disc concentration is nearly constant. The abrupt increase in current around  $-0.6\,\mathrm{V}$  is the prominent feature of the SET process. Oxygen vacancies drift from the plug to the disc as a negative potential is applied at the AE. Thus, the vacancy concentration in the disc increases and the resistances of the disc and the Schottky barrier decrease. The ion concentration in the plug remains constant during switching; the plug serves as an oxygen vacancy reservoir for the disc. A direct consequence from this model assumption is that the total number of oxygen vacancies is not constant during switching, see the inset in Fig. 3.2e. As the number of vacancies in the plug far exceeds the number of vacancies in the disc, the simplification is reasonable though.

The SET process is stopped by the current compliance, which prevents the current to rise above a certain level  $I_{\rm cc}$ , here  $|I_{\rm cc}|=100\,\mu{\rm A}$ . This is achieved by decreasing the applied voltage until  $I=I_{\rm cc}$  holds. Consequently, there exists a deviation between the actually applied voltage  $V_{\rm applied}$  and the predefined sweep voltage  $V_{\rm sweep}$ , see Fig. 3.2d. Unless otherwise stated, I-V curves are plotted over  $V_{\rm sweep}$ . The total resistance is calculated based on  $V_{\rm applied}$ . Due to the decrease in the driving electric field during SET, the increase of the vacancy concentration is decelerated. If no current compliance is set,

the concentration in this model would rise until its maximum value is reached, which equals the vacancy concentration in the plug.

In the LRS, the series and the disc resistance dominate the conductance. As the disc resistance is temperature dependent, its value is not constant in the LRS, even after the disc concentration has reached a constant level. For the same reason, the plug resistance changes slightly over the course of the sweep.

For positive voltages applied to the AE, the oxygen vacancies are repelled from the electrode and the RESET sets in. The concentration in the disc decreases until the minimum value is reached. Simultaneously, the disc and Schottky resistances increase. In contrast to the disc resistance, the Schottky resistance does not reach its initial value, although the final and the initial disc concentrations are identical. This difference is caused by a different voltage dependence of the conduction in forward and reverse direction.

The minimum oxygen vacancy concentration in the disc is one of the major parameters defining the resistance in the HRS. This is illustrated in Fig. 3.3. All three sweeps start with the same initial concentration but the minimum concentrations  $N_{\rm disc,min}$  differ (Fig. 3.3b). Consequently, the first half sweep is identical but the RESET leads to different HRS levels (Fig. 3.3a). The oxygen vacancy concentration is always reduced to its minimum value as long as the voltage is applied long enough because no counter force like diffusion is implemented that counterbalances the movement. It is not unreasonable per se to define a minimum value as it prevents a concentration that would convert to less than one oxygen vacancy in the disc. Here, however, it is used as fitting parameter for the maximum HRS resistance.

Figure 3.4 shows the influence of some other important parameters on the I-V characteristic. The series resistance determines the LRS and has a high impact on the RESET, see Fig. 3.4a and section 3.2.2. Moreover, the SET changes from an abrupt to a more gradual, mirrored S-shaped current increase if the series resistance increases. The potential barrier for the ion migration  $\Delta W_{\rm A}$  differs between oxides. To avoid any influence of the LRS on the RESET dynamics, the sweep voltages are chosen such that the disc concentration in the LRS reaches the same value in all cases. Otherwise, the RESET would be affected by the LRS in addition to the change in  $\Delta W_{\rm A}$ . The ionic current depends exponentially on the potential barrier. Thus, SET and RESET voltage differ clearly upon small changes in  $\Delta W_{\rm A}$ , see Fig. 3.4b. The higher the barrier is, the higher fields (voltage) and temperatures (current) are required to trigger the switching. For a low barrier, the SET switching is less abrupt. The effective thermal resistance

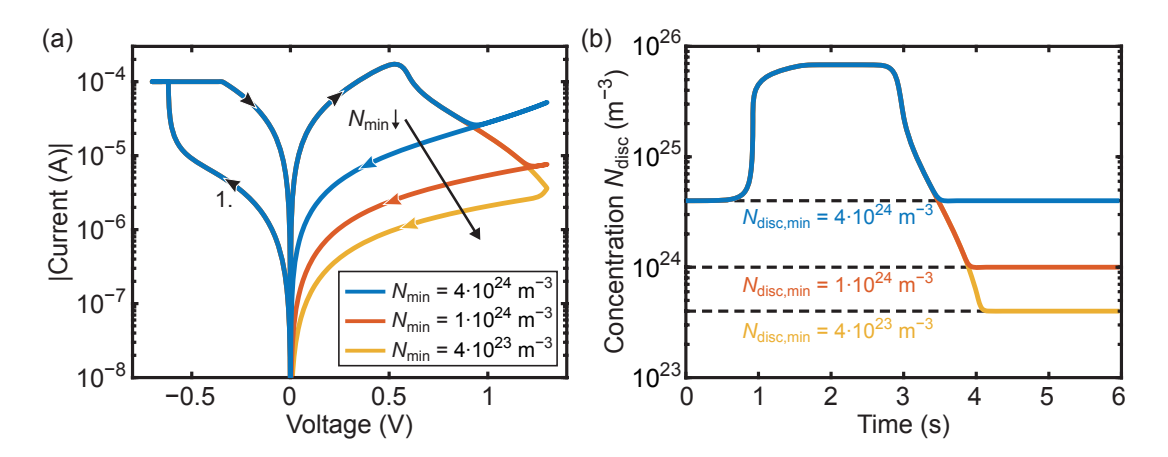


Figure 3.3: Influence of  $N_{\rm disc,min}$  on (a) the I-V curve and (b) the oxygen vacancy concentration in the disc. As only drift is included in the ionic current and no counter force, the migration of oxygen vacancies is only stopped by the artificially set minimum limit.

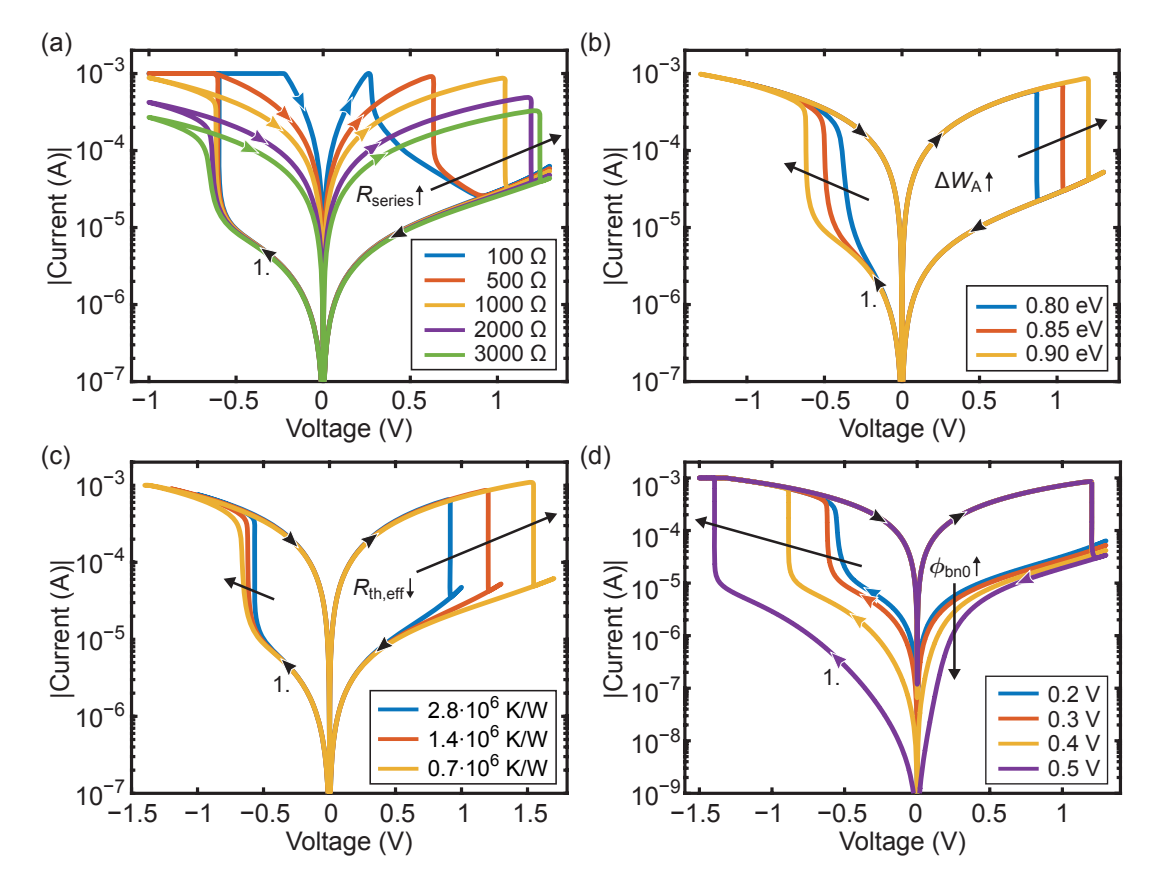


Figure 3.4: Influence of various parameters on the switching behavior. The parameters are taken from Table 3.1 with the exception of the parameter being varied as stated in the figures. Influence of (a) the series resistance  $R_{\rm series}$ , (b) the potential barrier  $\Delta W_{\rm A}$  for the ion migration process, (c) the effective thermal resistance  $R_{\rm th,eff}$ , and (d) the nominal Schottky barrier height  $e\phi_{\rm bn0}$ .

has a great influence on the temperature. Figure 3.4c illustrates the effect of a different temperature enhancement on the switching. For a lower thermal resistance, the SET is slowed down and becomes more gradual as the positive feedback via the temperature is reduced, see section 3.2.3. The effect on the HRS resistance via the temperature dependence of the conductivity is very small because the temperature in the HRS is hardly raised for small currents. The temperature in the LRS is distinctly lower for a reduced thermal resistance and consequently, the RESET is delayed considerably. A different nominal Schottky barrier height  $e\phi_{\rm bn0}$  mostly affects the HRS, and thus, the SET voltage, see Fig. 3.4d. The Schottky resistance strongly increases for a higher barrier, especially at low voltages. This reduces the current and thereby the temperature in the filament. Moreover, the driving electric field is reduced because the voltage across the disc decreases for an increasing voltage across the diode; this increases the SET voltage significantly.

#### 3.2.2 Gradual and Abrupt RESET

Experimentally, the RESET behavior was studied in detail on HfO<sub>x</sub>/TiO<sub>x</sub> bilayer nanocrossbar devices [81]. The oxide layers were deposited on a Pt bottom electrode using ALD (atomic layer deposition). A Ti layer was used as top electrode with a Pt layer as protecting layer on top. The final  $(100 \times 100) \, \mathrm{nm}^2$  devices have a layer stack of  $30 \text{ nm Pt}/3 \text{ nm HfO}_x/3 \text{ nm TiO}_x/10 \text{ nm Ti}/20 \text{ nm Pt}$ . Details on the fabrication can be found in [81]. Fabrication and electrical characterization were done by Alexander Hardtdegen. The electrical I-V measurements were carried out with a Keithley 2611 SCS. The sweep rate for all voltage sweeps was 0.67 V/s. The voltage is defined as being applied to the Pt bottom electrode, while the top electrode is grounded. After electroforming, the devices were switched by applying voltage sweeps from  $-1.3\,\mathrm{V}$  to  $1.3\,\mathrm{V}$ . A current compliance series was conducted, starting with 100 µA and increasing to 700 µA in steps of  $100 \,\mu\text{A}$  (in terms of absolute values). The resulting I-V curves are plotted in Fig. 3.5a. The device clearly shows two kinds of RESET, a gradual one for a low current compliance and an abrupt one for a high current compliance. Moreover, the RESET is shifted to higher voltages for an increasing current compliance. The shift of the RESET voltage (RESET current) for a higher current compliance was also reported in [151, 152]. The simulation parameters are fitted to the device to study whether both types of RESET can be modeled with one dynamical process, here drift of oxygen vacancies, or whether more dynamical processes have to be involved. All model parameters are chosen within physical reasonable limits and are listed in Table 3.1. Switching is

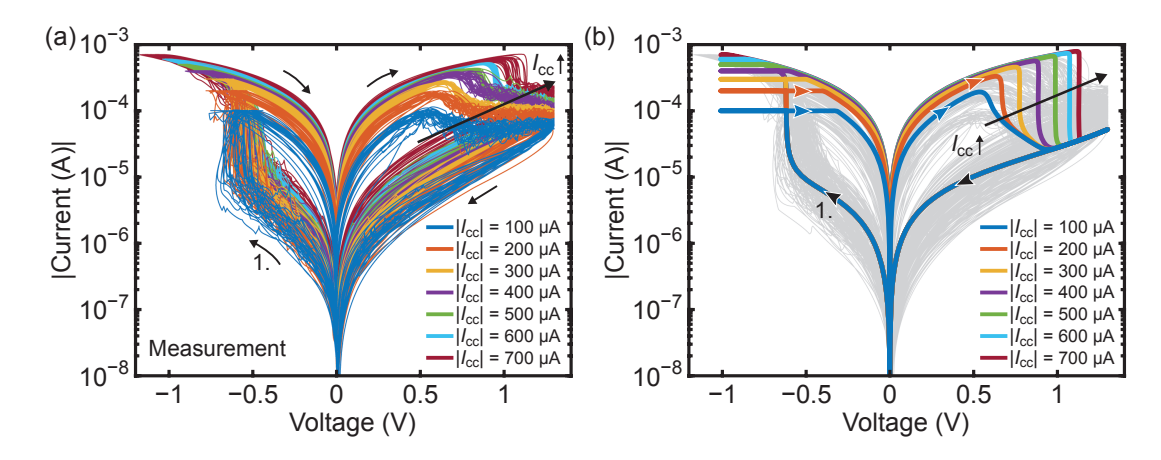


Figure 3.5: Gradual and abrupt RESET in experiment and simulation [81]. (a) Experimental data measured on a Ti/TiO<sub>x</sub>/HfO<sub>x</sub>/Pt device by Alexander Hardtdegen. For a low current compliance the RESET is gradual, whereas the RESET is abrupt after a SET with a high current compliance. Adapted from [81], © 2018 IEEE. (b) Simulation results obtained with the parameters from Table 3.1 are shown in comparison to the experimental data and reveal the same trend. The simulation differs from the published one in [81] regarding the parameters and Eqs. (3.5), (3.7) to (3.10) and (3.12).

assumed to take place solely in the  $HfO_x$  layer and the  $TiO_x$  layer is included in the series resistance. The simulated I-V curves are shown in Fig. 3.5b in comparison to the experimental data. The general trend is clear and matches the data: the higher the current compliance, the later the RESET sets in and the more abrupt the switching becomes. On the one hand, the differences between simulation and experimental data are related to the electrical conduction mechanism. The HRS after the RESET clearly shows a different voltage dependence. On the other hand, the gradual transition in the data is much more pronounced than in the simulation. Of course, this could also be related to the electrical model.

The origin of the RESET trend is illustrated in more detail in Fig. 3.6. The various current compliances slow down the SET at different progress levels. Thus, the higher the current compliance, i.e. the later the SET was slowed down, the higher the concentration of oxygen vacancies in the disc in the LRS becomes, see Fig. 3.6b. Because of the lower disc resistance, the LRS is more conductive for high  $|I_{cc}|$ . Although the current is higher, the temperature in the filament is smaller for high  $|I_{cc}|$ , see Fig. 3.6c. This is caused by a lower heat dissipation in the filament because less voltage drops across the actual cell as it is illustrated in Fig. 3.6d. In fact, only the voltage across the filament  $(V_{disc} + V_{plug})$  is used to calculate the temperature, see Eq. (3.12), but the relation is the same as in Fig. 3.6d. Thus, the higher the current compliance, the more voltage drops across

the series resistance. This reduces the temperature and the driving electric field (see Eq. (3.10)) and consequently, the RESET is delayed to higher voltages. Figure 3.6e displays the driving electric field over time. The start of the RESET event is visible as a sharp increase in the electric field between roughly  $3.8 \, \mathrm{s} - 4.8 \, \mathrm{s}$ . An abrupt increase always signifies a positive feedback in the model during the switching process. Thus, the RESET accelerates itself as the disc resistance, and thereby the electric field, rises due to the decrease of the oxygen vacancy concentration. The gradient of the increase in the electric field influences the steepness of the RESET. For  $|I_{cc}| = 100 \,\mu\text{A}$ , only at the beginning of the RESET, the gradient of the electric field increases, then the gradient is approximately constant. Consequently, the RESET process is fast upon start and then the gradient of the current decrease is reduced. In contrast for  $|I_{cc}| = 700 \,\mu\text{A}$ , the electric field increases sharply upon the start of the RESET and reaches very high values. This results in a fast decrease of oxygen vacancies in the disc down to the minimum concentration and the RESET is completely abrupt. In addition to the enhancement of the switching speed due to the electric field, the temperature accelerates the RESET even further. As the voltage across the filament rises during RESET, the temperature in the model rises during switching. In summary, the ratio between  $R_{\text{series}}$  and  $R_{\text{filament}}$ determines the RESET shape, see Fig. 3.6f. If the filament resistance, consisting of  $R_{\rm disc}$  and  $R_{\rm plug}$ , is higher than the series resistance, the RESET is gradual. Generally speaking, the ratio between the series resistance and the resistances used to calculate the driving electric field and the temperature is crucial.

To conclude, the experimental data shows two kinds of RESET processes — gradual and abrupt — depending on the height of the current compliance. In addition, the abrupt RESET starts at higher voltages. The compact model simulation, describing accurately all dynamical trends from the experiment, suggests that both RESETs do rely on the same dynamical process of field- and temperature-driven ion migration. For higher current compliances, the series resistance dominates the LRS, and the voltage across the filament (and thereby the driving electric field) is small. On the one hand, this delays the start of the RESET and on the other hand, it strongly accelerates the positive feedback of the electric field and the temperature on the resistance change in the model resulting in an abrupt switching.

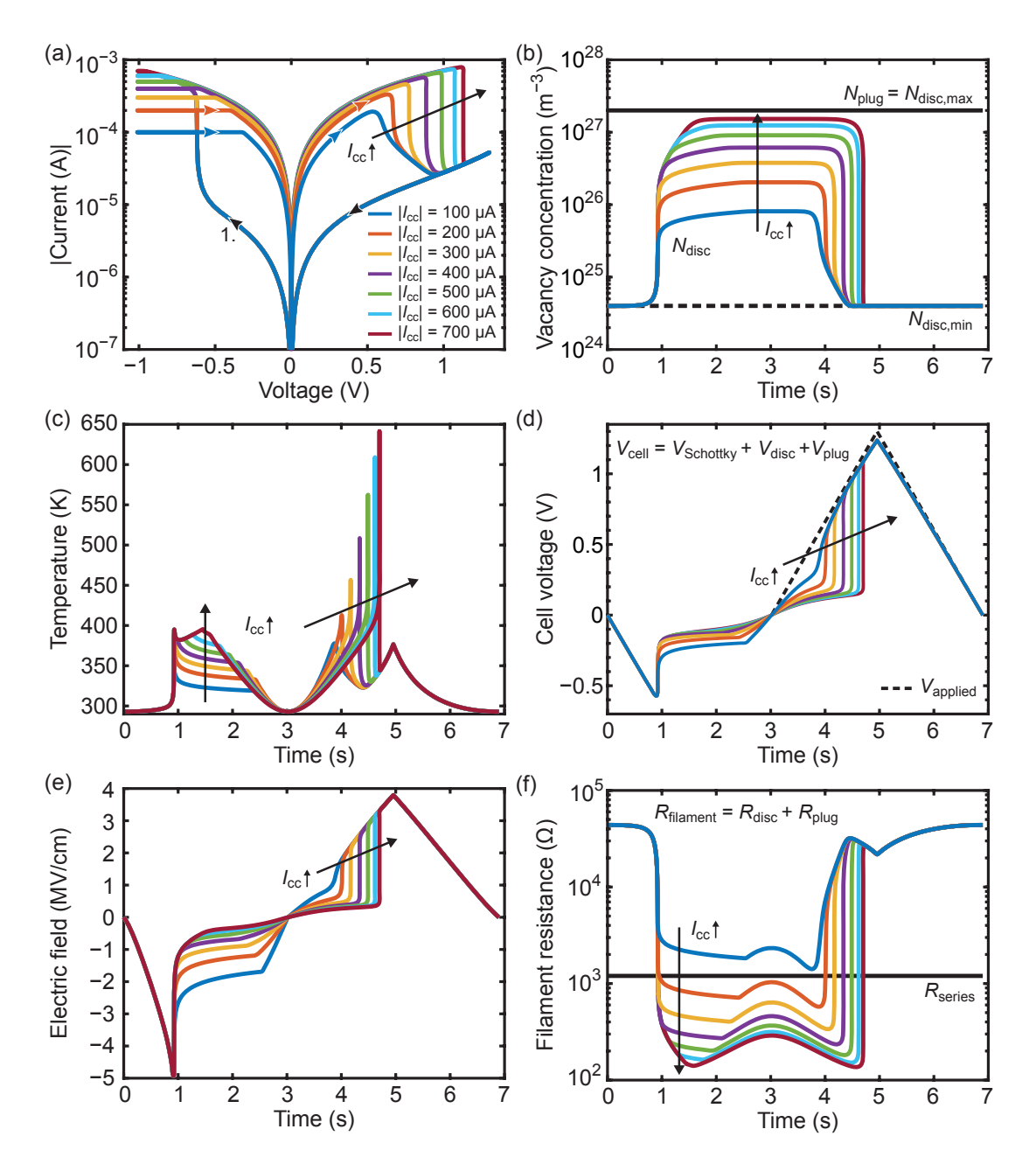


Figure 3.6: Origin of the different shapes of the RESET process for current compliances ranging from  $-100 \,\mu\text{A}$  to  $-700 \,\mu\text{A}$ . (a) I-V curves. (b) Oxygen vacancy concentration in the disc. The minimum concentration is included as dashed line; the maximum concentration, which equals the concentration in the plug, is shown as solid, black line. (c) Temperature in the filament. (d) Voltage across the cell being defined as  $V_{\text{cell}} = V_{\text{applied}} - V_{\text{series}}$  and the applied voltage (dashed line). (e) Electric field used to calculate the drift of the oxygen vacancies, see Eq. (3.10). (f) Filament resistance ( $R_{\text{disc}} + R_{\text{plug}}$ ) and series resistance (black line).

## 3.2.3 Gradual and Abrupt SET<sup>1</sup>

Experimentally, the SET kinetics were studied in detail on STO-based nanocrossbar devices [150]. The oxide was deposited on a Pt bottom electrode using ALD. A TiN layer was used as top electrode with a Pt layer as protecting layer on top. The final layer stack for the  $(100 \times 100) \, \mathrm{nm^2}$  devices was  $30 \, \mathrm{nm} \, \mathrm{Pt/8} \, \mathrm{nm} \, \mathrm{SrTiO_3/30} \, \mathrm{nm} \, \mathrm{TiN}$ . Details on the fabrication can be found in [150]. The electrical characterization and the analysis of the measured data were done by Karsten Fleck. On a time scale below 1s, the electrical pulse measurements were carried out with a Keithley 4200-SCS equipped with a 4225-PMU and two remote amplifiers. On a time scale above 1s, the measurements were performed using a Keithley 2636A source meter. The voltage was applied to the Pt bottom electrode, while the top electrode was grounded. After electroforming, cycles of RESET-READ-SET-READ pulse sequences are applied to the device. Every second cycle is a preparation cycle with fixed pulse amplitudes and lengths to switch the cell reliably into the LRS and HRS. The test cycles, i.e. every other cycle, use a SET with systematically varied amplitudes and lengths. All cycles start with a 10 µs RESET pulse of 2.3 V, which puts the cell in the target HRS of about  $100-200 \,\mathrm{k}\Omega$ . This is verified by a -0.5 V, 1 ms READ pulse. If the target resistance is not met, the results of this cycle are discarded.

Using this measurement routine and setup, voltage pulses from  $-0.8\,\mathrm{V}$  to  $-1.5\,\mathrm{V}$  are applied to the cells and the occurring current transients are recorded on a time scale from 10 ns to 10<sup>4</sup> s. In the measured current transients, the SET event is easily identified as large and abrupt current increase. The time between the pulse amplitude reaching 90 % of its maximum value and the sudden current jump is named SET time  $t_{\rm SET}$ . This SET transition is not completed instantaneously and the time difference between  $t_{\rm SET}$ and 90% of the absolute current maximum is recorded as transition time. Preceding the abrupt jump, the current increases linearly. The slope of this gradual increase, termed pre-SET slope, is extracted from a linear fitting of the current, starting at the beginning of the plateau and ending at  $t_{\text{SET}}$ . The mean current of the plateau is calculated based on the currents at the limits of the same interval. The volatility of the HRS degradation, i.e. the current increase before the SET event, was investigated in a further study [150]: The application of a voltage pulse, which is sufficiently long to cause the SET switching, is repeatedly interrupted with pauses of 1 s. No difference in the degradation is found and the current levels before and after the pause are similar. Thus, the resistance degradation is at least stable on a time scale of 1s and purely electronic effects can be excluded as

Parts of the text in this section are taken from [150] © 2016 American Physical Society.

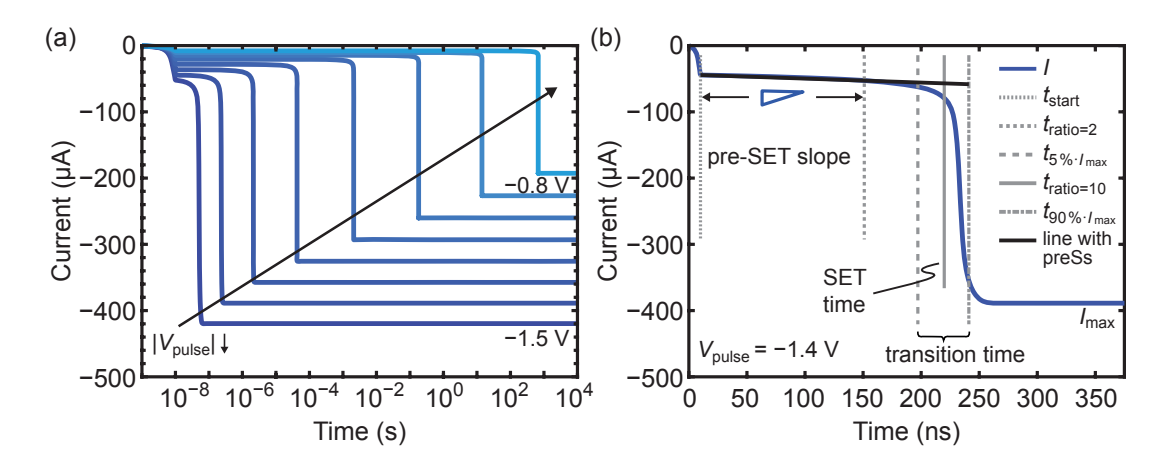


Figure 3.7: Simulation of SET pulses, performed with the parameters from Table 3.2. (a) Current transients for voltage pulses ranging from  $-1.5 \,\mathrm{V}$  to  $-0.8 \,\mathrm{V}$ . (b) Definition of criteria for several characteristic numbers used to analyze the SET switching and its dynamic, see Fig. 3.8. The simulation differs from the published result in [150] regarding the parameters, the definition of the criteria, and Eqs. (3.5), (3.7) to (3.10) and (3.12).

origin. Experimental findings of a linearly increasing current prior to the SET event are not unique to STO-based VCM devices. Similar experiments reveal the same behavior for other oxides, e.g.  $TaO_x$  and  $ZrO_x$  [150].

The model parameters were fitted to the measurement results to study the origin of the linear degradation and the possible connection to the subsequent abrupt SET event. Similar to the experiment, the SET current transients upon application of voltage pulses ranging from  $-0.8\,\mathrm{V}$  to  $-1.5\,\mathrm{V}$  are simulated as shown in Fig. 3.7a. All parameters are listed in Table 3.2. Note that a comparatively high value for the activation energy for the ion hopping process of 1.4 eV was chosen as it was necessary to obtain a steep SET kinetics. Accordingly, the required large value for the effective thermal resistance of  $1 \cdot 10^7\,\mathrm{K/W}$  leads to high simulated temperatures in the LRS up to 1800 K for  $V_{\mathrm{pulse}} = -1.5\,\mathrm{V}$ . For all pulses, the oxygen vacancy concentration in the disc equals its maximum value after the SET.

Analogous to the experiment, the current transients are analyzed in terms of SET time, pre-SET slope, transition time, and mean plateau current. The criteria for these characteristic numbers differ slightly between simulation and experiment. For example, due to the limited measurement resolution, an abrupt increase is easy to define as a specified ratio of current increase between two consecutive points. In contrast, the simulation does not use equidistant time steps and the time steps can be very small because they are chosen to ensure convergence. The criteria used to analyze the simulation results are marked exemplarily in the current transient for  $V_{\text{pulse}} = -1.4\,\text{V}$  in

Table 9.2. I diameters for the simulations in Sections 9.2.9.				
Value	Symbol	Value		
8 nm	$A^*$	$6.01 \cdot 10^5  \mathrm{A/(m^2 K^2)}$		
$1.5\mathrm{nm}$	$e\phi_{ m Bn0}$	$0.3\mathrm{eV}$		
$l_{ m cell} - l_{ m disc}$	$\mu_{ m n0}$	$1 \cdot 10^{-4}  \mathrm{m}^2 / (\mathrm{Vs})$		
$18\mathrm{nm}$	$\Delta E_{ m ac}$	$0.08\mathrm{eV}$		
2	$N_{ m plug}$	$5 \cdot 10^{26}  \mathrm{m}^{-3}$		
$0.5\mathrm{nm}$	$N_{\rm disc,max}$	$5 \cdot 10^{26}  \mathrm{m}^{-3}$		
$8\cdot 10^{12}\mathrm{Hz}$	$N_{ m disc,min}$	$8 \cdot 10^{24}  \mathrm{m}^{-3}$		
$1.4\mathrm{eV}$	$R_{\text{series}}$	$2500\Omega$		
$17  \varepsilon_0$	$R_{ m th,eff}$	$1\cdot 10^7\mathrm{K/W}$		
$5.5arepsilon_0$	rise time	$10\mathrm{ns}$		
$m_{ m e}$	$T_0$	$293\mathrm{K}$		
	$\begin{array}{c} 8\mathrm{nm} \\ 1.5\mathrm{nm} \\ l_{\mathrm{cell}} - l_{\mathrm{disc}} \\ 18\mathrm{nm} \\ 2 \\ 0.5\mathrm{nm} \\ 8 \cdot 10^{12}\mathrm{Hz} \\ 1.4\mathrm{eV} \\ 17\varepsilon_0 \\ 5.5\varepsilon_0 \end{array}$	$\begin{array}{cccccccccccccccccccccccccccccccccccc$		

**Table 3.2:** Parameters for the simulations in sections 3.2.3.

Fig. 3.7b. At any time t, the present change in current is described by the derivative  $\partial I(t)/\partial t$ , whereas the total change in current compared to the starting level is given as  $\Delta I(t)/\Delta t = [I(t)-I(t_{\rm start})]/[t-t_{\rm start}]$ . To analyze the ongoing change in current in the simulation, the relation of the present change to the total change  $[\partial I(t)/\partial t]/[\Delta I(t)/\Delta t]$  is an appropriate indicator. A ratio of two signifies that the current is increasing twice as fast as in the whole previous time  $\Delta t$ . To identify the SET event and the pre-SET slope accurately, two criteria are defined: The point in time with a ratio of  $\Delta I(t)/\Delta t = [I(t)-I(t_{\rm start})]/[t-t_{\rm start}]=2$  minus the rise time of the voltage pulse (10 ns) is used as SET time. To determine the pre-SET slope of the current plateau, a linear fit at the interval between the beginning of the plateau  $t_{\rm start}$  and the point with ratio  $\Delta I(t)/\Delta t = [I(t)-I(t_{\rm start})]/[t-t_{\rm start}]=2$  is performed. On the same interval, the mean plateau current is calculated as  $[I(t_{\rm ratio}=2)+I(t_{\rm start})]/2$ . The transition time is obtained as the time difference between the points where the current reaches 5% and 90% of the maximum current.

The resulting SET time, pre-SET slope, transition time, and mean plateau current are shown alongside the measured data in Fig. 3.8a-d, respectively. The kinetics of the SET process is known to be highly nonlinear [153, 154]. As expected, the SET time is highly dependent on the applied voltage and displays a high variability. Starting just above  $-0.8\,\mathrm{V}$  with a spreading between 1s and  $10^4\,\mathrm{s}$ , the experimentally obtained SET time decreases to a few ns at  $-1.49\,\mathrm{V}$ . For low pulse amplitudes, the transition of the SET event takes up to  $100\,\mathrm{s}$  and decreases rapidly down to about  $50\,\mathrm{ns}$  at  $-1.2\,\mathrm{V}$ , which is around the resolution limit of the setup. A highly nonlinear behavior is also found for the pre-SET slope ranging from  $10^{-10}\,\mathrm{A/s}$  for voltages around  $-0.8\,\mathrm{V}$  to around  $1\,\mathrm{A/s}$  for

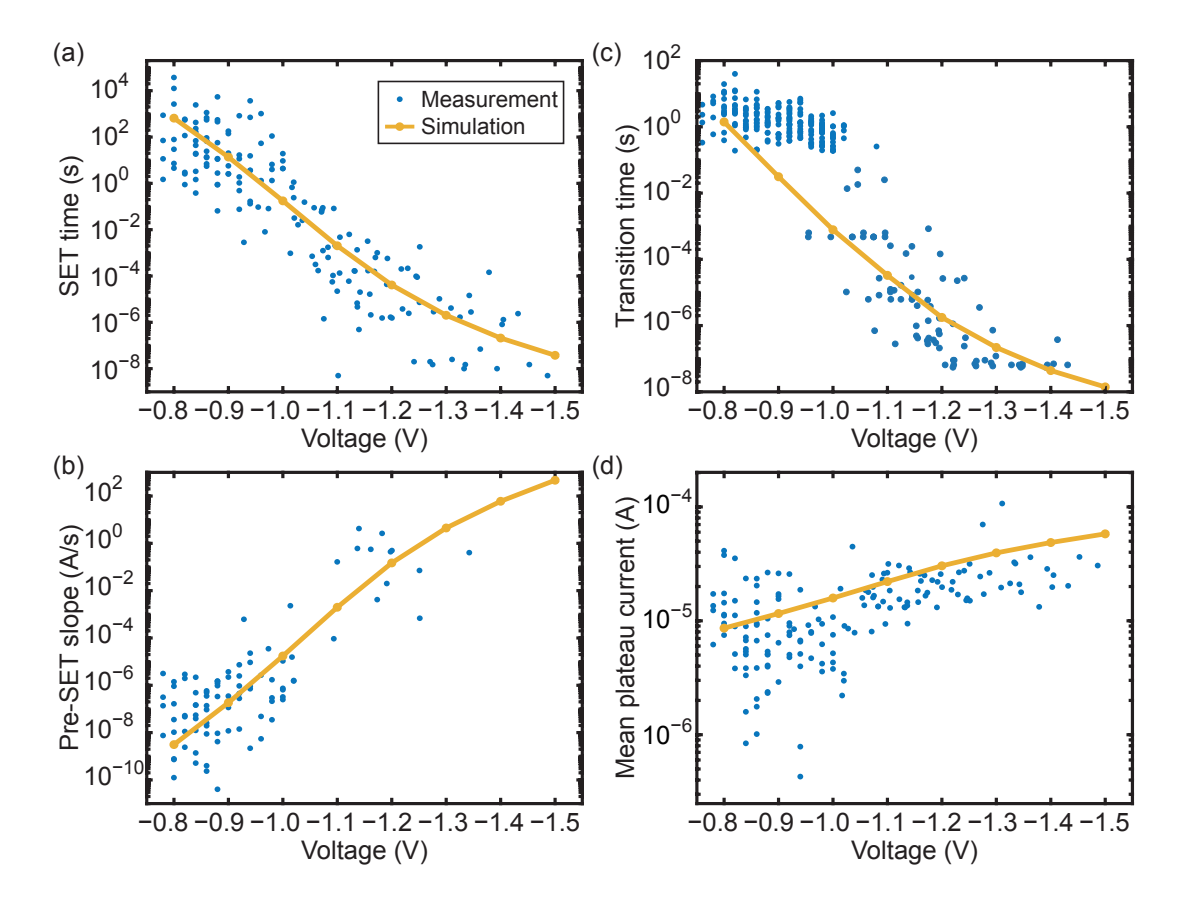


Figure 3.8: Highly voltage-dependent characteristic numbers of SET pulse switching, obtained with both experiments and simulations [150]. Experimental data were provided by Karsten Fleck. The simulation differs from the published result in [150] regarding the parameters, the definition of the criteria, and Eqs. (3.5), (3.7) to (3.10) and (3.12). (a) SET time to characterize the abrupt SET event. (b) Pre-SET slope of the linear degradation prior to the SET event. (c) Transition time to determine the speed of the abrupt SET event. (d) Mean plateau current used as additional information for fitting purposes.

voltages around  $-1.15\,\mathrm{V}$ , thus changing by more than ten orders of magnitude. For pulse amplitudes higher than  $|-1.2\,\mathrm{V}|$ , determining the pre-SET slope in the measured data becomes rather difficult because the effect of the degradation is small compared to the already high plateau currents at these voltages. This effect is illustrated using a rough estimation of the absolute current increase  $\Delta I_{\mathrm{rise}}$  with  $\Delta I_{\mathrm{rise}} = \mathrm{pre}$ -SET slope × SET time. In the case for low pulse voltages ( $V_{\mathrm{pulse}} = -0.8\,\mathrm{V}$ ), a pre-SET slope of  $10^{-8}\,\mathrm{A/s}$  with a SET time of  $10^2\,\mathrm{s}$  results in a total increase of 1  $\mu\mathrm{A}$  during the degradation process. This change is detected in a mean plateau current around 7  $\mu\mathrm{A}$ . For higher pulse voltages ( $V_{\mathrm{pulse}} = -1.1\,\mathrm{V}$ ), a much higher pre-SET slope of  $10^{-3}\,\mathrm{A/s}$  combined with a much lower SET time of  $10^{-3}\,\mathrm{s}$  also results in an absolute current increase of 1  $\mu\mathrm{A}$ . The mean plateau current, however, is higher and a change of 1  $\mu\mathrm{A}$  is harder to detect. In addi-

tion, the noise level of the setup for faster pulses is higher, being in the order of around  $1\,\mu\mathrm{A}$ . The source of problems to determine the characteristic numbers appropriately differ between simulation and measurement. In the simulation, there is no resolution limit, neither in current nor time, which prevents the calculation of the characteristic numbers. The smooth, precisely simulated transition between the linear current increase and the current jump impedes the clear distinction between the two regions though. In the experiment, this is rarely an issue. That is why the degradation before the abrupt jump is much more prominent in the simulation for high voltage amplitudes compared to low ones (see Fig. 3.7a). Consequently, the calculated absolute current increase rises from  $1.5\,\mu\mathrm{A}$  ( $V_{\mathrm{pulse}} = -0.8\,\mathrm{V}$ ) to  $11.6\,\mu\mathrm{A}$  ( $V_{\mathrm{pulse}} = -1.5\,\mathrm{V}$ ). All highly nonlinear trends, however, are present in the simulation and the overall match between experimental and simulated data is fairly well.

The question is whether the two nonvolatile processes — linear increase and abrupt jump — arise from the same origin or whether several dynamical processes are involved. A compact model simulation can provide insight whether several dynamical processes need to be involved. However, the simulation result cannot be seen as a proof for a suggested explanation of the experimental data. To understand the two switching regions in the simulation, the current transient I is plotted together with the crucial parameters temperature T and oxygen vacancy concentration in the disc  $N_{\rm disc}$  for an applied voltage of  $-1.4\,\rm V$  and  $-0.9\,\rm V$  in Fig. 3.9a and b, respectively. Although the values for the current, the temperature and the SET time differ strongly for the two pulse voltages, the overall process is quite similar. The current increase in both regions is induced by a rise in the disc concentration and the temperature, as both lower the overall resistance. Similar to the current magnitude, temperature and vacancy concentration first increase slowly and then change very rapidly in a short time, which coincides with the SET event. As the state variable  $N_{\rm disc}$  changes (and the ionic current only includes drift), the decrease in resistance over the whole pulse is nonvolatile, matching the experimental data.

The movement of oxygen vacancies and thereby the switching is field- and temperature-driven, see Eq. (3.7). Both field and temperature enhancement of the ion migration lead to a nonlinear switching time. Assuming exclusively field-driven migration, however, just results in a weak nonlinearity of very few orders of magnitude in time [155]. Consequently, the present nonlinearity covering eight orders of magnitude for voltages ranging from  $-0.8 \,\mathrm{V}$  to  $-1.5 \,\mathrm{V}$ , should be a result of temperature enhancement. To separate the contributions of field and temperature on the SET process, the current transient for  $V_{\mathrm{pulse}} = -1.4 \,\mathrm{V}$  is shown for two cases in Fig. 3.10a. The red transient shown already

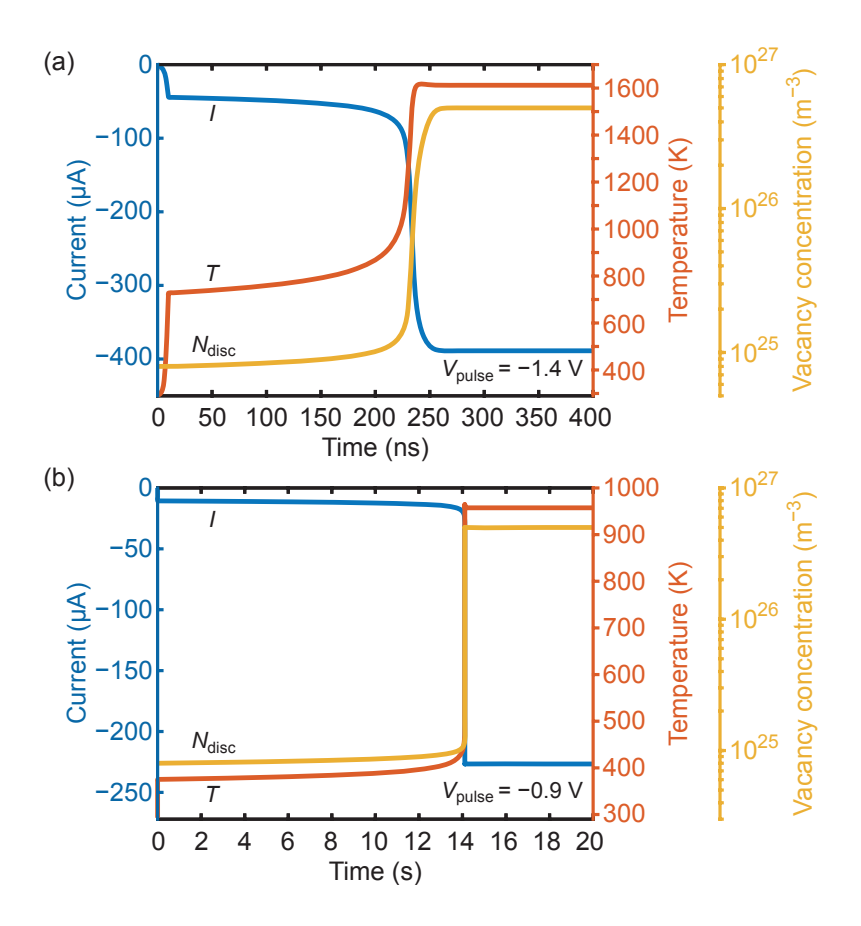


Figure 3.9: Analysis of the origin of the abrupt SET event and the preceding linear current increase. Simulated current, temperature and oxygen vacancy concentration in the disc are shown for (a)  $V_{\text{pulse}} = -1.4 \,\text{V}$  and (b)  $V_{\text{pulse}} = -0.9 \,\text{V}$ .

in Fig. 3.7 and Fig. 3.9 represents the case of field and temperature enhancement. The other transient, solely field-driven, is obtained with a model that equals the model described in section 3.1, except that the temperature T is not increased by Joule heating, so that  $T=T_0$  is valid at all times. Without temperature enhancement, the SET time increases and even more important, no abrupt switching takes place. Instead, a gradual transition over six orders of magnitude switches the cell into the LRS. The currents at the beginning of the voltage pulse and in the LRS differ due to the voltage and temperature dependence of  $R_{\rm Schottky}$ ,  $R_{\rm disc}$  and  $R_{\rm plug}$ , see Fig. 3.10b and c for the simulation with and without Joule heating, respectively. The disc resistance dominates the HRS; it is considerably lower for higher temperatures and thus, the mean plateau current is higher for the simulation with Joule heating. The LRS at a temperature of around 1600 K is dominated almost exclusively by the series resistance, whereas at room temperature the filament resistance is higher. In both cases, the oxygen vacancy concentration in the disc equals its maximum value in the LRS. The temperature and the driving electric

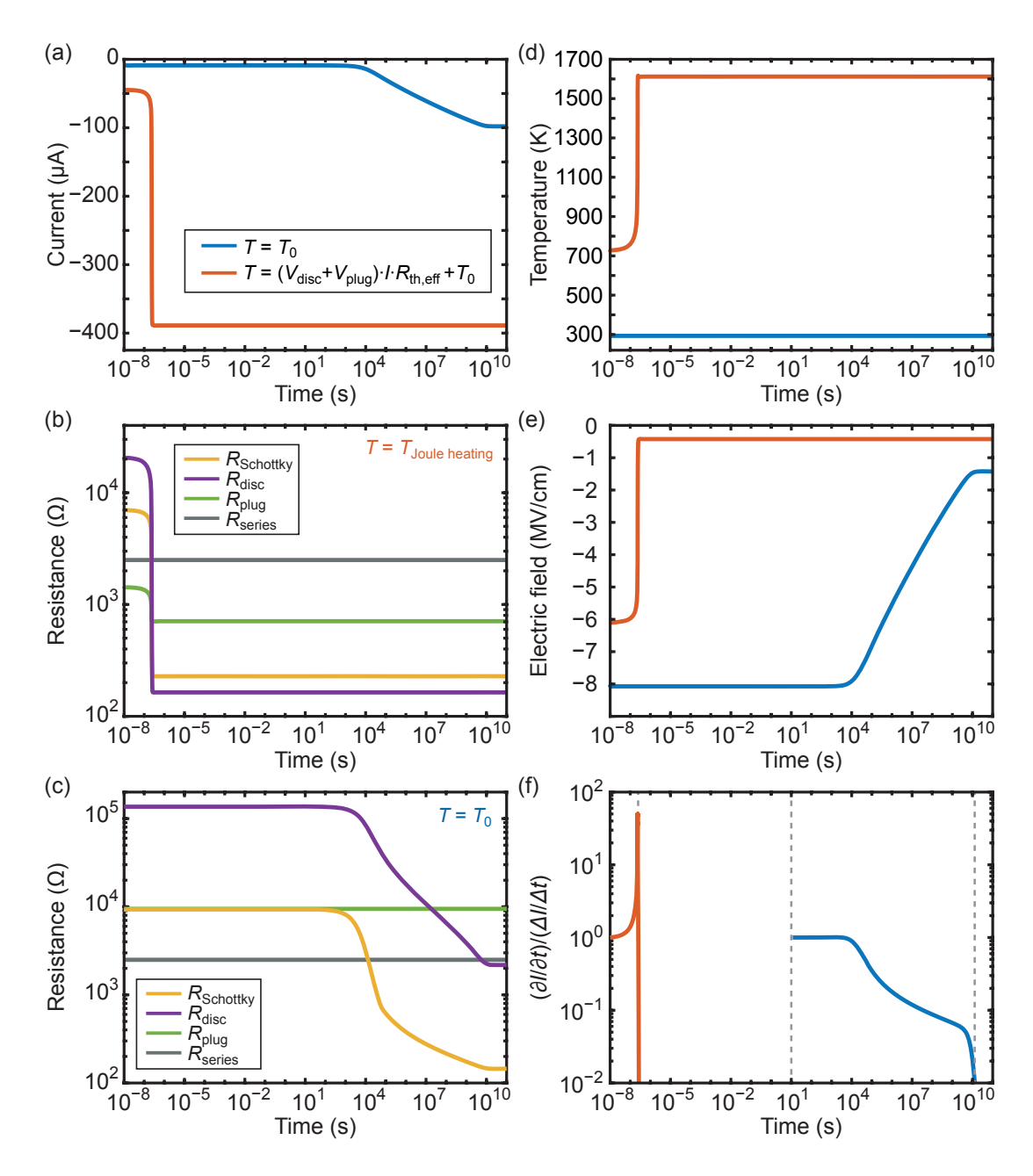


Figure 3.10: Contribution of Joule heating on the SET switching. The processes are analyzed for the example of  $V_{\text{pulse}} = -1.4 \,\text{V}$ . (a) Current transients modeled with Joule heating as before and without Joule heating. In the latter case, the temperature is constant and equals the room temperature  $T_0$ . The legend in (a) is also valid for (d)-(f). The resistances of the four lumped elements are shown for both cases, in (b) for the simulation with Joule heating and in (c) for the simulation without Joule heating. (d) Temperature. (e) Electric field used to calculate the drift of oxygen vacancies. (f) The ratio of present change in current  $\partial I(t)/\partial t$  and total change in current  $\Delta I(t)/\Delta t$  is displayed only in the intervals in which the switching takes place.

field for both simulations are illustrated in Fig. 3.10d and e, respectively. Although the electric field is higher for the case with  $T=T_0$ , as the voltage across disc and plug is larger, the SET transition starts later. Thus, it is the temperature enhancement that leads to a fast and abrupt switching. This thermal runaway is characterized by a positive feedback: The current rise increases the local temperature, causing a faster ion migration. The subsequent increase of the oxygen vacancy concentration in the disc, which results in a decrease of the resistances  $R_{\rm Schottky}$  and  $R_{\rm disc}$ , increases the current even further. In the case of a positive feedback, here caused by the thermal runaway, relating the present change in current to the total change  $[\partial I(t)/\partial t]/[\Delta I(t)/\Delta t]$  gives a monotonically increasing curve during switching, see Fig. 3.10f. On the contrary, the gradual transition for the solely field-driven simulation is characterized by a decreasing ratio, as in total no positive but a negative feedback dominates: The driving electric field reduces during the SET transition, as the voltage across the disc decreases due to a lower disc resistance, and the voltage drop across the plug does not increase enough to compensate for this effect.

For fitting purposes, several parameters that highly influence the SET kinetics can be adjusted. Exemplarily, the influences of the activation energy of the ion hopping process  $\Delta W_{\rm A}$ , the effective thermal resistance  $R_{\rm th,eff}$ , the disc length  $l_{\rm disc}$ , and the nominal Schottky barrier height  $e\phi_{bn0}$  are shown in Fig. 3.11a-d, respectively. The general trends are easy to motivate: A higher activation barrier increases the SET time as the ionic current is reduced. Increasing the effective resistance reduces the SET time due to a higher temperature. Note that for  $R_{\rm th,eff} = 1.5 \cdot 10^7 \, {\rm K/W}$ , the maximum temperature exceeds 2250 K for  $V_{\rm pulse} = -1.5\,\mathrm{V}$  ( $I = 420\,\mathrm{\mu A}$ ). This is below the melting point of SrTiO<sub>3</sub> (2333 K) but exceeds the melting point of platinum (2041 K) and other oxides like Ta<sub>2</sub>O<sub>5</sub> (2145 K) [156]. Thus, this specific simulation is only shown to illustrate the general trend, quantitative conclusions should not be drawn. The electric field for the ion drift during SET is calculated based on the disc length. Consequently, a shorter disc increases the electric field and the SET time is lowered. A raised intrinsic barrier height leads to a higher SET time as the resistance of the Schottky junction increases. Consequently, more voltage drops across the diode and less voltage drops across the disc, thereby reducing the electric field. Apart from the general trends, the situation is more complex as the ionic current is interlinked by temperature and electric field with the whole device. For example, increasing one resistance results in lower voltage drops across all other elements. In case of voltage-dependent resistances like the Schottky junction, a lower voltage drop changes the resistance in turn. Moreover, the temperature is influ-

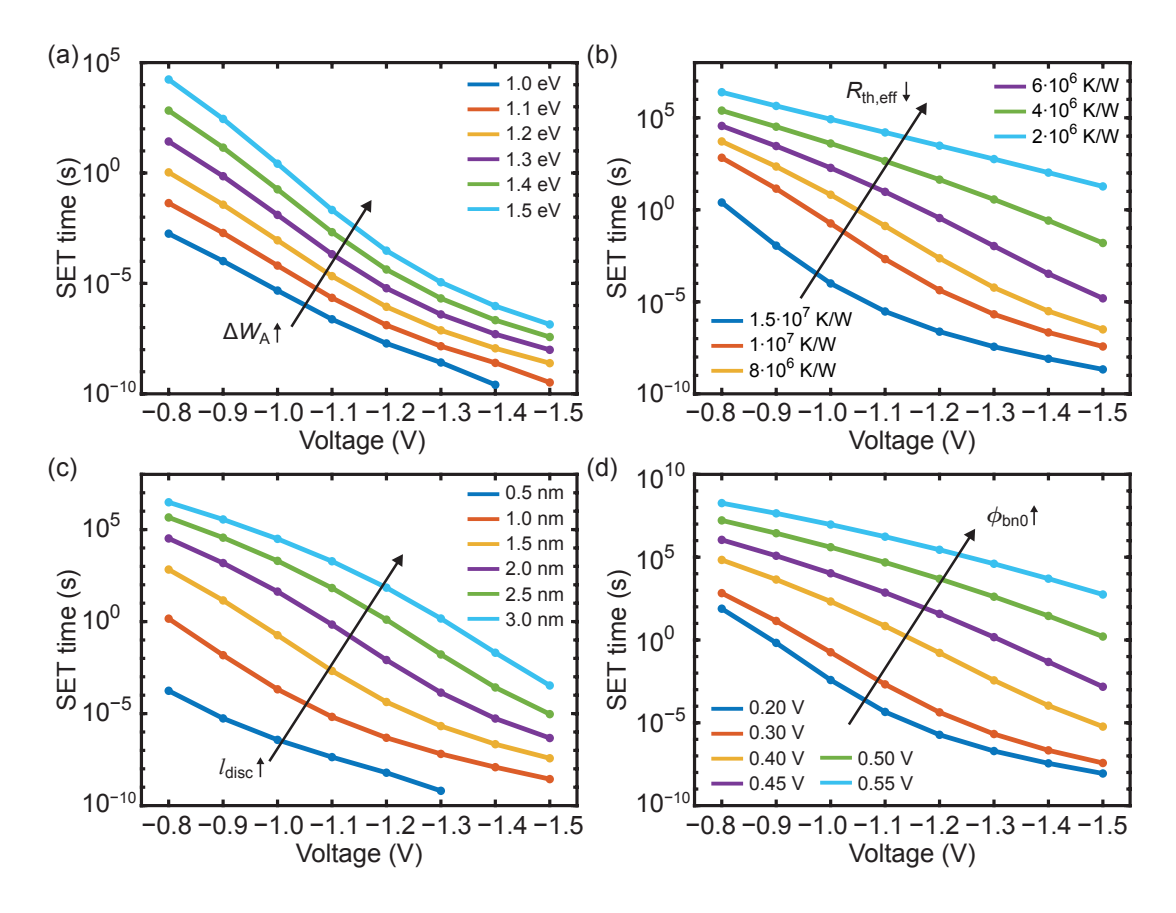


Figure 3.11: Influence of various parameters on the SET switching kinetics. The parameters are taken from Table 3.2 with the exception of the parameter being varied as stated in the figures. In contrast to the SET time analysis in Fig. 3.8, the SET time is defined as the time at which  $I = -100 \,\mu\text{A}$  is reached for the first time minus the rise time of the voltage pulse. This is necessary as the criterion based on the ratio between present change and total change in current being 10 cannot be evaluated for all parameter combinations. Influence of (a) the potential barrier  $\Delta W_{\rm A}$  for the ion migration process, (b) the effective thermal resistance  $R_{\rm th,eff}$ , (c) the disc length  $l_{\rm disc}$ , and (d) the nominal Schottky barrier height  $e\phi_{\rm bn0}$ .

enced by the lower current, but also by the electric field. Depending on which resistance is changed, the electric field used to calculate the temperature is raised or reduced. Consequently, the temperature may increase or decrease, which in turn influences all temperature-dependent resistances. Which effect is dominant depends on the chosen parameters and the applied voltage. As a result, the SET kinetics are not simply shifted uniformly upon variation of one parameter, but the magnitude of the shift depends on the pulse amplitude.

To conclude, the SET consists of two nonvolatile processes: a gradual degradation of the HRS, followed by a prominent and abrupt current jump. Experiments on different oxides ( $SrTiO_{3-x}$ ,  $TaO_x$ , and  $ZrO_x$ ) imply that the observed phenomena are part of the

general VCM switching. The compact model simulation, matching all trends from the experiment on STO-based nanocrossbars, suggests that both processes are actually of the same physical origin. Both can be accurately described by field- and temperature-driven ion migration. If the field enhancement dominates, the transition is very gradual. The abrupt current increase is the result of a positive feedback triggered by Joule heating ("thermal runaway"). Checking for the ratio  $[\partial I(t)/\partial t]/[\Delta I(t)/\Delta t]$  to rise monotonically is an option to identify a positive feedback crucial for a runaway. The existence of a nonvolatile degradation in the pre-SET regime in experimental data can be seen as clear indication that the HRS is dominated by the filament and not by any unrelated parallel current path.

### 3.3 Conclusion

The physics-based compact model presented in this chapter reproduces several complex findings of sweep and pulse experiments sufficiently well. The analysis of the simulation results shows that a gradual and an abrupt RESET can be obtained with the same dynamical process of field- and temperature-driven ion migration just by changing the voltage divider between the filament and a series resistance. This suggests that also in the experiment both RESET shapes can originate from the same origin. In addition, it underlines that a single I-V characteristic is not sufficient to characterize a ReRAM device as the internal series resistance is unknown. In both pulse experiment and simulation, the SET current transients can be subdivided into a linear degradation of the HRS that is followed by a prominent and abrupt current jump. The comparison allows to propose the physical origin of the degradation: An electric-field-driven increase of the oxygen vacancy concentration near the Schottky barrier results in a gradual current increase. If the field enhancement is accompanied by a steadily increasing temperature due to Joule heating, a positive feedback exists leading to a self-acceleration of the SET process and finally a thermal runaway.

The scope of this compact model is limited due to several model assumptions. As only drift due to an externally applied voltage is included, the concentration of oxygen vacancies in the disc always equals the defined minimum or maximum value,  $N_{\rm disc,min}$  and  $N_{\rm disc,max}$ , in the stable state. Due to the polarity dependence, the sign of the voltage determines whether the disc concentration reaches its maximum or minimum, given that the voltage is applied long enough. If no voltage is applied, the resistance state has an infinite retention. By setting a current compliance, the concentration can be prevented

from reaching its maximum value during SET. Carefully choosing the maximum sweep voltage during RESET will result in a concentration higher than the minimum. Nevertheless, the choice of these two parameters has a significant influence on the resulting I-V curve and it is mainly motivated by fitting rather than physical considerations. The assumption of the plug acting as infinite reservoir of oxygen vacancies for the disc is only appropriate if the number of oxygen vacancies in the plug is much higher than in the disc. Thus, the parameters for the lengths and concentrations of the plug and the disc have to be chosen cautiously, which increases the complexity during fitting. The effective thermal resistance in the model is constant and does not depend on the temperature, the defect concentration, or the polarity of the applied voltage. This may explain the very high temperatures that occur in the LRS in pulse simulations. If the parameter is not chosen carefully, the temperature easily exceeds the melting point of the used oxide and metals. At least for stable switching, this is physically unreasonable. A large value for the effective thermal resistance, however, is often required to match the experimentally observed steep SET kinetics and fast SET times. Thus, the thermal model needs to be improved by gaining more knowledge on the thermal conductivity of transition metal oxides and its dependence on defect concentration and temperature. Neglecting a possible oxygen exchange with the electrodes definitely limits the general applicability of the model. It is important to note that the electrical model has a huge influence on the dynamical processes. The voltage and temperature dependencies of the single elements are crucial regarding the existence of a positive or negative feedback during switching. In the presented model, disc and plug resistance depend directly on the temperature but only indirectly on the voltage via the temperature. Also the equation for the conduction through the Schottky barrier are based on simplifications that are not valid for all devices. Thus, reliable conclusions on the dynamical situation require a sufficiently accurate knowledge of the conduction mechanism. Therefore, finding precise compact formulations for the electrical conduction in the different devices is one crucial key to increase the predictability and accuracy of the model. Another approach is improving the description of the ion migration to reduce the dependence on non-material parameters like  $N_{\rm disc,min}$ .

# 4 Compact Model 1.5

The compact model 1.0 presented in chapter 3 successfully describes several aspects of resistive switching behavior, which are observed experimentally. The description of the ion migration, however, needs to be improved. In this chapter, the model is extended to include diffusion to improve the RESET. Adding diffusion allows the development of a dynamic drift-diffusion balance that can slow down the RESET process. In addition, the retention under zero bias is not infinite anymore. Moreover, the vacancy concentration in the plug is now variable. This extension enables the model to describe complementary switching (CS) alongside with bipolar switching (BS). The influence of various parameters on the I-V characteristic is discussed and the connection of bipolar and complementary switching is illustrated. Regarding gradual and abrupt complementary switching, the interdependencies of resistance change, temperature and electric field are analyzed in terms of positive and negative feedback. Besides modeling CS devices, the model improves the description of BS as it allows to reproduce and explain anomalies in BS switching curves. The simulation results are also compared to experimental data. Some results of this chapter have been published before in [157, 158]. The experimental data shown in this chapter were provided by Thomas Breuer and Andreas Kindsmüller. Compact model 1.5 is based on the following general assumptions:

- To enable switching, a sufficiently large number of oxygen vacancies is present in a filament. This is ensured by choosing the initial values appropriately. Forming is not covered by the model.
- The filament is cylindrical with a time-invariant, constant cross-sectional area. It is split into two regions of uniform oxygen vacancy concentration called plug and disc. These two oxygen vacancy concentrations are the state variables of the model.
- Both metal/oxide interfaces are modeled as Schottky contacts. In case of an asymmetric device stack, different values for the Schottky barrier heights are used.
- Oxygen vacancies are treated as mobile, doubly-charged donors. Their movement along the filament is described based on drift and diffusion. Internal electric fields

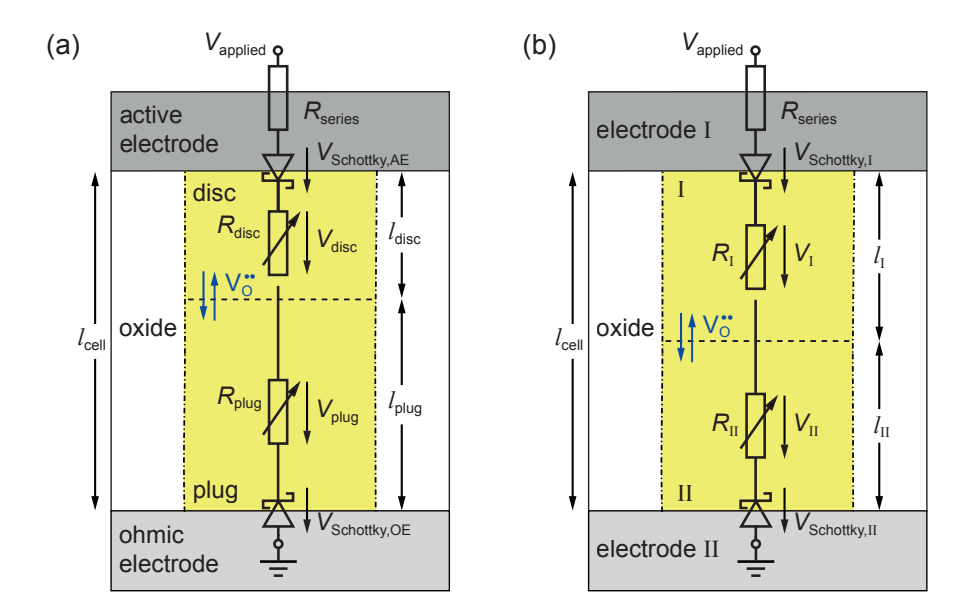


**Figure 4.1:** Equivalent circuit diagram for the electrical model of compact model 1.5 for (a) an asymmetric device and (b) a symmetric device. Fig. (a) and (b) are reproduced with permission from [157] and [158], respectively, © 2019 IEEE.

under zero bias, radial diffusion to the surrounding oxide, and thermodiffusion are neglected.

- The concentration of electrons is solely determined by the donor concentration.
- No electrode reactions, like an oxygen exchange, are considered.
- The temperature is approximated to be uniform in the filament.
- No stochastic processes are considered, the simulation results are deterministic.

## 4.1 Model Description and Equations

The whole ReRAM device is modeled using five elements, see Fig. 4.1: two Schottky diodes for the metal/oxide interfaces, two filament resistances and a series resistance  $R_{\rm series}$ . The length of the filament  $l_{\rm cell}$  is equivalent to the oxide thickness and its cross-sectional area A is calculated based on the filament radius  $r_{\rm fil}$  using  $A = \pi r_{\rm fil}^2$ . The model can be adapted to asymmetric and symmetric device stacks. For asymmetric device stacks, the filament is split into a disc and a plug of different lengths as in compact model 1.0, see Fig. 4.1a. As before, the disc is the region near the electrode of higher work function (active electrode). Consequently, all parameters concerning the Schottky barrier at this interface have an additional 'AE' in their name. For the ohmic

electrode, 'OE' is used in the subscript. The oxygen vacancy concentration and the length of the disc and the plug are denoted by  $N_{\rm disc}$ ,  $N_{\rm plug}$ ,  $l_{\rm disc}$  and  $l_{\rm plug}$ , respectively. For a completely symmetric device, the distinction of the electrodes in an active and an ohmic electrode and the distinction of the filament regions in a disc and a plug are not appropriate. Therefore, the filament is split into two regions I and II of identical volume  $(l_{\rm I} = l_{\rm I,II})$  and the electrodes are named I and II accordingly, see Fig. 4.1b. The equations in this section are given in terms of I and II, where 'I' can be interchanged with 'disc'/'AE' and 'II' with 'plug'/'OE' for the asymmetric case.

The voltage  $V_{\text{applied}}$  is applied to electrode I while electrode II is grounded. The current is denoted by I. Using Kirchhoff's law,

$$V_{\text{applied}} - \left[ V_{\text{Schottky,I}} + V_{\text{Schottky,II}} + I \cdot (R_{\text{I}} + R_{\text{II}} + R_{\text{series}}) \right] = 0 \tag{4.1}$$

is solved. Band conduction with temperature-dependent mobility  $\mu_n$  is assumed as electrical conduction mechanism in the filament. Thus, the two filament resistances are calculated using

$$R_{\rm I} = \frac{l_{\rm I}}{A \cdot z_{\rm Vo} e N_{\rm I} \mu_{\rm n}(T)} = \frac{l_{\rm I}}{A \cdot z_{\rm Vo} e N_{\rm I} \mu_{\rm n0}} \exp\left(\frac{\Delta E_{\rm ac}}{k_{\rm B} T}\right)$$
(4.2)

and

$$R_{\rm II} = \frac{l_{\rm II}}{A \cdot z_{\rm Vo} e N_{\rm II} \mu_{\rm n}(T)} = \frac{l_{\rm II}}{A \cdot z_{\rm Vo} e N_{\rm II} \mu_{\rm n0}} \exp\left(\frac{\Delta E_{\rm ac}}{k_{\rm B} T}\right),\tag{4.3}$$

where e is the elementary charge,  $z_{\text{Vo}}$  is the charge number of the oxygen vacancies relative to the perfect crystal lattice,  $k_{\text{B}}$  is the Boltzmann constant, T is the temperature, and  $\mu_{\text{n0}}$  is the temperature-independent prefactor of the mobility. The temperature dependence of the mobility is modeled using a (small) activation energy  $\Delta E_{\text{ac}}$ .

The current through the Schottky diodes is calculated based on the thermionic and thermionic field emission theory, see section 2.3:

$$I = \begin{cases} \operatorname{sign}(V_{\text{applied}}) \cdot I_{\text{TE}} & V_{\text{forward}} > 0 \text{ (forward)} \\ \operatorname{sign}(V_{\text{applied}}) \cdot I_{\text{TFE,reverse}} & V_{\text{forward}} \leq 0 \text{ (reverse)}. \end{cases}$$

$$(4.4)$$

As the two Schottky diodes are connected anti-serially, the definition of the voltage for which the junction is forward biased differs, see Fig. 4.1b. A positive voltage  $V_{\text{Schottky,I}}$  across diode I corresponds to a forward bias ( $V_{\text{forward}} = V_{\text{Schottky,I}}$ ,  $V_{\text{reverse}} = -V_{\text{Schottky,I}}$ ).

On the contrary, a positive voltage  $V_{\rm Schottky,II}$  across diode II equals a reverse bias ( $V_{\rm forward} = -V_{\rm Schottky,II}$ ,  $V_{\rm reverse} = V_{\rm Schottky,II}$ ). Thermionic emission is chosen for the forward direction as this ensures the current to be computable for all applied voltages, especially in the LRS with a high donor concentration, see the discussion in section 2.3. Under reverse bias, tunneling cannot be neglected given the moderate to high donor concentrations. The thermionic field emission equation also provides a real-valued result for a vanishing Schottky barrier ( $\phi_{\rm Bn} = 0\,{\rm V}$ ) and is therefore appropriate for the current description under reverse bias. For the donor concentrations in Eqs. (2.2) and (2.6),  $N_{\rm D,I/II} = z_{\rm Vo}N_{\rm I/II}$  holds.

The energy difference between the Fermi level and the conduction band edge  $e\phi_{n,I/II}$  depends on the donor concentration at interface I and II, respectively. Both values are approximated based on the Boltzmann statistics according to

$$\phi_{\rm n,I/II} = \frac{k_{\rm B}T}{e} \log \left( \frac{2(2\pi m_{\rm eff} k_{\rm B} T/h^2)^{3/2}}{z_{\rm Vo} N_{\rm I/II}} \right).$$
 (4.5)

Although the Boltzmann approximation does not hold for degenerate semiconductors, Eq. (4.5) still provides an approximation dependent on the concentrations  $N_{\rm I/II}$ , which is better than using constant values for  $\phi_{\rm n,I/II}$ .

The change of the oxygen vacancy concentration in the region I and the region II can be modeled in terms of an ionic current  $I_{\text{ion}}$  between the two regions according to

$$\frac{\mathrm{d}N_{\mathrm{I}}}{\mathrm{d}t} = -\frac{1}{z_{\mathrm{Vo}}e\,A\,l_{\mathrm{I}}} \cdot I_{\mathrm{ion}} \tag{4.6}$$

and

$$\frac{\mathrm{d}N_{\mathrm{II}}}{\mathrm{d}t} = \frac{1}{z_{\mathrm{Vo}}e\,A\,l_{\mathrm{II}}} \cdot I_{\mathrm{ion}}.\tag{4.7}$$

Thus, the same amount of oxygen vacancies that leaves the region I reappears in the region II. This results in a constant number of oxygen vacancies in the filament throughout the whole switching process. Note that the calculation is based on continuous concentrations and not on integer numbers of vacancies. The number of exchanged oxygen vacancies in every time step is a non-integer number. The ionic current  $I_{\rm ion}$  includes drift and diffusion and therefore depends on the local temperature, the electric field, and the concentration gradient between region I and region II. It describes an ion hop-

ping conduction over a potential barrier, see section 2.4. The barrier  $\Delta W_{\rm A}$  is lowered by the applied electric field E for forward jumps and raised for reverse jumps:

$$I_{\text{ion}} = A \left( J_{\text{ion,drift}} + J_{\text{ion,diffusion}} \right)$$

$$= A \left( CN \sinh \left( \frac{az_{\text{Vo}}eE}{2k_{\text{B}}T} \right) \cdot F_{\text{limit}} - C \frac{a}{2} \frac{dN}{dx} \cosh \left( \frac{az_{\text{Vo}}eE}{2k_{\text{B}}T} \right) \right)$$

$$(4.8)$$

with C as

$$C = 2z_{\text{Vo}}ea\nu_0 \exp\left(-\frac{\Delta W_{\text{A}}\left[\sqrt{1-\gamma^2} + \gamma \arcsin\gamma\right]}{k_{\text{B}}T}\right). \tag{4.9}$$

Here, a is the hopping distance,  $\nu_0$  is the attempt frequency, N is the ion concentration and dN/dx is the concentration gradient. The factor  $\gamma$  modifies the hopping barrier for forward and reverse jumps according to

$$\gamma = \frac{az_{\text{Vo}}eE}{\pi\Delta W_{\text{A}}}.\tag{4.10}$$

The ionic current is limited by the factor  $F_{\text{limit}}$  to ensure that the vacancy concentrations neither exceed a maximum nor fall below a minimum concentration,  $N_{\text{max}}$  and  $N_{\text{min}}$ , respectively:

$$F_{\text{limit}} = \begin{cases} \left[ 1 - \left( \frac{N_{\text{II}}}{N_{\text{max}}} \right)^{10} \right] \cdot \left[ 1 - \left( \frac{N_{\text{min}}}{N_{\text{I}}} \right)^{10} \right] & V_{\text{applied}} > 0 \\ \left[ 1 - \left( \frac{N_{\text{I}}}{N_{\text{max}}} \right)^{10} \right] \cdot \left[ 1 - \left( \frac{N_{\text{min}}}{N_{\text{II}}} \right)^{10} \right] & V_{\text{applied}} < 0. \end{cases}$$

$$(4.11)$$

The exponent of 10 is arbitrary but was chosen such that the ionic current is only influenced when  $N_{\rm I}$  or  $N_{\rm II}$  are close to the limits. An exponent of 10 ensures this much better than an exponent of 1.  $N_{\rm min}$  corresponds to the calculated concentration of one oxygen vacancy being present in region I. The ultimate maximum vacancy concentration is set by the density of oxygen sites in the crystal lattice. To prevent unreasonable high oxygen vacancy concentrations, a maximum site fraction of roughly 10% is chosen as  $N_{\rm max}$ .

To account for the non-uniform distribution of the ions in the filament, the driving concentration N for the drift current is chosen as the mean of both concentrations  $N_{\rm I}$  and  $N_{\rm II}$ . As the concentrations vary over several orders of magnitude and the concentration

profiles are assumed to resemble a sigmoid on a logarithmic scale, the geometrical mean is used instead of the arithmetic mean:

$$N = \sqrt{N_{\rm I} \cdot N_{\rm II}}.\tag{4.12}$$

For the concentration gradient applies

$$\frac{dN}{dx} = \frac{N_{\rm II} - N_{\rm I}}{0.5 \, l_{\rm cell}}.\tag{4.13}$$

Like the choice of the driving concentration for the ionic current, the selection of the driving electric field is nontrivial. A distinction between symmetric and asymmetric devices turned out to be necessary to obtain satisfactory results. For symmetric devices, the driving electric field is calculated using

$$E = \frac{V_{\rm I} + V_{\rm II}}{l_{\rm cell}} \tag{4.14}$$

for all  $V_{\text{applied}}$ . For asymmetric devices analogous to the approach for compact model 1.0, the equation differs for SET and RESET direction according to

$$E = \begin{cases} \frac{V_{\text{disc}} + V_{\text{plug}}}{l_{\text{cell}}} & V_{\text{applied}} > 0 \text{ (RESET)} \\ \frac{V_{\text{disc}}}{l_{\text{disc}}} & V_{\text{applied}} < 0 \text{ (SET)}. \end{cases}$$

$$(4.15)$$

Because 2D simulations have shown that the temperature along the filament is rather homogeneous [44], one single temperature for the whole filament is used. The local temperature is calculated based on the power dissipation in the filament due to the voltage drops across  $R_{\rm I}$  and  $R_{\rm II}$ :

$$T = (V_{\rm I} + V_{\rm II}) \cdot I \cdot R_{\rm th,eff} + T_0, \tag{4.16}$$

where  $T_0$  is the ambient temperature. The Joule heating is described using one effective thermal resistance  $R_{\text{th,eff}}$ , which comprises the heat loss to the surrounding oxide and to the metal electrodes.

The series resistance comprises the influence of the metal electrodes and the line resistances. It can be given a (metallic) temperature dependence using the temperature coefficient  $\alpha_{T,series}$ :

$$R_{\text{series}} = R_{\text{series},0} \left( 1 + \alpha_{\text{T,series}} (T - T_0) \right). \tag{4.17}$$

It is assumed that the series resistance is dominated by the spreading resistance of the metal, as there is only a small contact area to the filament, which leads to a non-uniform current density in the metal. Since this half-spherical spreading area is close to the filament, the filament temperature T is taken for the series resistance.

Details on the solver and on the simulation workflow can be found in section 2.6.

#### 4.2 Simulation Results

The simulation results cover two types of switching, bipolar and complementary switching. First, the general behavior of the model showing bipolar switching is described in section 4.2.1. The section focuses on the changes that occur by adding diffusion and a variable plug to compact model 1.0. In section 4.2.2, complementary switching is discussed in detail and compared to experimental data of a Pt/HfO<sub>x</sub>/Hf/Pt device. CS effects that occur in asymmetric BS devices are covered in section 4.2.3. An exemplary comparison is made to I-V curves obtained from a Pt/ZrO<sub>x</sub>/Ta/Pt device.

#### 4.2.1 General Model Characteristics

The general compact model behavior of compact model 1.5 regarding bipolar switching is shown in Fig. 4.2. The parameters for the simulation of an exemplary asymmetric device are listed in Table 4.1. The I-V characteristic and the oxygen vacancy concentration in the plug and the disc are depicted in Fig. 4.2a and b, respectively. When compared qualitatively to compact model 1.0 (see Fig. 3.2a and e), it is apparent that the RESET is more gradual. Moreover, the vacancy concentration in the plug decreases during SET and increases during RESET, opposite to the disc concentration. The changes in the concentration of the plug and the disc differ, but the number of vacancies that is exchanged between the plug and the disc is identical. That results in a constant number of oxygen vacancies in the filament throughout the whole switching process. This is illustrated in Fig. 4.2c, where the number of vacancies in the disc and the plug and the total number of vacancies in the filament are plotted over time on a logarithmic scale. All resistances, the voltages across the single elements, and the filament temperature are shown in Fig. 4.2d, e and f, respectively. The HRS is dominated by the disc resistance and the resistance of the Schottky diode AE/oxide as both depend on the vacancy concentration in the disc. Here, the disc resistance is higher and more crucial. Consequently, most of the voltage drops across the disc in the HRS, except for very low voltages. In the shown example, the LRS resistance is determined by the disc resistance, the plug resistance, and the

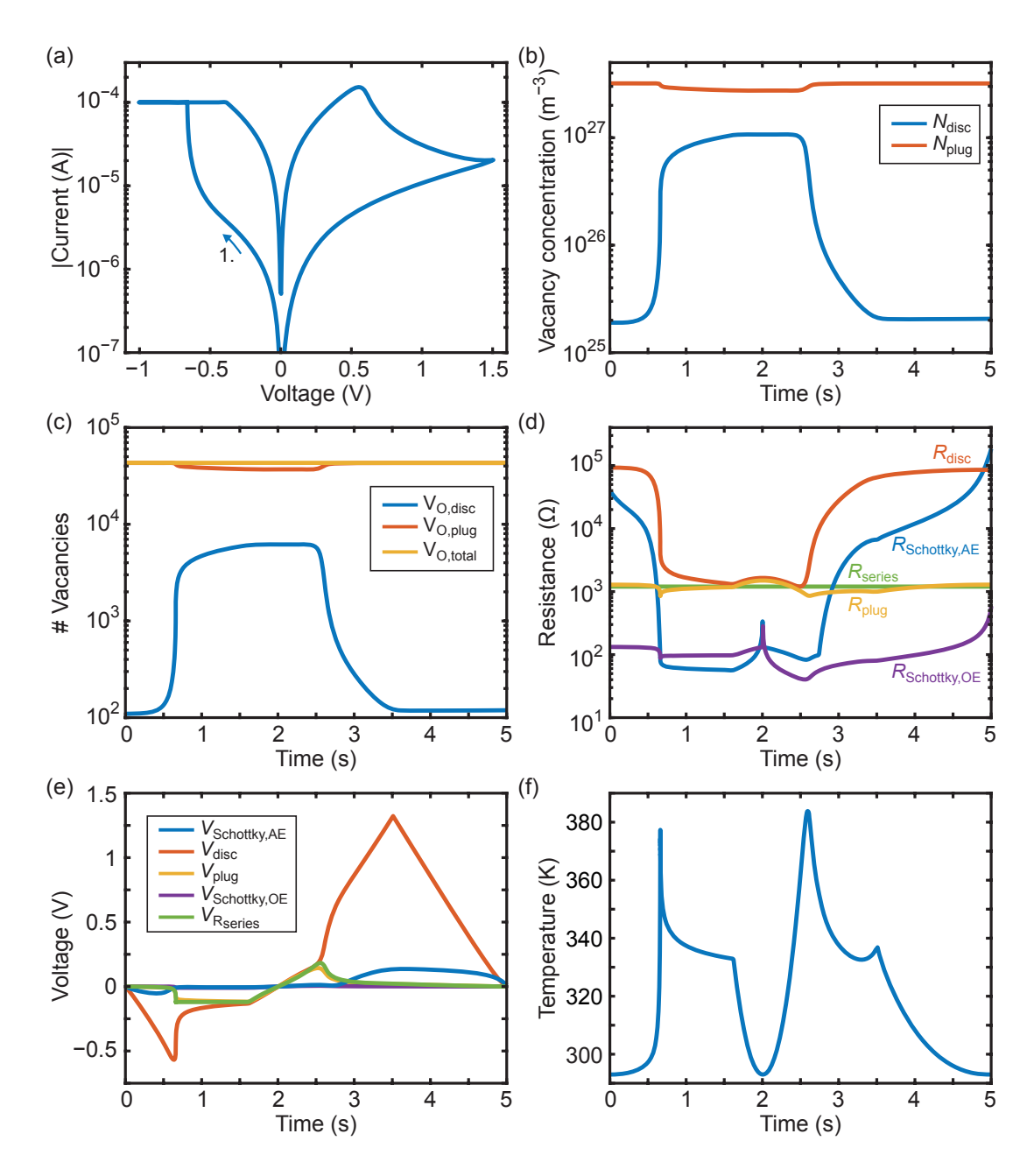


Figure 4.2: General model characteristics of compact model 1.5, in which the oxygen vacancy concentrations in the plug and the disc are variable. For the simulation the parameters in Table 4.1 are used. (a) *I-V* curve. (b) Oxygen vacancy concentration of the disc and the plug. (c) Number of oxygen vacancies in the disc and the plug, calculated based on the concentrations, and the sum of both. The total number of vacancies in the filament is constant during switching. (d) Resistances of all lumped circuit elements. (e) Voltages across the five lumped circuit elements. (f) Temperature in the filament.

Symbol	Value	Symbol	Value
$l_{ m cell}$	$5\mathrm{nm}$	$A^*$	$6.01 \cdot 10^5  A/(m^2 K^2)$
$l_{ m disc}$	$1.5\mathrm{nm}$	$\mu_{ m n0}$	$5 \cdot 10^{-6}  \mathrm{m}^2 / (\mathrm{Vs})$
$l_{ m plug}$	$l_{ m cell} - l_{ m disc}$	$\Delta E_{ m ac}$	$0.05\mathrm{eV}$
$r_{ m fil}$	$35\mathrm{nm}$	$N_{ m max}$	$6 \cdot 10^{27}  \mathrm{m}^{-3}$
$z_{ m Vo}$	2	$N_{ m min}$	$1/\left(A \cdot l_{\rm disc}\right)$
a	$0.4\mathrm{nm}$	$N_{ m disc,initial}$	$1.9 \cdot 10^{25}  \mathrm{m}^{-3}$
$\nu_0$	$8\cdot 10^{12}\mathrm{Hz}$	$N_{\rm plug,initial}$	$3.2 \cdot 10^{27}  \mathrm{m}^{-3}$
$\Delta W_{ m A}$	$0.9\mathrm{eV}$	$R_{\rm series,0}$	$1200\Omega$
$\varepsilon$	$17  \varepsilon_0$	$\alpha_{\mathrm{T,series}}$	$01/\mathrm{K}$
$arepsilon_{\phi_{ m B}}$	$5.5\varepsilon_0$	$R_{ m th,eff}$	$1.6 \cdot 10^6  {\rm K/W}$
$e\phi_{ m Bn0,AE}$	$0.5\mathrm{eV}$	sweep rate	$1\mathrm{V/s}$
$e\phi_{ m Bn0,OE}$	$0.1\mathrm{eV}$	$T_0$	293 K
$m_{ m eff}$	$m_{ m e}$		

**Table 4.1:** Parameters for the simulations in sections 4.2.1.

series resistance. The proportions strongly depend on the chosen parameters. Although the concentration of vacancies in the plug decreases during SET, the plug resistance does not increase for two reasons: First, the decrease is small as the number of vacancies is very high in the plug. Second, the temperature rises during SET and a higher temperature reduces the plug resistance based on the chosen temperature dependence. Thus, the influence of the reduced plug concentration is only visible around 0 V (i.e. t = 2 s), when Joule heating is insignificant. As the nominal barrier height  $e\phi_{\rm Bn0,OE}$  is lower than  $e\phi_{\rm Bn0,AE}$  and the vacancy concentration in the plug is constantly higher than in the disc, the resistance  $R_{\rm Schottky,OE}$  should be always lower than  $R_{\rm Schottky,AE}$ . This is correct except for the LRS at negative voltages when  $R_{\rm Schottky,AE}$  is lower. This is a consequence of the different conduction mechanisms used for reverse and forward direction, see section 2.3. Moreover, due to the high concentrations both barriers are reduced to 0 eV in the LRS.

The gradual RESET process is studied in more detail in Fig. 4.3. The simulation is performed with three different positive maximum sweep voltages, named  $V_{\text{stop}}$ . The simulation with  $V_{\text{stop}} = 1.5\,\text{V}$  equals the one already shown in Fig. 4.2. Figure 4.3a illustrates the influence of  $V_{\text{stop}} = 1.2\,\text{V}$ ,  $V_{\text{stop}} = 1.5\,\text{V}$ , and  $V_{\text{stop}} = 1.8\,\text{V}$  on the I-V characteristic. The corresponding oxygen vacancy concentrations of the plug and the disc in addition to the maximum and minimum concentration are plotted in Fig. 4.3b. To some extent, the stop voltage determines the HRS as it interrupts the decrease of oxygen vacancies in the disc during the gradual RESET process, see the example of  $V_{\text{stop}} = 1.2\,\text{V}$ . This effect also occurs with compact model 1.0. For high stop voltages, the

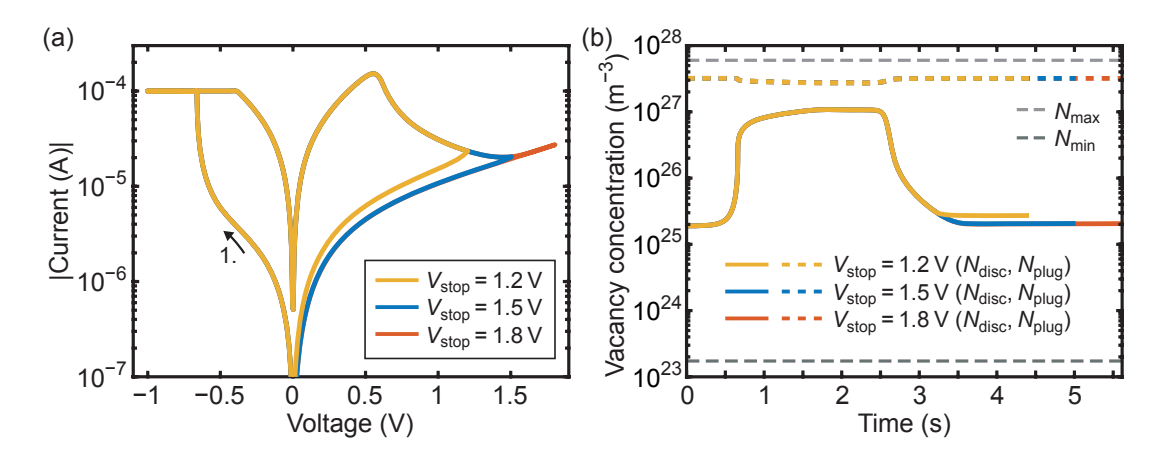


Figure 4.3: Influence of  $V_{\text{stop}}$  on the HRS during the RESET and its limit. (a) I-V curves with maximum positive sweep voltage of 1.2 V, 1.5 V, and 1.8 V, respectively. (b) Oxygen vacancy concentration in the plug and the disc for the three stop voltages. In addition, the maximum and minimum concentration are shown. In general, the disc concentration decreases more for an increasing stop voltage. This relation, however, is not valid for high stop voltages, although the concentration is far above the minimum limit. Reproduced with permission from [157], © 2019 IEEE.

HRS resistance is not increased further:  $V_{\text{stop}} = 1.5 \,\text{V}$  and  $V_{\text{stop}} = 1.8 \,\text{V}$  lead to the same HRS as the oxygen vacancy concentration does not decrease further for  $V_{\text{stop}} = 1.8 \,\text{V}$ . Thus, the RESET stops although the concentration is far above the minimum limit. This is a crucial difference between compact model 1.0 and compact model 1.5, compare Fig. 3.3 and Fig. 4.3. The limits  $N_{\text{max}}$  and  $N_{\text{min}}$  are included in the model in general to allow a wide range of parameters, but they do not influence the simulations shown in this chapter. Choosing different parameters, however, can result in a situation, in which SET or RESET are affected by the limits. The maximum concentration can be reached especially during SET when the plug concentration is chosen very high.

The origin of the self-limiting RESET is illustrated using a pulse simulation based on the parameters listed in Tables 4.1 and 4.2. The current transient of a RESET pulse with  $V_{\rm pulse} = 1.5 \, \rm V$  and the transients for the vacancy concentration in the disc and the plug are shown in Fig. 4.4a and b, respectively. During the first 100 ns, the voltage rises to its maximum of 1.5 V. Consequently, the current increases during this time while the

**Table 4.2:** Parameters for the RESET pulse simulations in sections 4.2.1.

Symbol	Value	Symbol	Value
$N_{\text{disc,initial}}$ rise time	$1.07 \cdot 10^{27} \mathrm{m}^{-3}$ $100 \mathrm{ns}$	$N_{ m plug,initial}$	$2.75 \cdot 10^{27} \mathrm{m}^{-3}$

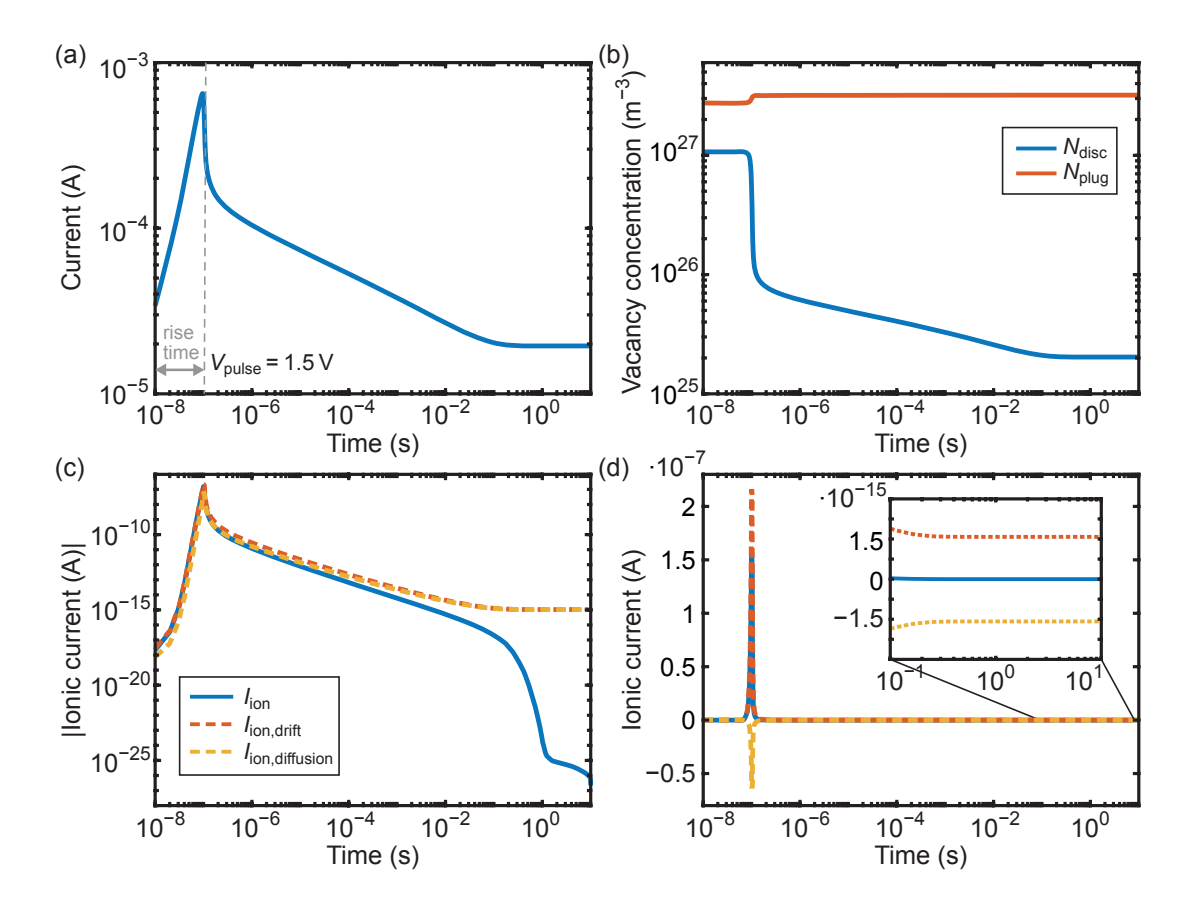


Figure 4.4: RESET pulse simulation with  $V_{\rm pulse} = 1.5\,\mathrm{V}$  starting in the LRS; simulated with the parameters in Tables 4.1 and 4.2. (a) Current transient. (b) Oxygen vacancy concentration of the plug and the disc. (c) Ionic current between the plug and the disc on logarithmic scale. The total ionic current  $I_{\rm ion}$  consists of a drift component  $I_{\rm ion,diffusion}$ . Drift and diffusion currents have opposite signs as shown in (d) on a linear scale. The total ionic flux is in direction of the drift current but becomes very small in the course of the pulse. The inset shows a zoom of the ionic currents for the time ranging from 0.1–10 s.

concentrations are constant. Shortly before the end of the rise time, the RESET starts as the disc concentration begins to decrease and the plug concentration begins to increase. The total ionic current and its two components — drift and diffusion — are shown on a logarithmic and a linear scale in Fig. 4.4c and d, respectively. Drift and diffusion current have opposite signs. The positive voltage applied to the AE leads to the drift of positively charged oxygen vacancies from the disc into the plug. On the other hand, a diffusion current of vacancies reduces the concentration gradient and therefore results in a movement from the plug into the disc. At first, the drift current predominates and the total ionic flux is in direction of the drift current. Consequently, the net flow of vacancies from the disc to the plug introduces a RESET. The decrease of the electrical

current leads to a reduction of the temperature and the level of both drift and diffusion current drops. During the RESET, the concentration gradient increases and thus, the influence of the diffusion on the net current rises. As a result, the total ionic current becomes very small in the course of the pulse. The inset in Fig. 4.4d shows a zoom of the ionic currents for the time ranging from 0.1–10 s. Drift and diffusion cancel each other out and the RESET stops.

The dynamics of the RESET process and the influence of the drift-diffusion balance are shown in Fig. 4.5 based on three pulses of  $V_{\text{pulse}} = 0.5 \,\text{V}$ ,  $V_{\text{pulse}} = 0.8 \,\text{V}$ , and  $V_{\text{pulse}} =$ 1.2 V. The I-V characteristics and the oxygen vacancy concentration in the plug and the disc are depicted in Fig. 4.5a and b, respectively. As expected, the time to reach the final state is smaller for higher pulse amplitudes. Naturally, the ionic current is smaller for lower pulse voltages, see the ionic current and its drift and diffusion components for  $V_{\rm pulse} = 0.5 \, \text{V}$  in Fig. 4.5c and d in comparison to Fig. 4.4c and d for  $V_{\rm pulse} = 1.5 \, \text{V}$ . This follows from a lower temperature due to a lower current, see Fig. 4.5e, and a smaller electric field, see Fig. 4.5f. Both the drift and the diffusion current depend on the temperature and the electric field. Thus, to achieve a dynamic equilibrium between drift and diffusion, the concentration gradient dN/dx and the driving concentration for the drift N will reach different values depending on the temperature and the electric field. Consequently, the concentrations in the stable state differ for the three voltage pulses. These final states, however, are very close to each other. Another difference lies in the abruptness of the RESET. For small pulse amplitudes, the overall RESET is gradual, whereas for higher amplitudes, the start of the RESET is abrupt followed by a long gradual current decrease. The explanation is comparable to the findings in section 3.2.2 about the gradual and abrupt RESET in I-V sweeps and based on the different feedback conditions. For higher pulse amplitudes, disc and plug resistances are lower due to the higher temperature and the series resistance dominates the LRS. As long as the filament resistance is lower than the series resistance, the RESET is more abrupt due to the steeper increase in the driving electric field.

Ionic processes that are not driven by the applied electric field continue to proceed under zero bias. Thus, including diffusion results in a finite retention. As no internal electric fields under zero bias are considered in the model, the diffusion of oxygen vacancies is the only process that determines the retention. Consequently, the retention is highly dependent on the potential barrier for the ion hopping  $\Delta W_A$ . The retention behavior of an HRS and a LRS is compared in Fig. 4.6. The oxygen vacancy concentrations for HRS and LRS are taken from the simulation in Fig. 4.2 at 0 V (0 s and 2 s):

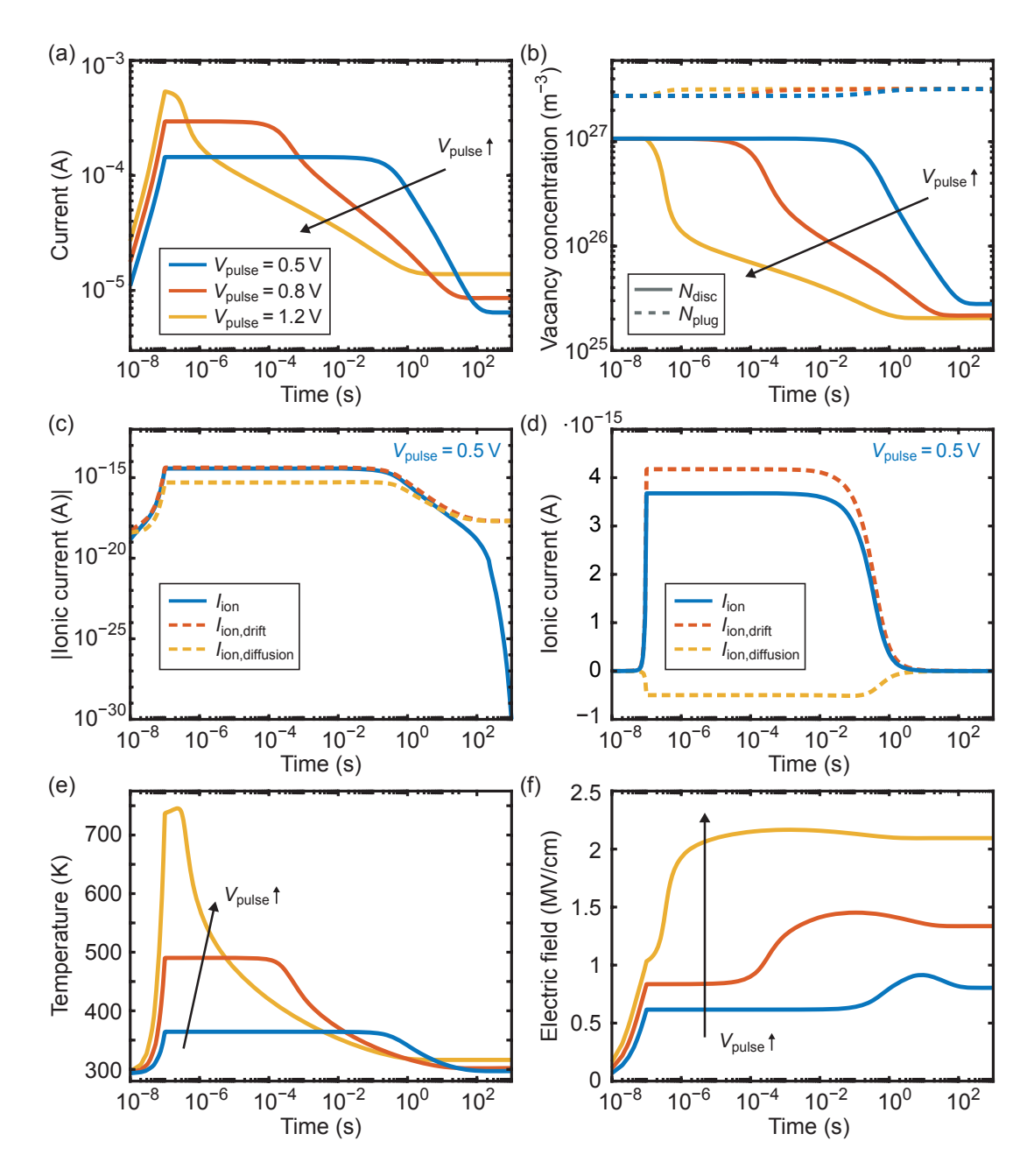


Figure 4.5: Comparison of three RESET pulses of  $V_{\rm pulse} = 0.5 \, \text{V}$ ,  $V_{\rm pulse} = 0.8 \, \text{V}$ , and  $V_{\rm pulse} = 1.2 \, \text{V}$ ; simulated with the parameters in Tables 4.1 and 4.2. (a) Current transients. (b) Oxygen vacancy concentrations in the plug and the disc. The concentrations in the HRS for the three voltage amplitudes are not identical but very close to each other. The total ionic current and its drift and diffusion component are plotted for  $V_{\rm pulse} = 0.5 \, \text{V}$  on a (c) logarithmic and (d) linear scale. (e) Temperature. (f) Driving electric field. Figs. (a)-(d) are reproduced with permission from [157], © 2019 IEEE.

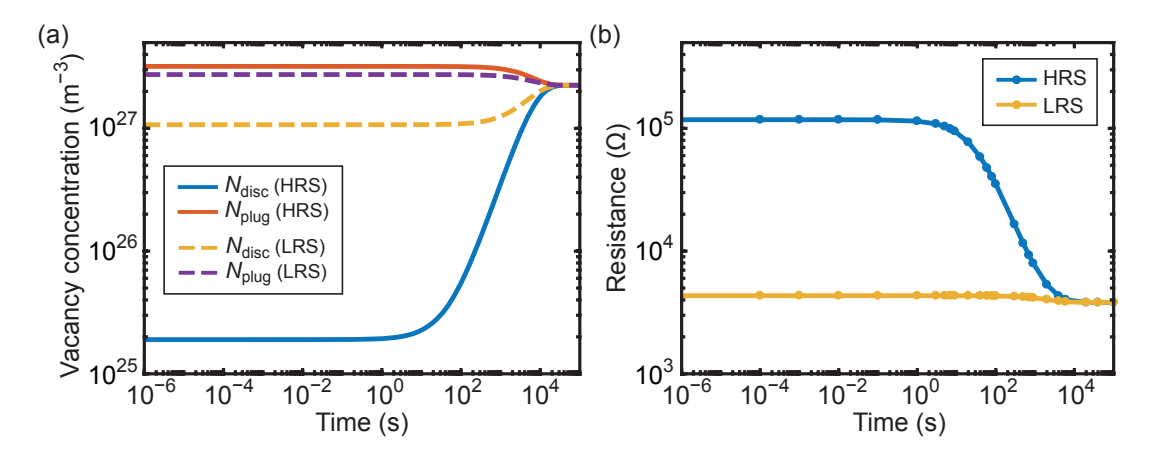


Figure 4.6: Retention of HRS and LRS. The oxygen vacancy concentrations for HRS and LRS are taken from the simulation in Fig. 4.2. (a) Transients of the vacancy concentration in the disc and the plug for two cases, HRS and LRS. (b) Evolution of HRS and LRS resistance. Except during the READ pulses ( $V_{\text{pulse,READ}} = -0.2 \,\text{V}$ ,  $t_{\text{pulse,READ}} = 10 \,\mu\text{s}$ ), no voltage is applied in the retention simulation.

for the HRS, the initial values for  $N_{\rm disc}$  and  $N_{\rm plug}$  are given in Table 4.1; for the LRS,  $N_{\rm disc} = 1.071 \cdot 10^{27} \, {\rm m}^{-3}$  and  $N_{\rm plug} = 2.745 \cdot 10^{27} \, {\rm m}^{-3}$  are used. The retention simulation is performed at room temperature and no voltage is applied except during the READ pulses to determine the resistance. The 10  $\mu$ s short READ pulses at a low READ voltage of  $-0.2\,V$  do not influence the simulation results. Independent of the initial values, the final states comprise a homogeneous distribution of vacancies in the filament, i.e. the vacancy concentration in the plug and the disc are equal, see Fig. 4.6a. Consequently, the total resistances of the HRS and LRS evolve into the same resistance, as shown in Fig. 4.6b. As the vacancy concentration in the disc is high for a homogeneous distribution, the final state in compact model 1.5 is always low resistive.

# 4.2.2 Complementary Switching (CS)<sup>1</sup>

The parameters of the simulation model for symmetric devices are fitted to describe the I-V characteristic of a  $HfO_x$ -based CS device with a cell size of  $(5 \times 5) \,\mu\text{m}^2$ . During fabrication, a stack of  $30 \,\text{nm} \,\text{Pt}/5 \,\text{nm} \,\text{Hf}O_2/5 \,\text{nm} \,\text{Hf}/30 \,\text{nm} \,\text{Pt}$  was sputtered, see [134] for details. The voltage with a sweep rate of  $0.4 \,\text{V/s}$  was applied to the Pt/Hf top electrode and the bottom electrode was grounded. A high-resolution transmission electron microscopy measurement indicated that the Hf layer is completely oxidized by oxygen from the HfO<sub>2</sub> layer, as both could not be distinguished [134]. Thus, it is reasonable to

Parts of the text in this section are taken from [158] © 2019 IEEE.

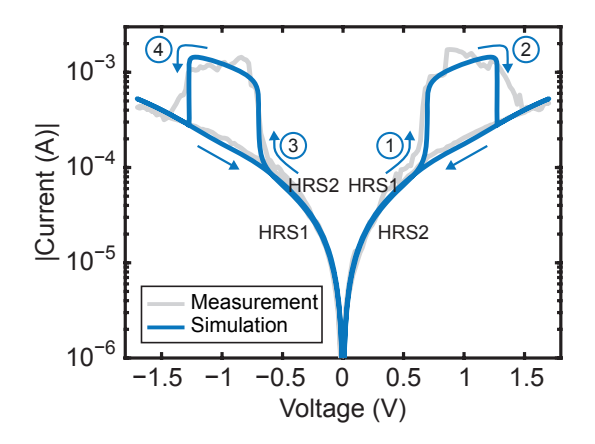


Figure 4.7: Complementary switching obtained by both experiment and simulation. The experimental I-V curve was measured by Thomas Breuer. Comparison of a symmetric I-V characteristic of a device with an effective device stack consisting of  $30 \, \mathrm{nm} \, \mathrm{Pt}/10 \, \mathrm{nm} \, \mathrm{HfO_x}/30 \, \mathrm{nm} \, \mathrm{Pt}$  and the simulated I-V curve. For the simulation, the parameters from Table 4.3 were used. Reproduced with permission from [158], © 2019 IEEE.

assume that the effective device stack is symmetric with  $30 \text{ nm Pt}/10 \text{ nm HfO}_x/30 \text{ nm Pt}$ . This is consistent with the measured I-V characteristic being symmetric, see Fig. 4.7. The simulated I-V curve of the symmetric model is shown in comparison in Fig. 4.7 and describes the data fairly well. The used parameters are listed in Table 4.3.

The CS switching is analyzed in detail in Fig. 4.8. The I-V characteristic on a linear scale, the current transient, and the oxygen vacancy concentration in the two filament regions are presented in Fig. 4.8a, b and c, respectively. The transients of the vacancy concentrations clearly show that the switching takes place at both interfaces. HRS1 is characterized by a low vacancy concentration in region II, i.e. the overall resistance is dominated by  $R_{\rm II}$ , see Fig. 4.8d. The resistance of the Schottky diode II  $R_{\rm Schottky,II}$ also contributes but is much lower than  $R_{\rm II}$ . Due to the positive potential applied to electrode I, the positively charged oxygen vacancies move from region I into II (transition (1)). The following low resistive state corresponds to a state in which the vacancy concentration in both regions is relatively high. Thus, the series resistance  $R_{\text{series}}$  defines the overall resistance and almost the entire voltage drops across the series resistance, see Fig. 4.8e. When more and more vacancies migrate into region II, the vacancy concentration in region I decreases until a voltage-dependent, dynamic equilibrium is reached, in which drift and diffusion currents balance each other (transition (2)), see section 4.2.1. Now, the resistance  $R_{\rm I}$  dominates the overall resistance and the device is in HRS2. At high voltages, the resistance of diode I  $R_{Schottky,I}$  is very small although the concentration  $N_{\rm I}$  is low. This results from the high temperature, see Fig. 4.8f, which enlarges the con-

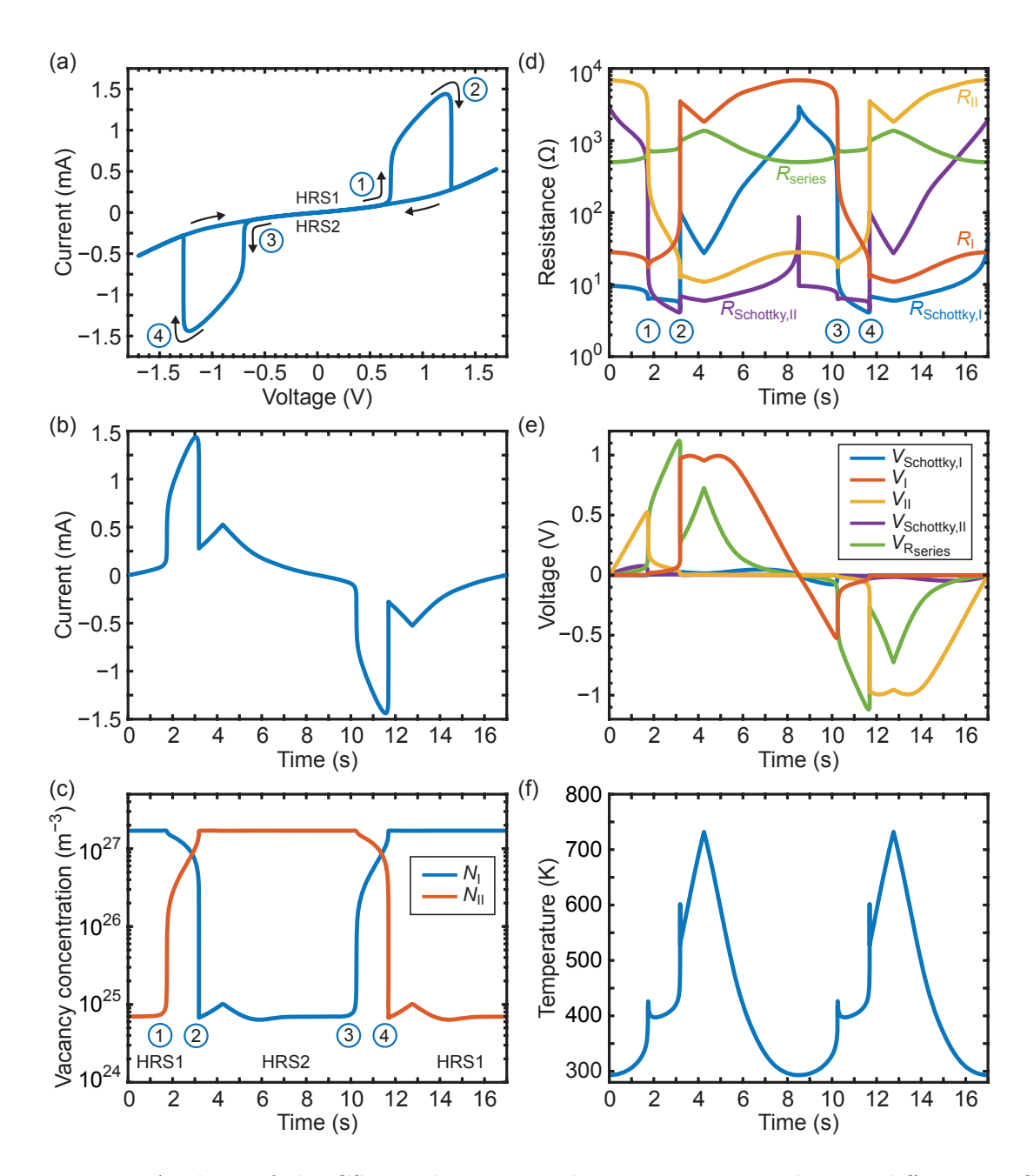


Figure 4.8: Analysis of the CS switching curve shown in Fig. 4.7. The two different HRS levels inherently present in CS devices and the characteristic transitions ① −④ are marked in several plots. (a) *I*−*V* curve on a linear scale. (b) Current transient. (c) Oxygen vacancy concentration in both filament regions I and II. The HRS levels are characterized by a balance between drift and diffusion. (d) Resistances of all lumped circuit elements. (e) Voltages across the five lumped circuit elements. (f) Temperature in the filament. Figs. (a) and (c) are reproduced with permission from [158], ©2019 IEEE.

Symbol	Value	Symbol	Value
$l_{\mathrm{cell}}$	10 nm	$\mu_{ m n0}$	$3 \cdot 10^{-5} \mathrm{m}^2/(\mathrm{Vs})$
$l_{ m I,II}$	$5\mathrm{nm}$	$\Delta E_{ m ac}$	$0.04\mathrm{eV}$
$r_{ m fil}$	$130\mathrm{nm}$	$N_{ m max}$	$5 \cdot 10^{27}  \mathrm{m}^{-3}$
$z_{ m Vo}$	2	$N_{ m min}$	$1/\left(A\cdot l_{\mathrm{I,II}}\right)$
a	$0.5\mathrm{nm}$	$N_{ m I,initial}$	$1.7 \cdot 10^{27}  \mathrm{m}^{-3}$
$\nu_0$	$4\cdot 10^{12}\mathrm{Hz}$	$N_{ m II,initial}$	$7 \cdot 10^{24}  \mathrm{m}^{-3}$
$\Delta W_{ m A}$	$0.9\mathrm{eV}$	$R_{ m series,0}$	$500\Omega$
$\varepsilon$	$17  \varepsilon_0$	$\alpha_{\mathrm{T,series}}$	$4 \cdot 10^{-3}  1/{ m K}$
$arepsilon_{\phi_{ m B}}$	$5.5arepsilon_0$	$R_{ m th,eff}$	$8.7\cdot 10^5\mathrm{K/W}$
$e\phi_{ m Bn0,I/II}$	$0.35\mathrm{eV}$	sweep rate	$0.4\mathrm{V/s}$
$A^*$	$6.01 \cdot 10^5  \mathrm{A/(m^2 K^2)}$	$T_0$	$293\mathrm{K}$
$m_{ m eff}$	$m_{ m e}$		

**Table 4.3:** Parameters for the simulations in section 4.2.2.

ductivity through the Schottky barrier. The different temperature also causes resistance  $R_{\rm I}$  exactly after (2) to be smaller than  $R_{\rm II}$  shortly before (1) even though the concentrations  $N_{\rm I}$  and  $N_{\rm II}$  are interchanged. The temperature dependence of the filament resistances, i.e.  $\Delta E_{\rm ac}$ , was chosen to match the measured I-V curve. Compared to the experimental data (Fig. 4.7), transition (2) is too abrupt. This is a direct consequence of the positive feedback through the electric field on one hand and through the temperature on the other hand. The driving electric field increases sharply during (2) due to the rise in the voltage  $V_{\rm I}$ , see Eq. (4.14). The higher the electric field, the faster the ion movement and the faster the increase in  $R_{\rm I}$  proceed. As a result, even more voltage drops across  $R_{\rm I}$  and the whole process is accelerated further. Because voltage  $V_{\rm I}$  is also crucial for the calculation of the temperature (Eq. (4.16)), the temperature rises during (2), thereby accelerating the transition in the same way. The resistances of HRS1 and HRS2 at 0 V are identical but the internal configuration is exactly the opposite. Only if the device is in HRS2, the application of a negative half sweep to electrode I leads to an opening of a CS window. Transitions (3) and (4) are analogous to (1) and (2) with interchanged roles of I and II. After a complete sweep, the final values of  $N_{\rm I}$  and  $N_{\rm II}$  are equal to the initial conditions so that the HRS obtained after a full sweep is identical to the state at the beginning (HRS1).

By using a current compliance, the CS device can be operated in bipolar switching mode. This is shown by both simulation and experimental data in Fig. 4.9a and b, respectively. If a current compliance is applied during transition ①, the device shows bipolar mode BS1. Analogously, bipolar mode BS2 is obtained by using a current compliance

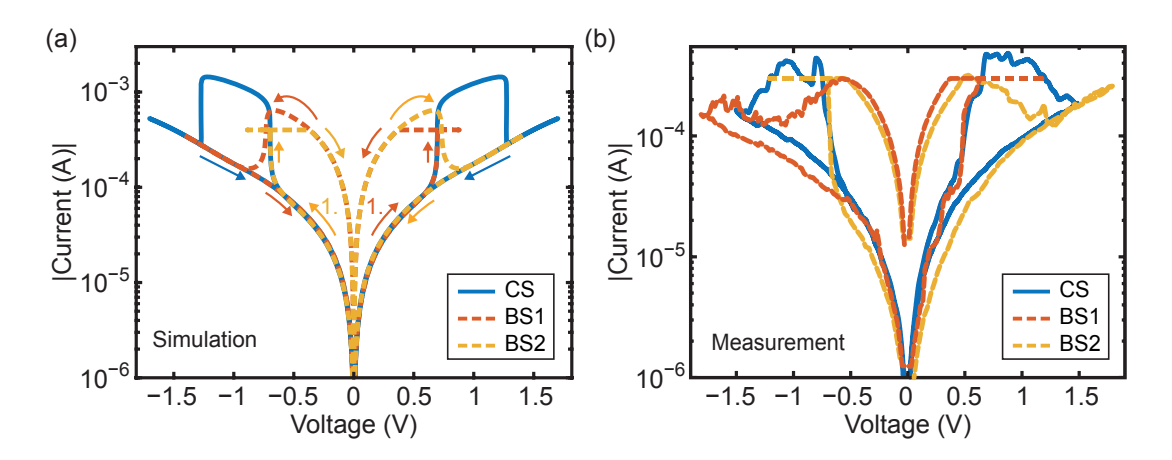


Figure 4.9: Link between complementary and bipolar switching in experiment and simulation. The experimental data were obtained by Thomas Breuer. (a) In the simulation, the BS modes are obtained by applying a current compliance of  $|I_{cc}| = 400 \,\mu\text{A}$ . (b) Experimental data of a CS device and corresponding BS modes using a current compliance of  $|I_{cc}| = 200 \,\mu\text{A}$ . The I-V curves were measured at another CS device than the one shown in Fig. 4.7.

during transition (3). The measured device shows the same behavior, only the simulated RESET is more abrupt because of the previously discussed reasons. Depending on the internal HRS configuration of the device, either bipolar mode BS1 or BS2 can be achieved. A voltage sweep sequence, which can be used to obtain both bipolar switching modes in a device starting in the configuration HRS1, is illustrated in Fig. 4.10a. Three voltage sweeps are applied consecutively: a full voltage sweep starting with positive voltages and a positive current compliance, a positive half sweep without current compliance, and a full sweep starting with negative voltages and a negative current compliance. Both the sweep voltage  $V_{\text{sweep}}$  (defined triangular signal) and the voltage applied to the device  $V_{\text{applied}}$  are shown. If the current compliance is active,  $|V_{\text{applied}}|$  is lower than  $|V_{\text{sweep}}|$ to prevent the current exceeding the compliance. The oxygen vacancy concentration in the two filament regions,  $N_{\rm I}$  and  $N_{\rm II}$ , over the course of the three voltage sweeps and the I-V curves for each voltage sweep are depicted in Fig. 4.10b and c, respectively. The results show that bipolar mode BS1 based on HRS1 is characterized by switching that takes place at interface II as only  $N_{\rm II}$  changes significantly. The current compliance limits the increase of  $N_{\rm II}$  and more important the decrease of  $N_{\rm I}$ . This prevents a rising of  $R_{\rm I}$ , which would result in the configuration of HRS2. The opposite processes occur for bipolar mode BS2 starting in HRS2, where the switching takes place at interface I.

The choice of the initial values for  $N_{\rm I}$  and  $N_{\rm II}$  is arbitrary to some extent but fixes the total number of oxygen vacancies in the filament. The influence of this decision on

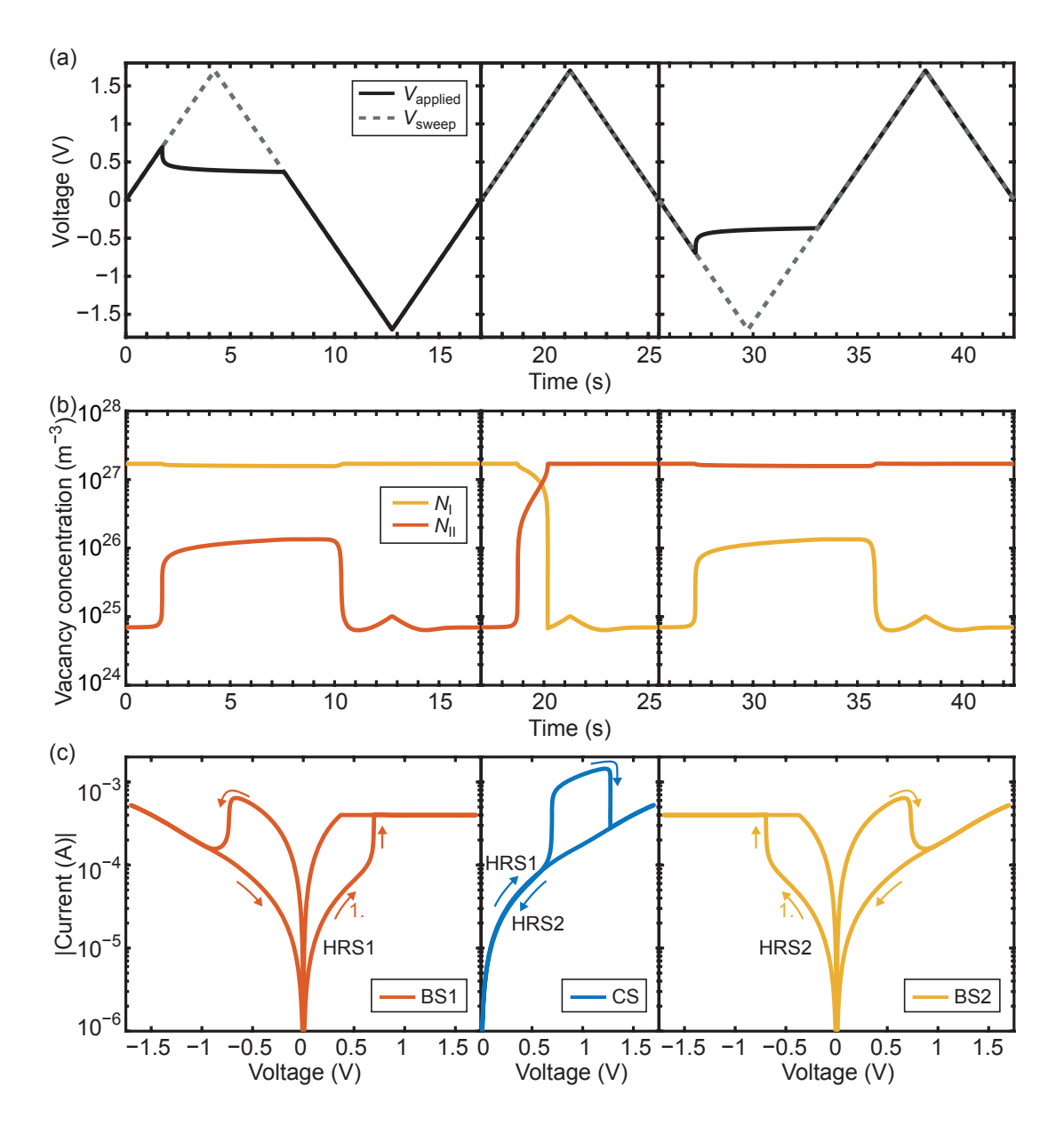


Figure 4.10: Switching between bipolar and complementary switching. Three voltage sweeps are applied consecutively: a full voltage sweep starting with positive voltages and a positive current compliance, a positive half sweep without current compliance, and a full sweep starting with negative voltages and a negative current compliance. (a) Transient sweep voltage  $V_{\text{sweep}}$  and the applied voltage  $V_{\text{applied}}$ . If the current compliance is active,  $|V_{\text{applied}}|$  is lower than  $|V_{\text{sweep}}|$ . (b) Oxygen vacancy concentration in the two filament regions I and II over the course of the three voltage sweeps. (c) I-V curves for each voltage sweep.

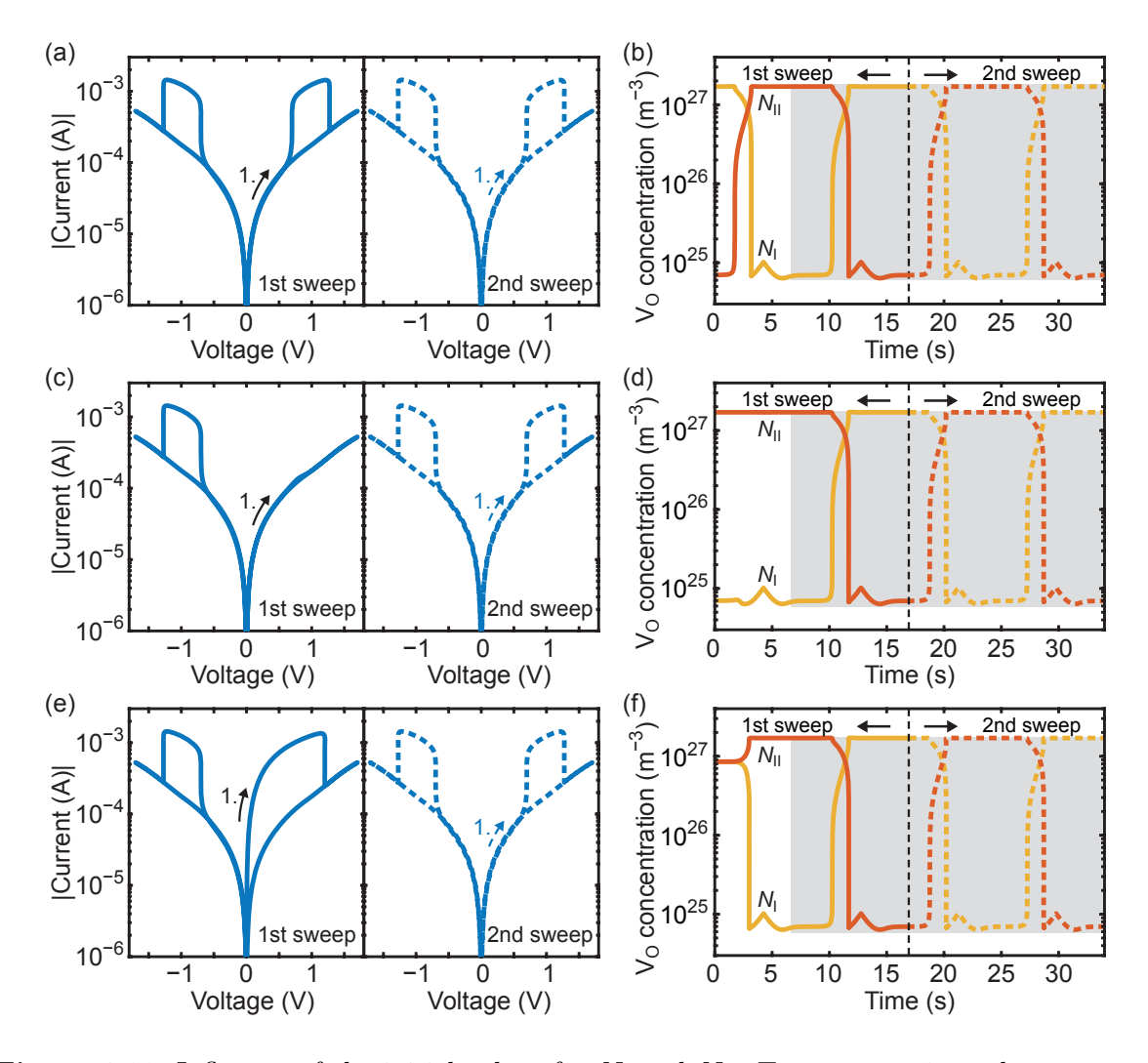


Figure 4.11: Influence of the initial values for  $N_{\rm I}$  and  $N_{\rm II}$ . Two consecutive voltage sweeps and the corresponding transients for the oxygen vacancy concentrations  $N_{\rm I}$  and  $N_{\rm II}$  are shown for three pairs of initial values: (a), (b)  $N_{\rm I,initial} = 1.7 \cdot 10^{27} \,\mathrm{m}^{-3}$  and  $N_{\rm II,initial} = 7 \cdot 10^{24} \,\mathrm{m}^{-3}$ . (c), (d)  $N_{\rm I,initial} = 7 \cdot 10^{24} \,\mathrm{m}^{-3}$  and  $N_{\rm II,initial} = 1.7 \cdot 10^{27} \,\mathrm{m}^{-3}$ . (e), (f)  $N_{\rm I,initial} = N_{\rm II,initial} = 0.5 \cdot (7 \cdot 10^{24} \,\mathrm{m}^{-3} + 1.7 \cdot 10^{27} \,\mathrm{m}^{-3})$ . Note that the number of vacancies (V<sub>O,total</sub> =  $(N_{\rm I,initial} + N_{\rm II,initial}) \cdot (Al_{\rm I,II})$ ) is identical in all three cases. Figs. (e) and (f) are reproduced with permission from [158], © 2019 IEEE.

the switching behavior is illustrated in Fig. 4.11. For three pairs of initial values, the I-V characteristic of two consecutive sweeps and the corresponding oxygen vacancy concentrations  $N_{\rm I}$  and  $N_{\rm II}$  are shown. First, the 'standard' initial values of Table 4.3 are used (Fig. 4.11a, b). The total number of vacancies in the filament can be calculated using  $V_{O,total} = (N_{I,initial} + N_{II,initial}) \cdot (Al_{I,II})$  as the volumes of region I and II are identical. Therefore, the total number remains the same when the initial concentrations of  $N_{\rm I}$  and  $N_{\rm II}$  are interchanged (Fig. 4.11c, d) or the mean is taken for both (Fig. 4.11e, f). The first half sweep (positive voltages,  $t = 0-8.5 \,\mathrm{s}$ ) differs in all three cases, but the second half of the first sweep and the second sweep are identical. Even more, the second half of the first sweeps  $(t = 8.5-17 \,\mathrm{s})$  and the second half of the second sweeps  $(t = 25.5-34 \,\mathrm{s})$ are already equal. Thus, it can be concluded that each total number of oxygen vacancies, under a certain applied stimulus, leads to a set of two stable values for  $N_{\rm I}$  and  $N_{\rm II}$ , which are interchanged in HRS1 and HRS2. These stable values are established after the first half sweep, see  $N_{\rm I}$  and  $N_{\rm II}$  at  $t=8.5\,{\rm s}$  and  $t=17\,{\rm s}$  at zero voltage. The second sweep is fully stable, as the initial  $(t = 17 \,\mathrm{s})$  and the final states  $(t = 34 \,\mathrm{s})$  coincide completely. Consequently, the first sweep can differ from a second one, if the initial values do not equal the stable values, but any additional sweep will coincide with the second one. In fact, the stable I-V characteristic can be extrapolated based on the second half of the first sweep by taking advantage of the symmetry. The first sweep starting in a LRS configuration in Fig. 4.11e could correspond to an initialization sweep that is necessary to obtain CS switching, examples of which are described in [159].

The set of stable values for  $N_{\rm I}$  and  $N_{\rm II}$  in the HRS also depends on the chosen parameters. Figure 4.12 illustrates the effect of some important parameters on the CS  $I\!-\!V$  characteristic. All simulations start in the same initial state and therefore, the direct effect of the varied parameter can be deduced from the first half sweep (positive voltages). As discussed before, the (new) stable states are established after the first half sweep and the influence of the changed HRS caused by the varied parameter is visible in the second half sweep (negative voltages). Consequently, the effective trends can be taken from the second half sweep. The series resistance dominates the LRS of the CS curve and therefore, its value is critical for the opening of the CS window, see Fig. 4.12a. The larger the voltage drop is across  $R_{\rm series}$ , the smaller the voltage drop is across the filament resistances  $R_{\rm I}$  and  $R_{\rm II}$  and the smaller the driving electric field is for the ion drift. Thus, for higher  $R_{\rm series}$ , transition ② is shifted to higher voltages. In addition, the series resistance limits the current in the LRS as inherent current compliance. If the series resistance is small, the opening becomes merely a spike. This could explain

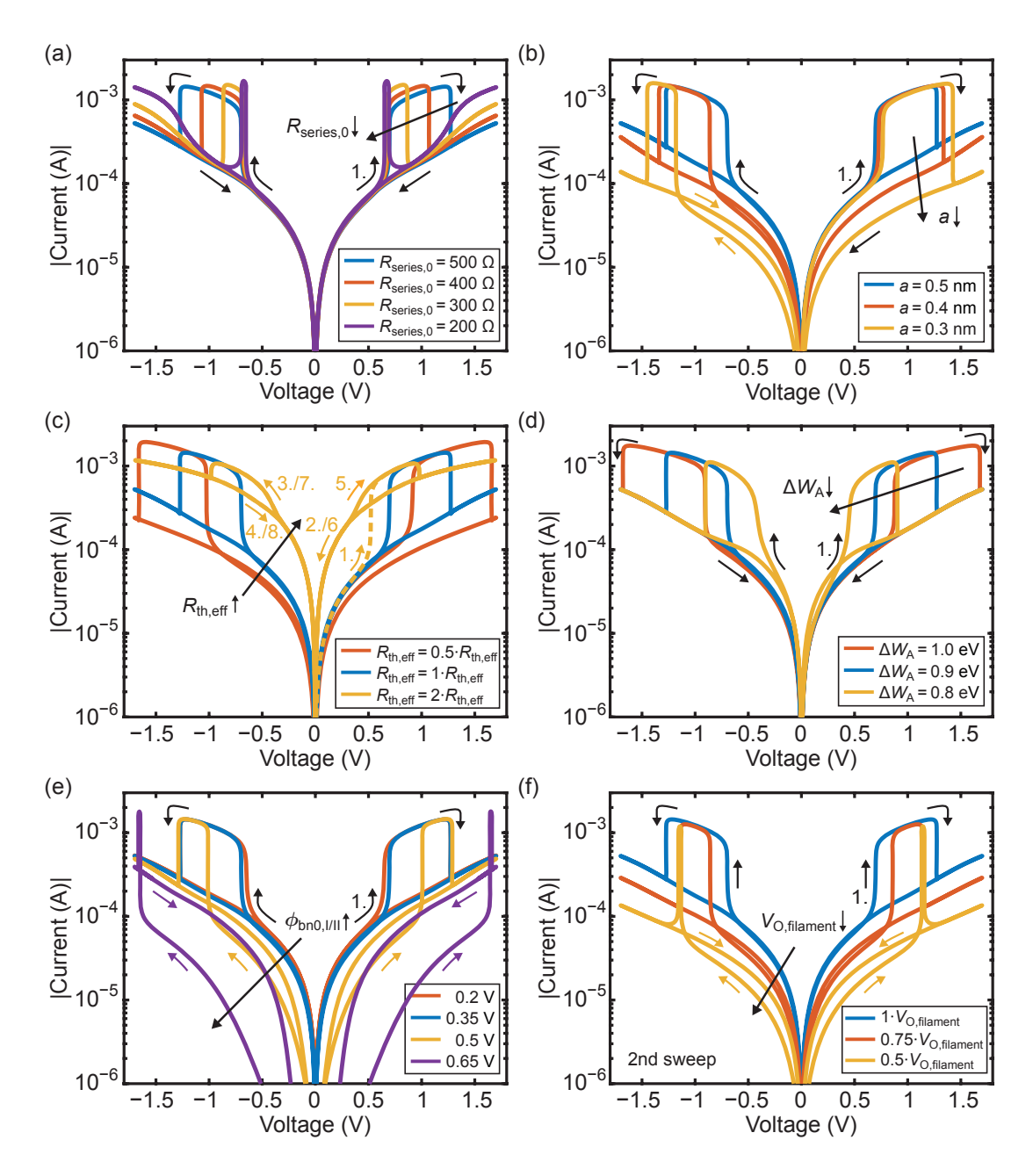


Figure 4.12: Influence of various parameters on the CS switching behavior. The parameters are taken from Table 4.3 with the exception of the parameter being varied as stated in the figures. The first half sweep (positive voltages) illustrates the direct effect of the varied parameter starting in an identical initial state, whereas the second half shows the effective trend. Influence of (a) the series resistance  $R_{\text{series},0}$  (reproduced with permission from [158], © 2019 IEEE), (b) the hopping distance a, (c) the effective thermal resistance  $R_{\text{th,eff}}$ , (d) the potential barrier  $\Delta W_{\text{A}}$  for the ion migration process, (e) the nominal Schottky barrier height  $e\phi_{\text{bn0}}$ , and (f) the total number of vacancies in the filament ( $V_{\text{O,total}} = V_{\text{O,filament}}$ ). As this changes the initial state, the second sweep is shown.

why there is a great variety in the shapes of CS curves obtained from measurements [117, 121, 123]. As an example, the line resistances can easily vary between cells obtained by different fabrication processes. The ratio between cell resistance and series resistance is the crucial factor for the CS window. The following parameter variations illustrate that a change of the HRS is always accompanied by a modification of the CS window (negative half sweeps).

Both HRS are characterized by an equilibrium between ion drift and diffusion. As a compact formulation for the ionic current is used, this sensitive balance highly depends on the hopping distance a, see Eq. (4.8). For a low value of a, the diffusion component is weakened and an equilibrium is only reached when a higher concentration gradient dN/dx has been established. Consequently, the lower concentration that evolves with lower hopping distance leads to a higher HRS resistance, see Fig. 4.12b. The change in the CS window opening is a consequence of these different HRS levels.

A higher effective thermal resistance  $R_{\rm th,eff}$ , caused for example by a reduced heat dissipation via the electrodes, leads to a higher temperature in the filament and thus strengthens the diffusion against the drift component. Consequently, the dynamic drift—diffusion equilibrium sets in at a lower concentration gradient and the HRS resistance is reduced, see Fig. 4.12c. To illustrate the effect that the stable I-V characteristic really can be extrapolated based on the second half of the first sweep using the symmetry, the first sweep (marked by no. 1.–4.) and the second sweep (marked by no. 5.–8.) are shown for the simulation with highest  $R_{\rm th,eff}$ . The I-V curve for 3.–4. is evidently symmetric to curve 5.–6. and identical to 7.–8..

The potential barrier  $\Delta W_{\rm A}$  for the ion hopping process is included in the prefactor of both drift and diffusion current and can therefore only influence the drift-diffusion balance indirectly. Thus, the HRS is only slightly affected, but the voltages to trigger the transitions shift considerably, see Fig. 4.12d. For higher barriers, higher fields (voltage) and temperatures (current) are required to induce switching, both for transition  $\widehat{1}$  and transition  $\widehat{2}$ . Moreover, transition  $\widehat{1}$  is less abrupt for a small barrier.

The nominal Schottky barrier height  $e\phi_{\rm bn0,I/II}$  is a crucial parameter for determining the resistance of the diodes. Naturally, this affects the HRS level, see Fig. 4.12e. The Schottky resistance near the region with low vacancy concentration strongly increases for a higher barrier. This reduces not only the current and thereby the temperature, but also the driving electric field as the voltage across the filament decreases for an increasing voltage across the diode. Therefore, the voltage for transition ① is significantly higher. The increased interface resistance for higher  $e\phi_{\rm bn0,I/II}$  reduces the influence of the series

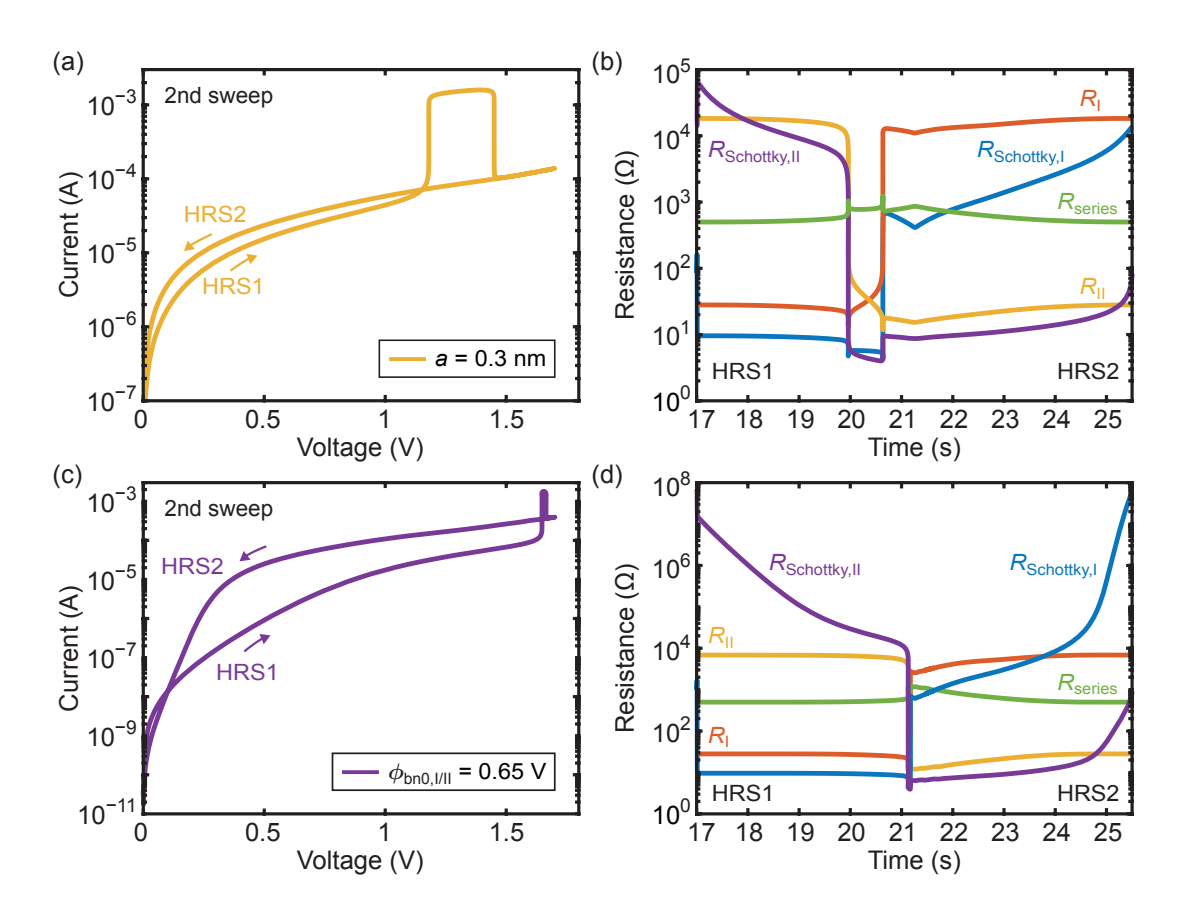


Figure 4.13: Analysis of the crossing in CS curves. The first half of the (second) sweep, which corresponds to a time between 17 s and 25.5 s, is shown for two parameters. The device starts in HRS1 and is in HRS2 after the half sweep. (a) I-V curve for a hopping distance of 0.3 nm. (b) Resistances of all five lumped circuit elements for a=0.3 nm. (c) I-V curve for a Schottky barrier height of 0.65 eV. (b) Resistances of all five lumped circuit elements for  $\phi_{\text{bn0,I/II}} = 0.65 \text{ V}$ .

resistance, comparable to the simulation with a small series resistance in Fig. 4.12a. As a result, the CS window becomes a spike. The clearly visible difference between the two HRS levels for  $\phi_{\rm bn0,I/II} = 0.5\,\rm V$  and  $\phi_{\rm bn0,I/II} = 0.65\,\rm V$  is discussed below.

Changing the total number of vacancies inevitably modifies the initial state and a comparison is only reasonable for the second (stable) sweep, as it is depicted in Fig. 4.12f. The lower the number of vacancies in the filament, the higher the HRS resistance is. The higher HRS level results in a voltage shift of transition  $\bigcirc 1/\bigcirc 3$  due to a reduced temperature and a reduced electric field as the influence of the Schottky barrier resistances increases. In addition, the ratio between series resistance and cell resistance changes and the CS window shrinks to a small spike.

A crossing between forward and backward curve is clearly visible in some curves in Fig. 4.12, e.g. for a hopping distance of 0.3 nm or a nominal Schottky barrier height of

0.5 eV and 0.65 eV. The crossing in the first half of the stable sweep and the corresponding resistance transients of all elements are shown in Fig. 4.13a and b, respectively, for the example of a = 0.3 nm. The difference in the current levels of HRS1 and HRS2 is caused by the polarity dependence of the conduction through the Schottky barriers. Thus, forward and backward curve are never identical but the effect is not visible as long as the filament resistances  $R_{\rm I}$  and  $R_{\rm II}$  dominate the HRS like for a hopping distance of  $0.5 \,\mathrm{nm}$ , see Fig. 4.8d. If the hopping distance equals  $0.3 \,\mathrm{nm}$ , lower values for  $N_{\mathrm{I}}$  and  $N_{\mathrm{II}}$ are reached in the HRS. Consequently, the resistances for the two filament regions and the Schottky diodes increase. As the conduction through the Schottky diodes depends nonlinearly on the donor concentration, the resistance increase of the Schottky diodes is higher. As a result, the HRS is influenced more by the Schottky diodes and the polarity dependence of the Schottky diode becomes visible in the I-V curve. The ionic states are still completely symmetrical as  $N_{\rm II}$  in HRS1 is identical to  $N_{\rm I}$  in HRS2. For the same doping concentration, however, the conduction under forward bias (diode I) is higher than under reverse bias (diode II). In general, the lower the concentrations  $N_{\rm I}$  and  $N_{\rm II}$  (i.e. the higher the HRS resistance), the more the HRS is dominated by the Schottky barriers. Thus, the occurrence of a crossing in the HRS I-V branches is not a direct consequence of a specific parameter but of a (high) HRS, in which the Schottky contacts determine the overall resistance. Experimentally, the occurrence of a crossing was observed in several CS cells [123, 159–161]. For highly dominating interface resistances, the CS I-V curve looses its characteristic shape, see the first half of the stable sweep and the corresponding resistance transients for the example of  $\phi_{\text{bn0.I/II}} =$ 0.65 V in Fig. 4.13c and d, respectively. In fact, the difference between the current levels of HRS1 and HRS2 is only more pronounced than in Fig. 4.13a. This kind of switching between two dominating Schottky barriers was also observed experimentally [124, 162].

# 4.2.3 CS Influence on Bipolar Switching<sup>2</sup>

Simulating bipolar switching with a model that is able to describe CS is advantageous regarding failure mechanisms and side-effects. For example, unwanted CS can occur if the current compliance and the applied voltages are chosen inappropriately. This is likely for (nearly) symmetric cells comparable to the one analyzed in section 4.2.2. In (strongly) asymmetric cells, CS effects can be identified in the I-V curve, depending on the current compliance, but the devices still show a BS switching characteristic. Such non-standard effects are shown in Fig. 4.14 and Fig. 4.15. The simulations in Fig. 4.14 and Fig. 4.15

 $<sup>^2</sup>$   $\,$  Parts of the text in this section are taken from [158] © 2019 IEEE.

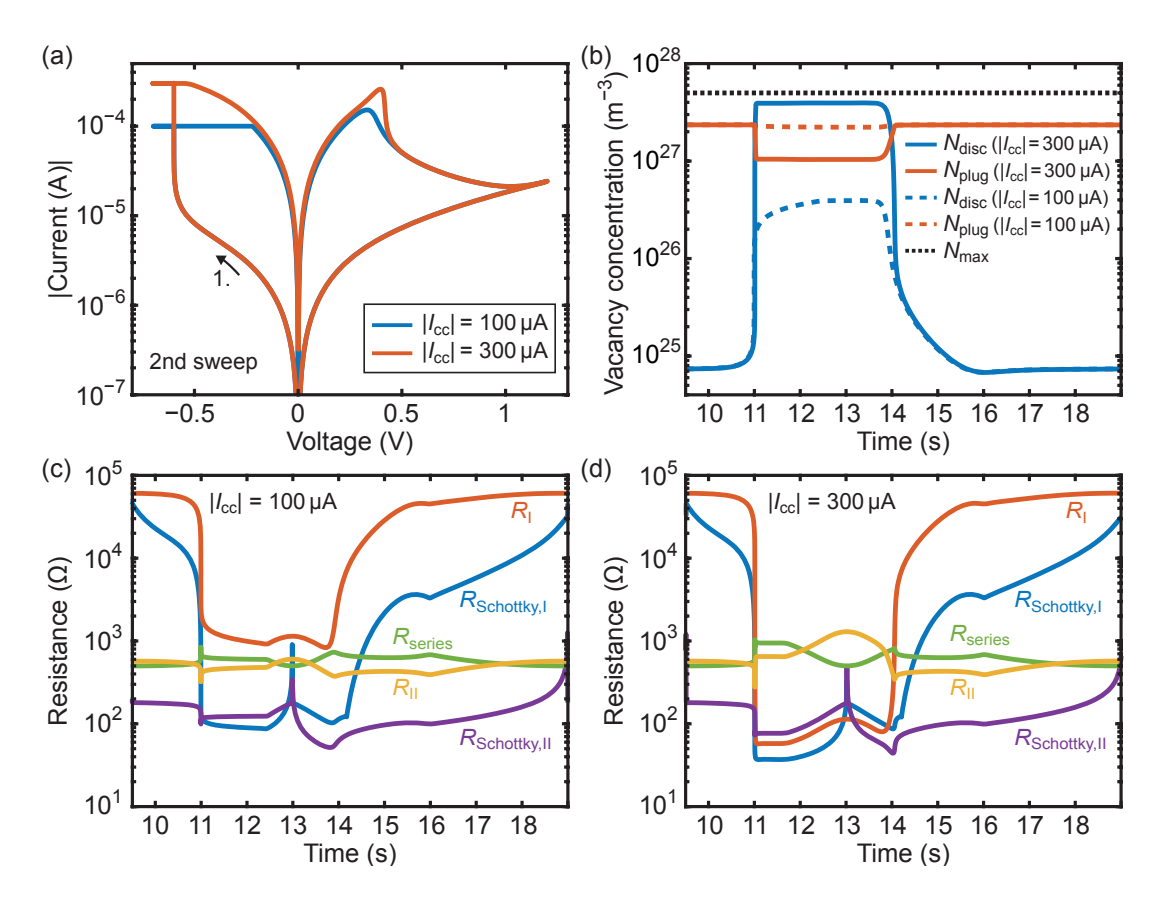


Figure 4.14: Occurrence and analysis of a RESET peak as consequence of CS in an asymmetric BS device. The used parameters are listed in Table 4.4. (a) I-V curves obtained with a current compliance of 100 μA and 300 μA, respectively. (b) Oxygen vacancy concentrations in the plug and the disc for both cases. The resistances of all lumped circuit elements are shown for the simulation with  $|I_{cc}| = 100 \,\mu\text{A}$  and  $|I_{cc}| = 300 \,\mu\text{A}$  in (c) and (d), respectively.

were performed with the parameters listed in Table 4.4 and Table 4.1, respectively. For a current compliance of  $|I_{cc}| = 100 \,\mu\text{A}$ , a standard BS curve evolves. In contrast, if a higher or no current compliance is used, the resistance decreases suddenly shortly before the start of the RESET, i.e. a small SET hump appears. Such anomalous RESET peaks are known from experiments and described in literature, e.g. in [119, 163]. Moreover in Fig. 4.15, a kind of SET overshoot exists as the current decreases slightly after the abrupt SET transition. Setting a current compliance does not necessarily prevent a RESET peak, the current level is critical as well. In both figures, the oxygen vacancy concentration in the plug and the disc is depicted for both  $I_{cc}$  cases in b. The resistance transients of the five elements are shown separately for the two current compliances in c and d, respectively. For the standard BS curve, the disc concentration is always lower than the plug concentration, also in the LRS. This is a result of the low current

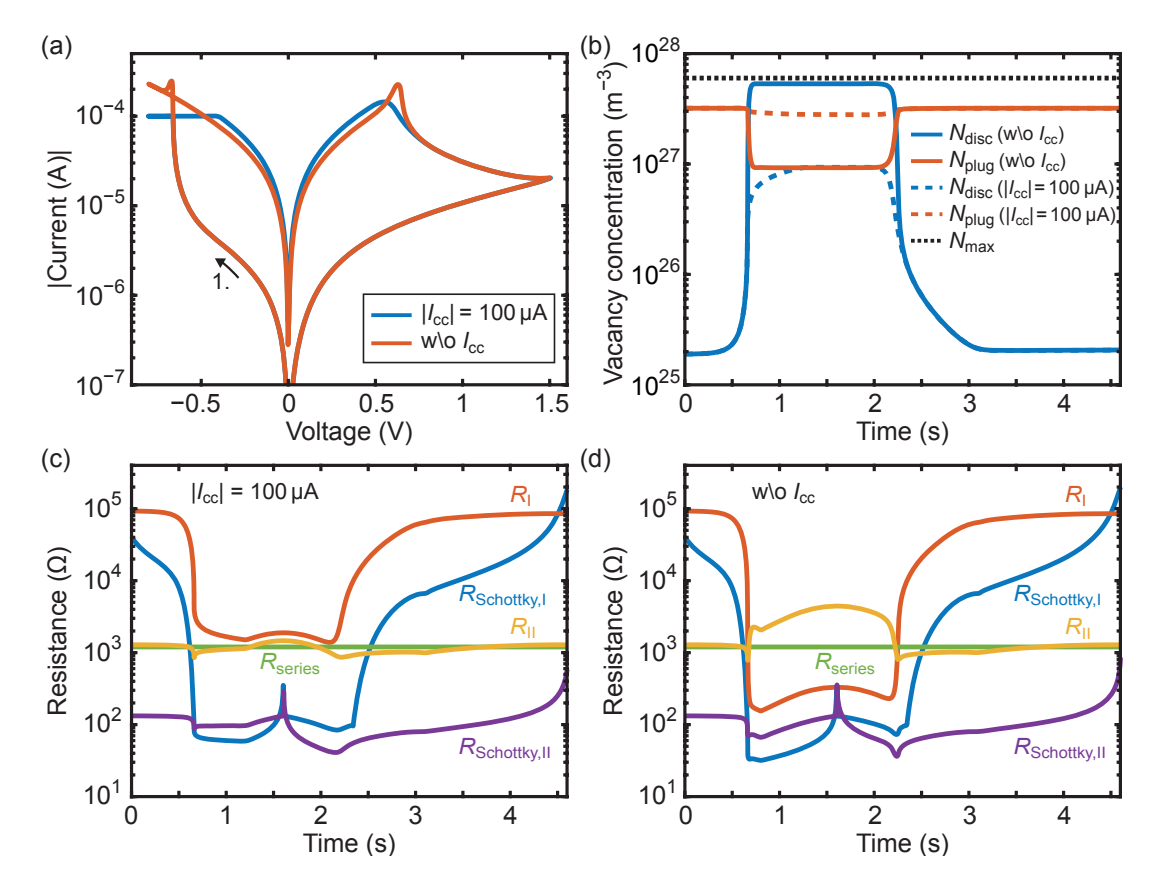


Figure 4.15: Occurrence and analysis of a RESET peak and a kind of SET overshoot as consequence of CS in another asymmetric BS device. The used parameters are listed in Table 4.1. (The initial values are identical to the stable values, thus, the shown first sweep is already the stable sweep.) (a) I-V curves obtained with a current compliance of 100  $\mu$ A and without a current limitation. (b) Oxygen vacancy concentrations in the plug and the disc for both cases. The resistances of all lumped circuit elements are shown for the simulation with  $|I_{cc}| = 100 \,\mu$ A and without current compliance in (c) and (d), respectively.

compliance that limits the migration of vacancies from the plug into the disc. If no low current compliance is set, the increase in disc concentration during the SET is only stopped by the maximum concentration limit. Now, the disc concentration considerably exceeds the plug concentration; the same holds for the total amount of vacancies. The start of the anomalous RESET peak is comparable to a CS SET, i.e. one filament resistance decreases considerably and one increases slightly. Comparable to the device in section 4.2.2, the total resistance decreases correspondingly. Due to the asymmetry, however, the movement of vacancies from the disc into the plug increases  $R_{\rm plug}$ . Consequently, a BS RESET evolves and not a full CS SET.

For the parameter set used in Fig. 4.14, the temperature-dependent series resistance limits the current in the LRS at high voltages for  $|I_{cc}| = 300 \,\mu\text{A}$ . In contrast, the

Table 4.4: Parameters for the	simulation	in Fig	4.14.	Parameters	that	are	not	listed	are
identical to those in Table 4.3	<b>3.</b>								

Symbol	Value	Symbol	Value
$egin{array}{c} l_{ m disc} \ l_{ m plug} \ r_{ m fil} \ R_{ m th,eff} \end{array}$	$2.5\mathrm{nm}$ $7.5\mathrm{nm}$ $30\mathrm{nm}$ $3.5\cdot 10^6\mathrm{K/W}$	$e\phi_{ m Bn0,AE} \ e\phi_{ m Bn0,OE} \  m V_{ m O,total}$	0.35  eV 0.1  eV $5 \cdot 10^4$

plug resistance dominates in the LRS for the simulation without current compliance in Fig. 4.15. The small SET current overshoot, which appears in this simulation, is in fact CS switching in the case of very asymmetric filament resistances and a series resistance that is low compared to the total filament resistance. Like in a standard CS cell, a CS LRS exists as a transitional state in which both filament resistances are relatively low. The vacancy distribution in the stable BS LRS, however, leads to a slightly higher resistance.

The occurrence of CS in asymmetric cells depends on the magnitude of the asymmetry and how the asymmetry is introduced. Asymmetry can be introduced into the model via the lengths of the filament regions, the barrier heights, or the electron mobility, i.e. assuming different electron mobilities in the plug and the disc. In general, CS also occurs in moderately asymmetric cells as long as it is not suppressed by a current compliance. Highly asymmetric models often show BS with CS-related spiking effects. In case of a very strong asymmetry, the model exhibits 'normal' BS without an active compliance. If different lengths or barrier heights are chosen, the resulting BS curves often display CS spikes even for high asymmetric values. Moreover, the HRS resistance level is strongly affected. Introducing a high asymmetry via the electron mobility leads to CS-spiking-free BS curves and the HRS level is not changed.

One example of experimental data showing a SET overshoot and an anomalous RESET peak is given on logarithmic and linear scale in Fig. 4.16a and b, respectively. The experimental data are taken from a  $(25\times25)\,\mu\text{m}^2$  ReRAM device consisting of 30 nm Pt/5 nm  $\text{ZrO}_x/10\,\text{nm}\,\text{Ta}/30\,\text{nm}\,\text{Pt}$ . The voltage is defined as being applied to the Pt bottom electrode, while the top electrode is grounded. Fabrication and measurement were performed by Andreas Kindsmüller. Compared to the simulated RESET peak in Fig. 4.15a, the measured RESET peak is significantly broader. This is consistent with other experimental observations that also show a wider peak, see for example a HfO<sub>x</sub>-based device in [119] and a NbO<sub>x</sub>-based device in [163]. The qualitative match between the simulated

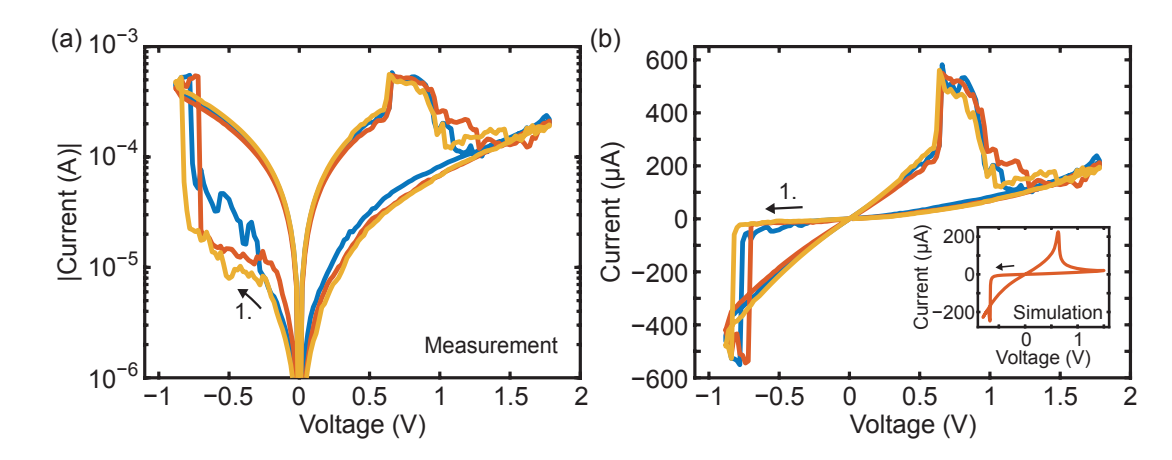


Figure 4.16: Experimental observation of RESET peaks and SET overshoots. The experimental data of a  $Pt/ZrO_x/Ta$  device were provided by Andreas Kindsmüller [164]. The three consecutive I-V curves are shown on (a) logarithmic and (b) linear scale. The inset shows the simulation result from Fig. 4.15a on linear scale for comparison.

and the experimental I–V curve is nevertheless remarkable and leads to the conclusion that strongly asymmetric CS switching can provide a reasonable explanation for the measured effects.

#### 4.3 Conclusion

The physics-based compact model presented in this chapter is able to describe both bipolar and complementary switching consistently. This is achieved by introducing the oxygen vacancy concentration in the plug as second state variable that changes according to the ionic current between the disc and the plug. In case of a symmetric device stack, a symmetric model is used with two filament regions I and II that have the same volume. Implementing both metal/oxide interfaces as Schottky barriers enables a complete symmetric model if required. The description of the ion migration process is extended to include diffusion. This results in a self-limiting RESET: the HRS evolves as a situation that is defined by a balance between the drift and the diffusion component of the ionic current. This dynamic drift-diffusion equilibrium is very sensitive to model parameters like the effective thermal resistance or the hopping distance. In addition, the diffusion leads to a finite retention under zero bias. As diffusion balances the concentration gradient, the stable state always comprises a homogeneous distribution of vacancies in the filament with  $N_{\rm disc}=N_{\rm plug}$ . The high vacancy concentration results in a low resistive stable state, irrespective of whether the initial state was an HRS or a LRS.

Given a fixed set of parameters, the choice of the initial values for the two vacancy concentrations is arbitrary as long as the total number of vacancies in the filament stays the same. In that case, the initial values are only relevant for the first sweep; the second and subsequent sweeps show a stable I-V characteristic independent of the initial values. This has to be taken into account when the model parameters are fitted to describe a certain I-V curve.

The model captures the experimental observation that CS and BS occur in one device depending on the applied current compliance. If chosen appropriately, the current compliance limits the ionic current and ensures that one region keeps a high conductivity throughout the entire switching process. Regarding the shape of the CS opening, it was shown that the ratio between the cell resistance and the series resistance determines the shape of the CS opening. Non-standard effects in BS devices like the occurrence of an anomalous RESET peak or a SET overshoot can be explained satisfactorily as asymmetric CS peaks.

Compared to compact model 1.0, the dependence of the I-V characteristic on non-material parameters like a predefined minimum and maximum concentration is reduced by implementing diffusion. Moreover, a finite retention under zero bias is realized. Crucial effects encountered in experiments like an endurance loss or a retention loss of the LRS, however, cannot be described by the model as the number of vacancies is set through the initial values and does not vary. In addition, different forming conditions, which are known to significantly influence the switching behavior, can only be represented by choosing a different total number of vacancies. Thus, non-material parameters still play a crucial role. Neglecting radial diffusion to the surrounding oxide and a possible oxygen exchange with the electrodes adds additional limits to the general applicability of the model. Similar to compact model 1.0, it is important to note that reliable conclusions on the dynamical situation require a sufficiently accurate knowledge of the conduction mechanism. Therefore, improvements concerning the ionic and/or the electrical description are desirable.

# 5 Compact Model 2.0

As powerful extension to compact model 1.5, the oxygen exchange at the metal/oxide interfaces is added in compact model 2.0. As a result, the number of vacancies in the filament is not determined anymore by the initial values. Depending on the oxygen affinity of the electrodes, the oxygen concentration in the electrode, and the applied voltage, the amount of vacancies can increase or decrease. This enables the investigation of many interesting effects. First, the forming step can be simulated allowing the analysis of the forming conditions on the subsequent switching. Second, the model covers the influence of the electrodes on the switching characteristics, on failures, and on the long-term endurance and retention. Third, if the parameters are chosen appropriately, the creation/annihilation of vacancies at the interface dominates over the redistribution of vacancies in the filament, resulting in eightwise switching.

The first section describes the derivation of the equations that are used for the oxygen exchange in the model. Deriving new equations was necessary because reliable compact model equations for the given problem are missing in the literature. The simulation results in this chapter cover all novel types of application of compact model 2.0. Thereby, special attention is paid to the forming process and to the endurance in sweep and pulse operation. The dependence of the forming voltage on the oxide thickness and the influence of various parameters are analyzed in detail. For the endurance, the effects of parameter sets leading to a decrease or increase in the amount of vacancies in the filament are compared. The experimental data regarding the forming and subsequent switching in c8w devices shown in this chapter were obtained by Andreas Kindsmüller. The endurance data were provided by Stefan Wiefels and Michael Hüttemann. The 8w switching I-V curve was measured by Christoph Bäumer.

Compact model 2.0 is based on the following general assumptions:

• The filament is cylindrical with a time-invariant, constant cross-sectional area. It is split into two regions of uniform oxygen vacancy concentration called plug and disc. Even before the forming step, the geometry of the filament that is to evolve is defined.

- Both metal/oxide interfaces are modeled as Schottky contacts. In case of an asymmetric device stack, different values for the Schottky barrier heights are used.
- Oxygen vacancies are treated as mobile, doubly-charged donors. Their movement
  along the filament is described based on drift and diffusion. Internal electric fields
  under zero bias, radial diffusion to the surrounding oxide, and thermodiffusion are
  neglected.
- An oxygen exchange between filament and electrodes is included based on the Butler-Volmer equation. Oxygen ions can be adsorbed in the metal or near the metal/oxide interface. The (metal) electrodes are modeled as reservoirs for oxygen ions with an effective volume.
- The two oxygen vacancy concentrations in the filament and the two oxygen ion concentrations in the electrodes are the state variables in the model.
- The concentration of electrons is solely determined by the donor concentration.
- The temperature is approximated to be uniform in the filament and at the metal/ oxide interfaces.
- No stochastic processes are considered, the simulation results are deterministic.

# 5.1 Oxygen Exchange at the Electrode

As the oxygen exchange at the electrodes plays a crucial role during forming and switching, it needs to be incorporated in the compact model. To this end, an expression for the ion flow in terms of a ionic current density is required. The equations in this section were developed based on the theory of an ion transfer process described in the fundamentals in section 2.5. An oxygen exchange process is likely to consist of several (charge transfer) steps. For example, ionization, adsorption, electron transfer, and ion transfer belong to the possible steps [146]. Among these, the rate-limiting step determines the transfer kinetics. Neither the reaction sequence nor the rate-limiting step of the oxygen exchange process in VCM-type ReRAM devices have been identified so far. From a modeling perspective, a compact model description needs to cover the influence of the applied electric field on the oxygen exchange. This can be achieved by choosing the transfer of a charged particle as rate-limiting step. In addition, oxygen vacancies that are created in the oxide should act as donors. Thus, the electrons have to remain in the oxide effectively. Based on these requirements, the following mechanism is assumed:

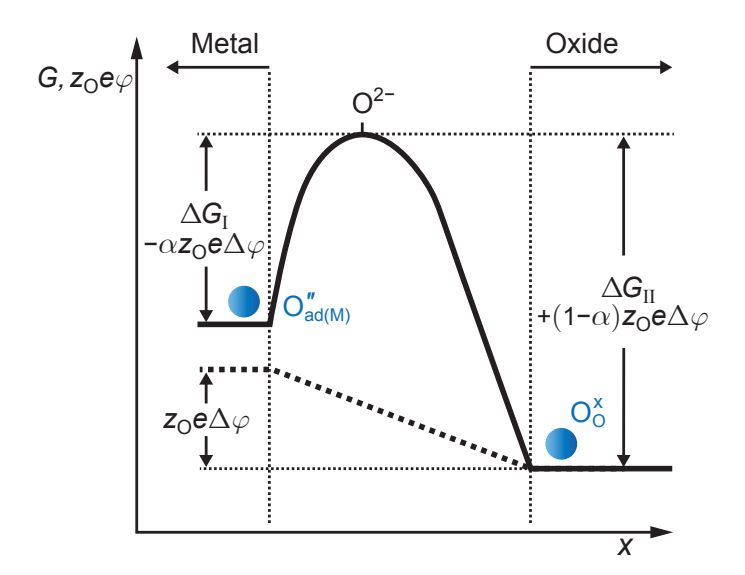


**Figure 5.1:** Oxygen transfer process at a metal/oxide interface referring to the exchange reaction described by Eqs. (5.1) to (5.3). The effective enthalpy profile is given by the solid line. The dashed line illustrates the potential profile.

The rate-limiting step of the oxygen exchange process is the transfer of a doubly negatively charged oxygen ion  $(O^{2-})$ . The oxygen ion is then adsorbed in the metal near or at the metal/oxide interface. After the adsorption, it is assumed that two electrons are transferred from the metal to the conduction band in the oxide. This electron transfer proceeds fast; therefore, it is not considered in the following description of the exchange kinetics.

The exact physics of the oxygen adsorption in the metal is not considered. Here, it is only relevant that there is an amount of places/states at or near the metal/oxide interface that can be occupied by oxygen ions. If these places are vacant, they are denoted by  $V_{ad(M)}^{\times}$ . Adsorbed oxygen ions  $O''_{ad(M)}$  are doubly negatively charged relative to the crystal lattice. A transfer of an oxygen ion from the oxide  $(O_{O(ox)}^{\times})$  to the metal is possible if a vacant site in the metal exists. The transferred oxygen ion leaves behind an oxygen vacancy in the oxide  $(V_{O(ox)}^{\bullet\bullet})$ . The opposite process, which reduces the amount of oxygen vacancies in the oxide, can take place if an oxygen ion is adsorbed in the metal and an oxygen vacancy in the oxide exists. The complete reaction reads

$$O''_{ad(M)} + V^{\bullet \bullet}_{O(ox)} \rightleftharpoons V^{\times}_{ad(M)} + O^{\times}_{O(ox)}.$$
 (5.1)

The assumed transfer of a doubly negatively charged oxygen ion can be split into two sub-processes. The forward reaction is given by

$$O''_{ad(M)} \rightarrow V^{\times}_{ad(M)} + O^{2-}$$

$$O^{2-} + V^{\bullet \bullet}_{O(ox)} \rightarrow O^{\times}_{O(ox)}$$
(5.2)

and the backward reaction reads

$$O_{O(ox)}^{\times} \rightarrow O^{2^{-}} + V_{O(ox)}^{\bullet \bullet}$$

$$O^{2^{-}} + V_{ad(M)}^{\times} \rightarrow O_{ad(M)}^{"}.$$
(5.3)

The kinetics of the oxygen exchange process are illustrated in Fig. 5.1. For the forward reaction, the kinetic enthalpy barrier  $\Delta G_{\rm I} - \alpha z_{\rm O} e \Delta \varphi$  has to be overcome with  $\Delta \varphi = \Delta \varphi_{\rm ref} + \eta$ . The barrier for the reverse process is  $\Delta G_{\rm II} + (1 - \alpha)z_{\rm O}e\Delta\varphi$ . Based on the barriers and analogous to Eqs. (2.28) to (2.32), the rate constants can be expressed as

$$k_{\rm I} = k_{\rm I}^0 \exp\left(-\frac{\Delta G_{\rm I}}{k_{\rm B}T}\right) \exp\left(\frac{\alpha z_{\rm O} e}{k_{\rm B}T}\eta\right),$$
 (5.4)

$$k_{\rm II} = k_{\rm II}^0 \exp\left(-\frac{\Delta G_{\rm II}}{k_{\rm B}T}\right) \exp\left(-\frac{(1-\alpha)z_{\rm O}e}{k_{\rm B}T}\eta\right). \tag{5.5}$$

Using Eq. (2.33), the forward and reverse current densities  $J_{\text{O,I}}$  and  $J_{\text{O,II}}$ , describing the oxidation and the reduction of the oxide respectively, are defined as

$$J_{\text{O,I}} = z_{\text{O}} e N_{\text{O,ad(M)}} k_{\text{I}}^{0} \exp\left(-\frac{\Delta G_{\text{I}}}{k_{\text{B}} T}\right) \exp\left(\frac{\alpha z_{\text{O}} e}{k_{\text{B}} T} \eta\right), \tag{5.6}$$

$$J_{\text{O,II}} = -z_{\text{O}} e N_{\text{O,ox}} k_{\text{II}}^{0} \exp\left(-\frac{\Delta G_{\text{II}}}{k_{\text{B}} T}\right) \exp\left(-\frac{(1-\alpha)z_{\text{O}} e}{k_{\text{B}} T} \eta\right). \tag{5.7}$$

Following the definition of the current densities in Eqs. (2.34) to (2.36), the reverse current density  $J_{\text{O,II}}$  is given a negative sign. The concentration of oxygen ions adsorbed in the metal  $N_{\text{O,ad(M)}}$  and the concentration of oxygen on lattice sites in the oxide  $N_{\text{O,ox}}$  are defined as volume concentrations (m<sup>-3</sup>). The prefactors for the rate constants  $k_{\text{I,II}}^0$  are given in m/s and the ionic current densities have the unit A/m. The net current density is given by the sum of forward and reverse current density in dependence of the overpotential  $\eta$ . The index M $\rightarrow$ Ox indicates that the current density is positive if oxygen ions flow from the metal to the oxide according to

$$J_{\text{O,M}\to\text{Ox}} = z_{\text{O}} e N_{\text{O,ad(M)}} k_{\text{I}}^{0} \exp\left(-\frac{\Delta G_{\text{I}}}{k_{\text{B}}T}\right) \exp\left(\frac{\alpha z_{\text{O}} e}{k_{\text{B}}T}\eta\right) - z_{\text{O}} e N_{\text{O,ox}} k_{\text{II}}^{0} \exp\left(-\frac{\Delta G_{\text{II}}}{k_{\text{B}}T}\right) \exp\left(-\frac{(1-\alpha)z_{\text{O}} e}{k_{\text{B}}T}\eta\right).$$
(5.8)

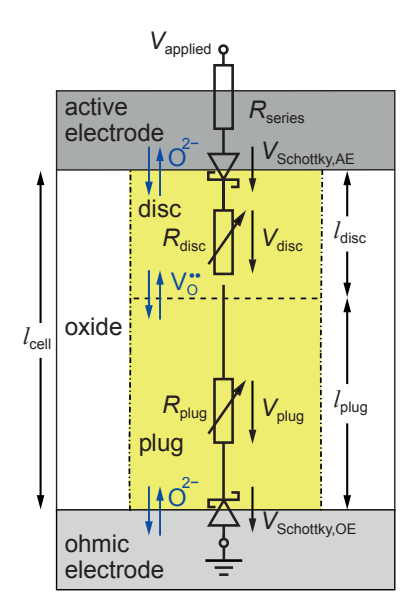


Figure 5.2: Equivalent circuit diagram for the electrical model of compact model 2.0.

### 5.2 Model Description and Equations

The whole ReRAM device is modeled using five elements, see Fig. 5.2: two Schottky diodes for the metal/oxide interfaces, two filament resistances and a series resistance  $R_{\rm series}$ . The length of the filament  $l_{\rm cell}$  is equivalent to the oxide thickness and its cross-sectional area A is calculated based on the filament radius  $r_{\rm fil}$  using  $A = \pi r_{\rm fil}^2$ . The model can be adapted to asymmetric and symmetric device stacks. For asymmetric device stacks, the filament is split into a disc and a plug of different lengths as in compact model 1.0 and 1.5. Note that the definition of the filament geometry also holds in the pristine (unformed) state. As before, the disc is the region near the electrode of higher work function (active electrode). Consequently, all parameters concerning the Schottky barrier at this interface have an additional 'AE' in their name. For the ohmic electrode, 'OE' is used in the subscript. The oxygen vacancy concentration and the length of the disc and the plug are denoted by  $N_{\rm disc}$ ,  $N_{\rm plug}$ ,  $l_{\rm disc}$ , and  $l_{\rm plug}$ , respectively. With N referring to a concentration of oxygen vacancies,  $N_{\rm O}$  indicates an oxygen ion concentration. Thus, the oxygen ion concentrations in the active electrode, ohmic electrode, disc, and plug are labeled by  $N_{\rm O,AE}$ ,  $N_{\rm O,OE}$ ,  $N_{\rm O,OE}$ ,  $N_{\rm O,disc}$ , and  $N_{\rm O,plug}$ , respectively.

The voltage  $V_{\text{applied}}$  is applied to the active electrode while the ohmic electrode is grounded. The current is denoted by I. Using Kirchhoff's law,

$$V_{\text{applied}} - [V_{\text{Schottky,AE}} + V_{\text{Schottky,OE}} + I \cdot (R_{\text{disc}} + R_{\text{plug}} + R_{\text{series}})] = 0$$
 (5.9)

is solved. The series resistance is constant and comprises electrode and line resistances. Band conduction with temperature-dependent mobility  $\mu_n$  is assumed as electrical conduction mechanism in the filament. Thus, the two filament resistances are calculated using

$$R_{\rm disc} = \frac{l_{\rm disc}}{A \cdot z_{\rm Vo} e N_{\rm disc} \mu_{\rm n}(T)} = \frac{l_{\rm disc}}{A \cdot z_{\rm Vo} e N_{\rm disc} \mu_{\rm n0}} \exp\left(\frac{\Delta E_{\rm ac}}{k_{\rm B} T}\right)$$
(5.10)

and

$$R_{\text{plug}} = \frac{l_{\text{plug}}}{A \cdot z_{\text{Vo}} e N_{\text{plug}} \mu_{\text{n}}(T)} = \frac{l_{\text{plug}}}{A \cdot z_{\text{Vo}} e N_{\text{plug}} \mu_{\text{n0}}} \exp\left(\frac{\Delta E_{\text{ac}}}{k_{\text{B}} T}\right), \tag{5.11}$$

where e is the elementary charge,  $z_{\text{Vo}}$  is the charge number of the oxygen vacancies relative to the perfect crystal lattice,  $k_{\text{B}}$  is the Boltzmann constant, T is the temperature, and  $\mu_{\text{n0}}$  is the temperature-independent prefactor of the mobility. The temperature dependence of the mobility is modeled using a (small) activation energy  $\Delta E_{\text{ac}}$ .

The current through the Schottky diodes is calculated based on the thermionic and thermionic field emission theory, see section 2.3:

$$I = \begin{cases} \operatorname{sign}(V_{\text{applied}}) \cdot I_{\text{TE}} & V_{\text{forward}} > 0 \text{ (forward)} \\ \operatorname{sign}(V_{\text{applied}}) \cdot I_{\text{TFE,reverse}} & V_{\text{forward}} \leq 0 \text{ (reverse)}. \end{cases}$$
(5.12)

As the two Schottky diodes are connected anti-serially, the definition of the voltage for which the junction is forward biased differs, see Fig. 5.2. A positive voltage  $V_{\text{Schottky,AE}}$  across the AE/oxide interface corresponds to a forward bias ( $V_{\text{forward}} = V_{\text{Schottky,AE}}$ ,  $V_{\text{reverse}} = -V_{\text{Schottky,AE}}$ ). On the contrary, a positive voltage  $V_{\text{Schottky,OE}}$  across the OE/oxide interface equals a reverse bias ( $V_{\text{forward}} = -V_{\text{Schottky,OE}}$ ,  $V_{\text{reverse}} = V_{\text{Schottky,OE}}$ ). Thermionic emission is chosen for the forward direction as this ensures the current to be computable for all applied voltages, especially in the LRS with a high donor concentration, see the discussion in section 2.3. Under reverse bias, tunneling cannot be neglected given the moderate to high donor concentrations. The thermionic field emission equation also provides a real-valued result for a vanishing Schottky barrier ( $\phi_{\text{Bn}} = 0 \text{ V}$ ) and is therefore appropriate for the current description under reverse bias. For the donor concentrations in Eqs. (2.2) and (2.6),  $N_{\text{D,AE/OE}} = z_{\text{Vo}}N_{\text{disc/plug}}$  holds.

The energy difference between the Fermi level and the conduction band edge  $e\phi_{n,AE/OE}$  depends on the donor concentration at the AE and OE interface, respectively. Both values are calculated based on the approximation of the inverse function of the Fermi-Dirac integral  $\mathcal{F}_{1/2}^{-1}$  by Nilsson [165]

$$\phi_{\text{n,AE/OE}} = -\frac{k_{\text{B}}T}{e} \mathcal{F}_{1/2}^{-1} \left( \frac{z_{\text{Vo}} N_{\text{disc/plug}}}{2(2\pi m_{\text{eff}} k_{\text{B}} T/h^2)^{3/2}} \right)$$
(5.13)

with

$$\mathcal{F}_{1/2}^{-1}(u) = \frac{\ln(u)}{1 - u^2} + \left(3\sqrt{\pi}u/4\right)^{2/3} - \frac{\left(3\sqrt{\pi}u/4\right)^{2/3}}{1 + \left(0.24 + 1.08\left(3\sqrt{\pi}u/4\right)^{2/3}\right)^{2/3}}.$$
 (5.14)

The change of the oxygen vacancy concentration in the disc and the plug can be modeled in terms of three ionic currents:  $I_{\text{ion}}$  denotes the flux of oxygen vacancies between the plug and the disc. The oxygen exchange between disc and active electrode and the oxygen exchange between plug and ohmic electrode are described by the ionic currents  $I_{\text{ion,BV,AE}}$  and  $I_{\text{ion,BV,OE}}$ , respectively. All ionic currents are defined regarding the flux of oxygen vacancies. In total, this results in

$$\frac{\mathrm{d}N_{\mathrm{disc}}}{\mathrm{d}t} = -\frac{1}{z_{\mathrm{Vo}}e\,A\,l_{\mathrm{disc}}} \cdot I_{\mathrm{ion}} + \frac{1}{z_{\mathrm{Vo}}e\,A\,l_{\mathrm{disc}}} \cdot I_{\mathrm{ion,BV,AE}} \tag{5.15}$$

and

$$\frac{\mathrm{d}N_{\mathrm{plug}}}{\mathrm{d}t} = +\frac{1}{z_{\mathrm{Vo}}e\,A\,l_{\mathrm{plug}}} \cdot I_{\mathrm{ion}} - \frac{1}{z_{\mathrm{Vo}}e\,A\,l_{\mathrm{plug}}} \cdot I_{\mathrm{ion,BV,OE}}.$$
 (5.16)

The signs are chosen such that the ionic currents are positive if a vacancy 'flows' from  $AE \to disc \to plug \to OE$ . The total amount of oxygen ions in the system (filament + electrodes) is constant at all times. Thus, the same number of oxygen ions that leaves for example the plug reappears in the disc or in the ohmic electrode. Note that the calculation is based on continuous concentrations and not on integer numbers of vacancies/ions. The number of exchanged oxygen vacancies/ions in every time step is a non-integer number. Accordingly, the change in oxygen ion concentration in AE and OE is given by

$$\frac{\mathrm{d}N_{\mathrm{O,AE}}}{\mathrm{d}t} = +\frac{1}{z_{\mathrm{Vo}}e\,A\,l_{\mathrm{AE,eff}}} \cdot I_{\mathrm{ion,BV,AE}} \tag{5.17}$$

and

$$\frac{\mathrm{d}N_{\mathrm{O,OE}}}{\mathrm{d}t} = -\frac{1}{z_{\mathrm{Vo}}e\,A\,l_{\mathrm{OE,eff}}} \cdot I_{\mathrm{ion,BV,OE}},\tag{5.18}$$

respectively. In the metal electrodes, the oxygen ions are adsorbed near/at the interface. As the oxygen exchange is modeled in terms of a volume concentration of oxygen ions at both sides of the interface, an effective volume of  $A \cdot l_{\text{AE,eff}}$  and  $A \cdot l_{\text{OE,eff}}$  is considered for the reservoir to calculate the ion concentration. The ionic exchange currents  $I_{\text{ion,BV,AE}}$ 

and  $I_{\text{ion,BV,OE}}$  are defined based on the Butler–Volmer approach as described in detail in section 5.1 and Fig. 5.1. The oxygen transfer reaction at the OE/oxide interface is modeled using

$$\begin{split} I_{\text{ion,BV,OE}} &= -A \, J_{\text{O,OE} \to \text{Ox}} \\ &= -A \left( z_{\text{O}} e N_{\text{O,OE}} k_{\text{I,OE}}^0 \exp \left( -\frac{\Delta G_{\text{I,OE}}}{k_{\text{B}} T} \right) \exp \left( \frac{\alpha_{\text{OE}} z_{\text{O}} e}{k_{\text{B}} T} (-V_{\text{Schottky,OE}}) \right) \cdot F_{\text{limit,OE,I}} \\ &- z_{\text{O}} e N_{\text{O,plug}} k_{\text{II,OE}}^0 \exp \left( -\frac{\Delta G_{\text{II,OE}}}{k_{\text{B}} T} \right) \exp \left( -\frac{(1 - \alpha_{\text{OE}}) z_{\text{O}} e}{k_{\text{B}} T} (-V_{\text{Schottky,OE}}) \right) \cdot F_{\text{limit,OE,II}} \right) \end{split}$$

with

$$F_{\text{limit,OE,I}} = \left[ 1 - \left( \frac{N_{\text{min}}}{N_{\text{plug}}} \right)^{10} \right] \cdot \left[ 1 - \left( \frac{N_{\text{O,OE,min}}}{N_{\text{O,OE}}} \right)^{10} \right], \tag{5.20}$$

$$F_{\text{limit,OE,II}} = \left[ 1 - \left( \frac{N_{\text{plug}}}{N_{\text{max}}} \right)^{10} \right]. \tag{5.21}$$

The ionic current is limited by the factors  $F_{\text{limit,OE,I}}$  and  $F_{\text{limit,OE,II}}$  to ensure that all concentrations neither exceed a maximum nor fall below a minimum concentration. The exponent of 10 is arbitrary but was chosen such that the ionic current is only influenced when the concentrations are close to the limits. An exponent of 10 ensures this much better than an exponent of 1. An oxygen ion in the OE has to overcome the kinetic barrier  $\Delta G_{\text{I,OE}}$ , which is modulated by the reference potential and the external voltage across the interface  $V_{\text{Schottky,OE}}$ , to get into the oxide. The influence of the reference potential is considered in the prefactor of the rate constant  $k_{\text{I,OE}}^0$ . The dimensionless charge transfer coefficient  $\alpha_{OE}$  defines which ratio of the potential difference affects the forward process; it is set to 0.5 in the standard model as no experimental or theoretical data exists on this parameter for the studied systems. The transfer of oxygen ions from the OE to the plug can take place as long as the concentration of oxygen ions in the OE does not fall below the minimum concentration  $N_{O,OE,min}$ . The minimum concentration corresponds to a calculated concentration of one absorbed oxygen ion in the electrode reservoir; a minimum concentration of zero is not possible to limit the concentration decrease, see Eq. (5.20). In addition, the exchange cannot proceed if the concentration of oxygen vacancies in the plug falls below the minimum concentration  $N_{\min}$  as an ion can only be transferred if there is a free site to occupy, i.e. a vacancy in the plug.

The concentration of oxygen ions in the plug  $N_{\text{O,plug}}$  is an important prefactor for the opposite process, the transfer of oxygen ions from the plug to the OE. Moreover, the

exchange is determined by the kinetic barrier  $\Delta G_{\rm II,OE}$  and the rate constant prefactor  $k_{\rm II,OE}^0$ . The transfer can proceed until the concentration of vacancies in the plug that are left behind by the exchanged ions increases to the maximum value  $N_{\rm max}$ . The concentration of oxygen ions in the plug can be calculated by simply subtracting the vacancy concentration from the concentration of oxygen in a stoichiometric crystal  $N_{\rm O,oxide,max}$ :

$$N_{\text{O,plug}} = N_{\text{O,oxide,max}} - N_{\text{plug}}.$$
 (5.22)

The oxygen exchange at the AE/disc interface is defined analogously to the exchange at the OE/plug interface. Due to the definition of the voltage  $V_{\text{Schottky,AE}}$  in Fig. 5.2,  $\eta = +V_{\text{Schottky,AE}}$  holds. The ionic exchange current reads

 $I_{\text{ion,BV,AE}} = A J_{\text{O,AE} \to \text{Ox}}$ 

$$= A \left( z_{\text{O}} e N_{\text{O,AE}} k_{\text{I,AE}}^{0} \exp \left( -\frac{\Delta G_{\text{I,AE}}}{k_{\text{B}} T} \right) \exp \left( \frac{\alpha_{\text{AE}} z_{\text{O}} e}{k_{\text{B}} T} V_{\text{Schottky,AE}} \right) \cdot F_{\text{limit,AE,I}} \right.$$
$$- z_{\text{O}} e N_{\text{O,disc}} k_{\text{II,AE}}^{0} \exp \left( -\frac{\Delta G_{\text{II,AE}}}{k_{\text{B}} T} \right) \exp \left( -\frac{(1 - \alpha_{\text{AE}}) z_{\text{O}} e}{k_{\text{B}} T} V_{\text{Schottky,AE}} \right) \cdot F_{\text{limit,AE,II}} \right)$$
(5.23)

with

$$F_{\text{limit,AE,I}} = \left[1 - \left(\frac{N_{\text{min}}}{N_{\text{disc}}}\right)^{10}\right] \cdot \left[1 - \left(\frac{N_{\text{O,AE,min}}}{N_{\text{O,AE}}}\right)^{10}\right], \tag{5.24}$$

$$F_{\text{limit,AE,II}} = \left[1 - \left(\frac{N_{\text{disc}}}{N_{\text{max}}}\right)^{10}\right],\tag{5.25}$$

and

$$N_{\text{O,disc}} = N_{\text{O,oxide,max}} - N_{\text{disc}}.$$
 (5.26)

The overpotential  $\eta$  in Eq. (5.8) corresponds to the voltage across the interface and, by definition,  $\eta$  is positive if a positive potential is applied at the metal electrode  $(V_{\text{M}\to\text{Ox}})$ . Thus,  $\eta = +V_{\text{Schottky,AE}}$  holds for the AE/disc interface. At the OE/plug interface, however, the voltage  $V_{\text{Schottky,OE}}$  is defined the other way round, being positive when the electrode is grounded  $(V_{\text{Ox}\to\text{M}})$ , see Fig. 5.2. Thus,  $\eta = -V_{\text{Schottky,OE}}$  is used. If a positive potential is applied to the electrode  $(V_{\text{Schottky,OE}} < 0, V_{\text{Schottky,AE}} > 0)$ , the effective barrier for the transfer of oxygen ions from the metal to the oxide is increased and the effective barrier for the transfer of oxygen ions from the oxide to the metal is reduced

(note that  $z_{\rm O} < 0$ ). However, this does not necessarily imply that the net ionic flux leads to an increase of oxygen ions in the metal, the prefactors  $k^0$  and  $N_{\rm O}$  are crucial as well. The ionic current  $I_{\rm ion}$  describes the migration of oxygen vacancies along the filament considering drift and diffusion between the plug and the disc. Apart from an adaption regarding the calculation of the electric field during forming, the definition of  $I_{\rm ion}$  is the same as in compact model 1.5. The ion migration depends on the local temperature, the electric field, and the concentration gradient between the plug and the disc. It describes an ion hopping conduction over a potential barrier, see section 2.4. The barrier  $\Delta W_{\rm A}$  is lowered by the applied electric field E for forward jumps and raised for reverse jumps:

$$I_{\text{ion}} = A \left( J_{\text{ion,drift}} + J_{\text{ion,diffusion}} \right)$$

$$= A \left( CN \sinh \left( \frac{az_{\text{Vo}}eE}{2k_{\text{B}}T} \right) \cdot F_{\text{limit}} - C \frac{a}{2} \frac{dN}{dx} \cosh \left( \frac{az_{\text{Vo}}eE}{2k_{\text{B}}T} \right) \right)$$
(5.27)

with C as

$$C = 2z_{\text{Vo}}ea\nu_0 \exp\left(-\frac{\Delta W_{\text{A}}\left[\sqrt{1-\gamma^2} + \gamma \arcsin\gamma\right]}{k_{\text{B}}T}\right). \tag{5.28}$$

Here, a is the hopping distance,  $\nu_0$  is the attempt frequency, N is the ion concentration and dN/dx is the concentration gradient. The factor  $\gamma$  modifies the hopping barrier for forward and reverse jumps according to

$$\gamma = \frac{az_{\text{Vo}}eE}{\pi\Delta W_{\text{A}}}.$$
 (5.29)

To account for the non-uniform distribution of the ions in the filament, the driving concentration N for the drift current is chosen as the mean of both concentrations  $N_{\rm disc}$  and  $N_{\rm plug}$ . As the concentrations vary over several orders of magnitude and the concentration profiles are assumed to resemble a sigmoid on a logarithmic scale, the geometrical mean is used instead of the arithmetic mean:

$$N = \sqrt{N_{\rm disc} \cdot N_{\rm plug}}.$$
 (5.30)

For the concentration gradient applies

$$\frac{\mathrm{d}N}{\mathrm{d}x} = \frac{N_{\mathrm{plug}} - N_{\mathrm{disc}}}{0.5 \, l_{\mathrm{cell}}}.\tag{5.31}$$

Like the choice of the driving concentration for the ionic current, the selection of the driving electric field is nontrivial. A distinction between pristine and formed devices

turned out to be necessary to obtain satisfactory results. For pristine devices, the driving electric field is calculated using

$$E = \frac{V_{\text{Schottky,AE}} + V_{\text{disc}} + V_{\text{plug}} + V_{\text{Schottky,OE}}}{l_{\text{cell}}}$$
 (5.32)

for all  $V_{\text{applied}}$ . After forming and analogous to the approaches for the compact models 1.0 and 1.5, the equation differs for SET and RESET direction according to

$$E = \begin{cases} \frac{V_{\text{disc}} + V_{\text{plug}}}{l_{\text{cell}}} & V_{\text{applied}} > 0 \text{ (RESET)} \\ \frac{V_{\text{disc}}}{l_{\text{disc}}} & V_{\text{applied}} < 0 \text{ (SET)}. \end{cases}$$
(5.33)

The ionic current is limited by the factor  $F_{\text{limit}}$  to ensure that the vacancy concentrations neither exceed a maximum nor fall below a minimum concentration,  $N_{\text{max}}$  and  $N_{\text{min}}$ , respectively:

$$F_{\text{limit}} = \begin{cases} \left[ 1 - \left( \frac{N_{\text{plug}}}{N_{\text{max}}} \right)^{10} \right] \cdot \left[ 1 - \left( \frac{N_{\text{min}}}{N_{\text{disc}}} \right)^{10} \right] & V_{\text{applied}} > 0 \\ \left[ 1 - \left( \frac{N_{\text{disc}}}{N_{\text{max}}} \right)^{10} \right] \cdot \left[ 1 - \left( \frac{N_{\text{min}}}{N_{\text{plug}}} \right)^{10} \right] & V_{\text{applied}} < 0. \end{cases}$$

$$(5.34)$$

 $N_{\rm min}$  corresponds to the calculated concentration of one oxygen vacancy being present in the filament. The ultimate maximum vacancy concentration is set by the density of oxygen sites in the crystal lattice. To prevent unreasonable high oxygen vacancy concentrations, a maximum site fraction of roughly 10% is chosen as  $N_{\rm max}$ .

Because 2D simulations have shown that the temperature along the filament is rather homogeneous [44], one single temperature for the whole filament and the adjacent interfaces is used. The local temperature is calculated based on the power dissipation in the filament due to the voltage drops across the disc and the plug:

$$T = (V_{\text{disc}} + V_{\text{plug}}) \cdot I \cdot R_{\text{th,eff}} + T_0, \tag{5.35}$$

where  $T_0$  is the ambient temperature. The Joule heating is described using one effective thermal resistance  $R_{\rm th,eff}$ , which comprises the heat loss to the surrounding oxide and to the metal electrodes. To account for the different conditions in pristine and formed devices, different thermal resistances are used during forming and subsequent switching sweeps. To limit the current during forming, an additional series resistance  $R_{\text{series,cc}}$  can be applied. In experiments, this is done to provide an effective limitation if there is no suitable current compliance by a transistor or an internal line resistance. Although the current compliance in a simulation can react as fast as it is defined, the increase in computing time can be disproportionately high. In these cases, the total series resistance is

$$R_{\text{series,total}} = R_{\text{series}} + R_{\text{series,cc}}.$$
 (5.36)

Details on the solver and on the simulation workflow can be found in section 2.6.

### 5.3 Simulation Results

Compact model 2.0 enables a wide range of new simulation studies. As one of them, the forming process is studied in detail. The dependence of the forming voltage on the oxide thickness and the influence of various parameters are described in section 5.3.1. Sweeps that are simulated subsequent to a forming step are analyzed in section 5.3.2. Endurance and retention are an extensive field of research and exemplary simulation studies covering the main trends are presented in section 5.3.3. Besides counter-eightwise switching, the model allows to describe eightwise switching. In section 5.3.4, the 8w switching simulation results of the standard compact model 2.0 are compared to the results of a modified version, which includes diffusion of oxygen ions in the active electrode.

## 5.3.1 Forming

In contrast to compact model 1.0 and 1.5, compact model 2.0 is capable of modeling the forming process. Thus, the number of vacancies in the filament during switching is not an arbitrary variable anymore but the result of the forming step if desired. Nevertheless, initial values referring to an already formed filament can still be chosen if the influence of the forming conditions is not of interest. The general compact model behavior regarding forming is shown in Fig. 5.3. For the sake of simplicity, only oxygen exchange at the OE is considered; the ionic current between disc and AE is set to zero. This assumptions represents a ReRAM cell where the oxygen exchange with the AE is not necessarily zero but negligible compared to the exchange at the OE. This is reasonable for stacks with highly asymmetric electrodes regarding the oxygen affinity, especially, if the OE is the top electrode. The parameters for the simulation are listed in Table 5.1 ( $\nu_0 = 4 \cdot 10^{12} \, \text{Hz}$ ,  $R_{\text{series,cc}} = 20 \, \text{k}\Omega$ ) and fitted to match the experimental data of some ZrO<sub>x</sub>-based devices,

<b>Table 5.1:</b> Par	rameters to	r the	simul	ations	in	sections	5.3.1	and $5.3.2$ .
-----------------------	-------------	-------	-------	--------	----	----------	-------	---------------

Symbol	Value	Symbol	Value
$l_{ m cell}$	$5\mathrm{nm}$	$arepsilon_{\phi_{ m B}}$	$5.5  \varepsilon_0$
$l_{ m disc}$	$l_{\rm cell}/4$	$e\phi_{ m Bn0,AE}$	$0.4\mathrm{eV}$
$l_{ m plug}$	$l_{ m cell}-l_{ m disc}$	$e\phi_{ m Bn0,OE}$	$0.3\mathrm{eV}$
$r_{ m fil}$	$30\mathrm{nm}$	$\mu_{ m n0}$	$5 \cdot 10^{-5}  \mathrm{m}^2 / (\mathrm{Vs})$
$l_{ m OE,eff}$	$1\mathrm{nm}$	$\Delta E_{ m ac}$	$0.05\mathrm{eV}$
$z_{ m Vo}$	2	$N_{ m O,oxide,max}$	$5.6 \cdot 10^{28} \mathrm{m}^{-3}$ (1)
$z_{ m O}$	-2	$N_{ m max}$	$5 \cdot 10^{27}  \mathrm{m}^{-3}$
a	$0.5\mathrm{nm}$	$N_{ m min}$	$1/\left(A \cdot l_{\text{cell}}\right)$
$\nu_0$	$4(2)\cdot 10^{12}\mathrm{Hz}$	$N_{ m O,OE,min}$	$1/\left(A \cdot l_{\text{OE,eff}}\right)$
$\Delta W_{ m A}$	$0.9\mathrm{eV}$	$N_{ m disc,initial}$	$N_{ m min}$
$\alpha_{\mathrm{OE}}$	0.5	$N_{ m plug,initial}$	$N_{ m min}$
$k_{\rm I,OE}^0$	$1 \cdot 10^4  \mathrm{m/s}$	$N_{ m O,OE,initial}$	$N_{ m O,OE,min}$
$k_{ m I,OE}^0 \ k_{ m II,OE}^0$	$2 \cdot 10^4 \mathrm{m/s}$	$R_{ m th,eff,Forming}$	$5 \cdot 10^7  \mathrm{K/W}$
$\Delta G_{ m I,OE}$	$1.3\mathrm{eV}$	$R_{ m th,eff,Sweep}$	$3.5\cdot 10^5\mathrm{K/W}$
$\Delta G_{ m II,OE}$	$1.05\mathrm{eV}$	$R_{ m series}$	$200\Omega$
$m_{ m eff}$	$m_{ m e}$	$R_{\rm series,cc}$	see below figures
$A^*$	see Eq. $(2.4)$	sweep rate	$1\mathrm{V/s}$
$\varepsilon$	$17  \varepsilon_0$	$T_0$	$293\mathrm{K}$

<sup>(1)</sup> see Table A.1 in Appendix A.2

see below. The I-V characteristic and the oxygen vacancy concentration in the plug and the disc are depicted in Fig. 5.3a and b, respectively. At first, the resistance decrease proceeds slowly, then it accelerates until an abrupt current jump sets in. The initial concentration of oxygen vacancies in the disc and the plug is set to the minimum value, which corresponds to one oxygen vacancy in the whole filament. Arithmetically, this results in a total number of vacancies in the plug and the disc below one at t = 0 s, see Fig. 5.3c. This may be physically unreasonable but it underlines that the model equations are based on concentrations and not integer numbers. For mathematical reasons, an initial concentration of zero vacancies cannot be chosen. The total number of vacancies in the filament increases during forming, slowly at the beginning and then abruptly. The number of oxygen ions in the OE does exactly the same (Fig. 5.3d) as the noninteger number of oxygen that is exchanged between plug and OE is identical. For the initial concentration of oxygen in the OE, the minimum concentration for a non-oxidized electrode is chosen. The concentration of vacancies in the filament is inherently linked to the concentration of oxygen in the oxide by the crystal lattice properties. Therefore, the number of oxygen ions in the filament is reduced during forming. As only a very small

fraction of the oxygen in the plug and the disc leaves the oxide, this is hardly visible in Fig. 5.3d. The inset shows a zoom for the oxygen ions in the plug. The total number of oxygen in the system  $O_{total} = O_{OE} + O_{plug} + O_{disc} (+ O_{AE})$  is always constant. As discussed in section 2.2, the growth direction of the filament during forming depends on the relation between migration kinetics in the oxide and the oxygen exchange kinetics at the anode [47, 92, 93]. With the chosen parameters, the filament "grows" from the anode (OE) to the cathode as the concentration of vacancies in the plug is higher than in the disc at all times during forming. The resistances of the single elements and the filament temperature are shown in Fig. 5.3e and f, respectively. The resistance of the AE/disc interface  $R_{\text{Schottky,AE}}$  dominates the pristine state as the nominal barrier  $e\phi_{\text{Bn0,AE}}$  is higher than  $e\phi_{\text{Bn0,OE}}$  and the donor concentration in the disc is lower than in the plug. Due to the low current in the pristine state, Joule heating is insignificant for voltages below 2 V. Similar to the SET switching described in detail in section 3.2.3, a positive feedback exists between temperature increase and generation of oxygen vacancies at the interface. This leads to a self-acceleration and finally a thermal runaway, which is characterized by a jump in temperature, vacancy concentration, and current.

It is known from experimental data that the oxide thickness influences the forming voltage. For all simulations, the forming voltage  $V_{\text{Forming}}$  is simply defined as the voltage at which the current exceeds 1 µA. Forming simulations with cell thicknesses of 3 nm, 5 nm, 7.5 nm, 10 nm, 12.5 nm, and 15 nm are performed with the parameters from Table 5.1 ( $\nu_0 = 2 \cdot 10^{12} \,\mathrm{Hz}$ ). The resulting I-V curves are shown in Fig. 5.4a. The corresponding forming voltages are plotted against the oxide thickness next to experimental data of ZrO<sub>x</sub>-based devices in Fig. 5.4b. Fabrication, measurement, and analysis of the experimental data were performed by Andreas Kindsmüller. The oxide with varying thickness was deposited on a 30 nm Pt bottom electrode by reactive sputter deposition. A 20 nm Ta layer was used as top electrode with a Pt layer on top to prevent oxidation of the Ta electrode. The final layer stack for the  $(50 \times 50) \,\mu\text{m}^2$  ReRAM devices consisted of  $30 \,\mathrm{nm}\,\mathrm{Pt}/3 \,\mathrm{nm}-15 \,\mathrm{nm}\,\mathrm{ZrO_x}/20 \,\mathrm{nm}\,\mathrm{Ta}$ . The voltage is defined as being applied to the Pt bottom electrode, while the top electrode is grounded. The forming voltages of at least 25 devices per ZrO<sub>x</sub> thickness were measured and the results are shown as box plot in Fig. 5.4b. In both the experimental data and the simulation results, the forming voltage increases linearly with the oxide thickness. For the simulation, this behavior can be explained by the effect that the higher filament volume has on the vacancy concentration. A mere increase in the plug and disc resistance according to the increase in length would not affect the current because the AE interface resistance  $R_{\text{Schottky,AE}}$  dominates the to-

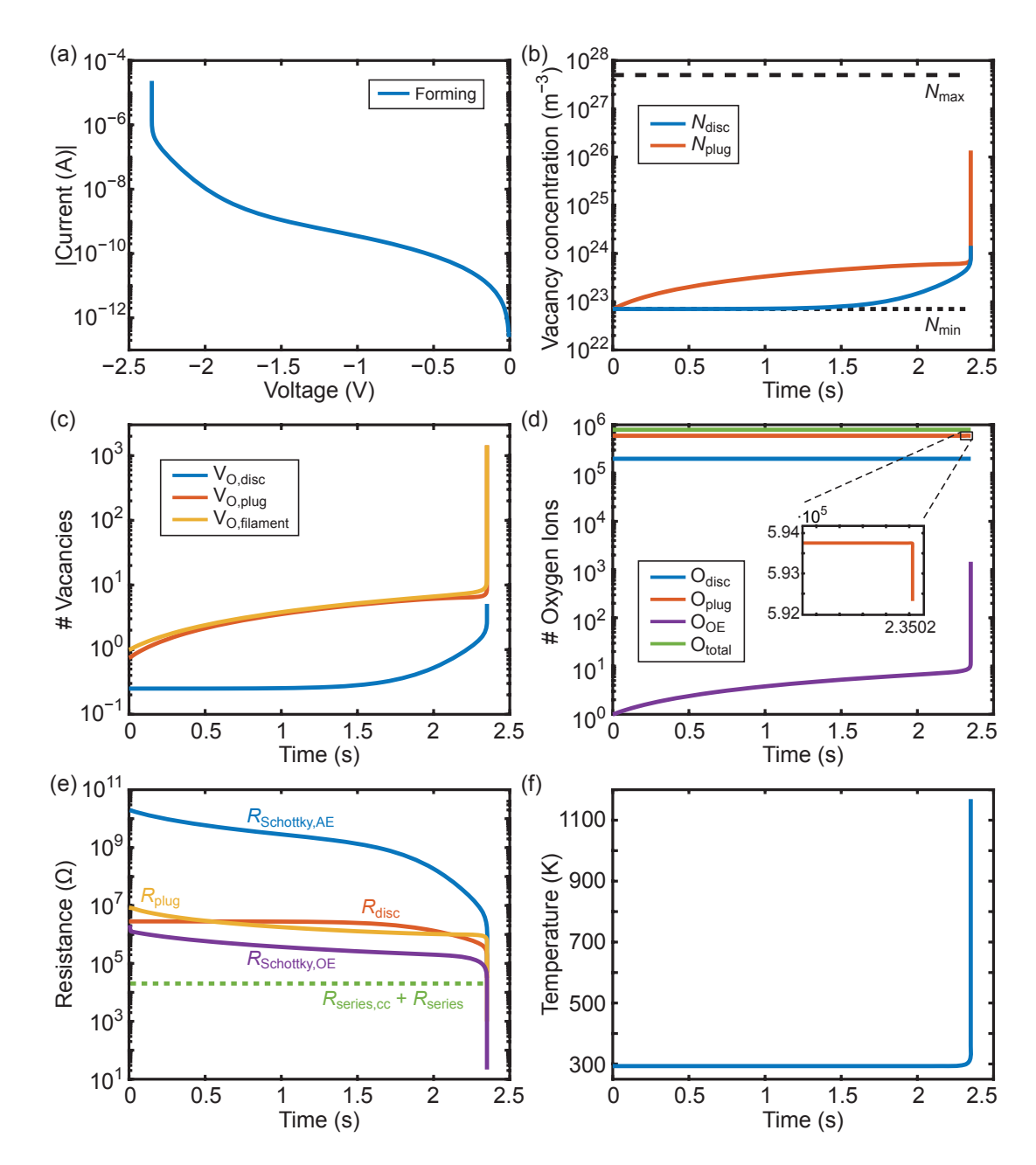


Figure 5.3: General forming characteristics of compact model 2.0. Here, only oxygen exchange at the OE is considered. The parameters in Table 5.1 with  $\nu_0 = 4 \cdot 10^{12} \, \mathrm{Hz}$  and  $R_{\mathrm{series,cc}} = 20 \, \mathrm{k}\Omega$  are used for the simulation. (a) I-V curve. (b) Oxygen vacancy concentration of the disc and the plug. (c) Number of oxygen vacancies in the disc and the plug, calculated based on the concentrations, and the sum of both. The total number of vacancies in the filament increases during forming. (d) Number of oxygen ions in disc, plug, OE, and the total number in the system (filament and electrodes). The number of oxygen in the disc and the plug decreases slightly during forming, see the zoom of  $O_{\mathrm{plug}}$  in the inset. The total number of oxygen ions in the system is constant during switching. (e) Resistances of all lumped circuit elements. (f) Temperature in the filament.

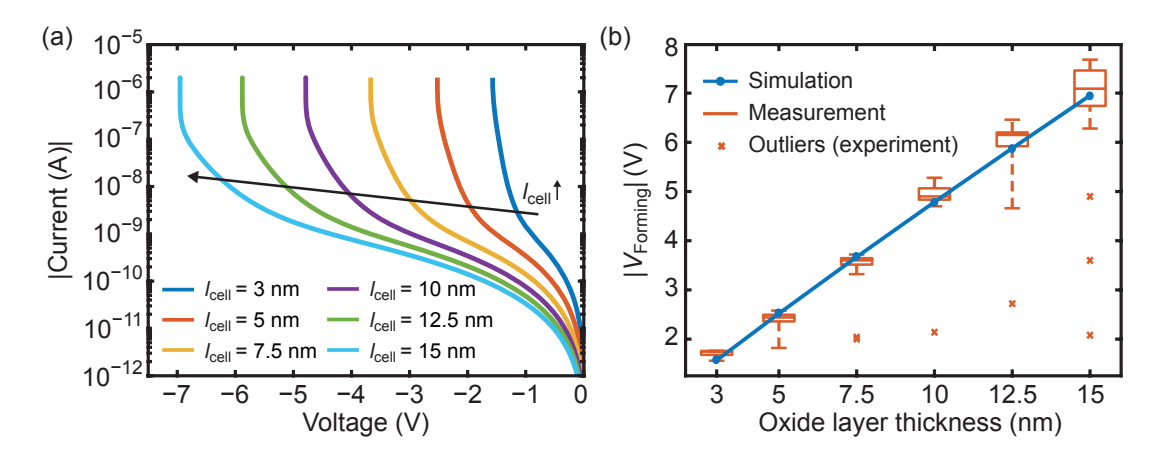


Figure 5.4: Measured and simulated dependence of the forming voltage on the oxide thickness. The experimental data were obtained by Andreas Kindsmüller on Pt/ZrO<sub>x</sub>/Ta devices [166]. For the simulation, the parameters in Table 5.1 with  $\nu_0 = 2 \cdot 10^{12}$  Hz are used. For  $l_{\rm cell} = 3$  nm, 5 nm, 7.5 nm, 10 nm, 12.5 nm, and 15 nm,  $R_{\rm series,cc} = 50$  kΩ, 80 kΩ, 120 kΩ, 160 kΩ, 200 kΩ, and 240 kΩ were applied, respectively. (a) Simulated I-V curves. (b) Simulated and measured forming voltage depending on the oxide layer thickness.

tal resistance, as shown in Fig. 5.3e. The thicker the oxide, the lower the concentration is for a given number of vacancies in the filament. Thus, the initial concentration, and thereby the initial resistance, varies for different cell lengths. Consequently, the thickest oxide shows the lowest current in the pristine state. During forming, a higher plug volume leads to a lower increase in concentration for a certain number of exchanged ions. It is therefore important that the plug and disc lengths are not fixed in this simulation but scale with the cell length. Accordingly, the current increase for the same amount of generated vacancies is highest for the smallest oxide thickness. The higher current leads to more Joule heating and the thermal runaway sets in earlier.

The exact dependence of the forming voltage on the oxide thickness highly depends on several parameters. The influence of eight of them is shown exemplary in Fig. 5.5a. To allow for an easy comparison, the reference from Fig. 5.4b with the parameters from Table 5.1 ( $\nu_0 = 2 \cdot 10^{12} \,\mathrm{Hz}$ ) is added as well. As the simple plot of forming voltage against cell thickness disguises important characteristics, the I-V forming curves are given separately for five simulations in Fig. 5.5b-f.  $\Delta G_{\mathrm{II,OE}}$  is the (nominal) barrier that an oxygen ion in the plug has to overcome to get into the OE leaving an oxygen vacancy behind. If  $\Delta G_{\mathrm{II,OE}}$  is increased, a higher voltage across the interface is needed to lower the nominal barrier sufficiently to generate the same amount of vacancies in the plug. Consequently, the forming voltage is higher if  $\Delta G_{\mathrm{II,OE}}$  is increased by 0.1 eV and lower if decreased by 0.1 eV (reference fit:  $\Delta G_{\mathrm{II,OE}} = 1.05 \,\mathrm{eV}$ ). The I-V forming

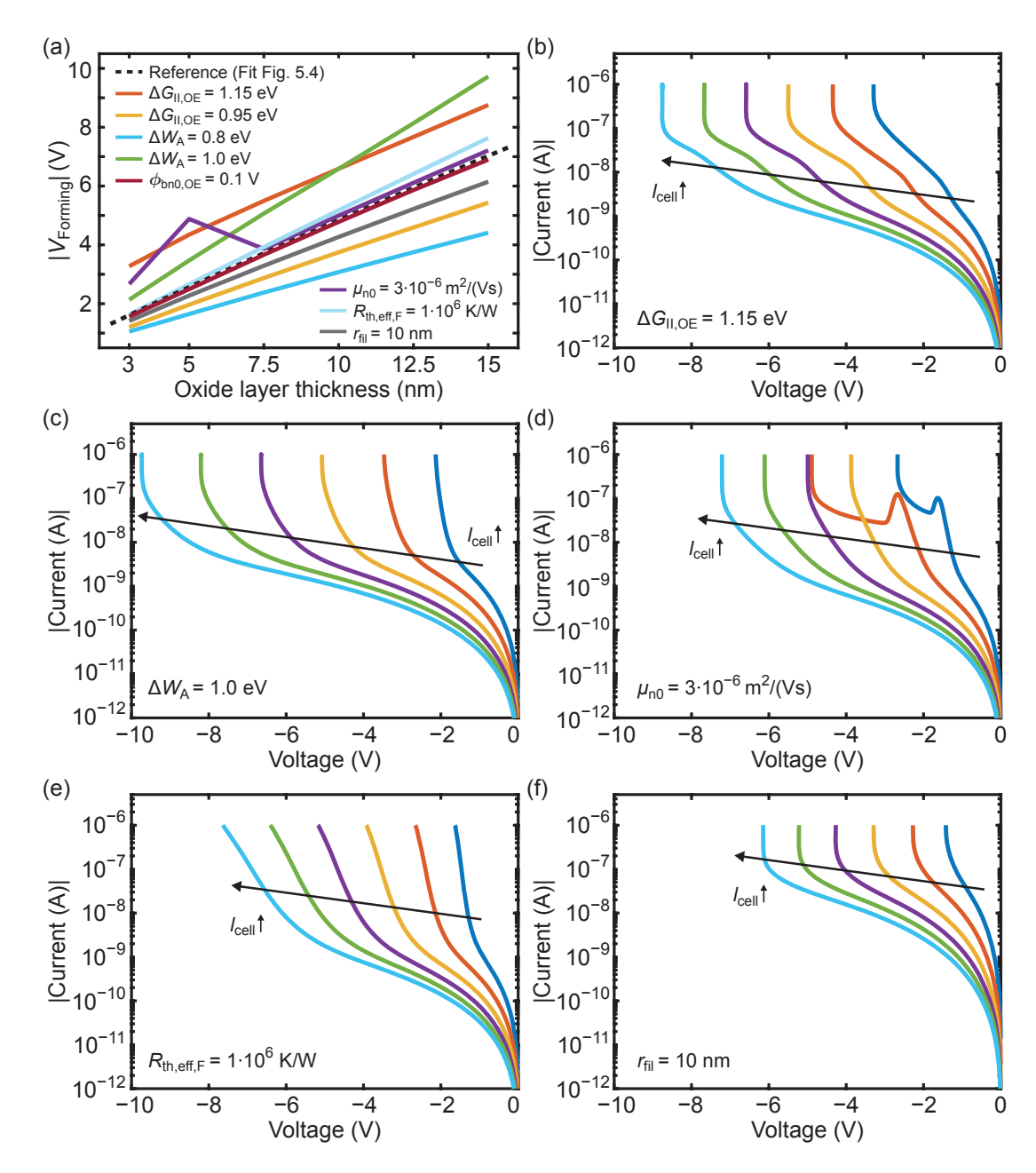


Figure 5.5: Influence of various parameters on the forming behavior. The parameters are taken from Table 5.1 ( $\nu_0 = 2 \cdot 10^{12} \,\mathrm{Hz}$ ) with the exception of the parameter being varied as stated in the figures. The used  $R_{\mathrm{series,cc}}$  values for each simulation are given in Table A.2 in Appendix A.2. (a) Forming voltage depending on the oxide thickness. For each different parameter, a simulation is done for  $l_{\mathrm{cell}} = 3 \,\mathrm{nm}$ ,  $5 \,\mathrm{nm}$ ,  $7.5 \,\mathrm{nm}$ ,  $10 \,\mathrm{nm}$ ,  $12.5 \,\mathrm{nm}$ , and  $15 \,\mathrm{nm}$ . I-V curves for (b)  $\Delta G_{\mathrm{II,OE}} = 1.15 \,\mathrm{eV}$ , (c)  $\Delta W_{\mathrm{A}} = 1.0 \,\mathrm{eV}$ , (d)  $\mu_{\mathrm{n}0} = 3 \cdot 10^{-6} \,\mathrm{m}^2/(\mathrm{Vs})$ , (e)  $R_{\mathrm{th,eff,Forming}} = 1 \cdot 10^6 \,\mathrm{K/W}$ , and (f)  $r_{\mathrm{fil}} = 10 \,\mathrm{nm}$ .

curves for  $\Delta G_{\text{II.OE}} = 1.15 \,\text{eV}$  show a noticeable ripple, see Fig. 5.5b. Their origin is explained below in Fig. 5.6. A lower ion hopping barrier in the filament  $\Delta W_{\rm A}$  decreases the forming voltage as the vacancies, which are generated in the plug, drift and diffuse faster into the disc, thereby decreasing the interface resistance at the AE (reference fit:  $\Delta W_{\rm A} = 0.9 \, {\rm eV}$ ). The opposite holds for a higher  $\Delta W_{\rm A}$  of 1 eV, see Fig. 5.5c, which leads to a very steep dependence of the forming voltage on the oxide thickness. For the chosen parameter set, the decrease of the nominal barrier at the OE interface by 0.2 eV down to 0.1 eV nearly has no influence. This signifies that the voltage drop across this interface is so small in the reference simulation that it has a negligible effect on the oxygen exchange. The I-V curves for an electron mobility of  $\mu_{n0} = 3 \cdot 10^{-6} \,\mathrm{m}^2/(\mathrm{Vs})$  (reference fit:  $\mu_{n0} = 5 \cdot 10^{-5} \,\mathrm{m}^2/(\mathrm{Vs})$  are shown in Fig. 5.5d. The kinks in the forming curves for  $l_{\text{cell}} = 3 \text{ nm}$  and 5 nm explain why the dependence of the forming voltage on the thickness is not a straight line in Fig. 5.5a. The origin of the kinks is analyzed below in Fig. 5.6. For  $l_{\rm cell} \geq 7.5\,{\rm nm},$  the change in electron mobility by more than one magnitude has nearly no influence on the forming behavior. This underlines the little impact which disc and plug resistance have on the total resistance in the pristine state. A smaller effective thermal resistance  $R_{\rm th,eff,Forming}$  (reference fit:  $R_{\rm th,eff,Forming} = 5 \cdot 10^7 \, {\rm K/W}$ ) slows down the self-acceleration of the forming process and impedes a thermal runaway. Therefore, the characteristic abrupt current jumps do not occur, see Fig. 5.5e. This has however little effect on the voltage at which the current reaches 1 µA; thus, the forming voltage increases only slightly. The filament radius defines the volume of the plug and the disc: the smaller the volume (radius), the higher the concentration for a certain amount of vacancies. As a result, the current is significantly higher in the pristine state for  $r_{\rm fil} = 10 \, \rm nm$  (reference fit:  $r_{\rm fil} = 30 \, \rm nm$ ), see Fig. 5.5f. Consequently, the thermal runaway sets in at a lower voltage and the forming voltage decreases.

The forming simulations with  $\Delta G_{\rm II,OE} = 1.15\,\mathrm{eV}$  (Fig. 5.5b) and the simulations with  $\mu_{\rm n0} = 3\cdot 10^{-6}\,\mathrm{m}^2/(\mathrm{Vs})$  for small oxide thicknesses (Fig. 5.5d) both show ripples or kinks in the I-V curves. These are the result of the change in the filament "growth direction", which can be extracted of the vacancy concentration transients. For the example of the clearly visible kink ( $\mu_{\rm n0} = 3\cdot 10^{-6}\,\mathrm{m}^2/(\mathrm{Vs})$ ,  $l_{\rm cell} = 3\,\mathrm{nm}$ ), the vacancy concentration of the plug and the disc and the resistances of all elements are plotted in Fig. 5.6a and b, respectively. At first, the vacancy concentration in the plug is higher than in the disc. Then, the concentration in the disc increases above the plug concentration while the latter decreases due to the migration of vacancies from the plug into the disc. From this point on, the plug resistance is higher than the interface resistance  $R_{\rm Schottky,AE}$ .

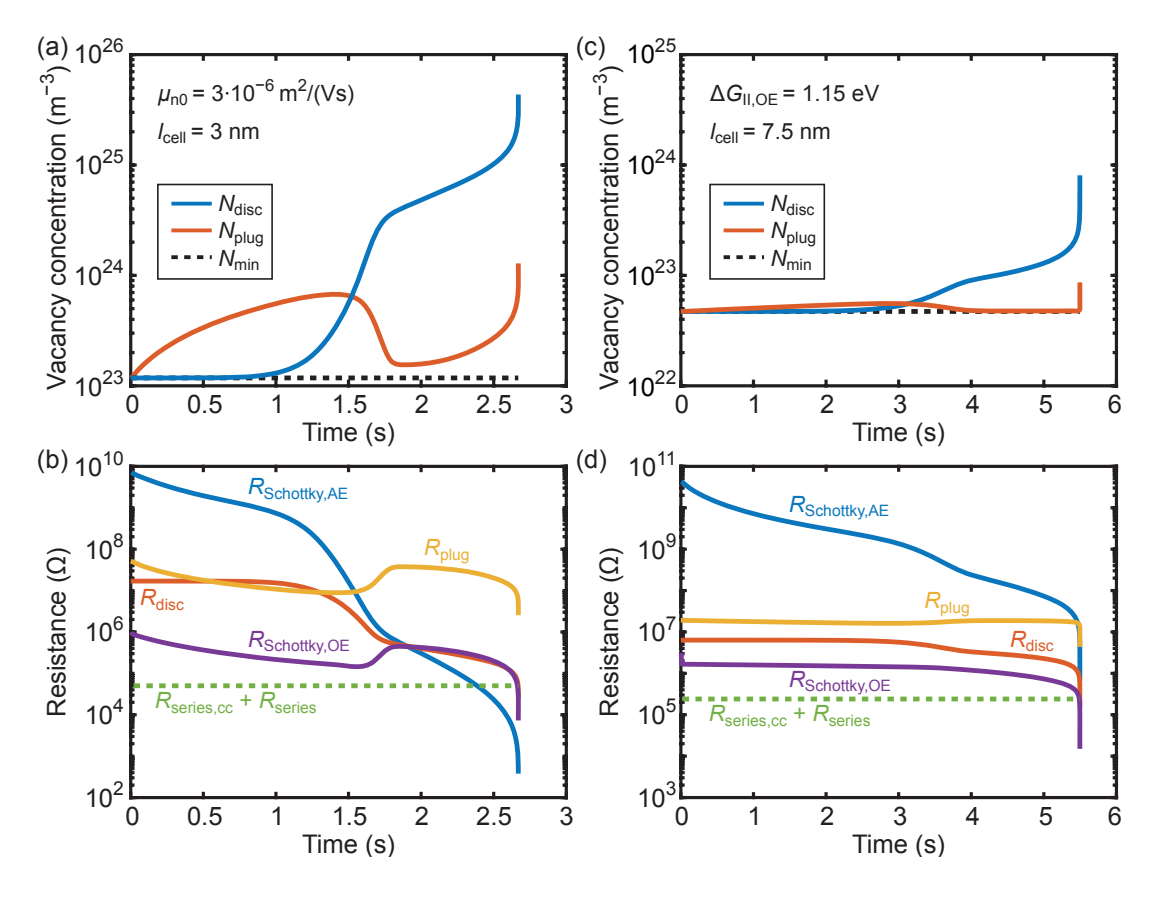


Figure 5.6: Filament "growth direction" changing during forming. Oxygen vacancy concentration and resistance transients for two parameter combinations shown in Fig. 5.5 are displayed for  $\mu_{\rm n0} = 3 \cdot 10^{-6} \, {\rm m}^2/({\rm Vs})$ ,  $l_{\rm cell} = 3 \, {\rm nm}$  in (a) and (b), and for  $\Delta G_{\rm II,OE} = 1.15 \, {\rm eV}$ ,  $l_{\rm cell} = 7.5 \, {\rm nm}$  in (c) and (d), respectively.

Compared to Fig. 5.3e, disc and plug resistance are considerably higher due to the lower electron mobility. Once  $R_{\rm plug}$  becomes the dominating resistance, the positive feedback between current increase and vacancy generation is stopped for the moment as the resistance is not decreasing but increasing due to the shift of vacancies from the plug to the disc. As soon as the concentration in the plug rises again, the positive feedback is reestablished leading to a thermal runaway. The ripple in the simulation with  $\Delta G_{\rm II,OE} = 1.15\,{\rm eV}$  can be explained analogously, see Fig. 5.6c and d. The small increase in  $R_{\rm plug}$  upon the decreasing vacancy concentration in the plug slightly slows down the total resistance decrease, which is visible in the I-V curve as change in slope. In general, a filament growth from the cathode to anode, i.e. from the disc to the plug, signifies that the exchange of oxygen is rate limiting compared to the fast migration of vacancies in the filament: The vacancies, which are generated at the anode, do not accumulate at the anode but migrate to the cathode and pile up there. This growth direction is

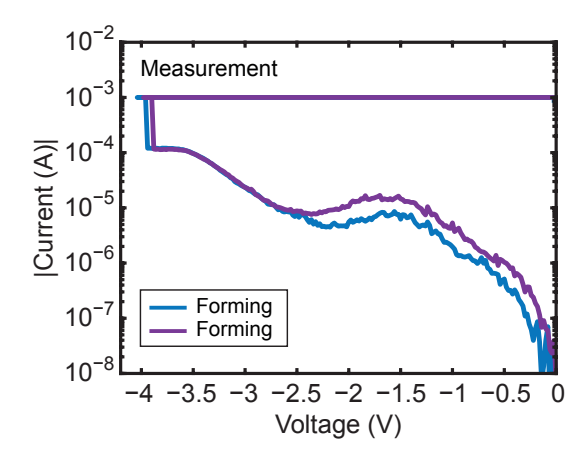


Figure 5.7: Experimental observation of a bump in I-V forming characteristics. The forming curves of two symmetric  $Pt/ZrO_x/Pt$  devices were provided by Andreas Kindsmüller [164].

also known as formation and propagation of a 'virtual cathode' [8]. Compared to the simulation with  $\Delta G_{\rm II,OE} = 1.05 \, {\rm eV}$  (Fig. 5.3b), the higher barrier of  $\Delta G_{\rm II,OE} = 1.15 \, {\rm eV}$  causes the oxygen exchange to be the rate-limiting step resulting in a filament growth from the disc to the plug (Fig. 5.6c).

Measured I-V forming characteristics do not always show a monotonically increasing current, ripples or bumps can be observed as well. Figure 5.7 displays two examples taken from  $(50 \times 50) \, \mu m^2$  symmetric devices consisting of  $30 \, \mathrm{nm} \, \mathrm{Pt} / 5 \, \mathrm{nm} \, \mathrm{ZrO_x} / 30 \, \mathrm{nm} \, \mathrm{Pt}$ . The voltage is defined as being applied to the Pt bottom electrode, while the top electrode is grounded. Fabrication and measurement were performed by Andreas Kindsmüller. The  $\mathrm{ZrO_x}$ -based devices with two Pt electrodes differ from the  $\mathrm{ZrO_x}$ -based devices with one Ta electrode regarding the forming behavior and current level, cp. Figs. 5.8a and 5.9a. The forming voltage and the current level at the inset of the abrupt forming event are significantly higher for the symmetric device stack. Between  $-1.5 \, \mathrm{V}$  and  $-2.5 \, \mathrm{V}$ , the current decreases, see Fig. 5.7, so that a bump develops at a current level of roughly  $10 \, \mu \mathrm{A}$ . Without an extensive study comprising electrical and spectroscopic characterization, a physical explanation for the experimentally observed bumps cannot be presented. A change in the filament growth direction due to a change of the rate-limiting process, like in the simulation in Fig. 5.6, presents at least a possible explanation.

# 5.3.2 Forming and Subsequent Sweeps

It was shown in the previous section that the model can be used to describe the dependence of the forming voltage on the oxide thickness in good agreement with experimental data. Besides forming, a convincing model needs to cover forming and subsequent

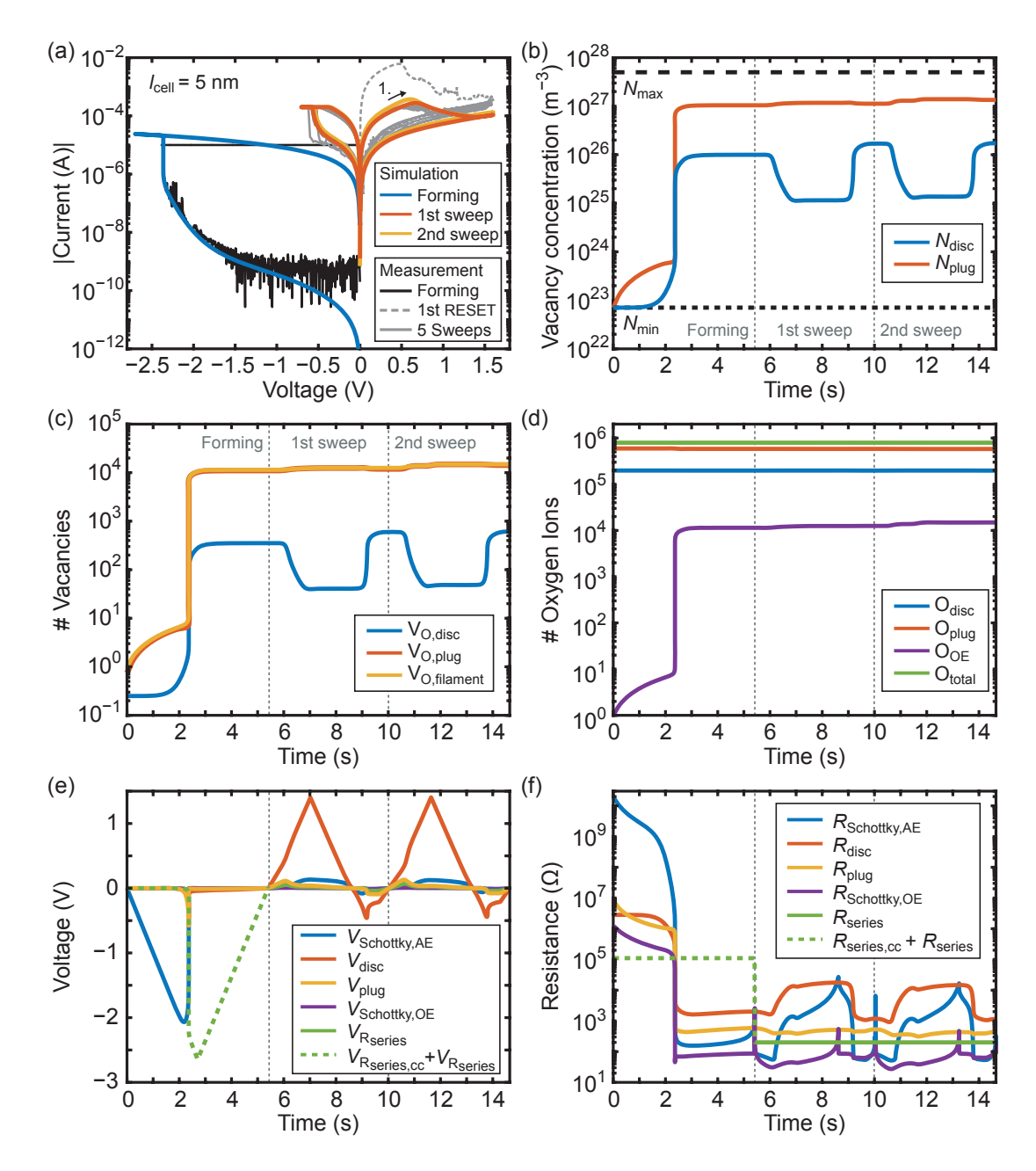


Figure 5.8: Forming and subsequent switching compared to experimental data. The parameters for the simulation are taken from Table 5.1 with  $\nu_0 = 4 \cdot 10^{12} \,\mathrm{Hz}$  and  $R_{\mathrm{series,cc}} = 110 \,\mathrm{k}\Omega$ . The same parameter set is used for forming and switching sweeps except for the effective thermal resistance and an additional series resistance during forming. The simulation is compared to experimental data of a Pt/5 nm ZrO<sub>x</sub>/Ta device measured by Andreas Kindsmüller [164]. The current resolution of the experimental setup is around 1 nA. (a) I-V curves. (b) Oxygen vacancy concentration of the disc and the plug. (c) Number of oxygen vacancies in the disc and the plug and the sum of both. The total number of vacancies in the filament increases during forming and is nearly constant during switching. (d) Number of oxygen ions in disc, plug, OE, and the total number in the system. The number of oxygen in the OE increases during forming and is nearly constant during switching. (e) Voltages across all lumped circuit elements.

switching with a physically reasonable parameter set. Compact model 2.0 does fulfill this requirement, as shown exemplary for  $l_{\text{cell}} = 5 \,\text{nm}$  in Fig. 5.8a. The parameters are taken from Table 5.1 ( $\nu_0 = 4 \cdot 10^{12} \,\mathrm{Hz}$ ,  $R_{\mathrm{series,cc}} = 110 \,\mathrm{k}\Omega$ ). Only the effective thermal resistance and the additional series resistance  $R_{\text{series.cc}}$  to limit the current during forming differ between forming and switching sweeps. The changed thermal resistance takes into account the different conditions in pristine and formed devices concerning the heat dissipation. The measured I-V curves in Fig. 5.8a are taken from one of the 25  $\rm ZrO_x$ -based devices with an oxide length of 5 nm, which were studied for the forming statistics in Fig. 5.4b and whose composition is explained in section 5.3.1. This particular forming curve can be fitted well with  $\nu_0 = 4 \cdot 10^{12} \, \text{Hz}$ , whereas the overall fit over all lengths is better with  $\nu_0 = 2 \cdot 10^{12} \, \text{Hz}$ . Therefore, only simulations that refer to a cell length of 5 nm are performed with  $\nu_0 = 4 \cdot 10^{12}$  Hz. The attempt frequency  $\nu_0$  is a prefactor in the equation for the ionic current  $I_{\text{ion}}$ , see Eqs. (5.27) and (5.28). If  $\nu_0$  is chosen higher, the ionic current increases and thus, the forming sets in earlier. As the exact values for the attempt frequency and nearly all other material parameters in the fabricated devices are unknown (except for the oxide thickness), the parameters are chosen within physically reasonable limits to fit the measured data.

In the measurement, only an external current compliance by the measurement unit of  $10\,\mu\mathrm{A}$  is applied during forming. It is well known that these kind of current compliances only react with a significant delay so that the real maximum current during forming is unknown. The very high current in the first RESET is an indication that the maximum forming current was pretty high. The subsequent sweeps are stable but the HRS is comparatively low resistive. Moreover, the HRS is asymmetric as the HRS current after the RESET is higher than the HRS current before the SET at the same voltage level. Previous results on  $\mathrm{ZrO}_x$ -based devices that have been fabricated similarly have shown that the HRS current before the SET is the stable one whereas the HRS current after the RESET is excited volatily, see Appendix A.3 [167]. The model does not consider this kind of excitation so that the parameters were fitted to match the HRS branch before the SET.

Analogous to the experiment, a current compliance of  $200\,\mu\mathrm{A}$  is applied during the SET and the same sweep voltage settings are used. The simulation comprises one forming sweep and two subsequent switching sweeps. After the forming, the device is in the LRS so that the switching sweeps start with the RESET. In contrast to the measurement, the first RESET does not show a higher current than the following sweep, in fact, the current is even slightly lower. The oxygen vacancy concentrations, the total number of

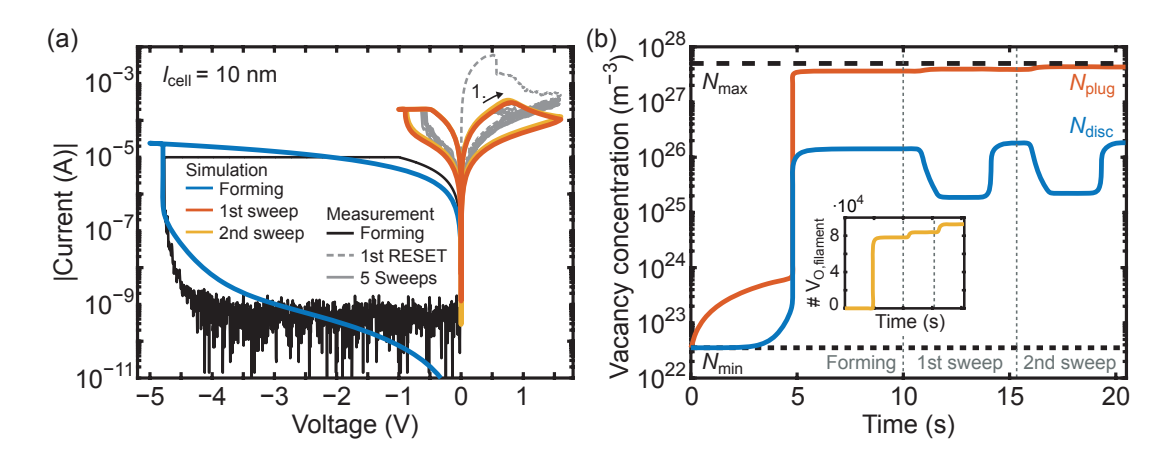


Figure 5.9: Comparison of simulated and measured forming and subsequent switching of a Pt/10 nm ZrO<sub>x</sub>/Ta cell. The measurement was performed by Andreas Kindsmüller. The experimental forming curve was obtained with a  $100 \,\mathrm{k}\Omega$  resistance in series, all subsequent switching curves were measured without additional series resistance [164]. For the simulation, the parameters in Table 5.1 with  $\nu_0 = 2 \cdot 10^{12} \,\mathrm{Hz}$  and  $R_{\mathrm{series,cc}} = 205 \,\mathrm{k}\Omega$  are used. (a) I-V curves. (b) Oxygen vacancy concentration of the disc and the plug. The inset shows the total number of vacancies in the filament.

vacancies, the total number of oxygen ions, all single voltage drops, and the resistances of all elements are given in Fig. 5.8b-f, respectively. The results demonstrate that the amount of vacancies increases by several orders of magnitude during forming whereas it changes only slightly during the switching sweeps. The vacancy concentration in the plug is considerably higher than in the disc for both LRS and HRS, as it is typical for c8w bipolar switching. Consequently, the disc resistance dominates the overall resistance in both LRS and HRS. The resistance of the Schottky barrier  $R_{\rm Schottky,AE}$ , which is most important during forming, is only relevant at low voltages. Of course, this is a result of the parameter choice for  $e\phi_{\rm Bn0,AE}$  and others.

The experimental I-V sweep data of the  $\rm ZrO_x$ -based devices presents an interesting feature: the characteristics of the switching sweeps — including HRS and LRS current level, SET and RESET voltage — do not depend on the oxide thickness, only the forming voltages differ. An example of the forming and subsequent sweeps of a device with 10 nm thick  $\rm ZrO_x$  layer is given in Fig. 5.9a. In fact, the measured HRS current level of this sample with 10 nm thick oxide is slightly more conductive than of the shown 5 nm thick example. The experimental forming sweep was measured with an additional series resistance of  $100~\rm k\Omega$ , whereas in the simulation  $R_{\rm series,cc}=205~\rm k\Omega$  was used. Remarkably, the first measured RESET shows the same high current as for the measurement of the 5 nm thick oxide although the current is limited effectively during forming. Except for  $\nu_0$ 

(and of course  $l_{\rm cell}$ ,  $l_{\rm disc}$ , and  $l_{\rm plug}$ ), the same parameters are used as in the simulation of the device with an oxide thickness of 5 nm. The simulation results of the switching sweeps fit less well to the experimental data as the SET voltages differ and the simulated HRS current is lower than the measured one, see Fig. 5.9a. Nevertheless, it is a remarkable result that only the cell length in the parameter set has to be adjusted to be applicable for the simulation of devices with varying oxide thicknesses. (For  $\nu_0 = 2 \cdot 10^{12} \, \mathrm{Hz}$ , the forming voltage of the 5 nm simulation increases by less than 0.2 V, still presenting a good fit to the forming curve.) The oxygen vacancy concentration of the plug and the disc are shown in Fig. 5.9b with the total number of vacancies in the filament as inset. For the given parameter set, the current compliance in the forming simulation ( $R_{\rm series,cc} = 205 \, \mathrm{k}\Omega$ ) is chosen in order to allow the best fit of the first two switching sweeps to the experimental data. This results, however, in a vacancy concentration in the plug after forming that is pretty close to the maximum concentration.

To describe the measured dependence of the forming voltage on the oxide thickness, it is crucial that both the disc and the plug length scale with the cell length instead of only the plug length. The higher disc length for  $l_{\rm cell}=10\,\mathrm{nm}$ , however, leads to a higher SET voltage as the driving electric field for the ion migration in the SET is lower, see Eq. (5.33). To match the experimental data of nearly identical SET voltages for different oxide thicknesses, the disc lengths would need to be equal. Thus, the two requirements for the disc length are contradicting. As a result, the model cannot describe both the similar SET voltages for different oxide thicknesses and the distinct dependence of the forming voltage on the oxide thickness, as long as the disc length is identical for forming and switching sweeps.

### 5.3.3 Endurance and Retention

#### **Endurance (Sweeps)**

An explicit drawback of the chosen parameter set used in sections 5.3.1 and 5.3.2 is shown in Fig. 5.9b and Fig. 5.8c: the number of vacancies during switching is not constant but increases constantly over cycling. Sooner or later, this leads to a RESET failure and the device is 'stuck in the LRS'. Thereby, 'stuck in the LRS' describes a very low resistive state in which the vacancy concentration of both plug and disc equals the maximum concentration. This kind of failure can be produced very easily, two examples are shown in Fig. 5.10. In Fig. 5.10a, the I-V curves of the forming and the subsequent switching sweep are given for a smaller compliance resistance during forming ( $R_{\rm series,cc} = 80 \,\mathrm{k}\Omega$ ).

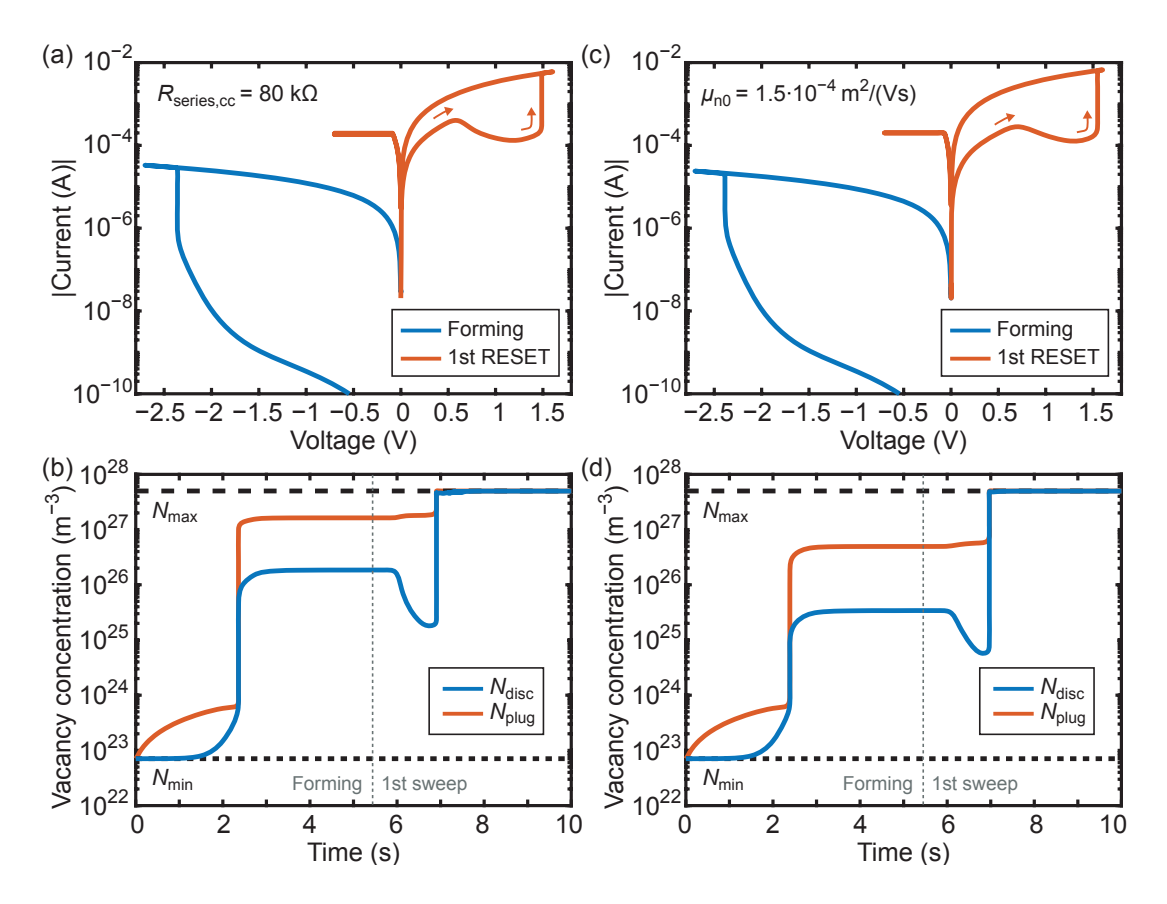


Figure 5.10: RESET failure after forming. The parameters are taken from Table 5.1 ( $l_{\text{cell}} = 5 \text{ nm}$ ,  $\nu_0 = 4 \cdot 10^{12} \text{ Hz}$ ) with exception of the parameter being varied. For  $R_{\text{series,cc}} = 80 \text{ k}\Omega$  and  $\mu_{\text{n0}} = 1.5 \cdot 10^{-4} \text{ m}^2/(\text{Vs})$  ( $R_{\text{series,cc}} = 110 \text{ k}\Omega$ ), I-V curves of the forming and the subsequent sweep showing a RESET failure are presented in (a) and (c), respectively. The corresponding transients of the oxygen vacancy concentrations in the plug and the disc are given in (b) and (d), respectively.

As can be seen from the oxygen vacancy concentrations of the plug and the disc in Fig. 5.10b, both concentrations are higher after the forming process compared to the simulation with  $R_{\rm series,cc}=110\,\mathrm{k}\Omega$  in Fig. 5.8b. The RESET failure occurs suddenly at the end of the first RESET in form of a current jump. Oxygen vacancies are generated at the OE/plug interface until the maximum limit defined by the parameters is reached. As usual, it is not solely the compliance resistance that creates the conditions for a RESET failure but a complex interplay between the parameters. Another example of a RESET failure occurs for a higher electron mobility (with  $R_{\rm series,cc}=110\,\mathrm{k}\Omega$ ), see Fig. 5.10c and the corresponding vacancy concentrations in Fig. 5.10d. The abruptness of the current jump indicates a thermal runaway: the more vacancies are generated, thereby reducing the dominant disc resistance, the higher the current is. This increases the temperature,

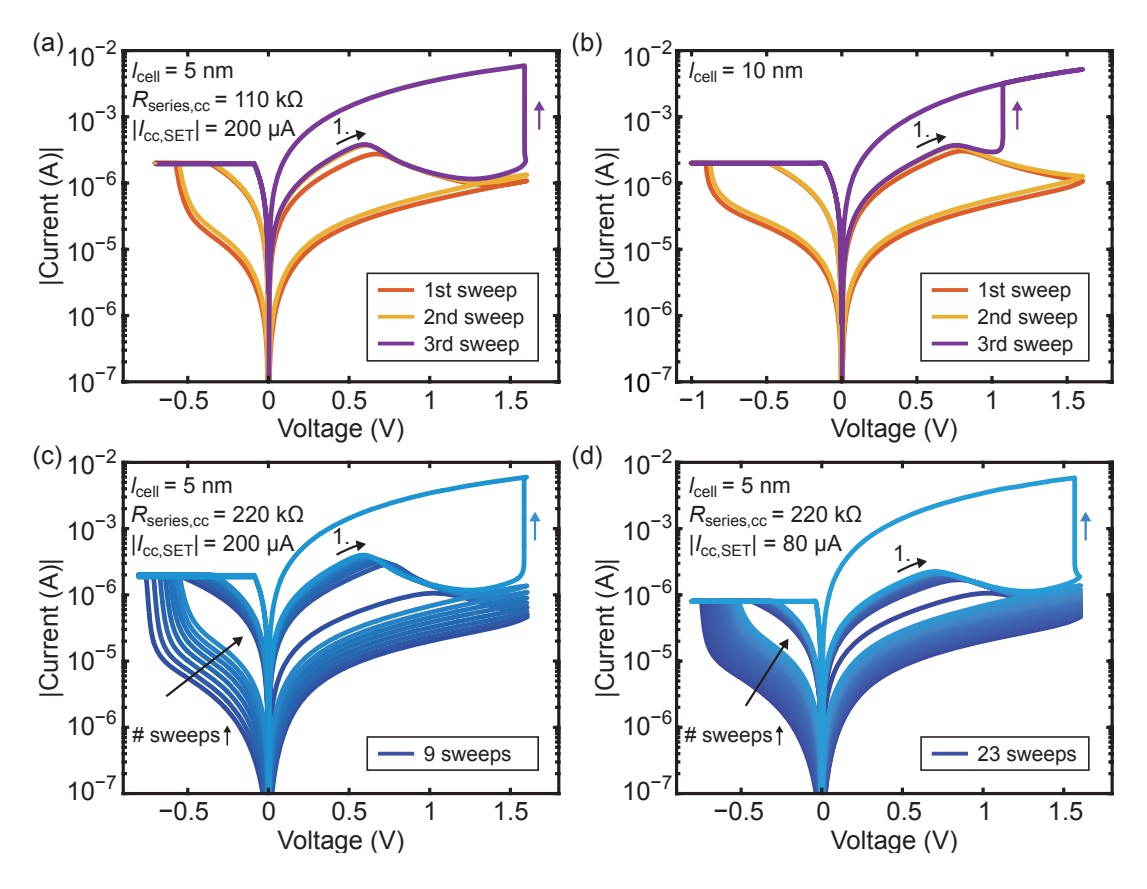


Figure 5.11: Endurance failure and its dependence on forming and SET conditions. The parameter sets that were used in Figs. 5.8 and 5.9 to fit the simulation to devices with a 5 nm and a 10 nm thick  $\rm ZrO_x$ -layer lead to a very low endurance; a RESET failure occurs in the third sweep after forming. (*I–V* forming curves are not shown.) (a) Standard parameter of the 5 nm cell as in Fig. 5.8. (b) Standard parameter of the 10 nm cell as in Fig. 5.9. The occurrence of the RESET failure can be delayed if the forming is performed with a higher  $R_{\rm series,cc}$ , as in (c)  $R_{\rm series,cc} = 220 \,\rm k\Omega$ . A lower current compliance during SET increases the endurance further, as in (d)  $|I_{\rm cc}| = 80 \,\mu\rm A$ .

and in turn, the generation of more vacancies is favored. In addition, the temperatures at the onset of the sudden current jumps are equal (not shown).

The RESET failures for the parameter sets used in Fig. 5.8 and Fig. 5.9 also occur pretty soon, namely in the third switching sweep, see Fig. 5.11a and b. This underlines the difficulties of finding a parameter set that provides a good fit to experimental data comprising first, the dependence of the forming voltage on the oxide thickness, second, the I-V switching sweeps, and third, the endurance. The current compliance during forming and SET has a high impact on the endurance because a RESET failures occurs if the LRS is too low resistive after too many vacancies have been generated at the interface. The lower the current compliance, or the higher the additional series resistance

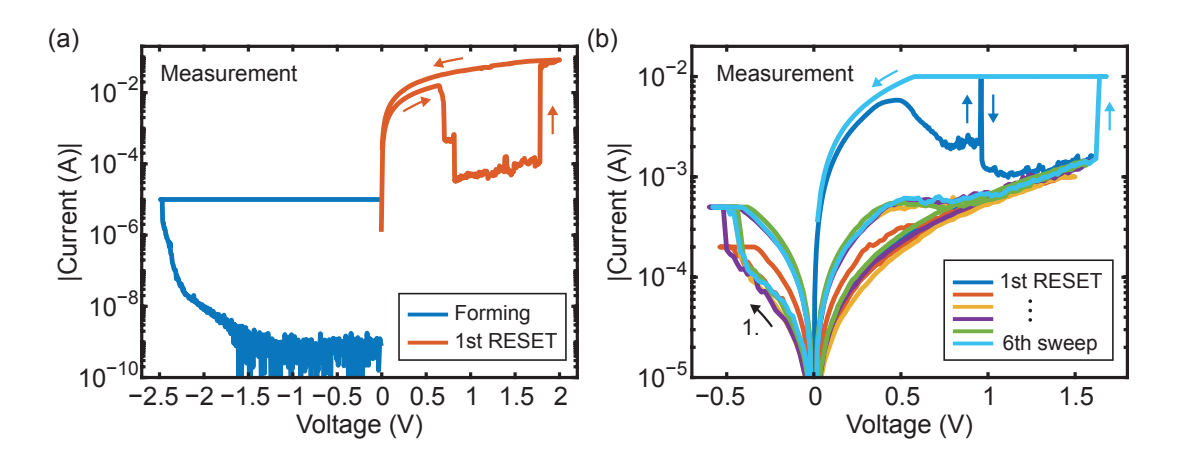


Figure 5.12: Experimental observation of RESET failures in  $\rm ZrO_x$ -based devices. The exemplary  $\it I-V$  data were provided by Andreas Kindsmüller [164]. (a) RESET failure in the first RESET after forming in a  $\rm Pt/ZrO_x/Ta/Pt$  device. (b) A RESET failure occurs after several successful switching sweeps in a  $\rm Pt/ZrO_x/Hf/Pt$  device. The first RESET shows a high current spike.

during forming  $R_{\rm series,cc}$ , the less vacancies are generated during forming and SET. By increasing  $R_{\rm series,cc}$  by a factor of two, the occurrence of the RESET failure can be postponed to the 9th sweep after forming, see Fig. 5.11c. Decreasing the current compliance during the SET from  $|I_{\rm cc}|=200\,\mu{\rm A}$  to  $|I_{\rm cc}|=80\,\mu{\rm A}$  further delays the appearance of the RESET failure, see Fig. 5.11d. Naturally, the endurance can comprise a much higher number of cycles if the parameters are chosen appropriately. Therefore, endurance simulations can help to improve future devices by finding appropriate voltage and current compliance settings.

RESET failures that occur in sweep measurements show a certain resemblance with the simulated ones, see the experimental data in Fig. 5.12 in comparison to the simulation results in Figs. 5.10a,c and 5.11. Like in the simulation, the failure can develop already during the first RESET after forming (Fig. 5.12a) or after several successful sweeps (Fig. 5.12b). The exemplary I-V characteristics were measured by Andreas Kindsmüller on  $(50\times50)~\mu\text{m}^2$  devices consisting of 30~nm Pt/5 nm ZrO<sub>x</sub>/20 nm Ta/30 nm Pt (Fig. 5.12a) and 30~nm Pt/5 nm ZrO<sub>x</sub>/20 nm Hf/30 nm Pt (Fig. 5.12b). The voltage is defined as being applied to the Pt bottom electrode, while the top electrode is grounded. The first RESET exhibits, like all other ZrO<sub>x</sub>-based devices shown in this chapter, a considerably higher current than the subsequent switching sweeps. The first RESET in Fig. 5.12b shows a short, high current spike, which looks like a RESET failure that quickly recovered. A resistance decrease proceeds the current spike. After the spike, the cell has a higher resistance than before. It is quite possible that the measured RESET failures

can be attributed to a generation of vacancies at one or both electrodes. In contrast to the simulation results in Figs. 5.10 and 5.11, which are obtained with a model that only allows an oxygen exchange at the OE, the generation could have taken place at the AE as well. The polarity of the applied voltage favors a generation at the AE (Pt) during the RESET; however, the oxygen affinity of the tantalum/hafnium top electrode is higher.

#### **Endurance (Pulses)**

Analogous to experiments, endurance tests can be performed by applying SET and RESET pulses. To study the exclusive influence of the oxygen exchange parameters on the endurance, forming is not considered. The initial vacancy concentrations for the plug and the disc are chosen to represent a formed device in an HRS. Assuming that a forming at the OE took place before, the initial number of oxygen ions in the OE equals the initial number of vacancies in the filament. First, a -2.0 V SET pulse of 10  $\mu$ s length is applied and the written LRS is recorded in a subsequent  $10 \,\mu s$ ,  $-0.2 \,V$  READ pulse. Another READ pulse to obtain the HRS is applied after a 100 µs RESET pulse at 3.8 V. The rise (and fall) time of all pulses is 100 ns and the pause between the pulses is  $10 \mu s$ . One cycle comprises one pulse sequence of SET-READ-RESET-READ. The parameters for the pulsed endurance simulations are given in Table 5.2. To keep the simulation time low, the parameters are chosen such that an effect is visible within 200 cycles. In Fig. 5.13ac,  $\Delta G_{\text{I,OE}}$  (the barrier for oxygen ions in the OE to get into the plug) is higher than  $\Delta G_{\text{ILOE}}$ . Thus, the generation of vacancies at the OE/plug interface is favored over time, see Fig. 5.13b. The steady increase is noticeable in a decreasing LRS resistance, see Fig. 5.13a. Both the vacancy concentration in the plug and the disc rise due to the additional vacancies, see Fig. 5.13c. First, the vacancy concentration in the disc is below the concentration in the plug in the LRS. After around 50 cycles, the concentration in the disc rises above the one in the plug in the LRS. Both during SET and RESET vacancies are generated, but as shown in the inset in Fig. 5.13b, the increase is higher during the RESET. This is counterintuitive at first sight as  $V_{\text{Schottky,OE}}$  is negative during the RESET and thus, the voltage impedes the transfer of an oxygen ion from the plug to the OE. For the given parameter set, however, the voltage drop across both interfaces is low; during the RESET  $V_{\text{Schottkv,OE}}$  is lower than [50 mV]. Consequently, the voltage has only a minor influence on the vacancy generation. It is the temperature that is crucial. At the beginning of the RESET pulse, the cell is in the LRS and, due to the high pulse voltage, the current is highest. Therefore, the temperature is highest during the RESET pulse

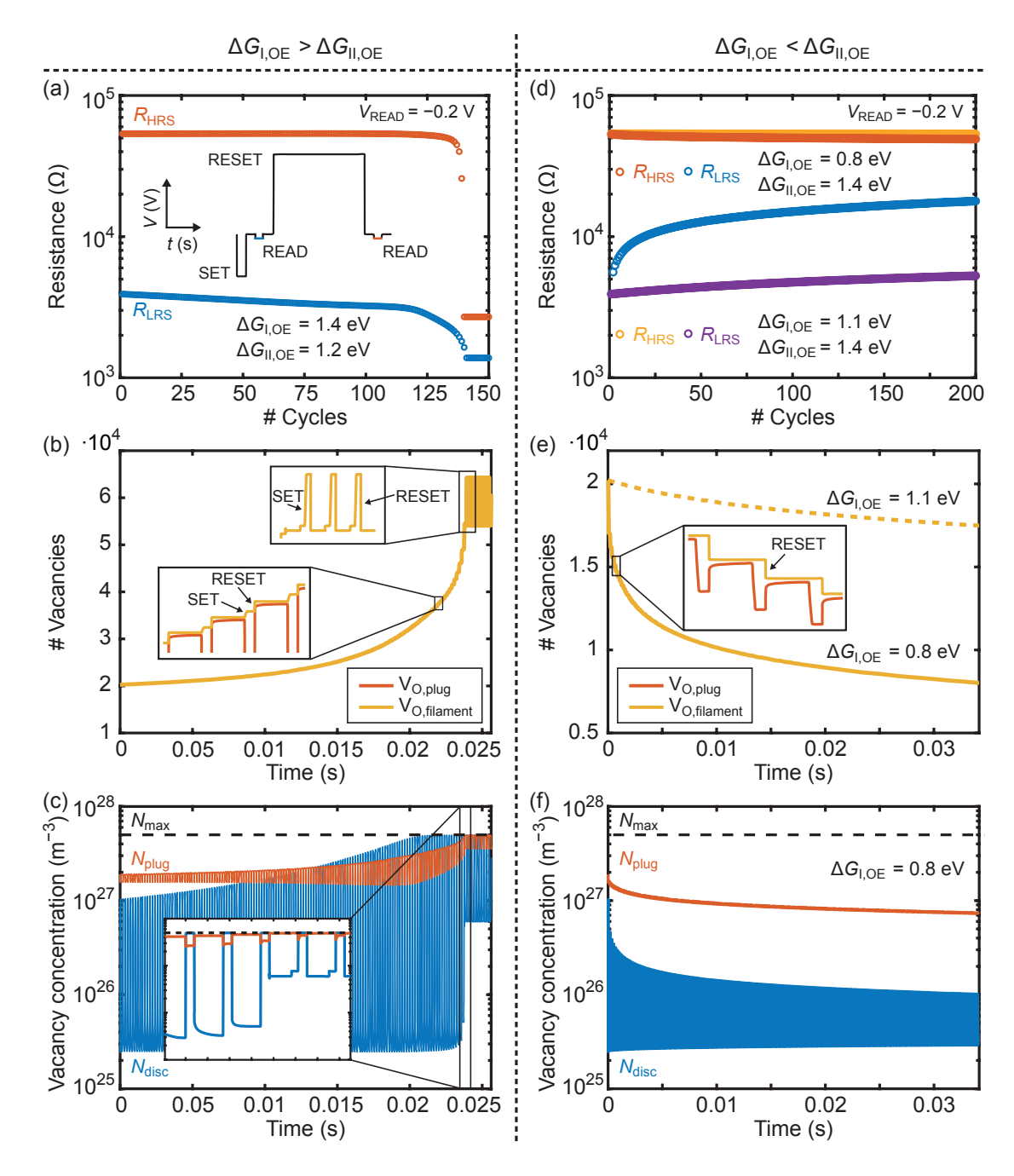


Figure 5.13: Dependence of the endurance on the oxygen exchange barrier at the OE. The simulation parameters including the pulse settings are given in Table 5.2. SET and RESET pulses are applied alternately and the resistance is obtained via READ pulses in between. The pulse sequence is shown in the inset in (a). Two fundamental cases are distinguished: In (a)-(c), the choice of  $\Delta G_{\rm I,OE} > \Delta G_{\rm II,OE}$  leads to an increase of vacancies in the filament with a subsequent loss of the HRS. In contrast, the number of vacancies decreases for  $\Delta G_{\rm I,OE} < \Delta G_{\rm II,OE}$  in (d)-(f), which results in a loss of the LRS. In (d) and (e), two parameter sets are compared. (a), (d) HRS and LRS resistance at  $-0.2\,\rm V$ . (b), (e) Total number of oxygen vacancies in the filament. (c), (f) Vacancy concentration in the plug and the disc and the maximum limit.

**Table 5.2:** Parameters for the endurance simulations in Figs. 5.13 and 5.14.

Symbol	Value	Symbol	Value		
$egin{aligned} l_{ m cell} \ l_{ m disc} \ l_{ m plug} \ r_{ m fil} \ z_{ m Vo} \ z_{ m O} \ a \  onumber \ \Delta W_{ m A} \ m_{ m eff} \ A^* \ arepsilon \end{array}$	$5  \mathrm{nm}$ $1.25  \mathrm{nm}$ $l_{\mathrm{cell}} - l_{\mathrm{disc}}$ $30  \mathrm{nm}$ $2$ $-2$ $0.3  \mathrm{nm}$ $4 \cdot 10^{12}  \mathrm{Hz}$ $0.8  \mathrm{eV}$ $m_{\mathrm{e}}$ see Eq. (2.4) $17  \varepsilon_0$	$e\phi_{ m Bn0,AE}$ $e\phi_{ m Bn0,OE}$ $\Delta E_{ m ac}$ $\mu_{ m n0}$ $N_{ m O,oxide,max}$ $N_{ m min}$ $N_{ m disc,initial}$ $N_{ m plug,initial}$ $R_{ m th,eff}$ $R_{ m series}$ $T_0$	$\begin{array}{c} 0.4\mathrm{eV} \\ 0.1\mathrm{eV} \\ 0.05\mathrm{eV} \\ 8\cdot 10^{-6}\mathrm{m}^2/(\mathrm{Vs}) \\ 5.6\cdot 10^{28}\mathrm{m}^{-3} \\ 5\cdot 10^{27}\mathrm{m}^{-3} \\ 1/\left(A\cdot l_{\mathrm{cell}}\right) \\ 2.4\cdot 10^{25}\mathrm{m}^{-3} \\ 1.9\cdot 10^{27}\mathrm{m}^{-3} \\ 1\cdot 10^{5}\mathrm{K/W} \\ 200\Omega \\ 293\mathrm{K} \end{array}$		
$\frac{\varepsilon_{\phi_{\rm B}}}{\text{Pulse setting}}$ $V_{\rm pulse, SET}$	-2.0 V	$t_{ m pulse,SET}$	10 μs		
$V_{ m pulse,RESET}$ $V_{ m pulse,READ}$	3.8 V -0.2 V	$t_{ m pulse,RESET}$ $t_{ m pulse,READ}$ $t_{ m pulse,rise\ time}$	100 μs 10 μs 100 ns		
Parameters for the oxygen exchange at the OE in Fig. 5.13					
$l_{ m OE,eff}$ $lpha_{ m OE}$ $N_{ m O,OE,min}$ $N_{ m O,OE,initial}$ $[{ m V}_{ m O,init}=A$	$egin{array}{l} 1 \ \mathrm{nm} \\ 0.5 \\ 1/\left(A \cdot l_{\mathrm{OE,eff}} ight) \\ \mathrm{V_{O,init}}/\left(A \cdot l_{\mathrm{OE,eff}} ight) \\ \left(N_{\mathrm{disc,initial}} \cdot l_{\mathrm{disc}} + N_{\mathrm{plug,initial}}  ight) \end{array}$	$k_{ m I,OE}^0 \ k_{ m II,OE}^0 \ \Delta G_{ m I,OE} \ \Delta G_{ m I,OE} \ \Delta l_{ m II,OE} \ l_{ m plug} $	$\begin{array}{c} 1 \cdot 10^{3}  \mathrm{m/s} \\ 1 \cdot 10^{3}  \mathrm{m/s} \\ 1.4  \mathrm{eV/1.1}  \mathrm{eV/0.8}  \mathrm{eV} \\ 1.2  \mathrm{eV/1.4}  \mathrm{eV/1.4}  \mathrm{eV} \end{array}$		
Parameters	for the oxygen exchange a	at the AE in I	Fig. 5.14		
$l_{ ext{AE,eff}}$ $lpha_{ ext{AE}}$ $N_{ ext{O,AE,min}}$ $N_{ ext{O,AE,initial}}$	$egin{array}{l} 1 \ { m nm} \\ 0.5 \\ 1/\left(A \cdot l_{ m AE,eff} ight) \\ 1/\left(A \cdot l_{ m AE,eff} ight) \end{array}$	$k_{ m I,AE}^0 \ k_{ m II,AE}^0 \ \Delta G_{ m I,AE} \ \Delta G_{ m II,AE}$	$1 \cdot 10^{3} \mathrm{m/s}$ $1 \cdot 10^{3} \mathrm{m/s}$ $1.4 \mathrm{eV}$ $1.2 \mathrm{eV}$		

and more vacancies are generated. The increase in vacancies is not constant but proceeds exponentially due to a positive feedback. The more vacancies are generated, the more conductive the LRS becomes. The higher the current, the higher the temperature rises. At some point, an abrupt RESET failure occurs and the resistance after the RESET pulse is not high resistive anymore but low resistive. The occurrence is linked to the moment when the vacancy concentration in the plug cannot increase anymore because it is limited by the maximum vacancy concentration  $N_{\text{max}}$ , see the inset in Fig. 5.13c. During a successful RESET, vacancies drift from the disc to the plug. This migration and thereby the resistance increase stops immediately upon  $N_{\text{plug}}$  reaching  $N_{\text{max}}$ . Before the RESET failure, the resistance degradation is accelerated further when  $N_{\rm disc}$  reaches  $N_{\rm max}$  during the SET. From this point on, the vacancy concentration in the plug starts to increase considerably. After the RESET failure, the cell switches constantly between two low resistive states; the cell is 'stuck in the LRS'. The resistance that is read after application of the RESET pulse is still higher than the one read after application of the SET pulse. This results from the different amount of vacancies in the filament, which increases slightly during SET and decreases during RESET, see the inset in Fig. 5.13b.

In Fig. 5.13d-f,  $\Delta G_{\text{I,OE}}$  (the barrier for oxygen ions in the OE to get into the plug) is lower than  $\Delta G_{\text{II,OE}}$ . Thus, the annihilation of vacancies at the OE/plug interface is favored over time, see Fig. 5.13e. The resistance and the vacancy evolution are shown for two  $\Delta G_{\text{I,OE}}$  values to highlight the trend: the lower  $\Delta G_{\text{I,OE}}$ , the faster the decrease in the number of vacancies, see Fig. 5.13e. This decline leads to a considerable increase of the LRS resistance, see Fig. 5.13d. Over time, the resistance window shrinks as the LRS gets more resistive and the HRS gets less resistive. Both the vacancy concentration in the plug and the disc decline due to the continuous drop in vacancies, see Fig. 5.13f. The decrease only proceeds during the RESET, see the inset in Fig. 5.13e. This is consistent with the positive sign of  $V_{\text{Schottky,OE}}$  favoring the transfer of an oxygen ion from the OE to the plug. As for the simulation with an increasing number of vacancies, the voltage across the interface is however pretty low and thus, the higher temperature during the RESET is essential. This also explains why the degradation is highest at the beginning and then slows down. The increase in LRS resistance due to the oxygen transfer reduces the current and thereby the temperature, creating a negative feedback.

So far, only the exchange of oxygen at the plug/OE interface was analyzed. Naturally, also an exchange at the disc/AE interface can limit the endurance. The simulation is performed with the parameters from Table 5.2; oxygen exchange is solely considered at the disc/AE interface ( $\Delta G_{\rm I,OE} = \Delta G_{\rm II,OE} = 0 \, \text{eV}$ ). The initial conditions are the same

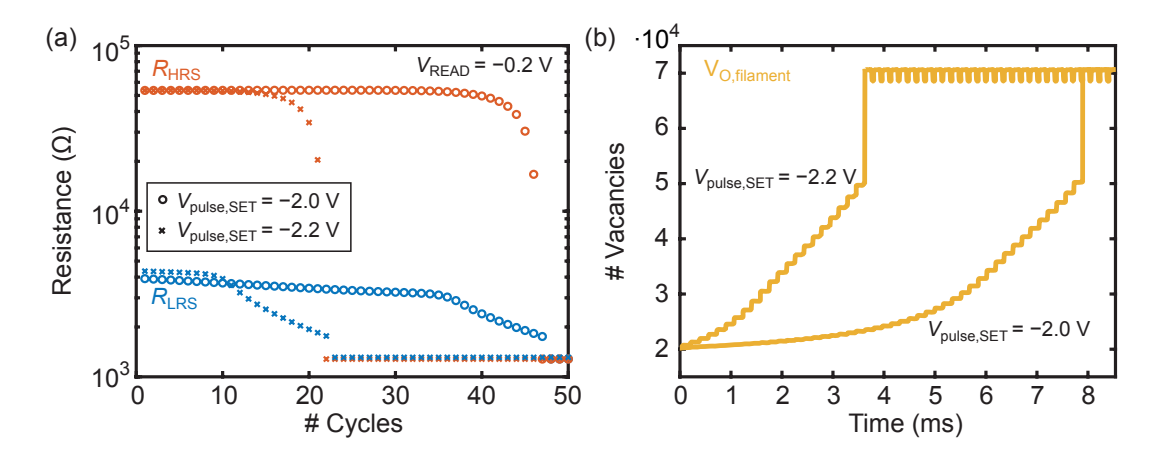


Figure 5.14: Dependence of the endurance on write conditions. The parameters and the pulse settings are given in Table 5.2. SET and RESET pulses are applied alternately and the resistance is obtained via READ pulses in between. In contrast to the results shown in Fig. 5.13, an oxygen exchange at the AE (instead of at the OE) is considered. Two SET pulse voltages of −2.0 V and −2.2 V are compared. (a) HRS and LRS resistance at −0.2 V. (b) Total number of oxygen vacancies in the filament.

as before with one exception. As the forming is still assumed to have taken place at the OE, only the minimum concentration of oxygen in the AE is used as initial condition for  $N_{\rm O,AE}$ . Thus in the beginning, vacancies can only be generated at the AE in this simulation. Later of course, the recombination of these generated vacancies with the stored oxygen ions in the AE is basically possible. For two SET pulse voltages, the resistance degradation and the vacancy transient are depicted in Fig. 5.14a and b, respectively. Given that the same values for  $\Delta G_{\rm I}$  and  $\Delta G_{\rm II}$  as for the simulation in Fig. 5.13a are taken, the RESET failure occurs considerably earlier. The increase of vacancies only proceeds during the RESET. The higher temperature as well as the sign of  $V_{\text{Schottky,AE}}$ favor the generation of vacancies at the AE during the RESET. Compared to an exchange at the OE interface with the same barriers, more vacancies are generated because the voltage is higher. Although the voltage drop across the interface does not exceed 70 mV, the time in which the voltage stays comparatively high is much longer. During the RESET, the vacancy concentration in the disc decreases and thus, the interface resistance increases. Consequently, the voltage drop across the interface  $V_{\rm Schottky,AE}$  steadily rises during the course of the RESET. This is different for the exchange at the OE as  $V_{\text{Schottkv,OE}}$  decreases during the RESET due to the increase of the vacancy concentration in the plug. If the SET pulse voltage is increased by [0.2 V], the number of cycles up to the RESET failure decreases. Due to the stronger SET pulse, the vacancy concentration in the disc exceeds the vacancy concentration in the plug in the LRS. Thus, the plug

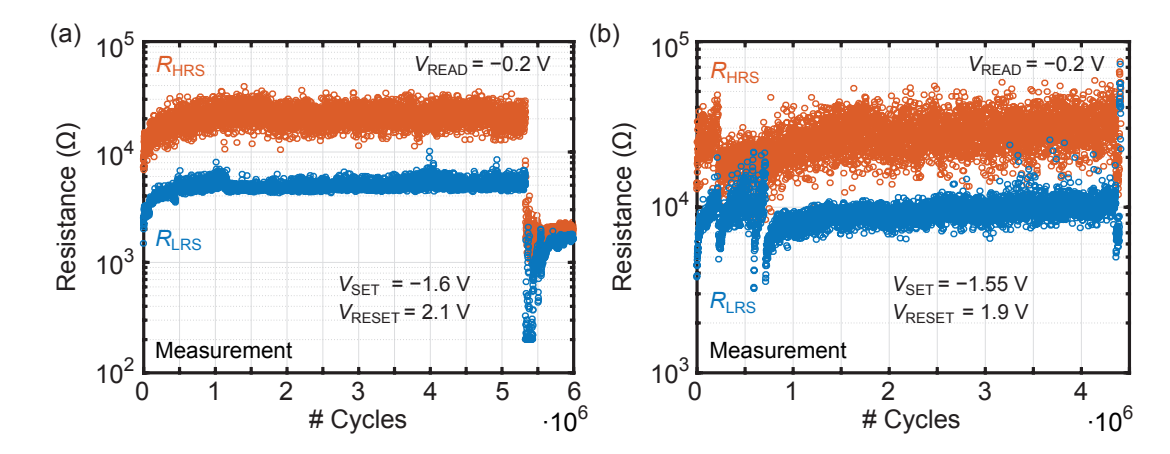


Figure 5.15: Experimental endurance data.  $Pt/ZrO_x/Ta$  devices are switched repeatedly using 10  $\mu$ s pulses. The LRS and HRS resistances are obtained in every 1000th pulse sequence by READ pulses. The data were provided by Stefan Wiefels and Michael Hüttemann [168]. Two exemplary endurance measurements show devices that are finally (a) stuck in the LRS and (b) stuck in the HRS.

resistance dominates and the total LRS resistance is slightly higher for the stronger SET pulse. In principle, this is a CS-related effect in BS switching, see the discussion on the SET overshoot in section 4.2.3. Strangely enough, the voltage  $V_{\text{Schottky,AE}}$  and the current, and thereby the temperature, are higher during the RESET after the LRS with slightly higher resistance. All together, this increases hugely the number of vacancies that are generated during each RESET. As in the case with the oxygen exchange at the OE, the RESET failure sets in upon  $N_{\text{plug}}$  reaching  $N_{\text{max}}$ .

Experimentally, all different kinds of endurance failures are reported in the literature: The resistance window can close rather suddenly after a high number of cycles with stable resistance levels [169–171], or it closes gradually over orders of magnitude [172–175]. After the endurance loss, the device can be stuck in the HRS [170, 176, 177] or stuck in the LRS [169, 171, 175]. Figure 5.15 displays two exemplary endurance failures measured on  $30 \, \mathrm{nm} \, \mathrm{Pt/5} \, \mathrm{nm} \, \mathrm{ZrO_x/20} \, \mathrm{nm} \, \mathrm{Ta}$  devices with a pad size of  $(7 \times 7) \, \mu \mathrm{m}^2$ . The experimental data were provided by Stefan Wiefels and Michael Hüttemann [168]. The voltage is defined as being applied to the Pt bottom electrode, while the top electrode is grounded. The two endurance measurements differ in the programming voltages: with  $V_{\mathrm{pulse,SET}} = -1.6 \, \mathrm{V}$  and  $V_{\mathrm{pulse,RESET}} = 2.1 \, \mathrm{V}$ , higher SET and RESET pulse voltages were applied in Fig. 5.15a compared to  $V_{\mathrm{pulse,SET}} = -1.55 \, \mathrm{V}$  and  $V_{\mathrm{pulse,RESET}} = 1.9 \, \mathrm{V}$  in Fig. 5.15b. To enable the measurement of a high number of pulse cycles, the LRS and HRS resistances were obtained only in every 1000th cycle. To this end, every 1000th cycle comprised two READ pulses of  $V_{\mathrm{pulse,READ}} = -0.2 \, \mathrm{V}$ . All pulses had a pulse length

of 10 µs. No programming algorithm or read-verify scheme was applied. The studied devices usually need some time to become attuned and thus, the first 10<sup>6</sup> cycles are discarded in the analysis regarding the endurance loss. The experimental data in Fig. 5.15a show an example of an abrupt endurance failure, after which the device is stuck in the LRS. In contrast, the resistance levels in Fig. 5.15b are not stable but drift before the final failure, which leads to a permanent HRS. These results are a good illustration for the well-known fact that the endurance depends on the programming scheme; thus, it can be improved by optimizing the pulse scheme regarding the pulse voltages and lengths [172, 175, 178, 179] or the rising/falling times in case of capacitive overshoots [171]. The balance between the SET and RESET pulses can also affect whether the LRS or the HRS causes the endurance loss [175]. Besides the programming scheme, the materials of the electrodes and the oxide have been shown to influence the endurance [172, 173, 180–182]. In [172, 181], the higher endurance of Ru/TaO<sub>x</sub>/Ta devices compared to TiN/TaO<sub>x</sub>/Ta devices is attributed to the oxygen interaction with the TiN botttom electrode during the RESET. In [178], the gradual degradation of the resistance window is assumed to result from the insufficient recombination of oxygen vacancies at the interface during the RESET process leading to a proceeding accumulation of vacancies. Without aiming to provide an explanation for specific experimental data, the simulation results in Figs. 5.13 and 5.14 show that an endurance loss can be motivated by both unbalanced programming conditions and an unbalanced oxygen exchange with the electrodes. Depending on the oxygen affinities of the electrodes, which are represented by the exchange barriers and the prefactors of the oxygen transfer reaction in the model, a permanent LRS or HRS after the endurance loss can be explained. Of course, other processes that are not covered by the model like the radial diffusion of vacancies can cause an endurance loss as well.

#### Retention

To make fitting of experimental data even more complicated, retention has to be considered in addition, besides forming characteristics, I-V switching sweeps, and endurance. The ionic processes that are not (solely) electric field driven — diffusion and oxygen exchange at the interfaces — result in a finite retention. As no internal electric fields under zero bias are considered in the model, the final and stable state always comprises a homogeneous distribution of vacancies in the filament, i.e. the vacancy concentration in the plug and the disc are equal. Whether the stable state has a high or a low resistance depends on the number of vacancies that remain in the filament. For this, the parameters

determining the oxygen exchange are crucial, see Eq. (5.19).  $\Delta G_{\text{I,OE}}$  and  $\Delta G_{\text{II,OE}}$  have a high impact as the ionic current is exponentially dependent on the nominal barriers. However, also the prefactors,  $k_{\text{I,OE}}^0$  and  $k_{\text{II,OE}}^0$  and especially the oxygen concentration in plug and OE, are crucial. If both  $k^0$  and  $\Delta G$  values are identical, the transfer will proceed until the oxygen concentrations at both sides of the interface are balanced, at least if the maximum and minimum limits do not interfere. This implies that the choice of the effective volume of the oxygen reservoir in the OE is significant.

The pristine state, i.e. the set of initial values that were chosen to describe the unformed state, is usually not the thermodynamically stable state. Typically, the oxide is reduced over time but it depends on the parameters whether the stable state has a very high resistance, a high resistance, or a low resistance. The parameters that were used in section 5.3.1 to model the forming statistics of ZrO<sub>x</sub>-based devices lead to a very low retention of the high-resistive pristine state. The resistance degradation is shown in Fig. 5.16a; the corresponding transients of the oxygen vacancy concentration in the plug and the disc and the oxygen concentration in the plug and the OE are plotted in Fig. 5.16c. The simulation is performed at room temperature and no voltage is applied except during the READ pulses to determine the resistance. The  $10\,\mu s$  short READ pulses at a low read voltage of  $-0.2\,\mathrm{V}$  do not influence the simulation results. Initially, the oxygen concentration in the plug and the oxygen concentration in the OE differ by five orders of magnitude and together with the  $k^0$ - and  $\Delta G$ -values, this presents an unbalanced state. First, oxygen ions are transferred from the plug into the OE. This process already sets in after 0.1s due to the low barrier  $\Delta G_{\rm II,OE}$ . After 10s, vacancies start to diffuse from the plug to the disc to balance the concentration gradient. At around 10<sup>4</sup> s, the maximum concentration of vacancies is reached in both plug and disc and thus, the oxygen transfer is stopped by the parameter  $F_{\text{limit.OE.II}}$  in Eq. (5.19), which sets the partial ionic current to zero. Without this limitation the amount of vacancies would further increase until a balance of the products out of  $k^0$ ,  $N_0$ , and  $\exp(-\Delta G/(k_{\rm B}T))$ would be established. Effectively, a device with this material parameters does not need to be formed, the oxide would be completely reduced several minutes after fabrication. This does not match the experimental observations; the retention of the pristine state is in the order of months ( $\sim 10^7 \, \mathrm{s}$ ). The retention and forming behavior of three other parameter combinations is also covered in Fig. 5.16. To allow a rational evaluation of the parameters, the forming I-V curves are shown in Fig. 5.16b. Compared to the standard parameters, the retention can be slightly increased by raising  $\Delta G_{\rm II,OE}$  and decreasing  $\Delta G_{\rm I,OE}$  to both 1.1 eV (Fig. 5.16d). Note that the rate constant prefactors  $k_{\rm I,OE}^0$  and

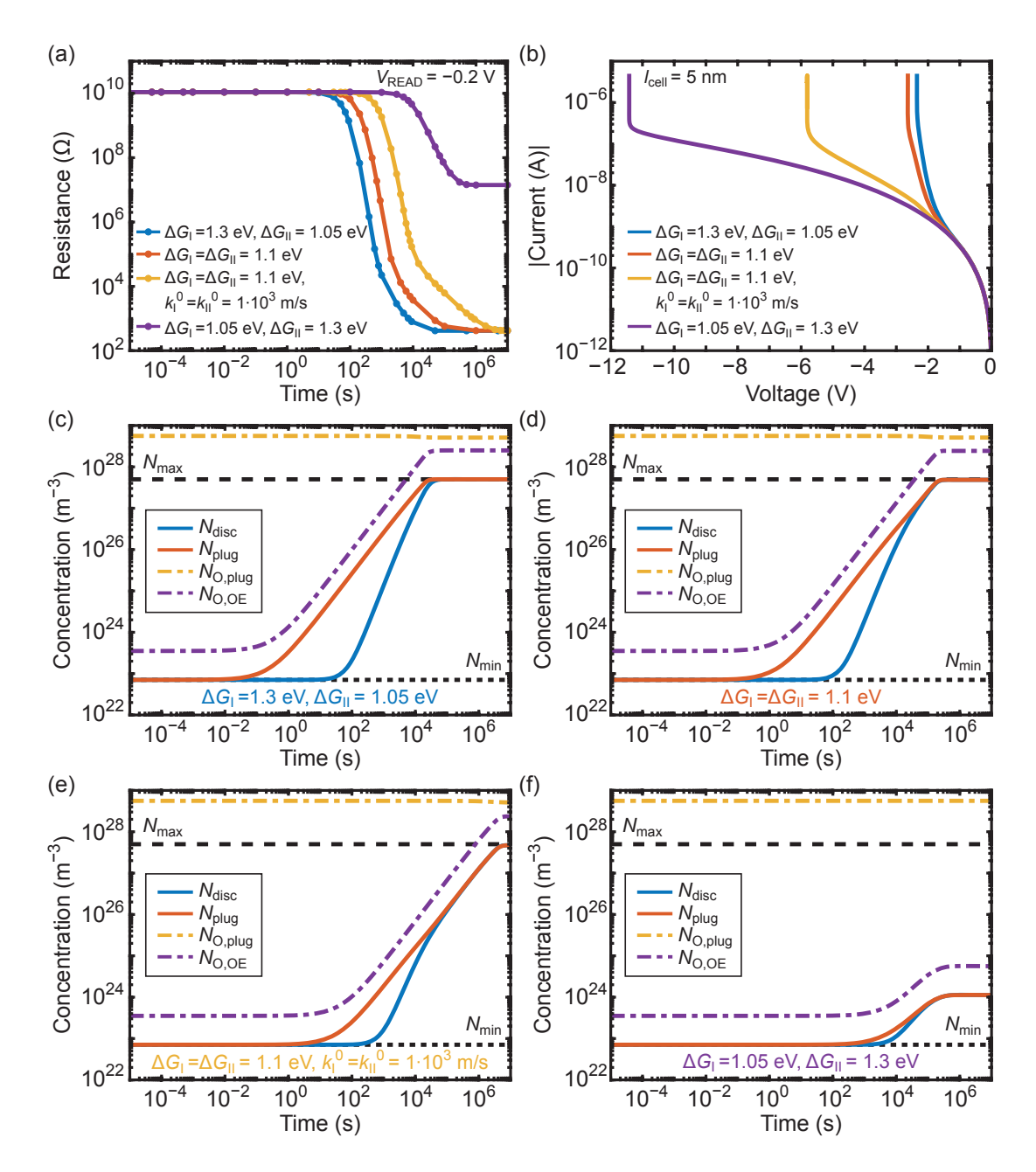


Figure 5.16: Retention of the pristine state. Parameters are taken from Table 5.1 ( $l_{\text{cell}} = 5 \text{ nm}$ ,  $\nu_0 = 4 \cdot 10^{12} \,\text{Hz}$ ) with the exception of the parameters being varied as stated in the legend. (a) The resistance of the pristine state is shown over time for four cases. Except during the READ pulses ( $V_{\text{pulse,READ}} = -0.2 \,\text{V}$ ,  $t_{\text{pulse,READ}} = 10 \,\mu\text{s}$ ), no voltage is applied in the retention simulation. (b) For comparison, the forming I-V curves for the four cases are displayed as well. Values for  $R_{\text{series,cc}}$  are given in Table A.3 in Appendix A.2. (c)-(f) The oxygen vacancy concentration in the plug and the disc, the minimum and maximum vacancy concentration in the filament, and the oxygen concentration in the plug and the ohmic electrode are shown for (c) standard parameter, (d)  $\Delta G_{\text{I,OE}} = \Delta G_{\text{II,OE}} = 1.1 \,\text{eV}$ , (e)  $\Delta G_{\text{I,OE}} = \Delta G_{\text{II,OE}} = 1.1 \,\text{eV}$ ,  $k_{\text{I,OE}}^0 = k_{\text{II,OE}}^0 = 1 \cdot 10^3 \,\text{m/s}$ , and (f)  $\Delta G_{\text{I,OE}} = 1.05 \,\text{eV}$ ,  $\Delta G_{\text{II,OE}} = 1.3 \,\text{eV}$ , respectively.

 $k_{\rm II,OE}^0$  differ by a factor of two, see Table 5.1. If the prefactors  $k_{\rm I,OE}^0$  and  $k_{\rm II,OE}^0$  are reduced by one order of magnitude to  $1\cdot 10^3$  m/s (Fig. 5.16e), the resistance degradation is postponed by one order of magnitude, compared to the preceding case. Compared to the experimental observations, however, the retention is still far too low. Fig. 5.16e presents an example how the choice of the maximum vacancy concentration affects the balance. As both  $k^0$  and  $\Delta G$  are equal,  $N_{\rm O,plug}$  and  $N_{\rm O,OE}$  should be equal as well in the stable state. In the last case (Fig. 5.16f), the nominal barriers  $\Delta G_{\rm I}$  and  $\Delta G_{\rm II}$  are interchanged. Here, the stable state is not low resistive but has a high resistance of around  $10^7 \Omega$ . This is lower than in the experiments but, of the four cases, a stable, high resistive pristine state would fit best to the experimental data. With these parameters, however, more than  $-11 \, {\rm V}$  would have to be applied in a sweep with a sweep rate of  $1 \, {\rm V/s}$  to initiate a forming. This is far more than the measured forming voltage for an oxide thickness of 5 nm, see Fig. 5.4b.

To summarize, the model is capable of describing the retention of the pristine state and of capturing the forming behavior but different parameters need to be used if the simulation result should fit to experimental data.

# 5.3.4 Eightwise Switching<sup>1</sup>

In eightwise switching devices, the oxygen exchange at the active electrode dominates over the redistribution of vacancies between the plug and the disc, see section 2.2. Typically, 8w switching devices show a very high ratio between the HRS and LRS resistance. A switching sweep covers around eight orders of magnitude in current and both SET and RESET proceed very gradually, see an exemplary measurement in Fig. 5.17a. The experimental curve was measured on a Pt/20 nm SrTiO<sub>3</sub>/Nb:SrTiO<sub>3</sub> device by Christoph Bäumer [103]. To fit to this characteristic, a high nominal barrier of 1.5 eV is assumed for the AE/oxide interface. As a result, the Schottky contact dominates the overall electrical conduction and a high ON/OFF-ratio should develop. To allow for a comparatively high current in the LRS, the filament radius is set to 200 nm. This is consistent with the estimation of 500 nm as upper limit for the filament diameter in these devices [115]. The effective thermal resistance is chosen low as the very gradual transitions indicate that Joule heating is not significant. To reduce the influence of the vacancy migration in the filament, the activation barrier for the ion hopping process is considerably high with 1.5 eV but still in the physically reasonable range. As there is no indication to

The simulation results in this section are based on the collaboration with the bachelor student Kaihua Zhang [183].

differentiate between SET and RESET in the calculation of the electric field for the ion migration in the filament,

$$E = \frac{V_{\text{disc}} + V_{\text{plug}}}{l_{\text{cell}}} \tag{5.37}$$

is used instead of Eq. (5.33).

For the given parameter set with a comparatively low donor concentration in the LRS, thermionic field emission can be chosen as conduction mechanism for the Schottky diodes under forward and reverse bias, changing Eq. (5.12) to

$$I = \begin{cases} sign(V_{applied}) \cdot I_{TFE,forward} & V_{forward} > 0 \text{ (forward)} \\ sign(V_{applied}) \cdot I_{TFE,reverse} & V_{forward} \leq 0 \text{ (reverse)}. \end{cases}$$
(5.38)

A further limit is introduced for the ionic exchange current  $I_{\text{ion,BV,AE}}$  in Eq. (5.23). Besides the minimum limit for the oxygen concentration in the AE  $N_{\text{O,AE,min}}$ , a maximum concentration  $N_{\text{O,AE,max}}$  is defined that reflects the limited capability of the electrode (interface) to store oxygen ions. Therefore, Eq. (5.25) is changed to

$$F_{\text{limit,AE,II}} = \left[1 - \left(\frac{N_{\text{disc}}}{N_{\text{max}}}\right)^{10}\right] \cdot \left[1 - \left(\frac{N_{\text{O,AE}}}{N_{\text{O,AE,max}}}\right)^{10}\right]. \tag{5.39}$$

Forming is not considered in this section, the simulation starts in the LRS. Analogous to the measurement, a sweep rate of  $0.5\,\mathrm{V/s}$  is chosen. All parameters are listed in Table 5.3.

The simulation results are shown in Fig. 5.17. The I-V characteristic and the oxygen vacancy concentration in the plug and the disc are depicted in Fig. 5.17a and b, respectively. The initial concentration in the plug and the disc are equal and as they are high, the cell is in the LRS. First, negative sweep voltages are applied. At around  $-0.6\,\mathrm{V}$ , the current decreases sharply over 20 orders of magnitude. This abrupt drop is stopped by the vacancy concentration in the disc reaching the minimum limit. The vacancy concentration in the plug does not change at all during the RESET. The number of vacancies in the disc decreases because oxygen is transferred from the AE to the disc. This is illustrated in Fig. 5.17c, where the number of vacancies in the filament and the total number of oxygen ions stored in the AE are depicted. The amount of vacancies that vanish during the RESET equals the amount of oxygen ions leaving the AE. By applying positive voltages to the AE, the SET process starts. Oxygen is transferred from the disc to the AE, thereby increasing the concentration of vacancies in the disc. The rising donor concentration reduces the resistance of the Schottky barrier and the

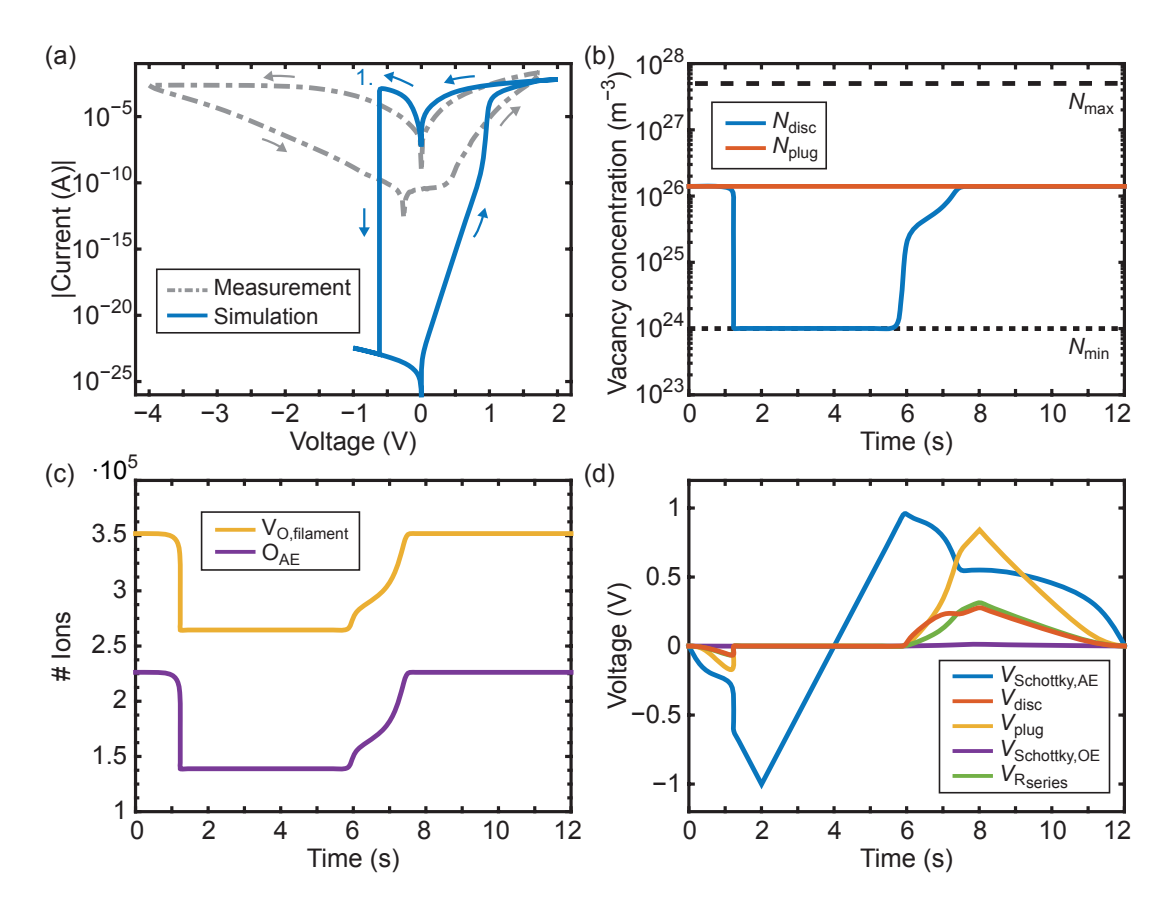


Figure 5.17: Eightwise switching using compact model 2.0. The simulation is performed using the parameters from Table 5.3. The experimental I-V curve is taken from a  $Pt/SrTiO_3/Nb:SrTiO_3$  device and was measured by Christoph Bäumer. The switching describes the 8w direction as the change of vacancies in the disc, which causes the resistance variation, results from the oxygen exchange with the AE and is not based on an ion redistribution between the plug and the disc. (a) Measured and simulated I-V curve. (b) Oxygen vacancy concentration in the plug and the disc. (c) Total number of vacancies in the filament and total number of oxygen ions stored in the AE. (d) Voltage drops across all lumped circuit elements.

current increases. The increase of the oxygen ions in the AE, and thereby the SET, is stopped as the concentration of oxygen in the AE reaches the maximum limit  $N_{\rm O,AE,max}$  (not shown). The final concentrations of oxygen ions in the AE and vacancies in the filament equal the initial concentrations; thus, the shown I-V curve is the stable one.

From a macroscopic point of view, with the RESET proceeding at negative voltages (applied to the AE) and the SET proceeding at positive voltages, the simulated cell clearly exhibits eightwise switching. Also from a microscopic point of view, the switching differ from the previously discussed c8w switching as the oxygen exchange at the electrode does not only influence the resistance change but is the elementary origin.

Symbol	Value	Symbol	Value
$l_{\text{cell}}$	20 nm	$\varepsilon$	$17  \varepsilon_0$
$l_{ m disc}$	$5\mathrm{nm}$	$arepsilon_{\phi_{ m B}}$	$5.5\varepsilon_0$
$l_{ m plug}$	$l_{\rm cell} - l_{\rm disc}$	$e\phi_{ m Bn0,AE}$	$1.5\mathrm{eV}$
$r_{ m fil}$	$200\mathrm{nm}$	$e\phi_{ m Bn0,OE}$	$0.1\mathrm{eV}$
$l_{ m AE,eff}$	$30\mathrm{nm}$	$\mu_{ m n0}$	$2 \cdot 10^{-5} \mathrm{m}^2/(\mathrm{Vs})$
$z_{ m Vo}$	2	$\Delta E_{ m ac}$	$0\mathrm{eV}$
$z_{ m O}$	-2	$N_{ m O,oxide,max}$	$5.6 \cdot 10^{28}  \mathrm{m}^{-3}$
a	$0.5\mathrm{nm}$	$N_{ m max}$	$5 \cdot 10^{27}  \mathrm{m}^{-3}$
$\nu_0$	$1\cdot 10^{12}\mathrm{Hz}$	$N_{ m min}$	$1 \cdot 10^{24}  \mathrm{m}^{-3}$
$\Delta W_{ m A}$	$1.5\mathrm{eV}$	$N_{ m O,AE,min}$	$1 \cdot 10^{22}  \mathrm{m}^{-3}$
$lpha_{ m AE}$	0.5	$N_{ m O,AE,max}$	$6 \cdot 10^{25}  \mathrm{m}^{-3}$
$k_{ m I,AE}^0$	$1 \cdot 10^4 \mathrm{m/s}$	$N_{ m disc,initial}$	$1.4 \cdot 10^{26}  \mathrm{m}^{-3}$
$k_{ m II,AE}^0$	$1 \cdot 10^4 \mathrm{m/s}$	$N_{ m plug,initial}$	$1.4 \cdot 10^{26}  \mathrm{m}^{-3}$
$\Delta G_{ m I,AE}$	$1.0\mathrm{eV}$	$N_{ m O,AE,initial}$	$N_{ m O,AE,max}$
$\Delta G_{ m II,AE}$	$1.8\mathrm{eV}$	$R_{ m th,eff}$	$4 \cdot 10^4  \mathrm{K/W}$
$m_{ m eff}$	$m_{ m e}$	$R_{ m series}$	$50\Omega$
$A^*$	see Eq. (2.4)	sweep rate	$0.5\mathrm{V/s}$
	_	$T_0$	$293\mathrm{K}$

**Table 5.3:** Parameters for the simulation of an eightwise switching device in Fig. 5.17.

Compared to the measured I-V characteristic, the simulated switching is much too abrupt. This is the result of a positive feedback between the voltage across the Schottky barrier  $V_{\rm Schottky,AE}$  and the oxygen transfer reaction: Due to the high nominal barrier, the highest voltage drop (in terms of absolute values) is across the Schottky barrier in the LRS, see Fig. 5.17d. A non-negligible part of the voltage drops however across the filament. If oxygen ions start to migrate from the AE to the disc, the decreasing vacancy concentration in the disc increases the resistance of the Schottky contact. Consequently, the voltage  $V_{\rm Schottky,AE}$  rises and less voltage drops across the other elements. As the negative sign of  $V_{\rm Schottky,AE}$  favors the transfer of oxygen ions from the AE to the disc, an increasing voltage  $V_{\rm Schottky,AE}$  accelerates the oxygen exchange. Thus, the more voltage drops across the interface, the more vacancies are annihilated in the disc and thereby, the interface resistance increases leading to a higher voltage drop in turn.

#### Modified Model with Diffusion in the AE

The analysis of the simulation results in Fig. 5.17 revealed that the model lacks some kind of physics that lead to the experimentally observed, very gradual RESET. The oxygen exchange process needs to be kinetically limited to prevent the positive feedback

through the voltage enhancement. One possibility could comprise a limitation of the reaction partners, for example by restricting the number of oxygen ions stored near the interface in the AE or the oxygen vacancies in the disc. If the inflow of at least one reaction partner to the interface is limited, the kinetics of this process becomes dominant. Without limiting the general hypothesis, it is assumed that not all of the oxygen ions stored in the AE are present at the interface and therefore cannot interact with the oxygen vacancies in the disc. Thus, the active electrode is split into two reservoirs, one near the interface called  $AE_{inter(face)}$  and one far away from the interface named  $AE_{far}$ , see the sketch in Fig. 5.18. The corresponding oxygen concentrations and lengths are  $N_{O,AE,inter}$ ,  $N_{O,AE,far}$ ,  $l_{AE,inter}$ , and  $l_{AE,far}$ , respectively. The diffusion of oxygen ions between these two reservoirs is described in terms of an ionic current  $I_{ion,AE}$  with

$$I_{\text{ion,AE}} = -A \left( z_{\text{O}} e D_{\text{ion,AE}} \frac{dN_{\text{O,AE}}}{dx} \right)$$

$$= -A \left( z_{\text{O}} e D_{\text{ion,AE,0}} \exp \left( -\frac{\Delta W_{\text{A,AE}}}{k_{\text{B}}T} \right) \frac{N_{\text{O,AE,far}} - N_{\text{O,AE,inter}}}{0.5 \left( l_{\text{AE,far}} + l_{\text{AE,inter}} \right)} \right). \tag{5.40}$$

The diffusion coefficient  $D_{\text{ion,AE}}$  follows an Arrhenius-type equation with  $D_{\text{ion,AE,0}}$  as prefactor and  $\Delta W_{\text{A,AE}}$  as activation barrier for the hopping process. Drift is neglected due to the high conductivity of the Pt electrode, which leads to a very low electric field. The oxygen exchange at the  $\text{AE}_{\text{inter}}/\text{disc}$  interface is still described by the ionic current  $I_{\text{ion,BV,AE}}$  and in Eq. (5.23) only  $N_{\text{O,AE}}$  has to be replaced by  $N_{\text{O,AE,inter}}$ . The limiting factors  $F_{\text{limit,AE,I}}$  and  $F_{\text{limit,AE,II}}$  in Eq. (5.23) convert to

$$F_{\text{limit,AE,I}} = \left[1 - \left(\frac{N_{\text{min}}}{N_{\text{disc}}}\right)^{10}\right] \cdot \left[1 - \left(\frac{N_{\text{O,AE,inter,min}}}{N_{\text{O,AE,inter}}}\right)^{10}\right], \tag{5.41}$$

$$F_{\text{limit,AE,II}} = \left[1 - \left(\frac{N_{\text{disc}}}{N_{\text{max}}}\right)^{10}\right] \cdot \left[1 - \left(\frac{N_{\text{O,AE,inter}}}{N_{\text{O,AE,inter,max}}}\right)^{10}\right]. \tag{5.42}$$

In total, the changes in the oxygen concentrations are given by

$$\frac{\mathrm{d}N_{\mathrm{O,AE,inter}}}{\mathrm{d}t} = +\frac{1}{z_{\mathrm{Vo}}e\,A\,l_{\mathrm{AE,inter}}} \cdot I_{\mathrm{ion,BV,AE}} - \frac{1}{z_{\mathrm{O}}e\,A\,l_{\mathrm{AE,inter}}} \cdot I_{\mathrm{ion,AE}}$$
(5.43)

and

$$\frac{\mathrm{d}N_{\mathrm{O,AE,far}}}{\mathrm{d}t} = +\frac{1}{z_{\mathrm{O}}e\,A\,l_{\mathrm{AE\,far}}} \cdot I_{\mathrm{ion,AE}}.\tag{5.44}$$

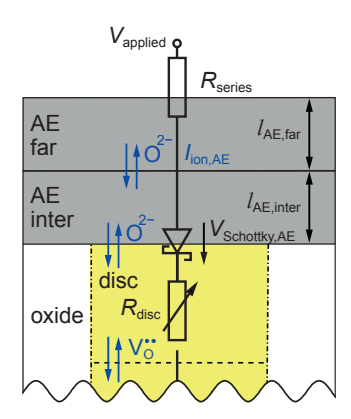


Figure 5.18: Sketch of the electrical and ionic description of the eightwise switching model including diffusion of oxygen ions in the active electrode. Therefore, the active electrode is split into two parts named  $AE_{inter(face)}$  and  $AE_{far}$ .

**Table 5.4:** Parameters for the simulation of an eightwise switching device with the modified model including the diffusion in the AE in Fig 5.19.

Symbol	Value	Symbol	Value
$l_{\text{cell}}$	$20\mathrm{nm}$	$e\phi_{ m Bn0,AE}$	$1.5\mathrm{eV}$
$l_{ m disc}$	$5\mathrm{nm}$	$e\phi_{ m Bn0,OE}$	$0.1\mathrm{eV}$
$l_{ m plug}$	$l_{ m cell} - l_{ m disc}$	$\mu_{ m n0}$	$2 \cdot 10^{-5}  \mathrm{m}^2 / (\mathrm{Vs})$
$r_{ m fil}$	$200\mathrm{nm}$	$\Delta E_{ m ac}$	$0\mathrm{eV}$
$l_{ m AE,inter}$	$5\mathrm{nm}$	$N_{ m O,oxide,max}$	$5.6 \cdot 10^{28}  \mathrm{m}^{-3}$
$l_{ m AE,far}$	$5\mathrm{nm}$	$N_{ m max}$	$5 \cdot 10^{27}  \mathrm{m}^{-3}$
$z_{ m Vo}$	2	$N_{ m min}$	$1 \cdot 10^{24}  \mathrm{m}^{-3}$
$z_{ m O}$	-2	$N_{ m O,AE,inter,min}$	$1 \cdot 10^{22}  \mathrm{m}^{-3}$
a	$0.5\mathrm{nm}$	$N_{ m O,AE,inter,max}$	$6 \cdot 10^{25}  \mathrm{m}^{-3}$
$\nu_0$	$1\cdot 10^{12}\mathrm{Hz}$	$N_{ m disc,initial}$	$1.4 \cdot 10^{26}  \mathrm{m}^{-3}$
$\Delta W_{ m A}$	$1.5\mathrm{eV}$	$N_{ m plug,initial}$	$1.4 \cdot 10^{26}  \mathrm{m}^{-3}$
$lpha_{ m AE}$	0.5	$N_{ m O,AE,inter,initial}$	$N_{ m O,AE,inter,max}$
$k_{ m I,AE}^0$	$1 \cdot 10^4  \mathrm{m/s}$	$N_{ m O,AE,far,initial}$	$N_{ m O,AE,inter,max}$
$k_{ m II,AE}^{0}$	$1 \cdot 10^4  \mathrm{m/s}$	$D_{\mathrm{ion,AE,0}}$	$1 \cdot 10^{-7}  \mathrm{m}^2/(\mathrm{s})$
$\Delta G_{ m I,AE}$	$0.6\mathrm{eV}$	$\Delta W_{ m A,AE}$	$0.6\mathrm{eV}$
$\Delta G_{ m II,AE}$	$1.8\mathrm{eV}$	$R_{ m th,eff}$	$1 \cdot 10^4  \mathrm{K/W}$
$m_{ m eff}$	$m_{ m e}$	$R_{ m series}$	$50\Omega$
$A^*$	see Eq. $(2.4)$	sweep rate	$0.5\mathrm{V/s}$
$\varepsilon$	$17  \varepsilon_0$	$T_0$	$293\mathrm{K}$
$arepsilon_{\phi_{ m B}}$	$5.5\varepsilon_0$		

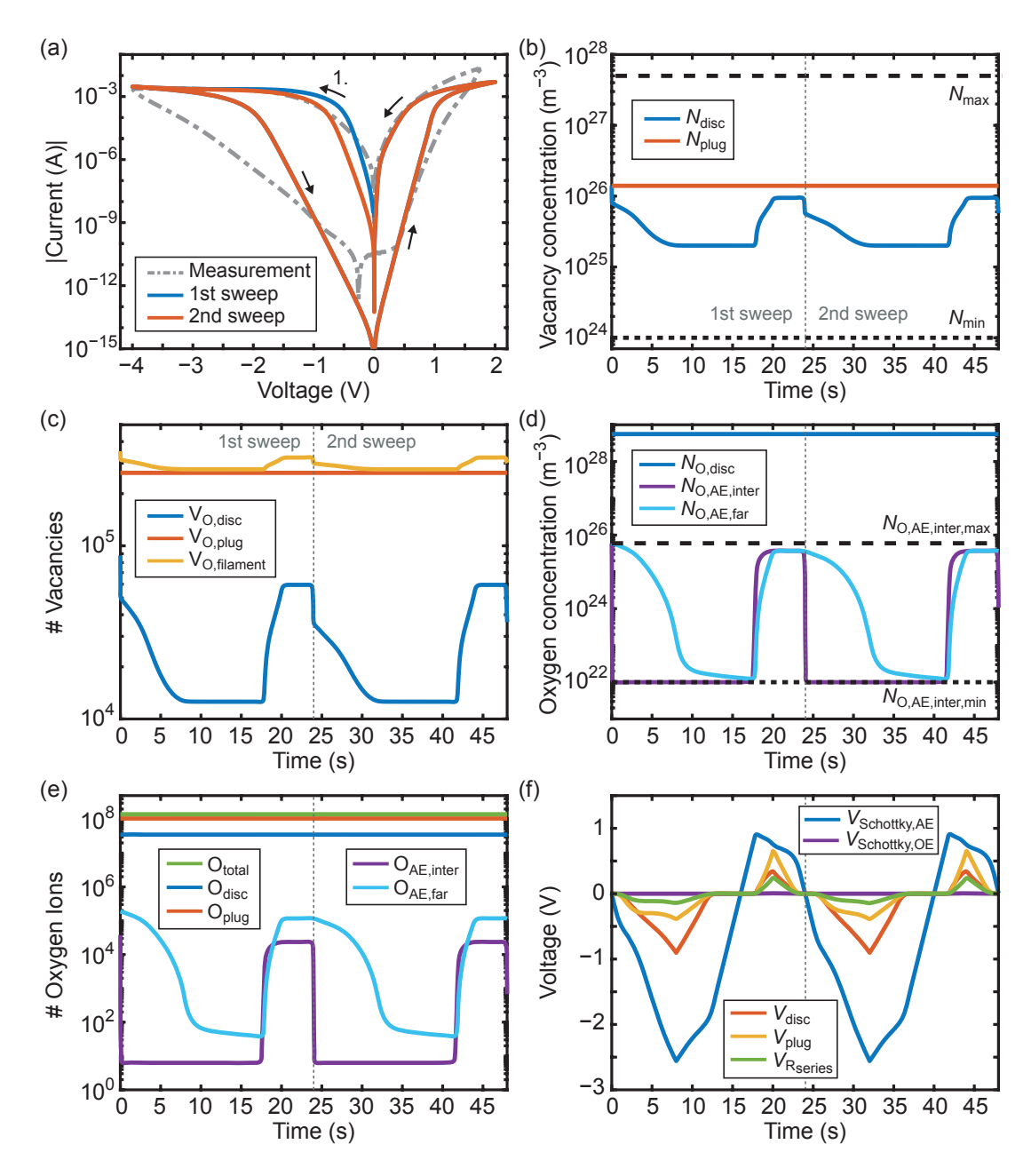


Figure 5.19: Eightwise switching using the modified model with diffusion in the AE. The parameters for the simulation are given in Table 5.4. The experimental I-V curve is taken from a Pt/SrTiO<sub>3</sub>/Nb:SrTiO<sub>3</sub> device and was measured by Christoph Bäumer. (a) Measured and simulated I-V curves. (b) Oxygen vacancy concentration in the plug and the disc. (c) Total number of vacancies in the disc, in the plug, and the sum of both. (d) Oxygen concentration in the disc and in both parts of the AE, AE<sub>inter</sub> and AE<sub>far</sub>. (e) Total number of oxygen ions in the disc, in the plug, in both AE parts, and the sum of all. The change in O<sub>disc</sub> is not visible due to the scale. (f) Voltage drops across all lumped circuit elements.

The simulation results of the modified model are depicted in Fig. 5.19, Table 5.4 summarizes all parameters. Initially, the cell is in the LRS and the oxygen concentration in  $AE_{inter}$  and  $AE_{far}$  equal the maximum concentration. The I-V characteristics of the first two sweeps are shown next to the experimental data in Fig. 5.19a. Negative voltages are applied first and the low value for  $\Delta G_{\rm I,AE}$  together with the high value for  $\Delta G_{\rm II,AE}$ results in an almost instant transfer of the oxygen ions stored in the AE<sub>inter</sub> to the disc. Accordingly, the concentration of vacancies in the disc and the total amount of vacancies in the filament decrease, see Fig. 5.19b and c, respectively. The concentration of oxygen in the AE<sub>inter</sub> reduces to its minimum value and thus, the exchange is stopped, see Fig. 5.19d. Solely due to fitting purposes, the minimum concentration does not convert to one remaining oxygen ion in the AE<sub>inter</sub> but to slightly more than six (Fig. 5.19e). As this exchange happens directly at the beginning, no small, sharp drop in current is visible in the I-V curve. As the measured characteristic does not show any sharp drop,  $\Delta G_{\rm IAE}$ was chosen deliberately so low. After the initial exchange, the RESET proceeds further but slower. This can be deduced by the slowly decreasing vacancy concentration in the disc. Oxygen ions from the AE<sub>far</sub> diffuse into the AE<sub>inter</sub> and are transferred directly to the disc. That is why the oxygen concentration in the  $AE_{far}$  decreases continuously but the oxygen concentration near the interface  $N_{\text{O,AE,inter}}$  does not increase and remains at its minimum limit. When the voltage reaches the maximum negative sweep voltage at -4 V (t = 8 s), the oxygen concentration in the AE<sub>far</sub> has declined to  $1.6 \cdot 10^{23} \text{ m}^{-3}$ . During the voltage sweep back to 0 V, oxygen ions further diffuse from the AE<sub>far</sub> to the AE<sub>inter</sub> and are transferred to the disc, but the total number of migrating oxygen ions is small. Thus, the vacancy concentration in the disc does not change considerably during this time. During the SET, which proceeds at positive voltages, oxygen ions from the disc are transferred to the AE<sub>inter</sub>, increasing the concentration of oxygen there quickly. Due to the concentration gradient, the ions diffuse to the  $AE_{far}$ . The rising concentration of vacancies in the disc results in a current increase.

The Schottky barrier at the AE<sub>inter</sub>/disc interface dominates the overall conduction throughout the whole sweep, see Fig. 5.19f. Thus, the high voltage drop is an important driving force for the oxygen exchange and it ensures that the electric field is low in the filament. Due to the low field and the high activation barrier for ion hopping in the filament, no redistribution of vacancies between the plug and the disc occurs; the amount of vacancies in the plug stays constant. The generation of vacancies during the SET proceeds faster than the annihilation during the RESET, possibly due to the positive feedback between the current increase and a rise in temperature. A higher temperature accelerates the oxygen exchange and the diffusion in the AE because the

same temperature is taken in both equations. After the first sweep, the final values of the oxygen ion and the oxygen vacancy concentrations do not fully equal the initial ones. Consequently, the I-V curves of the first and the second sweep are slightly different. All subsequent sweeps, however, coincide with the second sweep as the final conditions at the end of the second sweep agree with the initial values.

Although some qualitative trends of the measured 8w I-V curve regarding the high ON/OFF-ratio and the gradual switching are captured by the simulation, obvious differences remain. Especially in the HRS after the RESET, a fundamental mismatch in the current level exists. In addition to the I-V curve, the model characteristics have been analyzed further [183]: the temperature dependence is quite high. A variation in the ambient temperature by a few Kelvin causes a change in the ionic motion that leads to a difference in the HRS current of several orders of magnitude. This prediction is contradicted by experimental results [38]. Moreover, the state variables in the simulation start changing from the beginning, whereas in the experiments, a nonvolatile change can only be detected upon applying a sweep beyond  $-2 \,\mathrm{V}$ . A further difference lies in the amount of the changing oxygen vacancy concentration near the Pt electrode. Experimentally, the charge carrier concentration was determined to change by a factor of two to three between LRS and HRS [115]. The simulated oxygen vacancy concentration in the disc, however, changes by a factor of five. In summary, the presented model is a rough model that successfully describes a switching based on the oxygen exchange at the AE, which gives the 8w switching polarity.

#### 5.4 Conclusion

Adding the oxygen exchange at the metal/oxide interfaces changes the number of state variables in compact model 2.0 to four (three, if only the exchange at one electrode is considered). This increases the complexity but enables the investigation of many interesting effects like the simulation of forming, endurance, retention, and 8w switching. In contrast to compact model 1.5, the number of vacancies in the filament is not constant and determined solely by the initial values. The possible creation of vacancies at the interfaces allows the simulation of the forming process. Thereby, the kinetic barriers for the oxygen exchange,  $\Delta G_{\rm I}$  and  $\Delta G_{\rm II}$ , and the migration barrier for the ion hopping in the filament,  $\Delta W_{\rm A}$ , have a high impact on the forming voltage. In accordance with space-resolved continuum model simulations, the growth direction of the filament during forming is determined by the rate-limiting step. Assuming a generation of vacancies at

the OE/plug interface, the concentration of vacancies in the plug is higher than in the disc during forming if the migration of vacancies in the oxide is rate limiting. This corresponds to a filament growth direction from anode to cathode. The opposite growth direction occurs for a rate-limiting oxygen exchange process. In this case, the vacancy concentration in the disc is higher than in the plug. A change in the filament growth direction during forming causes ripples or kinks in the I-V curve.

The forming voltage also depends on the plug length as the plug volume determines the increase in concentration for a certain number of exchanged ions. If the plug length is chosen to scale with the oxide thickness, the forming voltage depends on the oxide thickness: the current increase for the same amount of generated vacancies is higher for a small oxide thickness. The higher current leads to more Joule heating and the thermal runaway sets in earlier. Accordingly, the experimentally observed dependence of the forming voltage on the oxide thickness in  $\rm ZrO_x$ -based devices could be described in good overall agreement. A further highlight of the model is the applicability for switching sweeps in addition to the forming step. The model does not only match the forming data but successfully describes the subsequent switching sweeps with the same parameter set. Only the calculation of the driving electric field for the ion migration in the filament and the effective thermal resistance differ for forming and switching sweeps. Comparable to experimental observations, an appropriate current compliance is necessary to limit the amount of vacancies that is generated during the forming process to enable subsequent switching.

In general, the exchange barriers and the prefactors in the oxygen transfer reaction determine whether the total number of vacancies increases or decreases over time, crucially influencing the endurance and retention. A continuous decrease of vacancies leads to a shrinking read window between LRS and HRS because the LRS becomes more resistive and the HRS becomes less resistive over time. On the other hand, a continuous increase of vacancies results in a decrease of the HRS resistance that is followed by an abrupt RESET failure. Afterwards, the cell is 'stuck in the LRS'. In the endurance studies, the abrupt RESET failure is triggered by the vacancy concentration in the plug reaching the maximum limit. This is one example for the renewed importance of the, to some extent arbitrary, limits  $N_{\rm max}$  and  $N_{\rm min}$ , which play a significant role in compact model 1.0, but were nearly negligible in compact model 1.5. In addition, limits for the oxygen concentration in the electrodes have to be defined as well. Especially for 8w switching, these limits are relevant.

8w switching is defined by the condition that the change of vacancies in the disc, which causes the resistance variation, results from the oxygen exchange with the AE and is not based on an ion redistribution between the plug and the disc. By choosing the parameters appropriately, the 8w switching direction can be described successfully. However, a positive feedback between the voltage across the Schottky barrier and the oxygen transfer reaction causes the switching to be far more abrupt than the very gradual switching that is observed experimentally. To prevent this positive feedback, the oxygen exchange process is kinetically limited by restricting the number of oxygen ions stored near the interface. This is achieved by splitting the electrode into two reservoirs, which exchange oxygen by diffusion. If the parameters are chosen accordingly, the diffusion from the second reservoir to the interface becomes the rate-limiting step. This results in the desired gradual RESET, though many differences between measurement and simulation remain.

The pristine state is usually not the stable state in the simulation and the oxide is reduced over time. Whether the stable state has a high or a low resistance depends on the number of vacancies that remain in the filament. Simulations with parameters that lead to a reasonable forming voltage show a retention time of the pristine state in the range of seconds to minutes. Effectively, a device with these material parameters would not need to be formed because the time between fabrication and measurements usually exceeds this timescale.

The major drawback of the model is that the influence of the electric field on the oxygen exchange process is too weak and that the polarity of the applied voltage is therefore almost insignificant for the exchange reaction: The forming at the OE proceeds at low applied voltages although the voltage drop across the plug/OE interface is below |50 mV|. Thus, the forming is not triggered by the applied voltage but induced by the parameters for the exchange reaction that favor a reduction of the oxide. That is also the reason why the retention of the pristine state is only in the range of minutes. In addition, the analysis of the endurance simulation revealed that the generation of vacancies at the plug/OE interface takes place in large part during the RESET, although the negative potential at the OE should favor an annihilation. This results from the higher temperature during the RESET.

To summarize, the implementation of the oxygen exchange at the interfaces significantly extends the general applicability and turns compact model 2.0 into a powerful model covering forming, c8w and 8w switching, endurance, and retention. However, it is impossible to find a parameter set that provides a good fit to experimental data comprising first, the forming characteristics, second, the subsequent I-V switching sweeps, third, the endurance, and fourth, the retention. This clearly illustrates that some important physical processes are missing or that the included ones, such as the oxygen exchange reaction, are not sufficiently well described. In addition, it needs to be emphasized that a reliable dynamical model requires an accurate electrical model. Sufficiently accurate knowledge of the electrical conduction mechanism, however, is missing so far. Therefore, improvements concerning the ionic and/or the electrical description are important milestones for future modeling of ReRAM devices.

## 6 Conclusions

## 6.1 Summary

In this thesis, three physics-based compact models with different levels of detail were developed in MATLAB to study various switching effects in filamentary VCM-type ReRAM devices. By modeling the migration of oxygen vacancies along the filament and the exchange of oxygen at the metal/oxide interfaces, all three switching modes — counter-eightwise, eightwise, and complementary switching — are successfully described. Comparable to experimental observations, switching failures or artifacts can occur in the simulation that are related to side processes or unintended switching modes. For all three models, the used assumptions and the models limits were emphasized to allow a correct interpretation of the simulation results for those potentially using the models in circuit simulations. Various parameter studies were performed to identify the influence of material parameters, applied voltage, and current compliance on the resulting switching. The understanding gained from the simulations will help to control the occurrence/suppression of intended/unintended effects in future devices by material choice or external excitation design.

Compact model 1.0 describes bipolar switching based on the drift of oxygen vacancies along a filament. As no process is implemented that counterbalances the migration, the definition and choice of a minimum and maximum vacancy concentration are crucial. The oxygen vacancy concentration in the disc at the active electrode is the only state variable and the electrode/disc interface is modeled as Schottky barrier. This basic model is well suited for the simulation of the counter-eightwise switching mode including the experimentally observed nonlinear SET kinetics. In addition, it covers the remarkable influence of an (internal) series resistance on the externally accessible I-V characteristic: a gradual and an abrupt RESET can be obtained both with the same dynamical process of field- and temperature-driven ion migration just by changing the voltage divider between the filament and a series resistance. Moreover, a series resistance can disguise the abrupt part of the SET process. The SET current transients can be subdivided into

a linear degradation of the HRS that is followed by a prominent and abrupt current jump. The first is caused by an electric-field-driven increase of the oxygen vacancy concentration near the Schottky barrier. If the field enhancement is accompanied by a steadily increasing temperature due to Joule heating, the positive feedback between current and temperature results in a self-acceleration of the SET process. Consequently, an abrupt current jump is always the characteristic of a thermal runaway. A similar (but not identical) compact model called JART VCM v1 is part of the Juelich Aachen Resistive Switching Tools. Its model implementations can be downloaded from [184].

In compact model 1.5, the description of the ion migration process is extended to include diffusion, and the oxygen vacancy concentration in the plug is introduced as second state variable. As a result, the number of vacancies is constant throughout the whole switching process, and the choice of the minimum and maximum vacancy concentration becomes less important to insignificant. The HRS evolves as a situation that is defined by a balance between drift and diffusion, representing a self-limiting RESET. In addition, the inclusion of diffusion leads to a finite retention. In the stable state, the oxygen vacancies in the filament are always distributed homogeneously due to the absence of internal electric fields under zero bias. This results in a low resistive stable state independent of the initial resistance. The simulation results also revealed that the initial values for the two vacancy concentrations are only relevant for the first sweep; the second and subsequent sweeps show a stable I-V characteristic that is only dependent on the total number of vacancies in the filament. With both the plug and the disc containing a variable vacancy concentration, both interfaces are modeled as Schottky contacts. In case of an asymmetric device stack, different values for the Schottky barrier height are used. If the nominal barrier height is chosen low and/or the vacancy concentration is high, the interface resistance becomes negligible, forming an ohmic contact. As the nominal barriers can also be chosen symmetric and high, the model successfully describes both bipolar and complementary switching consistently. Comparable to experimental observations, the occurrence of bipolar and complementary switching depends on the application of a current compliance in case of symmetric to moderately asymmetric device stacks. Moreover, the model captures non-standard effects in bipolar switching devices like the occurrence of an anomalous RESET peak or a SET overshoot. These can be explained satisfactorily as strongly asymmetric complementary switching peaks. This compact model is part of the Juelich Aachen Resistive Switching Tools as JART VCM v2; its model implementations in Verilog-A and as MATLAB App can be downloaded from [184].

In compact model 2.0, an oxygen exchange at the metal/oxide interfaces is added based on an adapted Butler-Volmer equation. Considering the concentration of oxygen ions that are adsorbed in the electrodes near the interfaces increases the number of state variables to four. As a result, the number of vacancies in the filament is not constant, whereas the total amount of oxygen ions in the whole system is preserved. The possible creation of vacancies at the interfaces allows the simulation of the forming process. The model well describes the dependence of the forming voltage on the oxide thickness. In addition, it covers that the growth direction of the filament during forming is determined by the rate-limiting step between vacancy generation and migration. Comparable to experimental observations, an appropriate current compliance is necessary to limit the amount of vacancies that is generated during the forming step to enable subsequent switching. Both, the forming process and the subsequent switching, can be described successfully by the same parameter set, excluding the effective thermal resistance. In general, the exchange barriers and the prefactors in the oxygen transfer reaction determine whether the total number of vacancies increases or decreases over time, crucially influencing the endurance and retention. The first results in a loss of the HRS, whereas the latter corresponds to a device where the HRS is the thermodynamically stable state. One drawback of the model is that it is so far impossible to find one single parameter set that provides a good fit to experimental data comprising the forming characteristics, the subsequent I-V switching sweeps, the endurance, and the retention. This is due in part to the weak influence that the voltage across the interface has on the oxygen exchange reaction; the oxygen exchange is mostly determined by the parameters for the exchange reaction. In addition, the temperature is more important than the polarity of the applied voltage. Compact model 2.0 also captures eightwise switching, which relies on the modulation of the Schottky barrier through oxygen exchange at the active electrode. Different from experimental data, the model predicts an abrupt RESET as a positive feedback exists between the voltage across the Schottky barrier and the oxygen transfer reaction. To prevent the positive feedback, the oxygen exchange process is kinetically limited by restricting the number of oxygen ions stored near the interface. This is achieved by splitting the electrode into two reservoirs, which exchange oxygen by diffusion. The diffusion from the second reservoir to the interface becomes the rate-limiting step, resulting in a gradual RESET.

Depending on the level of detail that is required, all three models are well suited for predictive circuit simulations.

#### 6.2 Outlook

The simulation results revealed that the compact models need to be improved further to cover all relevant switching features. Special attention should be paid to the calculation of the filament temperature and the electric field for the ion migration. The presented description based on the voltage drop across both the disc and the plug during the RESET can impede gradual switching: the increase in the disc resistance results in a temperature rise if the increasing voltage drop is significant compared to the decrease in current. Moreover, the electric field increases as the voltage across the disc rises more than the voltage across the plug decreases. Both effects, an increasing temperature and an increasing electric field, accelerate the RESET. As a result, the model cannot capture the kind of gradual RESET that is experimentally observed in some complementary switching devices. To weaken the disadvantageous feedback during the RESET, the voltage drops across the plug and the disc could be weighted by the ion concentration for the calculation of the electric field. Furthermore, voltage-dependent filament resistances could be advantageous. Using different temperatures for the filament regions might also help. Possibly, a detailed comparison with a space-resolved continuum model could provide essential input for improvement. In any case, further research on the thermal conductivity of transition metal oxides and its dependence on defect concentration and temperature is necessary.

Further work is necessary to improve the modeling of the oxygen exchange reaction. For example, the dependence of the reaction on the applied electric field has to be strengthened. Or the other way round, the driving force that results from the differing oxygen concentrations is too strong and its influence needs to be weakened. Consequently, deriving novel equations is fundamental. Changing the definition of the reservoir for the absorbed oxygen ions in the electrode could improve the balance between the concentration- and the field-driven oxygen exchange. Moreover, modeling the migration of the oxygen ions in the electrode as in the approach for eightwise switching devices could be considered. To this end, the maximum concentration of absorbed oxygen ions has to be chosen more material specific. An improved model also needs to consider the influence of hydrogen (moisture) because its presence is discussed to be necessary during the forming process [99] and to be significant during switching in counter-eightwise [41, 100–102] and eightwise [185] switching devices. The presented description is based on the Butler-Volmer equation, which is often used in electrochemical kinetics studies. The Butler-Volmer equation, however, was deduced for an ion transfer reaction at an interface between a metal and an ion conductor, where a conduction of electrons detached from the ion transfer is not considered. In contrast, the transfer of oxygen ions in VCM-type ReRAM occurs at interfaces between metals and mixed ionic electronic conductors. In general, sufficiently accurate knowledge on the adsorption mechanism of the oxygen ions in the metal electrodes and their subsequent migration is crucial but missing so far. For example, the transfer of electrons may be the rate-limiting step and/or takes place at the opposite electrode.

To increase the model accuracy, the equations for the electrical conduction through the Schottky contacts need to be revised. So far, especially the tunneling component is not described appropriately. As a consequence, the filament resistances need to dominate the overall resistance in the model in order to get a symmetric I-V curve. Therefore, the development of suitable compact model equations for the tunneling currents through the metal/oxide contacts of ReRAM devices is crucial. In addition, further research on the (dominant) electrical conduction mechanism in the filament, which could comprise for example trap-assisted tunneling, is necessary.

Compared to experimental data, the simulated retention times are usually far too short if the same parameters are used that are necessary to obtain realistic switching times. Choosing a higher ion activation barrier results in the desired retention behavior but it increases inevitably the switching voltage/time. Fundamental research is necessary to address this open question.

A future version of the model should address radial diffusion of oxygen vacancies to the surrounding oxide as it is a potential source for retention loss. Thermodiffusion, i.e. diffusion due to a temperature gradient, could be considered as well although the opinions on its importance in resistive switching diverge.

Reliability is one of the most crucial problem of filamentary VCM-type ReRAM on the way towards application. So far, variability is not covered by the presented deterministic compact models. A variability approach, however, can be set on top of all three models by randomly varying some material and geometry parameters in a predefined range after each switching cycle. For compact model 1.0, one example was already implemented [69]. Besides pursuing the variability approach, future work should comprise the implementation of compact model 1.5 and 2.0 in Verilog-A or SPICE to enable circuit simulations. Future studies could analyze for example the forming behavior of devices in crossbar arrays or the influence of transistors as voltage-dependent series resistances on the switching in compact model 2.0.

A major challenging milestone for a future physics-based compact model will be the presentation of an improved model with one single parameter set that provides a good fit to experimental data comprising forming characteristics, subsequent I-V switching sweeps, endurance, and retention. Ideally, the individual parameters would be determined by independent physical measurements.

# **A** Appendices

## A.1 Derivation of the Ionic Current Density

With the general parameter for the energy barriers in forward and reverse direction  $W_{\rm A}^{\rm f/r}$  Eq. (2.17) becomes

$$J_{\rm ion} = zeN_{\rm L}a\nu_0 \exp\left(-\frac{\Delta W_{\rm A}^{\rm f}}{k_{\rm B}T}\right) \left(1 - \frac{N_{\rm R}}{N_{\rm max}}\right) - zeN_{\rm R}a\nu_0 \exp\left(-\frac{\Delta W_{\rm A}^{\rm r}}{k_{\rm B}T}\right) \left(1 - \frac{N_{\rm L}}{N_{\rm max}}\right). \tag{A.1}$$

Substituting  $N_{\rm L}$  by (2.18) and  $N_{\rm R}$  by (2.19) yields

$$J_{\text{ion}} = zea\nu_{0} \exp\left(-\frac{\Delta W_{A}^{f}}{k_{B}T}\right) \left(N - \frac{a}{2}\frac{dN}{dx}\right) \left(1 - \frac{N}{N_{\text{max}}} - \frac{a}{2N_{\text{max}}}\frac{dN}{dx}\right)$$

$$- zea\nu_{0} \exp\left(-\frac{\Delta W_{A}^{f}}{k_{B}T}\right) \left(N + \frac{a}{2}\frac{dN}{dx}\right) \left(1 - \frac{N}{N_{\text{max}}} + \frac{a}{2N_{\text{max}}}\frac{dN}{dx}\right)$$

$$= zea\nu_{0} \exp\left(-\frac{\Delta W_{A}^{f}}{k_{B}T}\right) \left[N - \frac{N^{2}}{N_{\text{max}}} - \frac{Na}{2N_{\text{max}}}\frac{dN}{dx} - \frac{a}{2}\frac{dN}{dx} + \frac{Na}{2N_{\text{max}}}\frac{dN}{dx} + \frac{a^{2}}{4N_{\text{max}}}\frac{dN}{dx}\right]$$

$$- zea\nu_{0} \exp\left(-\frac{\Delta W_{A}^{f}}{k_{B}T}\right) \left[N - \frac{N^{2}}{N_{\text{max}}} + \frac{Na}{2N_{\text{max}}}\frac{dN}{dx} + \frac{a}{2}\frac{dN}{dx} - \frac{Na}{2N_{\text{max}}}\frac{dN}{dx} + \frac{a^{2}}{4N_{\text{max}}}\frac{dN}{dx}\right]$$

$$(A.2)$$

In Eq. (A.2), the second-order terms are neglected. Substituting  $W_{\rm A}^{\rm f/r}$  by (2.15) results in

$$J_{\text{ion}} = zea\nu_{0} \exp\left(-\frac{\Delta W_{\text{A}}}{k_{\text{B}}T} \left[\sqrt{1-\gamma^{2}} - \gamma\left(\frac{\pi}{2}\right) + \gamma \arcsin\gamma\right]\right) \left[N - \frac{N^{2}}{N_{\text{max}}} - \frac{a}{2} \frac{dN}{dx}\right] - zea\nu_{0} \exp\left(-\frac{\Delta W_{\text{A}}}{k_{\text{B}}T} \left[\sqrt{1-\gamma^{2}} + \gamma\left(\frac{\pi}{2}\right) + \gamma \arcsin\gamma\right]\right) \left[N - \frac{N^{2}}{N_{\text{max}}} + \frac{a}{2} \frac{dN}{dx}\right] = zea\nu_{0} \exp\left(-\frac{\Delta W_{\text{A}}}{k_{\text{B}}T} \left[\sqrt{1-\gamma^{2}} + \gamma \arcsin\gamma\right]\right) \left[N - \frac{N^{2}}{N_{\text{max}}}\right].$$

$$\left\{\exp\left(\frac{\Delta W_{\text{A}}}{k_{\text{B}}T} \gamma\left(\frac{\pi}{2}\right)\right) - \exp\left(-\frac{\Delta W_{\text{A}}}{k_{\text{B}}T} \gamma\left(\frac{\pi}{2}\right)\right)\right\} - zea\nu_{0} \exp\left(-\frac{\Delta W_{\text{A}}}{k_{\text{B}}T} \left[\sqrt{1-\gamma^{2}} + \gamma \arcsin\gamma\right]\right) \left[\frac{a}{2} \frac{dN}{dx}\right].$$

$$\left\{\exp\left(\frac{\Delta W_{\text{A}}}{k_{\text{B}}T} \gamma\left(\frac{\pi}{2}\right)\right) + \exp\left(-\frac{\Delta W_{\text{A}}}{k_{\text{B}}T} \gamma\left(\frac{\pi}{2}\right)\right)\right\}$$

$$= zea\nu_{0} \exp\left(-\frac{\Delta W_{\text{A}}}{k_{\text{B}}T} \left[\sqrt{1-\gamma^{2}} + \gamma \arcsin\gamma\right]\right) N \left[1 - \frac{N}{N_{\text{max}}}\right].$$

$$2 \sinh\left(\frac{\Delta W_{\text{A}}}{k_{\text{B}}T} \gamma\left(\frac{\pi}{2}\right)\right) - zea\nu_{0} \exp\left(-\frac{\Delta W_{\text{A}}}{k_{\text{B}}T} \left[\sqrt{1-\gamma^{2}} + \gamma \arcsin\gamma\right]\right) \left[\frac{a}{2} \frac{dN}{dx}\right].$$

$$2 \cosh\left(\frac{\Delta W_{\text{A}}}{k_{\text{B}}T} \gamma\left(\frac{\pi}{2}\right)\right).$$
(A.3)

Substituting  $\gamma$  (Eq. (2.16)) in the sinh / cosh-terms yields

$$\sinh\left(\frac{\Delta W_{\rm A}}{k_{\rm B}T}\gamma\left(\frac{\pi}{2}\right)\right) = \sinh\left(\frac{\Delta W_{\rm A}}{k_{\rm B}T}\left(\frac{|z|eEa}{\pi\Delta W_{\rm A}}\right)\left(\frac{\pi}{2}\right)\right) = \sinh\left(\frac{|z|eEa}{2k_{\rm B}T}\right). \tag{A.4}$$

Finally, combining Eqs. (A.3) and (A.4) gives

$$J_{\text{ion}} = CN \sinh\left(\frac{|z|eEa}{2k_{\text{B}}T}\right) \left(1 - \frac{N}{N_{\text{max}}}\right) - C\frac{a}{2}\frac{dN}{dx} \cosh\left(\frac{|z|eEa}{2k_{\text{B}}T}\right)$$
(A.5)

with C as

$$C = 2zea\nu_0 \exp\left(-\frac{\Delta W_{\rm A} \left[\sqrt{1-\gamma^2} + \gamma \arcsin \gamma\right]}{k_{\rm B}T}\right). \tag{A.6}$$

## A.2 Additional Parameters

**Table A.1:** Calculation of the oxygen concentration in a stoichiometric oxide. Three examples are given for a rough estimation of  $N_{\text{O,oxide,max}}$ . All material parameters are takten from [186].

$Ta_2O_5$		
molar mass	$M = 442 \mathrm{g/mol}$	
density	$\rho = 8.2  \mathrm{g/cm^3}$	
Avogadro constant	$N_{\rm A} = 6.022 \cdot 10^{23}  \rm mol^{-1}$	
$N_{\rm O} = \rho  \frac{N_{\rm A}}{M} \cdot 5 = 5.6  \cdot 10^{5}$	$^{22}\mathrm{cm}^3$	
$HfO_2$		
$M = 210 \mathrm{g/mol}$	$\rho = 9.7\mathrm{g/cm^3}$	
$N_{\rm O} = \rho  \frac{N_{\rm A}}{M} \cdot 2 = 5.6  \cdot 10^{22}  {\rm cm}^3$		
$ m ZrO_2$		
$M = 123 \mathrm{g/mol}$	$\rho = 5.7 \mathrm{g/cm^3}$	
$N_{\rm O} = \rho  \frac{N_{\rm A}}{M} \cdot 2 = 5.6 \cdot 10^5$	$^{22}\mathrm{cm}^3$	

**Table A.2:** Used series resistance  $R_{\text{series,cc}}$  for the simulations in Fig. 5.5.

	Scries,ee 3
Simulation	$l_{\text{cell}} = 3 \text{nm},  5 \text{nm},  7.5 \text{nm},  10 \text{nm},  12.5 \text{nm},  15 \text{nm}$
$G_{\rm II,OE} = 1.15 \mathrm{eV}$	$R_{\rm series,cc} = 100 \mathrm{k}\Omega,  160 \mathrm{k}\Omega,  240 \mathrm{k}\Omega,  320 \mathrm{k}\Omega,  400 \mathrm{k}\Omega,  480 \mathrm{k}\Omega$
$G_{\rm II,OE} = 0.95 \mathrm{eV}$	$R_{\rm series,cc} = 50 \mathrm{k}\Omega, 80 \mathrm{k}\Omega, 120 \mathrm{k}\Omega, 160 \mathrm{k}\Omega, 200 \mathrm{k}\Omega, 240 \mathrm{k}\Omega$
$\Delta W_{\rm A} = 0.8  {\rm eV}$	$R_{\rm series,cc} = 50\mathrm{k}\Omega,80\mathrm{k}\Omega,120\mathrm{k}\Omega,160\mathrm{k}\Omega,200\mathrm{k}\Omega,240\mathrm{k}\Omega$
$\Delta W_{\rm A} = 1.0  {\rm eV}$	$R_{\rm series,cc} = 50\mathrm{k}\Omega,130\mathrm{k}\Omega,180\mathrm{k}\Omega,250\mathrm{k}\Omega,600\mathrm{k}\Omega,1000\mathrm{k}\Omega$
$\varphi_{\mathrm{Bn0,OE}} = 0.1\mathrm{V}$	$R_{\rm series,cc} = 50\mathrm{k}\Omega,80\mathrm{k}\Omega,120\mathrm{k}\Omega,160\mathrm{k}\Omega,200\mathrm{k}\Omega,240\mathrm{k}\Omega$
$\mu_{\rm n0} = 3 \cdot 10^{-6}  \rm m^2/(Vs)$	$R_{\rm series,cc} = 50\mathrm{k}\Omega,80\mathrm{k}\Omega,120\mathrm{k}\Omega,160\mathrm{k}\Omega,200\mathrm{k}\Omega,240\mathrm{k}\Omega$
$R_{\mathrm{th,eff,F}} = 1 \cdot 10^6  \mathrm{K/W}$	$R_{\rm series,cc} = 50\mathrm{k}\Omega,80\mathrm{k}\Omega,120\mathrm{k}\Omega,160\mathrm{k}\Omega,200\mathrm{k}\Omega,240\mathrm{k}\Omega$
$r_{\rm fil} = 10{ m nm}$	$R_{\rm series,cc} = 50\mathrm{k}\Omega,80\mathrm{k}\Omega,120\mathrm{k}\Omega,160\mathrm{k}\Omega,200\mathrm{k}\Omega,240\mathrm{k}\Omega$

**Table A.3:** Used series resistance  $R_{\text{series,cc}}$  for the simulations in Fig. 5.16b.

Simulation	$l_{\rm cell} = 5  \mathrm{nm}$
$\Delta G_{\mathrm{I,OE}} = 1.3 \mathrm{eV},  \Delta G_{\mathrm{II,OE}} = 1.05 \mathrm{eV}$	$R_{\rm series,cc} = 20 \mathrm{k}\Omega$
$\Delta G_{ m I,OE} = \Delta G_{ m II,OE} = 1.1  { m eV}$	$R_{\rm series,cc} = 30 \mathrm{k}\Omega$
$\Delta G_{\rm I,OE} = \Delta G_{\rm II,OE} = 1.1 \text{eV}, \ k_{\rm I,OE}^0 = k_{\rm II,OE}^0 = 1 \cdot 10^3 \text{m/s}$	$R_{\rm series,cc} = 100 \mathrm{k}\Omega$
$\Delta G_{\mathrm{I,OE}} = 1.05 \mathrm{eV}, \ \Delta G_{\mathrm{II,OE}} = 1.3 \mathrm{eV}$	$R_{\rm series,cc} = 1.4 \mathrm{M}\Omega$

## A.3 Volatile HRS Asymmetry and Subloops

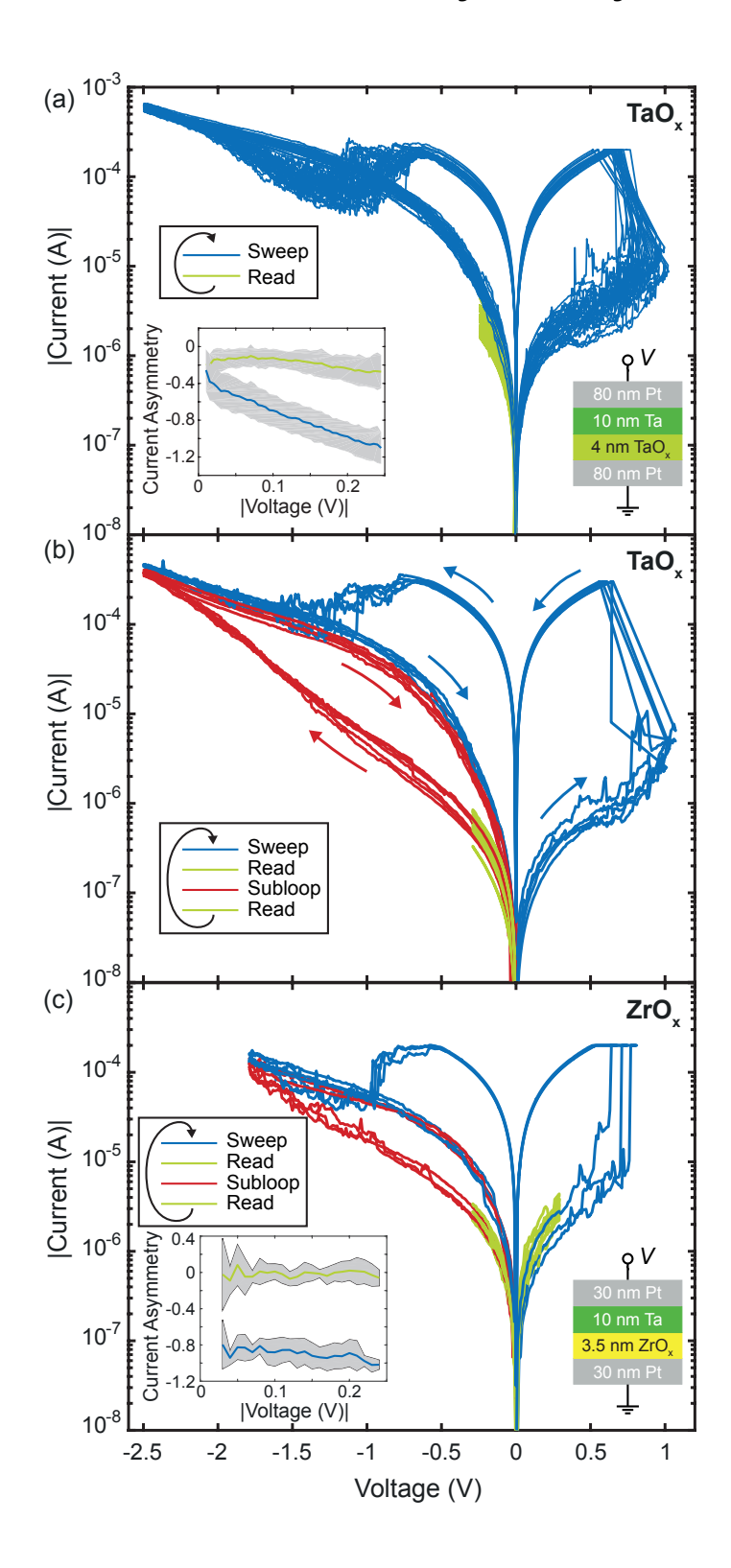


Figure A.1: Experimental study on the volatile asymmetry appearance of subloops Pt/TaO<sub>x</sub>/Ta/Pt and Pt/ZrO<sub>x</sub>/Ta/Pt devices, see [167] for details. Fabrication and measurement of the ZrO<sub>x</sub> device were done by Andreas Kindsmüller. Note that the voltage is applied to the ohmic electrode in these measurements, in contrast to the convention used in this thesis. Thus, the RESET proceeds for negative applied voltages, which convert to a positive potential applied at the AE. (a) In a TaO<sub>x</sub> device, BS and read sweeps are performed alternatingly. A clear asymmetry is visible in the switching sweeps. The read sweeps (green) do not coincide with the switching sweeps (blue) and the HRS is more symmetric during the read than during the BS. The calculated mean current asymmetries of all read and switching sweeps are shown in the inset, the gray area describes the interval of mean  $\pm$  standard deviation. The current asymmetry is defined as (I(+V) -|I(-V)|/mean[I(+V), |I(-V)|][187]. (b) Subloops occur upon applying a voltage half sweep with negative polarity. (c) In a ZrO<sub>x</sub> device, subloops occur under the same conditions. Like in the  $TaO_x$ device, the read sweeps show a more symmetric HRS than the switching sweeps, see the inset. Reproduced with permission from [167], © The Royal Society of Chemistry 2017

# **Bibliography**

- [1] G. E. Moore, "Cramming more components onto integrated circuits," *Electronics*, vol. 38, no. 8, 1965.
- [2] ITRS, "The International Technology Roadmap for Semiconductors 2.0 ITRS 2015 Edition," International Technology Roadmap for Semiconductors 2.0, 2015.
- [3] R. Waser, "Memory Devices and Storage Systems Introduction to Part V," in *Nanoelectronics and Information Technology* (R. Waser, ed.), pp. 603–620, Wiley-VCH, 3 ed., 2012.
- [4] J. J. Yang, D. B. Strukov, and D. R. Stewart, "Memristive devices for computing," *Nat. Nanotechnol.*, vol. 8, no. 1, pp. 13–24, 2013.
- [5] U. Schröder, H. Schröder, A. Kingon, S. Summerfelt, C. S. Hwang, and U. Böttger, "Capacitor-based Random Access Memories," in *Nanoelectronics and Information Technology* (R. Waser, ed.), pp. 635–654, Wiley-VCH, 3 ed., 2012.
- [6] V. Zhirnov and T. Mikolajick, "Flash Memories," in *Nanoelectronics and Information Technology* (R. Waser, ed.), pp. 621–634, Wiley-VCH, 3 ed., 2012.
- [7] A. Sawa, "Resistive switching in transition metal oxides," *Mater. Today*, vol. 11, no. 6, pp. 28–36, 2008.
- [8] R. Waser, R. Dittmann, G. Staikov, and K. Szot, "Redox-Based Resistive Switching Memories - Nanoionic Mechanisms, Prospects, and Challenges," Adv. Mater., vol. 21, no. 25-26, pp. 2632–2663, 2009.
- [9] H.-S. P. Wong, H.-Y. Lee, S. Yu, Y.-S. Chen, Y. Wu, P.-S. Chen, B. Lee, F. T. Chen, and M.-J. Tsai, "Metal-Oxide RRAM," Proc. IEEE, vol. 100, no. 6, pp. 1951–1970, 2012.
- [10] H. Akinaga, "Recent Advances and Future Prospects in Functional-Oxide Nanoelectronics: The Emerging Materials and Novel Functionalities that are Accelerating Semiconductor Device Research and Development," Jpn. J. Appl. Phys., vol. 52, pp. 100001/1–12, 2013.
- [11] R. Waser, D. Ielmini, H. Akinaga, H. Shima, H.-S. P. Wong, J. J. Yang, and S. Yu, "Introduction to Nanoionic Elements for Information Technology," in *Resistive Switching: From Fundamentals of Nanoionic Redox Processes to Memristive Device Applications* (D. Ielmini, R. Waser, ed.), pp. 1–29, Wiley-VCH, 1 ed., 2016.
- [12] M. A. Zidan, J. P. Strachan, and W. D. Lu, "The future of electronics based on memristive systems," *Nat. Electron.*, vol. 1, pp. 22–29, 2018.

- [13] J. Borghetti, G. S. Snider, P. J. Kuekes, J. J. Yang, D. R. Stewart, and R. S. Williams, "'Memristive' switches enable 'stateful' logic operations via material implication," *Nature*, vol. 464, no. 7290, pp. 873–876, 2010.
- [14] M. Prezioso, F. Merrikh-Bayat, B. D. Hoskins, G. C. Adam, K. K. Likharev, and D. B. Strukov, "Training and operation of an integrated neuromorphic network based on metal-oxide memristors," *Nature*, vol. 521, no. 7550, pp. 61–64, 2015.
- [15] A. Siemon, T. Breuer, N. Aslam, S. Ferch, W. Kim, J. van den Hurk, V. Rana, S. Hoffmann-Eifert, R. Waser, S. Menzel, and E. Linn, "Realization of Boolean Logic Functionality using Redox-based Memristive Devices," *Adv. Funct. Mater.*, vol. 25, no. 40, pp. 6414–6423, 2015.
- [16] M. M. Shulaker, G. Hills, R. S. Park, R. T. Howe, K. Saraswat, H.-S. P. Wong, and S. Mitra, "Three-dimensional integration of nanotechnologies for computing and data storage on a single chip," *Nature*, vol. 547, pp. 74–78, 2017.
- [17] C. Yoshida, K. Tsunoda, H. Noshiro, and Y. Sugiyama, "High speed resistive switching in Pt/TiO<sub>2</sub>/TiN film for nonvolatile memory application," *Appl. Phys. Lett.*, vol. 91, no. 22, pp. 223510/1–3, 2007.
- [18] M. Terai, Y. Sakotsubo, S. Kotsuji, and H. Hada, "Resistance Controllability of Ta<sub>2</sub>O<sub>5</sub>/TiO<sub>2</sub> Stack ReRAM for Low-Voltage and Multilevel Operation," *IEEE Electron Device Lett.*, vol. 31, no. 3, pp. 204–206, 2010.
- [19] E. J. Merced-Grafals, N. Davila, N. Ge, R. S. Williams, and J. P. Strachan, "Repeatable, accurate, and high speed multi-level programming of memristor 1T1R arrays for power efficient analog computing applications," *Nanotechnology*, vol. 27, no. 36, pp. 365202/1–9, 2016.
- [20] J. Y. Seok, S. J. Song, J. H. Yoon, K. J. Yoon, T. H. Park, D. E. Kwon, H. Lim, G. H. Kim, D. S. Jeong, and C. S. Hwang, "A Review of Three-Dimensional Resistive Switching Cross-Bar Array Memories from the Integration and Materials Property Points of View," Adv. Funct. Mater., vol. 24, pp. 5316–5339, 2014.
- [21] M. Yu, Y. Cai, Z. Wang, Y. Fang, Y. Liu, Z. Yu, Y. Pan, Z. Thang, J. Tan, X. Yang, M. Li, and R. Huang, "Novel Vertical 3D Structure of TaO<sub>x</sub>-based RRAM with Self-localized Switching Region by Sidewall Electrode Oxidation," Sci. Rep., vol. 6, pp. 21020/1–10, 2016.
- [22] A. C. Torrezan, J. P. Strachan, G. Medeiros-Ribeiro, and R. S. Williams, "Subnanosecond switching of a tantalum oxide memristor," *Nanotechnology*, vol. 22, pp. 485203/1–7, 2011.
- [23] H. Y. Lee, Y. S. Chen, P. S. Chen, P. Y. Gu, Y. Y. Hsu, S. M. Wang, W. H. Liu, C. H. Tsai, S. S. Sheu, P. C. Chiang, W. P. Lin, C. H. Lin, W. S. Chen, F. T. Chen, C. H. Lien, and M. Tsai, "Evidence and solution of Over-RESET Problem for HfO<sub>x</sub> Based Resistive Memory with Sub-ns Switching Speed and High Endurance," in 2010 International Electron Devices Meeting (IEDM), pp. 19.7.1–19.7.4, 2010.

- [24] V. Havel, K. Fleck, B. Rösgen, V. Rana, S. Menzel, U. Böttger, and R. Waser, "Ultra-fast Switching in Ta<sub>2</sub>O<sub>5</sub>-based Resistive Memories," in *Silicon Nanoelectronics Worshop SNW*, pp. 82–83, 2016.
- [25] B. Govoreanu, G. S. Kar, Y.-Y. Chen, V. Paraschiv, S. Kubicek, A. Fantini, I. P. Radu, L. Goux, S. Clima, R. Degraeve, N. Jossart, O. Richard, T. Vandeweyer, K. Seo, P. Hendrickx, G. Pourtois, H. Bender, L. Altimime, D. J. Wouters, J. A. Kittl, and M. Jurczak, "10x10 nm² Hf/HfOx Crossbar Resistive RAM with Excellent Performance, Reliability and Low-Energy Operation," in 2011 IEEE International Electron Devices Meeting (IEDM), pp. 31.6.1–31.6.4, 2011.
- [26] F. Miao, J. P. Strachan, J. J. Yang, M.-X. Zhang, I. Goldfarb, A. C. Torrezan, P. Eschbach, R. D. Kelly, G. Medeiros-Ribeiro, and R. S. Williams, "Anatomy of a Nanoscale Conduction Channel Reveals the Mechanism of a High-Performance Memristor," Adv. Mater., vol. 23, pp. 5633–5640, 2011.
- [27] M.-J. Lee, C. B. Lee, D. Lee, S. R. Lee, M. Chang, J. H. Hur, Y.-B. Kim, C. J. Kim, D. H. Seo, S. Seo, U.-I. Chung, I.-K. Yoo, and K. Kim, "A fast, high-endurance and scalable non-volatile memory device made from asymmetric Ta<sub>2</sub>O<sub>5-x</sub>/TaO<sub>2-x</sub> bilayer structures," Nat. Mater., vol. 10, no. 8, pp. 625–630, 2011.
- [28] B. Traoré, P. Blaise, E. Vianello, H. Grampeix, S. Jeannot, L. Perniola, B. De Salvo and Y. Nishi, "On the Origin of Low-Resistance State Retention Failure in HfO<sub>2</sub>-Based RRAM and Impact of Doping/Alloying," *IEEE Trans. Electron Devices*, vol. 62, pp. 4029–4036, 2015.
- [29] G. Dearnaley, A. M. Stoneham, and D. V. Morgan, "Electrical phenomena in amorphous oxide films," *Rep. Prog. Phys.*, vol. 33, no. 3, pp. 1129–1191, 1970.
- [30] D. P. Oxley, "Electroforming, switching and memory effects in oxide thin films," *Electrocomponent Science and Technology*, UK, vol. 3, no. 4, pp. 217–24, 1977.
- [31] H. Pagnia and N. Sotnik, "Bistable Switching in Electroformed Metal-Insulator-Metal Devices," *Phys. Stat. Sol.*, vol. 108, no. 1, pp. 11–65, 1988.
- [32] D. B. Strukov, G. S. Snider, D. R. Stewart, and R. S. Williams, "The missing memristor found," *Nature*, vol. 453, no. 7191, pp. 80–83, 2008.
- [33] L. Chua, "Memristor-The Missing Circuit Element," *IEEE Trans. Circuit Theory*, vol. 18, no. 5, pp. 507–519, 1971.
- [34] L. Chua and S. Kang, "Memristive Devices and Systems," *Proc. IEEE*, vol. 64, no. 2, pp. 209–223, 1976.
- [35] S. Vongehr and X. Meng, "The Missing Memristor has Not been Found," Sci. Rep., vol. 5, pp. 11657/1–7, 2015.
- [36] G. Indiveri, B. Linares-Barranco, R. Legenstein, G. Deligeorgis, and T. Prodromakis, "Integration of nanoscale memristor synapses in neuromorphic computing architectures," *Nanotechnology*, vol. 24, pp. 384010/1–13, 2013.

- [37] S. Yu, B. Gao, Z. Fang, H. Yu, J. Kang, and H. Wong, "Stochastic learning in oxide binary synaptic device for neuromorphic computing," *Frontiers in Neuroscience*, vol. 7, pp. 186/1–9, 2013.
- [38] C. Funck, A. Marchewka, C. Bäumer, P. C. Schmidt, P. Müller, R. Dittmann, M. Martin, R. Waser, and S. Menzel, "A Theoretical and Experimental View on the Temperature Dependence of the Electronic Conduction through a Schottky Barrier in a Resistively Switching SrTiO<sub>3</sub>-based Memory Cell," *Adv. Electron. Mater.*, vol. 4, no. 7, pp. 1800062/1–12, 2018.
- [39] M. Schie, M. P. Müller, M. Salinga, R. Waser, and R. A. De Souza, "Ion migration in crystalline and amorphous HfO<sub>x</sub>," *J. Chem. Phys.*, vol. 146, no. 9, pp. 94508/1–9, 2017.
- [40] S. Clima, Y. Y. Chen, C. Y. Chen, L. Goux, B. Govoreanu, R. Degraeve, A. Fantini, M. Jurczak, and G. Pourtois, "First-principles thermodynamics and defect kinetics guidelines for engineering a tailored RRAM device," J. Appl. Phys., vol. 119, pp. 225107/1–8, 2016.
- [41] D. Duncan, B. Magyari-Köpe, and Y. Nishi, "Hydrogen doping in HfO<sub>2</sub> resistance change random access memory," *Appl. Phys. Lett.*, vol. 108, no. 4, pp. 43501/1–5, 2016.
- [42] S. Larentis, F. Nardi, S. Balatti, D. C. Gilmer, and D. Ielmini, "Resistive Switching by Voltage-Driven Ion Migration in Bipolar RRAM-Part II: Modeling," *IEEE Trans. Electron Devices*, vol. 59, no. 9, pp. 2468–2475, 2012.
- [43] S. Kim, S. Choi, and W. Lu, "Comprehensive Physical Model of Dynamic Resistive Switching in an Oxide Memristor," *ACS Nano*, vol. 8, pp. 2369–2376, 2014.
- [44] A. Marchewka, B. Rösgen, K. Skaja, H. Du, C. L. Jia, J. Mayer, V. Rana, R. Waser, and S. Menzel, "Nanoionic Resistive Switching Memories: On the Physical Nature of the Dynamic Reset Process," Adv. Electron. Mater., vol. 2, no. 1, pp. 1500233/1–13, 2016.
- [45] X. Guan, S. Yu, and H. Wong, "On the Switching Parameter Variation of Metal-Oxide RRAM-Part I: Physical Modeling and Simulation Methodology," *IEEE Trans. Electron Devices*, vol. 59, no. 4, pp. 1172–1182, 2012.
- [46] A. Padovani, L. Larcher, O. Pirrotta, L. Vandelli, and G. Bersuker, "Microscopic Modeling of HfO<sub>x</sub> RRAM Operations: From Forming to Switching," *IEEE Trans. Electron Devices*, vol. 62, no. 6, pp. 1998–2006, 2015.
- [47] E. Abbaspour, S. Menzel, A. Hardtdegen, S. Hoffmann-Eifert, and C. Jungemann, "KMC Simulation of the Electroforming, Set and Reset Processes in Redox-based Resistive Switching Devices," *IEEE Trans. Nanotechnol.*, vol. 17, no. 6, pp. 1181–1188, 2018.
- [48] J. H. Hur, M.-J. Lee, C. B. Lee, Y.-B. Kim, and C.-J. Kim, "Modeling for bipolar resistive memory switching in transition-metal oxides," *Phys. Rev. B*, vol. 82, pp. 155321/1–5, 2010.
- [49] X. Guan, S. Yu, and H. S. P. Wong, "A SPICE Compact Model of Metal Oxide Resistive Switching Memory With Variations," *IEEE Electron Device Lett.*, vol. 33, no. 10, pp. 1405–1407, 2012.

- [50] R. Degraeve, A. Fantini, S. Clima, B. Govoreanu, L. Goux, Y. Chen, D. Wouters, P. Roussel, G. Kar, G. Pourtois, S. Cosemans, J. Kittl, G. Groeseneken, M. Jurczak, and L. Altimime, "Dynamic 'Hour Glass' Model for SET and RESET in HfO<sub>2</sub> RRAM," in 2012 Symposium on VLSI Technology (VLSIT), pp. 75–76, 2012.
- [51] J. P. Strachan, A. C. Torrezan, F. Miao, M. D. Pickett, J. J. Yang, W. Yi, G. Medeiros-Ribeiro, and R. S. Williams, "State Dynamics and Modeling of Tantalum Oxide Memristors," *IEEE Trans. Electron Devices*, vol. 60, no. 7, pp. 2194–2202, 2013.
- [52] A. Siemon, S. Menzel, A. Marchewka, Y. Nishi, R. Waser, and E. Linn, "Simulation of TaO<sub>x</sub>-based Complementary Resistive Switches by a Physics-based Memristive Model," in 2014 IEEE International Symposium on Circuits and Systems (ISCAS), pp. 1420– 1423, 2014.
- [53] S. Ambrogio, S. Balatti, D. C. Gilmer, and D. Ielmini, "Analytical Modeling of Oxide-Based Bipolar Resistive Memories and Complementary Resistive Switches," *IEEE Trans. Electron Devices*, vol. 61, no. 7, pp. 2378–2386, 2014.
- [54] L. Zhang, N. Ge, J. J. Yang, Z. Li, R. S. Williams, and Y. Chen, "Low voltage two-state-variable memristor model of vacancy-drift resistive switches," *Appl. Phys. A Mater. Sci. Process.*, vol. 119, no. 1, pp. 1–9, 2015.
- [55] Z. Jiang, Y. Wu, S. Yu, L. Yang, K. Song, Z. Karim, and H.-P. Wong, "A Compact Model for Metal-Oxide Resistive Random Access Memory With Experiment Verification," *IEEE Trans. Electron Devices*, vol. 63, pp. 1884–1892, 2016.
- [56] S. Kim, H. Kim, and S. Choi, "Compact Two-State-Variable Second-Order Memristor Model," Small, vol. 12, pp. 3320–3326, 2016.
- [57] E. Linn, A. Siemon, R. Waser, and S. Menzel, "Applicability of Well-Established Memristive Models for Simulations of Resistive Switching Devices," *IEEE Trans. Circuits Syst. I, Reg. Papers*, vol. 61, no. 8, pp. 2402–2410, 2014.
- [58] S. Menzel, A. Siemon, A. Ascoli, and R. Tetzlaff, "Requirements and Challenges for Modelling Redox-based Memristive Devices," in 2018 IEEE International Symposium on Circuits and Systems (ISCAS), pp. 1–5, 2018.
- [59] M. D. Pickett, D. B. Strukov, J. L. Borghetti, J. J. Yang, G. S. Snider, D. R. Stewart, and R. S. Williams, "Switching dynamics in titanium dioxide memristive devices," J. Appl. Phys., vol. 106, no. 7, pp. 074508/1–6, 2009.
- [60] H. Abdalla and M. D. Pickett, "SPICE Modeling of Memristors," in *IEEE International Symposium on Circuits and Systems (ISCAS)*, pp. 1832–1835, 2011.
- [61] D. Ielmini, "Modeling the Universal Set/Reset Characteristics of Bipolar RRAM by Field- and Temperature-Driven Filament Growth," *IEEE Trans. Electron. Devices*, vol. 58, no. 12, pp. 4309–4317, 2011.
- [62] J. Noh, M. Jo, C. Y. Kang, D. Gilmer, P. Kirsch, J. C. Lee, and B. H. Lee, "Development of a Semiempirical Compact Model for DC/AC Cell Operation of HfO<sub>x</sub>-Based ReRAMs," *IEEE Electron Device Lett.*, vol. 34, no. 9, pp. 1133–1135, 2013.

- [63] E. Miranda, D. Jimenez, and J. Suñé, "The Quantum Point-Contact Memristor," *IEEE Electron Device Lett.*, vol. 33, no. 10, pp. 1474–1476, 2012.
- [64] G. González-Cordero, J. B. Roldan, F. Jiménez-Molinos, J. Suñé, S. Long, and M. Liu, "A new compact model for bipolar RRAMs based on truncated-cone conductive filaments-a Verilog-A approach," Semicond. Sci. Tech., vol. 31, pp. 115013/1–13, 2016.
- [65] P. Huang, D. Zhu, S. Chen, Z. Zhou, Z. Chen, B. Gao, L. Liu, X. Liu, and J. Kang, "Compact Model of HfO<sub>x</sub>-Based Electronic Synaptic Devices for Neuromorphic Computing," *IEEE Trans. Electron Devices*, vol. 64, no. 2, pp. 614–621, 2017.
- [66] P. Huang, X. Y. liu, B. Chen, H. T. Li, Y. J. Wang, Y. X. Deng, K. L. Wei, L. Zeng, B. Gao, G. Du, X. Zhang, and J. F. Kang, "A Physics-Based Compact Model of Metal-Oxide-Based RRAM DC and AC Operations," *IEEE Trans. Electron Devices*, vol. 60, no. 12, pp. 4090–4097, 2013.
- [67] C. La Torre, "Statistische Charakterisierung und Modellierung von resistiv schaltenden VCM-Speicherzellen." Master thesis, RWTH Aachen University, 2014.
- [68] P. Chen and S. Yu, "Compact Modeling of RRAM Devices and Its Applications in 1T1R and 1S1R Array Design," *IEEE Trans. Electron Devices*, vol. 62, pp. 4022–4028, 2015.
- [69] C. Bengel, "Influence of the Variability of ReRAM cells on Neuromorphic Circuits." Master thesis, RWTH Aachen University, 2018.
- [70] B. Gao, H. Zhang, B. Chen, L. Liu, X. Liu, R. Han, J. Kang, Z. Fang, H. Yu, B. Yu, and D.-L. Kwong, "Modeling of Retention Failure Behavior in Bipolar Oxide-Based Resistive Switching Memory," *IEEE Electron Device Lett.*, vol. 32, no. 3, pp. 276–278, 2011.
- [71] P. Huang, Y. C. Xiang, Y. D. Zhao, C. Liu, B. Gao, H. Q. Wu, H. Qian, X. Y. Liu, and J. F. Kang, "Analytic Model for Statistical State Instability and Retention Behaviors of Filamentary Analog RRAM Array and Its Applications in Design of Neural Network," in 2018 IEEE International Electron Devices Meeting (IEDM), pp. 40.4.1–40.4.4, 2018.
- [72] R. Waser, R. Bruchhaus, and S. Menzel, "Redox-based Resistive Switching Memories," in *Nanoelectronics and Information Technology* (R. Waser, ed.), pp. 683–710, Wiley-VCH, 3 ed., 2012.
- [73] L. Goux and I. Valov, "Electrochemical processes and device improvement in conductive bridge RAM cells," Phys. Status Solidi A, vol. 213, pp. 274–288, 2016.
- [74] M. N. Kozicki, M. Mitkova, and I.Valov, "Electrochemical Metallization Memories," in Resistive Switching: From Fundamentals of Nanoionic Redox Processes to Memristive Device Applications (D. Ielmini, R. Waser, ed.), pp. 483–514, Wiley-VCH, 1 ed., 2016.
- [75] S. Menzel and J.-H. Hur, "Modeling the VCM- and ECM-Type Switching Kinetics," in Resistive Switching: From Fundamentals of Nanoionic Redox Processes to Memristive Device Applications (D. Ielmini, R. Waser, ed.), pp. 395–436, Wiley-VCH, 1 ed., 2016.

- [76] I. Valov, R. Waser, J. R. Jameson, and M. N. Kozicki, "Electrochemical metallization memories—fundamentals, applications, prospects," *Nanotechnology*, vol. 22, no. 25, pp. 254003/1–22, 2011.
- [77] L. Goux and S. Spiga, "Unipolar Resistive-Switching Mechanisms," in Resistive Switching: From Fundamentals of Nanoionic Redox Processes to Memristive Device Applications (D. Ielmini, R. Waser, ed.), pp. 363–393, Wiley-VCH, 1 ed., 2016.
- [78] D. Ielmini, R. Bruchhaus, and R. Waser, "Thermochemical resistive switching: materials, mechanisms, and scaling projections," *Phase Transit.*, vol. 84, no. 7, pp. 570–602, 2011.
- [79] D. Cho, M. Lübben, S. Wiefels, K. Lee, and I. Valov, "Interfacial Metal Oxide Interactions in Resistive Switching Memories," ACS Appl. Mater. Interfaces, vol. 9, no. 22, pp. 19287–19295, 2017.
- [80] J. Lee, E. M. Bourim, W. Lee, J. Park, M. Jo, S. Jung, J. Shin, and H. Hwang, "Effect of ZrO<sub>x</sub>/HfO<sub>x</sub> bilayer structure on switching uniformity and reliability in nonvolatile memory applications," Appl. Phys. Lett., vol. 97, pp. 172105/1–3, 2010.
- [81] A. Hardtdegen, C. La Torre, F. Cüppers, S. Menzel, R. Waser, and S. Hoffmann-Eifert, "Improved Switching Stability and the Effect of an Internal Series Resistor in HfO<sub>2</sub>/TiO<sub>x</sub> Bilayer ReRAM Cells," *IEEE Trans. Electron Devices*, vol. 65, no. 8, pp. 3229–3236, 2018.
- [82] J. J. Yang, F. Miao, M. D. Pickett, D. A. A. Ohlberg, D. Stewart, C. N. Lau, and R. S. Williams, "The mechanism of electroforming of metal oxide memristive switches," *Nanotechnology*, vol. 20, no. 21, pp. 215201/1–9, 2009.
- [83] R. Münstermann, T. Menke, R. Dittmann, and R. Waser, "Coexistence of Filamentary and Homogeneous Resistive Switching in Fe-doped SrTiO<sub>3</sub> Thin-Film Memristive Devices," Adv. Mater., vol. 22, no. 43, pp. 4819–4822, 2010.
- [84] S. Schmelzer, "Ultra Thin Oxide Films for Dielectric and Resistive Memory Applications." *PhD thesis*, RWTH Aachen University, 2013.
- [85] M. Schie, S. Menzel, J. Robertson, R. Waser, and R. A. De Souza, "Field-enhanced route to generating anti-Frenkel pairs in HfO<sub>2</sub>," *Phys. Rev. Materials*, vol. 2, no. 3, pp. 035002/1–8, 2018.
- [86] A. O'Hara, G. Bersuker, and A. A. Demkov, "Assessing hafnium on hafnia as an oxygen getter," J. Appl. Phys., vol. 115, no. 18, pp. 183703/1–8, 2014.
- [87] S. Clima, B. Govoreanu, M. Jurczak, and G. Pourtois, "HfO $_{\rm x}$  as RRAM material First principles insights on the working principles," *Microelectronic Eng.*, vol. 120, pp. 13–18, 2014.
- [88] M. Sowinska, T. Bertaud, D. Walczyk, S. Thiess, M. A. Schubert, M. Lukosius, W. Drube, C. Walczyk, and T. Schröder, "Hard x-ray photoelectron spectroscopy study of the electroforming in Ti/HfO<sub>2</sub>-based resistive switching structures," Appl. Phys. Lett., vol. 100, pp. 233509/1–5, 2012.

- [89] K. Szot, W. Speier, G. Bihlmayer, and R. Waser, "Switching the electrical resistance of individual dislocations in single-crystalline SrTiO<sub>3</sub>," *Nat. Mater.*, vol. 5, no. 4, pp. 312– 320, 2006.
- [90] F. A. Kröger and H. J. Vink, "Relations between the Concentrations of Imperfections in Crystalline Solids," *Solid State Physics*, vol. 3, pp. 307–435, 1956.
- [91] E. Yalon, I. Karpov, V. Karpov, I. Riess, D. Kalaev, and D. Ritter, "Detection of the insulating gap and conductive filament growth direction in resistive memories," *Nanoscale*, vol. 7, no. 37, pp. 15434–15441, 2015.
- [92] A. Marchewka, R. Waser, and S. Menzel, "Physical Modeling of the Electroforming Process in Resistive-Switching Devices," in 2017 International Conference on Simulation of Semiconductor Processes and Devices (SISPAD), pp. 133–136, 2017.
- [93] D. Kalaev, E. Yalon, and I. Riess, "On the direction of the conductive filament growth in valence change memory devices during electroforming," *Solid State Ionics*, vol. 276, pp. 9–17, 2015.
- [94] U. Celano, L. Goux, R. Degraeve, A. Fantini, O. Richard, H. Bender, M. Jurczak, and W. Vandervorst, "Imaging the Three-Dimensional Conductive Channel in Filamentary-Based Oxide Resistive Switching Memory," *Nano Letters*, vol. 15, no. 12, pp. 7970–7975, 2015.
- [95] H. Du, C. Jia, A. Koehl, J. Barthel, R. Dittmann, R. Waser, and J. Mayer, "Nanosized conducting filaments formed by atomic-scale defects in redox-based resistive switching memories," *Chem. Mater.*, vol. 29, pp. 3164–3173, 2017.
- [96] A. Sharma, M. Noman, M. Abdelmoula, M. Skowronski, and J. Bain, "Electronic Instabilities Leading to Electroformation of Binary Metal Oxide-based Resistive Switches," Adv. Funct. Mater., vol. 24, pp. 5522–5529, 2014.
- [97] S. P. Waldow and R. A. De Souza, "Computational Study of Oxygen Diffusion along a[100] Dislocations in the Perovskite Oxide SrTiO<sub>3</sub>," ACS Appl. Mater. Interfaces, vol. 8, pp. 12246–56, 2016.
- [98] R. A. De Souza, "Oxygen Diffusion in SrTiO<sub>3</sub> and Related Perovskite Oxides," Adv. Funct. Mater., vol. 25, no. 40, pp. 6326–42, 2015.
- [99] M. Lübben and S. Wiefels and R. Waser and I. Valov, "Processes and Effects of Oxygen and Moisture in Resistively Switching  $TaO_x$  and  $HfO_x$ ," Adv. Electron. Mater., vol. 4, no. 1, pp. 1700458/1–11, 2018.
- [100] Y. Y. Chen, L. Goux, J. Swerts, M. Toeller, C. Adelmann, J. Kittl, M. Jurczak, G. Groeseneken, and D. J. Wouters, "Hydrogen-Induced Resistive Switching in TiN/ALD HfO<sub>2</sub>/PEALD TiN RRAM Device," *IEEE Electron Device Lett.*, vol. 33, pp. 483–485, 2012.
- [101] S. Kim, D. Lee, J. Park, S. Jung, W. Lee, J. Shin, J. Woo, G. Choi, and H. Hwang, "Defect engineering: reduction effect of hydrogen atom impurities in HfO<sub>2</sub>-based resistive-switching memory devices," *Nanotechnology*, vol. 23, no. 32, pp. 325702/1–6, 2012.

- [102] L. Goux, J. Y. Kim, B. Magyari-Kope, Y. Nishi, A. Redolfi, and M. Jurczak, "H-treatment impact on conductive-filament formation and stability in Ta<sub>2</sub>O<sub>5</sub>-based resistive-switching memory cells," *J. Appl. Phys.*, vol. 117, pp. 124501/1–5, 2015.
- [103] D. Cooper, C. Bäumer, N. Bernier, A. Marchewka, C. La Torre, R. E. Dunin-Borkowski, S. Menzel, R. Waser, and R. Dittmann, "Anomalous Resistance Hysteresis in Oxide ReRAM: Oxygen Evolution and Reincorporation Revealed by in situ TEM," Adv. Mater., vol. 29, no. 23, pp. 1700212/1–8, 2017.
- [104] F. Miao, J. J. Yang, J. Borghetti, G. Medeiros-Ribeiro, and R. S. Williams, "Observation of two resistance switching modes in TiO<sub>2</sub> memristive devices electroformed at low current," *Nanotechnology*, vol. 22, no. 25, pp. 254007/1–7, 2011.
- [105] X. Sun, G. Li, L. Chen, Z. Shi, and W. Zhang, "Bipolar resistance switching characteristics with opposite polarity of Au/SrTiO<sub>3</sub>/Ti memory cells," *Nanoscale Res. Lett.*, vol. 6, pp. 599/1–8, 2011.
- [106] A. Schönhals and C. M. M. Rosario and S. Hoffmann-Eifert and R. Waser and S. Menzel and D. J. Wouters, "Role of the Electrode Material on the RESET Limitation in Oxide ReRAM Devices," Adv. Electron. Mater., vol. 4, no. 2, pp. 1700243/1–11, 2017.
- [107] H. Zhang, S. Yoo, S. Menzel, C. Funck, F. Cüppers, D. J. Wouters, C. S. Hwang, R. Waser, and S. Hoffmann-Eifert, "Resistive Switching Modes with Opposite Polarity in Pt/TiO<sub>2</sub>/Ti/Pt Nano-sized ReRAM Devices," ACS Appl. Mater. Interfaces, vol. 10, no. 35, pp. 29766–29778, 2018.
- [108] A. Marchewka, R. Waser, and S. Menzel, "Physical Simulation of Dynamic Resistive Switching in Metal Oxides Using a Schottky Contact Barrier Model," in 2015 International Conference On Simulation of Semiconductor Processes and Devices (SISPAD), pp. 297–300, 2015.
- [109] A. Marchewka, R. Waser, and S. Menzel, "A 2D Axisymmetric Dynamic Drift-Diffusion Model for Numerical Simulation of Resistive Switching Phenomena in Metal Oxides," in 2016 International Conference On Simulation of Semiconductor Processes and Devices (SISPAD), pp. 145–148, 2016.
- [110] A. Wedig, M. Lübben, D.-Y. Cho, M. Moors, K. Skaja, V. Rana, T. Hasegawa, K. Adepalli, B. Yildiz, R. Waser, and I. Valov, "Nanoscale cation motion in TaO<sub>x</sub>, HfO<sub>x</sub> and TiO<sub>x</sub> memristive systems," *Nat. Nanotechnol.*, vol. 11, no. 1, pp. 67–74, 2016.
- [111] C.-Y. Lin, C.-Y.Wu, C.-Y. Wu, T.-C. Lee, F.-L. Yang, C. Hu, and T.-Y. Tseng, "Effect of Top Electrode Material on Resistive Switching Properties of ZrO<sub>2</sub> Film Memory Devices," *IEEE Electron Device Lett.*, vol. 28, no. 5, pp. 366–368, 2007.
- [112] T. Bertaud, D. Walczyk, C. Walczyk, S. Kubotsch, M. Sowinska, T. Schroeder, C. Wenger, C. Vallee, P. Gonon, C. Mannequin, V. Jousseaume, and H. Grampeix, "Resistive switching of HfO<sub>2</sub>-based Metal-Insulator-Metal diodes: Impact of the top electrode material," *Thin Solid Films*, vol. 520, no. 14, pp. 4551–4555, 2012.

- [113] Z. Fang, X. P. Wang, J. Sohn, B. B. Weng, Z. P. Zhang, Z. X. Chen, Y. Z. Tang, G. Lo, J. Provine, S. S. Wong, H.-P. Wong, and D. Kwong, "The Role of Ti Capping Layer in HfO<sub>x</sub>-Based RRAM Devices," *IEEE Electron Device Lett.*, vol. 35, no. 9, pp. 912–914, 2014.
- [114] W. Kim, S. Menzel, D. J. Wouters, Y. Guo, J. Robertson, B. Rösgen, R. Waser, and V. Rana, "Impact of oxygen exchange reaction at the ohmic interface in Ta<sub>2</sub>O<sub>5</sub>-based ReRAM devices," *Nanoscale*, vol. 8, no. 41, pp. 17774–17781, 2016.
- [115] C. Bäumer, C. Schmitz, A. Marchewka, D. N. Müller, R. Valenta, J. Hackl, N. Raab, S. P. Rogers, M. I. Khan, S. Nemsak, M. Shim, S. Menzel, C. M. Schneider, R. Waser, and R. Dittmann, "Quantifying redox-induced Schottky barrier variations in memristive devices via in operando spectromicroscopy with graphene electrodes," Nat. Commun., vol. 7, pp. 12398/1–7, 2016.
- [116] F. Nardi, S. Balatti, S. Larentis, and D. Ielmini, "Complementary switching in metal oxides: toward diode-less crossbar RRAMs," in 2011 IEEE International Electron Devices Meeting (IEDM), pp. 31.1/1–4, 2011.
- [117] Y. Yang, P. Sheridan, and W. Lu, "Complementary resistive switching in tantalum oxide-based resistive memory devices," *Appl. Phys. Lett.*, vol. 100, no. 20, pp. 203112/1–4, 2012.
- [118] S. A. Mojarad, J. P. Goss, K. S. K. Kwa, P. K. Petrov, B. Zou, N. Alford, and A. O'Neill, "Anomalous resistive switching phenomenon," *J. Appl. Phys.*, vol. 112, no. 12, pp. 124516/1–7, 2012.
- [119] S. Brivio, J. Frascaroli, and S. Spiga, "Role of metal-oxide interfaces in the multiple resistance switching regimes of  $Pt/HfO_2/TiN$  devices," *Appl. Phys. Lett.*, vol. 107, no. 2, pp. 23504/1–5, 2015.
- [120] K. V. Egorov, R. V. Kirtaev, Y. Y. Lebedinskii, A. M. Markeev, Y. A. Matveyev, O. M. Orlov, A. V. Zablotskiy, and A. V. Zenkevich, "Complementary and bipolar regimes of resistive switching in TiN/HfO<sub>2</sub>/TiN stacks grown by atomic-layer deposition," *Phys. Status Solidi A*, vol. 212, no. 4, pp. 809–816, 2015.
- [121] F. Nardi, S. Balatti, S. Larentis, D. Gilmer, and D. Ielmini, "Complementary Switching in Oxide-Based Bipolar Resistive-Switching Random Memory," *IEEE Trans. Electron Devices*, vol. 60, no. 1, pp. 70–77, 2013.
- [122] A. Marchewka, "A numerical simulation model of valence-change-based resistive switching." *PhD thesis*, RWTH Aachen University, 2017.
- [123] A. Schönhals, J. Mohr, D. J. Wouters, R. Waser, and S. Menzel, "3-bit Resistive RAM Write-Read Scheme Based on Complementary Switching Mechanism," *IEEE Electron Device Lett.*, vol. 38, no. 4, pp. 449–452, 2017.
- [124] J. J. Yang, J. Borghetti, D. Murphy, D. R. Stewart, and R. S. Williams, "A Family of Electronically Reconfigurable Nanodevices," Adv. Mater., vol. 21, no. 37, pp. 3754–3758, 2009.

- [125] S. Balatti, S. Ambrogio, D. C. Gilmer, and D. Ielmini, "Set Variability and Failure Induced by Complementary Switching in Bipolar RRAM," *IEEE Electron Device Lett.*, vol. 34, no. 7, pp. 861–863, 2013.
- [126] X. Chen, W. Hu, Y. Li, S. Wu, and D. Bao, "Complementary resistive switching behaviors evolved from bipolar TiN/HfO<sub>2</sub>/Pt device," *Appl. Phys. Lett.*, vol. 108, pp. 053504/1–4, 2016.
- [127] W. Banerjee, W. F. Cai, X. Zhao, Q. Liu, H. Lv, S. Long, and M. Liu, "Intrinsic anionic rearrangement by extrinsic control: transition of RS and CRS in thermally elevated TiN/HfO<sub>2</sub>/Pt RRAM," *Nanoscale*, vol. 9, no. 47, pp. 18908–18917, 2017.
- [128] L. Zhu, W. Hu, C. Gao, and Y. Guo, "Parasitic resistive switching uncovered from complementary resistive switching in single active-layer oxide memory device," *Semicond. Sci. Tech.*, vol. 32, no. 12, pp. 125018/1–7, 2017.
- [129] E. Linn, R. Rosezin, C. Kügeler, and R. Waser, "Complementary Resistive Switches for Passive Nanocrossbar Memories," *Nat. Mater.*, vol. 9, no. 5, pp. 403–406, 2010.
- [130] E. Linn, R. Rosezin, S. Tappertzhofen, U. Böttger, and R. Waser, "Beyond von neumann-logic operations in passive crossbar arrays alongside memory operations," *Nanotechnology*, vol. 23, pp. 305205/1–6, 2012.
- [131] A. Siemon, S. Menzel, R. Waser, and E. Linn, "A Complementary Resistive Switchbased Crossbar Array Adder," *IEEE J. Emerging Sel. Top. Circuits Syst.*, vol. 5, no. 1, pp. 64–74, 2015.
- [132] Y. Yang, J. Mathew, S. Pontarelli, M. Ottavi, and D. Pradhan, "Complementary Resistive Switch Based Arithmetic Logic Implementations Using Material Implication," *IEEE Trans. Nanotechnol.*, vol. 15, no. 1, pp. 94–108, 2016.
- [133] S. Ferch, E. Linn, R. Waser, and S. Menzel, "Simulation and comparison of two sequential logic-in-memory approaches using a dynamic electrochemical metallization cell model," *Microelectron. J.*, vol. 45, no. 11, pp. 1416–1428, 2014.
- [134] T. Breuer, A. Siemon, E. Linn, S. Menzel, R. Waser, and V. Rana, "A HfO<sub>2</sub>-Based Complementary Switching Crossbar Adder," *Adv. Electron. Mater.*, vol. 1, no. 10, pp. 1500138/1–10, 2015.
- [135] S. Gao, F. Zeng, M. Wang, G. Wang, C. Song, and F. Pan, "Implementation of Complete Boolean Logic Functions in Single Complementary Resistive Switch," *Sci. Rep.*, vol. 5, pp. 15467/1–10, 2015.
- [136] A. Gehring, "Simulation of Tunneling in Semiconductor Devices." *PhD thesis*, TU Wien, 2003.
- [137] R. Tsu and L. Esaki, "Tunneling in a finite superlattice," Appl. Phys. Lett., vol. 22, no. 11, pp. 562–564, 1973.
- [138] S. M. Sze and K. K. Ng, Physics of Semiconductor Devices. Wiley, 3 ed., 2007.

- [139] H. Bethe, "Theory of the Boundary Layer of Crystal Rectifiers," Radiation Laboratory, Massachusetts Institute of Technology, vol. 185, 1942.
- [140] F. Padovani and R. Stratton, "Field and thermionic-field emission in Schottky barriers," Solid-State Electron., vol. 9, no. 7, pp. 695–707, 1966.
- [141] S. Menzel, "Modeling and Simulation of Resistive Switching Devices." *PhD thesis*, RWTH Aachen University, 2012.
- [142] N. F. Mott and R. W. Gurney, *Electronic Processes in Ionic Crystals*. Oxford at the Clarendon Press, 2 ed., 1950.
- [143] A. R. Genreith-Schriever and R. A. De Souza, "Field-enhanced ion transport in solids: Reexamination with molecular dynamics simulations," *Phys. Rev. B*, vol. 94, no. 22, pp. 224304/1–5, 2016.
- [144] S. Menzel, M. von Witzleben, V. Havel, and U. Böttger, "The ultimate switching speed limit of redox-based restive switching devices," *Faraday Discuss.*, vol. 213, pp. 197–213, 2019.
- [145] M. Noman, W. Jiang, P. A. Salvador, M. Skowronski, and J. A. Bain, "Computational investigations into the operating window for memristive devices based on homogeneous ionic motion," *Appl. Phys. A*, vol. 102, no. 4, pp. 877–883, 2011.
- [146] J. Fleig, "On the current–voltage characteristics of charge transfer reactions at mixed conducting electrodes on solid electrolytes," *Phys. Chem. Chem. Phys.*, vol. 7, no. 9, pp. 2027–2037, 2005.
- [147] G. Wedler and H.-J. Freund, Lehrbuch der Physikalischen Chemie, ch. 6.8. Wiley-VCH, 6 ed., 2012.
- [148] W. Dahmen and A. Reusken, Numerik für Ingenieure und Naturwissenschaftler. Springer, 2 ed., 2008.
- [149] A. Hardtdegen, C. La Torre, H. Zhang, C. Funck, S. Menzel, R. Waser, and S. Hoffmann-Eifert, "Internal Cell Resistance as the Origin of Abrupt Reset Behavior in HfO<sub>2</sub>-based Devices determined from Current Compliance Series," in 2016 IEEE 8th International Memory Workshop (IMW), pp. 1–4, 2016.
- [150] K. Fleck, C. La Torre, N. Aslam, S. Hoffmann-Eifert, U. Böttger, and S. Menzel, "Uniting Gradual and Abrupt SET Processes in Resistive Switching Oxides," *Phys. Rev. Applied*, vol. 6, no. 6, pp. 064015/1–11, 2016.
- [151] S. Ambrogio, S. Balatti, A. Cubeta, A. Calderoni, N. Ramaswamy, and D. Ielmini, "Understanding switching variability and random telegraph noise in resistive RAM," in 2013 IEEE International Electron Devices Meeting (IEDM), pp. 31.5.1–31.5.4, 2013.
- [152] C. Y. Chen, A. Fantini, L. Goux, R. Degraeve, S. Clima, A. Redolfi, G. Groeseneken, and M. Jurczak, "Programming-conditions solutions towards suppression of retention tails of scaled Oxide-Based RRAM," in 2015 IEEE International Electron Devices Meeting (IEDM), pp. 10.6.1–10.6.4, 2015.

- [153] S. Menzel, M. Waters, A. Marchewka, U. Böttger, R. Dittmann, and R. Waser, "Origin of the Ultra-nonlinear Switching Kinetics in Oxide-Based Resistive Switches," Adv. Funct. Mater., vol. 21, no. 23, pp. 4487–4492, 2011.
- [154] S. Yu, Y. Wu, and H. Wong, "Investigating the switching dynamics and multilevel capability of bipolar metal oxide resistive switching memory," *Appl. Phys. Lett.*, vol. 98, no. 10, pp. 103514/1–3, 2011.
- [155] S. Menzel, M. Salinga, U. Böttger, and M. Wimmer, "Physics of the Switching Kinetics in Resistive Memories," Adv. Funct. Mater., vol. 25, no. 40, pp. 6306–6325, 2015.
- [156] GESTIS Substance Database. http://gestis-en.itrust.de, accessed 23 April 2019.
- [157] C. La Torre, A. F. Zurhelle, and S. Menzel, "Compact Modelling of Resistive Switching Devices based on the Valence Change Mechanism," in 2019 International Conference on Simulation of Semiconductor Processes and Devices (SISPAD), 2019.
- [158] C. La Torre, A. F. Zurhelle, T. Breuer, R. Waser, and S. Menzel, "Compact Modeling of Complementary Switching in Oxide-Based ReRAM Devices," *IEEE Trans. Electron Devices*, vol. 66, no. 3, pp. 1268–1275, 2019.
- [159] H. Z. Zhang, D. S. Ang, K. S. Yew, and X. P. Wang, "Enhanced stability of complementary resistance switching in the TiN/HfO<sub>x</sub>/TiN resistive random access memory device via interface engineering," *Appl. Phys. Lett.*, vol. 108, no. 8, pp. 83505/1–5, 2016.
- [160] M. J. Wang, F. Zeng, S. Gao, C. Song, and F. Pan, "Multi-mode resistive switching behaviors induced by modifying Ti interlayer thickness and operation scheme," J. Alloy. Compd., vol. 667, pp. 219–224, 2016.
- [161] W. Lee, S. Yoo, K. J. Yoon, I. W. Yeu, H. J. Chang, J. H. Choi, S. Hoffmann-Eifert, R. Waser, and C. S. Hwang, "Resistance switching behavior of atomic layer deposited SrTiO<sub>3</sub> film through possible formation of Sr<sub>2</sub>Ti<sub>6</sub>O<sub>13</sub> or Sr<sub>1</sub>Ti<sub>11</sub>O<sub>20</sub> phases," Sci. Rep., vol. 6, pp. 20550/1–16, 2016.
- [162] T. You, Y. Shuai, W. Luo, N. Du, D. Bürger, I. Skorupa, R. Hübner, S. Henker, C. Mayr, R. Schüffny, T. Mikolajick, O. G. Schmidt, and H. Schmidt, "Exploiting Memristive BiFeO<sub>3</sub> Bilayer Structures for Compact Sequential Logics," *Adv. Funct. Mater.*, vol. 24, pp. 3357–3365, 2014.
- [163] X. Liu, S. Sadaf, S. Park, S. Kim, E. Cha, D. Lee, G. Jung, and H. Hwang, "Complementary Resistive Switching in Niobium Oxide-Based Resistive Memory Devices," *IEEE Electron Device Lett.*, vol. 34, no. 2, pp. 235–237, 2013.
- [164] A. Kindsmüller unpublished results.
- [165] N. G. Nilsson, "An Accurate Approximation of the Generalized Einstein Relation for Degenerate Semiconductors," *Phys. Status Solidi A*, vol. 19, no. 1, pp. K75–K78, 1973.
- [166] A. Kindsmüller, A. Meledin, J. Mayer, R. Waser, and D. J. Wouters, "On the role of the metal oxide/reactive electrode interface during the forming procedure of valence change ReRAM devices," *submitted to Nanoscale*.

- [167] C. La Torre, A. Kindsmüller, D. J. Wouters, C. E. Graves, G. A. Gibson, J. P. Strachan, R. S. Williams, R. Waser, and S. Menzel, "Volatile HRS asymmetry and subloops in resistive switching oxides," *Nanoscale*, vol. 9, pp. 14414–14422, 2017.
- [168] M. Hüttemann, "Optimierung der Endurance resistiv schaltender Valenzwechsel-Speicherzellen." Bachelor thesis, RWTH Aachen University, 2019.
- [169] M. Zhao, H. Wu, B. Gao, X. Sun, Y. Liu, P. Yao, Y. Xi, X. Li, Q. Zhang, K. Wang, S. Yu, and H. Qian, "Characterizing Endurance Degradation of Incremental Switching in Analog RRAM for Neuromorphic Systems," in 2018 IEEE International Electron Devices Meeting (IEDM), pp. 20.2.1–20.2.4, 2018.
- [170] Y. Y. Chen, R. Degraeve, S. Clima, B. Govoreanu, L. Goux, and A. Fantini, "Understanding of the Endurance Failure in Scaled HfO<sub>2</sub>-based 1T1R RRAM through Vacancy Mobility Degradation," in 2012 IEEE International Electron Devices Meeting (IEDM), pp. 20.3.1 20.3.4, 2012.
- [171] J. Song, D. Lee, J. Woo, Y. Koo, E. Cha, S. Lee, J. Park, K. Moon, S. H. Misha, A. Prakash, and H. Hwang, "Effects of RESET Current Overshoot and Resistance State on Reliability of RRAM," *IEEE Electron Device Lett.*, vol. 35, no. 6, pp. 636–638, 2014.
- [172] C. Y. Chen, L. Goux, A. Fantini, A. Redolfi, S. Clima, R. Degraeve, Y. Y. Chen, G. Groeseneken, and M. Jurczak, "Understanding the Impact of Programming Pulses and Electrode Materials on the Endurance Properties of Scaled Ta<sub>2</sub>O<sub>5</sub> RRAM Cells," in 2014 IEEE International Electron Devices Meeting (IEDM), pp. 14.2.1–14.2.4, 2014.
- [173] M. Azzaz, E. Vianello, B. Sklenard, P. Blaise, A. Roule, C. Sabbione, S. Bernasconi, C. Charpin, C. Cagli, E. Jalaguier, S. Jeannot, S. Denorme, P. Candelier, M. Yu, L. Nistor, C. Fenouillet-Beranger, and L. Perniola, "Endurance/Retention Trade Off in HfO<sub>x</sub> and TaO<sub>x</sub> Based RRAM," in 2016 IEEE 8th International Memory Workshop (IMW), pp. 1–4, 2016.
- [174] B. Chen, Y. Lu, B. Gao, Y. H. Fu, F. F. Zhang, P. Huang, Y. S. Chen, L. F. Liu, X. Y. Liu, J. F. Kang, Y. Y. Wang, Z. Fang, H. Y. Yu, X. Li, X. P. Wang, N. Singh, G. Q. Lo, and D. L. Kwong, "Physical Mechanisms of Endurance Degradation in TMO-RRAM," in 2011 IEEE International Electron Devices Meeting (IEDM), pp. 12.3.1 12.3.4, 2011.
- [175] G. Sassine, D. Alfaro Robayo, C. Nail, J.-F. Nodin, J. Coignus, G. Molas, and E. Nowak, "Optimizing Programming Energy for Improved RRAM Reliability for High Endurance Applications," in 2018 IEEE International Memory Workshop (IMW), pp. 1–4, 2018.
- [176] B. Govoreanu, A. Ajaykumar, H. Lipowicz, Y. Chen, J. Liu, R. Degraeve, L. Zhang, S. Clima, L. Goux, I. Radu, A. Fantini, N. Raghavan, G. Kar, W. Kim, A. Redolfi, D. Wouters, L. Altimime, and M. Jurczak, "Performance and Reliability of Ultra-Thin HfO<sub>2</sub>-based RRAM (UTO-RRAM)," in 2013 5th IEEE International Memory Workshop (IMW), pp. 48–51, 2013.
- [177] D. R. B. Ly, B. Giraud, J. Noel, A. Grossi, N. Castellani, G. Sassine, J. Nodin, G. Molas, C. Fenouillet-Beranger, G. Indiveri, E. Nowak, and E. Vianello, "In-depth Characterization of Resistive Memory-Based Ternary Content Addressable Memories," in 2018 IEEE International Electron Devices Meeting (IEDM), pp. 20.3.1–20.3.4, 2018.

- [178] Y. Lu, B. Chen, B. Gao, Z. Fang, Y. H. Fu, J. Q. Yang, L. F. Liu, X. Y. Liu, H. Y. Yu, and J. F. Kang, "Improvement of Endurance Degradation for Oxide Based Resistive Switching Memory Devices Correlated With Oxygen Vacancy Accumulation Effect," in 2012 IEEE International Reliability Physics Symposium (IRPS), pp. MY.4.1–4, 2012.
- [179] C. Sung, J. Song, S. Lee, and H. Hwang, "Improved Endurance of RRAM by Optimizing Reset Bias Scheme in 1T1R Configuration to Suppress Reset Breakdown," in 2016 IEEE Silicon Nanoelectronics Workshop (SNW), pp. 84–85, 2016.
- [180] Y. Chen, L. Goux, S. Clima, B. Govoreanu, R. Degraeve, G. Kar, A. Fantini, G. Groeseneken, D. Wouters, and M. Jurczak, "Endurance/Retention Trade-off on HfO<sub>2</sub>/Metal Cap 1T1R Bipolar RRAM," *IEEE Trans. Electron Devices*, vol. 60, no. 3, pp. 1114–1121, 2013.
- [181] C. Chen, L. Goux, A. Fantini, S. Clima, R. Degraeve, A. Redolfi, Y. Chen, G. Groeseneken, and M. Jurczak, "Endurance degradation mechanisms in TiN/Ta<sub>2</sub>O<sub>5</sub>/Ta resistive random-access memory cells," *Appl. Phys. Lett.*, vol. 106, no. 5, pp. 053501/1–3, 2015.
- [182] C. Nail, G. Molas, P. Blaise, G. Piccolboni, B. Sklenard, C. Cagli, M. Bernard, A. Roule, M. Azzaz, E. Vianello, C. Carabasse, R. Berthier, D. Cooper, C. Pelissier, T. Magis, G. Ghibaudo, C. Vallee, D. Bedeau, O. Mosendz, B. D. Salvo, and L. Perniola, "Understanding RRAM endurance, retention and window margin trade-off using experimental results and simulations," in 2016 IEEE International Electron Devices Meeting (IEDM), pp. 4.5.1–4.5.4, 2016.
- [183] D. K. Zhang, "Kompaktmodellierung des Sauerstoffaustauschs an der aktiven Elektrode von Valenzwechselspeicherzellen." Bachelor thesis, RWTH Aachen University, 2018.
- [184] JART, "Juelich Aachen Resistive Switching Tools (JART)". www.emrl.de/JART.html, 2019.
- [185] T. Heisig, C. Baeumer, U. N. Gries, M. P. Müller, C. La Torre, M. Lübben, N. Raab, H. Du, S. Menzel, D. N. Müller, C.-L. Jia, J. Mayer, R. Waser, I. Valov, R. A. De Souza, and R. Dittmann, "Oxygen exchange processes between oxide memristive devices and water molecules," Adv. Mater., vol. 30, no. 29, pp. 1800957/1–7, 2018.
- [186] WebElements. https://www.webelements.com, accessed 06 March 2019.
- [187] C. E. Graves, N. Dávila, E. J. Merced-Grafals, S.-T. Lam, J. P. Strachan, and R. S. Williams, "Temperature and field-dependent transport measurements in continuously tunable tantalum oxide memristors expose the dominant state variable," Appl. Phys. Lett., vol. 110, pp. 123501/1–5, 2017.

## List of Publications

#### **Peer Reviewed Journals**

- C. La Torre, A. F. Zurhelle, T. Breuer, R. Waser, and S. Menzel, "Compact Modeling of Complementary Switching in Oxide-Based ReRAM Devices," *IEEE Trans. Electron Devices*, vol. 66, no. 3, pp. 1268-1275, 2019
- A. Hardtdegen\*, C. La Torre\*, F. Cüppers, S. Menzel, R. Waser, and S. Hoffmann-Eifert, "Improved Switching Stability and the Effect of an Internal Series Resistor in HfO<sub>2</sub>/TiO<sub>x</sub> Bilayer ReRAM Cells," *IEEE Trans. Electron Devices*, vol. 65, no. 8, pp. 3229-3236, 2018
- T. Heisig, C. Bäumer, U. N. Gries, M. P. Müller, C. La Torre, M. Lübben, N. Raab, H. Du, S. Menzel, D. N. Müller, C.-L. Jia, J. Mayer, R. Waser, I. Valov, R. A. De Souza, and R. Dittmann, "Oxygen Exchange Processes between Oxide Memristive Devices and Water Molecules," *Adv. Mater.*, vol. 30, no. 29, pp. 1800957/1-7, 2018
- C. La Torre\*, A. Kindsmüller\*, D. J. Wouters, C. E. Graves, G. A. Gibson, J. P. Strachan, R. S. Williams, R. Waser, and S. Menzel, "Volatile HRS asymmetry and subloops in resistive switching oxides," *Nanoscale*, vol. 9, pp. 14414-14422, 2017
- D. Cooper, C. Bäumer, N. Bernier, A. Marchewka, C. La Torre, R. E. Dunin-Borkowski, S. Menzel, R. Waser, and R. Dittmann, "Anomalous Resistance Hysteresis in Oxide ReRAM: Oxygen Evolution and Reincorporation Revealed by in situ TEM," *Adv. Mater.*, vol. 29, no. 23, pp. 1700212/1-8, 2017
- K. Fleck\*, C. La Torre\*, N. Aslam, S. Hoffmann-Eifert, U. Böttger, and S. Menzel, "Uniting Gradual and Abrupt SET Processes in Resistive Switching Oxides," *Phys. Rev. Applied*, vol. 6, no. 6, pp. 064015/1-11, 2016
- C. La Torre, K. Fleck, S. Starschich, E. Linn, R. Waser, and S. Menzel, "Dependence of the SET switching variability on the initial state in  $HfO_x$ -based ReRAM," *Phys. Status Solidi A*, vol. 213, no. 2, pp. 316-319, 2016
- D. O. Schmidt, S. Hoffmann-Eifert, H. Zhang, C. La Torre, A. Besmehn, M. Noyong, R. Waser, and U. Simon, "Resistive Switching of Individual, Chemically Synthesized TiO<sub>2</sub> Nanoparticles," *Small*, vol. 11, no. 48, pp. 6444-6456, 2015

<sup>\*</sup>Authors contributed equally

### **Conference Proceedings**

- C. La Torre, A. F. Zurhelle, and S. Menzel, "Compact Modelling of Resistive Switching Devices based on the Valence Change Mechanism," 2019 International Conference on Simulation of Semiconductor Processes and Devices (SISPAD), 2019
- A. Schönhals, A. Kindsmüller, C. La Torre, H. Zhang, S. Hoffmann-Eifert, S. Menzel, R. Waser, and D. J. Wouters, "Overcoming the RESET Limitation in Tantalum Oxide-Based ReRAM Using an Oxygen-Blocking Layer," 2017 IEEE International Memory Workshop (IMW), 2017
- A. Hardtdegen, C. La Torre, H. Zhang, C. Funck, S. Menzel, R. Waser, and S. Hoffmann-Eifert, "Internal Cell-Resistance as the Origin of Abrupt Reset Behavior in HfO<sub>2</sub>-Based Devices Determined from Current Compliance Series," 2016 IEEE International Memory Workshop (IMW), 2016

#### **Conference Talks and Posters**

- C. La Torre, A. Zurhelle, M. Frentzen, M. Burgardt, R. Waser, and S. Menzel, "Modeling the Influence of the Oxygen Exchange at the Ohmic Electrode in Oxide-Based ReRAM Devices," *The International Conference on Memristive Materials, Devices & Systems (MEMRISYS)*, Beijing, China, 03-05 July, 2018
- C. La Torre, K. Fleck, N. Aslam, S. Hoffmann-Eifert, U. Böttger, R. Waser, and S. Menzel, "Analysis of the Two-Part SET Switching Process in STO-based ReRAM," MRS Fall Meeting, Boston, USA, 27 Nov 2 Dec, 2016
- C. La Torre, S. Starschich, K. Fleck, E. Linn, R. Waser, and S. Menzel, "Measurement and Modeling of the Cycle-to-Cycle Variability of the SET Switching Time in  $HfO_x$ -based ReRAM," *EMRS Spring Meeting*, Lille, France, 11-15 May, 2015
- C. La Torre, M. Kühn, S. Starschich, S. Menzel, U. Böttger, and R. Waser, "Parameter Study of HfO<sub>x</sub>-based ReRAM (Poster)," *Nanoelectronic Days*, Jülich, Germany, 27-29 April, 2015